

ON THE DYNAMICAL EVOLUTION OF MULTI-PLANET SYSTEMS

A Dissertation

Presented to the Faculty of the Graduate School

of Cornell University

in Partial Fulfillment of the Requirements for the Degree of

Doctor of Philosophy

by

Bonan Pu (濮勃南)

August 2020

© 2020 Bonan Pu

ALL RIGHTS RESERVED

ON THE DYNAMICAL EVOLUTION OF MULTI-PLANET SYSTEMS

Bonan Pu (濮勃南), Ph.D.

Cornell University 2020

Recent advances in radial velocity and transit surveys have led to a large increase in the number of detected multi-planet systems, indicating that such systems are common in the Galaxy. These multi-planet systems bear little resemblance to our own Solar System: most of the detected exo-planets are Super-Earths or Mini-Neptunes, and have periods shorter than 200 days. The discovery of these systems have challenged conventional notions of planetary dynamics, and exposed fertile areas of research. In this thesis, I present three papers on the dynamical evolution of multi-planet systems in the context of findings by Kepler and similar missions. (1) I study the dynamical effects of eccentric and/or misaligned external companions on inner multi-planet systems. (2) I study the effect of hard scatterings between outer giant planets on inner multi-planet systems, and derive a mathematical model to compute the distribution of the final system parameters. (3) Turning my attention inward, I propose a low-eccentricity migration mechanism to explain the origins of ultra-short-period planets, an unusual subset of Kepler planets whose origins are presently not well understood.

BIOGRAPHICAL SKETCH

Bonan Pu was born in Harbin, China. At the age of 9, he moved across the Pacific Ocean to Ames, Iowa, USA, and later settled in Toronto, Canada in 2003. He attended Forest Manor Public School, St. Andrews JHS and Don Mills Collegiate Institute. In 2011 he attended the University of Toronto, and earned a B. Sc in Physics and Astronomy in 2015. He began to pursue a PhD at Cornell University in the same year, working with Professor Dong Lai on planetary dynamics. Bonan has three lifelong interests: natural science, existentialism and politics. He will move to New York City in Fall 2020 in pursuit of this trifecta.

This document is dedicated to humanity's pursuit of knowledge.

ACKNOWLEDGEMENTS

First and foremost I thank my advisor Dong Lai. Long before I came to Cornell, I had already heard about Dong having a great track record of advising students. When I got to Cornell I quickly understood why. Not only is Dong an extremely productive and excellent researcher, but he also pours his heart and soul into his students' work. Dong had great ways to keep me motivated and productive, without being pressuring or overbearing. I am truly lucky to have Dong as my advisor.

In addition, I must thank my undergraduate advisor Yanqin Wu, who was my first introduction to research in astrophysics. I found Yanqin to be a really special astrophysicist: Her work is always technically and scientifically interesting, and almost always correct. She had left a great impression on me and gave me a great foundation to start my graduate school career.

My PhD was funded in large part by the United States National Aeronautics and Space Administration (NASA) through the NASA Earth and Space Sciences Fellowship, for which I am grateful.

I thank Kristine for providing company through difficult times, and my parents for raising me and bringing me to Canada.

I thank the members of my PhD committee: David Chernoff, James Lloyd and Jonathan Lunine for their on-going support. I also thank Monica Lee Carpenter and Bez Thomas for their help throughout my PhD studies.

I acknowledge my collaborators Wei Zhu and Songhu Wang for interesting discussions that helped re-ignite my interest in research.

During my four years at DMCI, I was strongly influenced by the teachers and peers around me, who played a big role in my decision to pursue graduate studies. I would like to acknowledge my wonderful teachers and fellow 'gifties', with special thanks to Monica Segall, Chamkaur Sidhu, Vida Ghaem-Maghami, and David Carter.

I would also like to thank the professors at the University of Toronto that I've had the pleasure of learning from and working with. Special thanks to professors Diana Valencia, Marten van Kerkwijk and Dylan Jones.

I enjoyed my interactions with members of Dong's research group, in particular conversations and collaborations with Kassandra Anderson, Michelle Vick, J. J. Zanazzi, Yubo Su, Jiaru Li, and Chris O' Connor. I also acknowledge Zhengze Zhou and Li'Ao Zhu for getting me interested in statistics.

I am thankful to the wonderful Cornell Astronomy professors that I've had the pleasure of taking classes from: Phil Nicholson, Ira Wasserman, Jonathan Lunine, Jim Cordes, and David Chernoff. I am also thankful to Bart Selman and Chris De Sa for introducing me to machine learning and AI, and to Uriel Abulof for being the inspiration of much contemplation and reflection.

I thank Benjamin Woodcock for his help in guiding me to gainful employment.

Finally, I thank the people of Toronto and Canada for accepting me as one of their own.

CONTENTS

Biographical Sketch	iii
Dedication	iv
Acknowledgements	v
Contents	vii
List of Figures	x
1 Introduction	1
2 Eccentricities and Inclinations of Multiplanet Systems with External Perturbers	9
2.1 Introduction	9
2.2 Eccentricity and Inclination Excitation in Linearized Secular Theory . .	13
2.2.1 “One Planet + Perturber” System: Eccentricity	16
2.2.2 “Two Planets + Perturber” System: Mutual Inclination	17
2.2.3 “Two Planets + Perturber” System: Eccentricity	20
2.3 Extension to Moderately Inclined and Eccentric Perturbers	25
2.3.1 Secular Equations	28
2.3.2 Results for “Two Planets + Perturber” System	31
2.3.3 Resonance Feature and Internal Lidov-Kozai Oscillations	32
2.4 Comparison with N-body Integrations	33
2.5 $N > 2$ Inner Planets + Perturber	41
2.5.1 Multi-planet Eccentricity Evolution : Linear Theory	42
2.5.2 Multi-planet Inclination: Linear Theory	44
2.5.3 Extension to Modest Eccentricities and Inclinations	46
2.6 Application to the Kepler-11 System	47
2.7 Summary and Discussion	50
3 On the Scattering of Cold Jupiters and its Influence on Inner Planet Systems: Theory and Simulation	54
3.1 Introduction	54
3.2 Gravitational Scatterings of Two Giant Planets	59
3.2.1 Numerical Set-Up	60
3.2.2 Final Outcomes of Scatterings: Orbital Parameters	61
3.2.3 Timescale to Ejection	65
3.2.4 Theoretical Model for CJ Scattering	71
3.2.5 Scattering into inner system	75
3.3 Semi-Secular Algorithm for “N+2” Scatterings	77
3.4 1+2 Scattering	81
3.4.1 Empirical Results	82
3.4.2 Analytic Model for “1+2” Secular Evolution: Eccentricity	87
3.4.3 Inclination Evolution	96
3.4.4 Marginal Distribution of the Boost Factor	97

3.4.5	Theoretical Model: Simplifications and Refinements	99
3.5	Extension to More Inner Planets	101
3.5.1	Two inner planets	102
3.5.2	3 or More Inner Planets	103
3.6	Summary and Discussion	106
3.6.1	Summary	106
3.6.2	Caveats	108
3.6.3	Application to Specific Systems	110
4	Low-Eccentricity Migration of Ultra-Short Period Planets in Multiplanet Systems	114
4.1	Introduction	114
4.2	Eccentricity Evolution and Orbital Decay: Formalism	118
4.2.1	Eccentricity Evolution in the Framework of Eigenmodes	123
4.3	Two-Planet Systems	127
4.3.1	Mode Properties and General Evolution Behaviors	127
4.3.2	Criteria for Orbital Decay	131
4.4	Three-Planet Systems	134
4.4.1	Set-up	134
4.4.2	Time Evolution & Mode Mixing	136
4.4.3	Criteria for Orbital Decay	139
4.5	Inclination Evolution	143
4.5.1	Inclination Evolution in the Framework of Eigenmodes	148
4.5.2	Resonance Crossing and Mutual Inclination Excitation	153
4.6	Population Synthesis Model	155
4.7	Discussion	160
4.7.1	Low- e USP migration and observations	162
4.7.2	Specific sources	169
4.7.3	Are USPs photo-evaporated cores of mini-Neptunes?	170
4.7.4	Uncertainties and Future Work	171
4.8	Summary and Conclusion	173
A	Hybrid Secular Equations	177
B	Prescription for Eccentricity and Inclination of “N Planets + Perturber” Systems	181
C	Calculation of Moments of \mathcal{E}_a	183
D	Branching Ratio of Unstable Systems	184
D.1	Introduction	184
D.2	Theoretical Model	186
D.2.1	Collisional Timescale	187
D.2.2	Ejection Timescale	188

D.2.3	The Branching Ratio	189
D.3	Gravitational Focussing	190
D.4	Finite Integration Time-limit Effects	193

LIST OF FIGURES

- 2.1 RMS values of the mutual inclination between the inner planets in a fiducial two-planet system under the influence of a mis-aligned perturber. The perturber has initial eccentricity $e_p = 0$ and inclination $\theta_p = 0.1$ rad. Planet 1 has a fixed mass at $m_1 = M_\oplus$ while the mass of planet 2 varies from $0.3M_\oplus$ to $30M_\oplus$ and are represented by different colors. The perturber has a mass of $m_p = 3M_J$ and its semi-major axis is varied to produce different ϵ_{12} , the coupling strength of the perturbation (Eq. 2.15). The solid colored points represent the results of numerical integrations using secular equations, while the solid colored curves are calculated using linearized theory. The dashed vertical line corresponds to $\epsilon_{12} = 1$, where a resonance feature occurs. Note that the resonance feature becomes sharper and more pronounced as the mass ratio m_2/m_1 increases. The horizontal dashed line corresponds to the weak-coupling limit $\text{RMS}(\theta_{12}) \simeq \sqrt{2}\theta_p$, which holds when $\epsilon_{12} \gg 1$. The solid black line is the prediction from secular theory, when the planets are strongly coupled ($\epsilon_{12} \ll 1$). 15
- 2.2 RMS values of the eccentricities of the planets in a fiducial two-planet system under the influence of an eccentric perturber. The perturber has initial eccentricity $e_p = 0.1$ and has an orbit co-planar with the inner system. The other parameters are the same as Fig. 2.1. The solid colored points represent the results of numerical integrations using secular equations, while the solid colored curves are calculated using linearized theory; the dashed colored lines show the forced eccentricity (Eq. 2.26). The dashed vertical line corresponds to $\epsilon_{12} = 1$ 16
- 2.3 RMS values of e_1 , e_2 and θ_{12} (top to bottom) as a function of ϵ_{12} and a_p for a 2-planet system with different spacings a_2/a_1 . The solid curves are results of numerical integrations using the hybrid secular equations (Eqs. A.2 - A.5) while the results of N-body simulations are marked with an “×” if the system becomes gravitationally unstable with respect to orbit crossings within 10^5 yr, otherwise they are marked with a filled square. The different colored lines represent different values of a_2/a_1 , with red, green and blue being $a_2/a_1 = 1.2, 1.3, 1.4$ respectively. In each case, $a_1 = 0.3$ au, and a_p is varied from 0.6 to 3.0 au. The planet masses are $m_1 = m_2 = 3M_\oplus$ and $m_p = 3M_J$. The inner planets are initially on circular and co-planar orbits while the perturber has $e_p = 0.05$ and $\theta_p = 0.1$ 18

- 2.4 RMS values of the inner planet eccentricities e_1, e_2 and their mutual inclination θ_{12} as a function of e_p for a “2-planet plus perturber system” with $a_1 = 0.3$ au, $a_2 = 0.5$ au, $m_1 = 3M_\oplus$ and $m_2 = 5m_1$, perturbed by a $m_p = 5M_J$ planet. The panels, from left to right, represent three different perturber strengths ϵ_{12} , which is varied by adjusting a_p . The different colors are for different values of θ_p , with red, blue and green being $\theta_p = 0.2, 0.3, 0.4$ respectively. The points are the results of numerical secular equation integrations using Eqs. (A.2) - (A.5) while the solid lines are analytical results based on non-linear extensions to linear secular theory (Sec. 2.2). For the left and center panels where $\epsilon_{12} > 1$, we obtain the solid curves from Eqs. (2.54) - (2.56), while for the right panel they were obtained from Eqs. (2.51) - (2.53). A point is marked with an ‘o’ if the inner system is stable, and ‘x’ if it is unstable with respect to the stability criterion (Eq. 2.57). Each point represents 3 different numerical secular simulations with otherwise identical initial parameters, except with the initial longitude of ascending node and longitude of perihelion sampled randomly in the interval $[0, 2\pi]$ 26
- 2.5 Same as Fig. 2.4, except that the results are plotted as a function of θ_p . The different colors are for different values of e_p with red, blue and green being $e_p = 0.2, 0.3, 0.4$ respectively. The dashed line in the center bottom panel corresponds to $\theta_{12} = 0.68$ rad. (39°), the Lidov-Kozai critical angle. Note that when $\theta_{12} \leq 0.68$ rad., the inner planets experience mutual Lidov-Kozai oscillations leading to large excitation of e_1 (see the middle column). 27
- 2.6 Same as Fig. 2.4, except that the results are plotted as a function of ϵ_{12} . The variation of ϵ_{12} is achieved by fixing $m_p = 5M_J$ while varying a_p . The different colors are for different values of e_p , with red, blue and green being $e_p = 0.2, 0.3, 0.4$ respectively. The panels from left to right have different values of $\theta_p = 0.2, 0.3, 0.4$ respectively. For the bottom three panels, the solid lines are derived from Eq. (2.16), but with ω_{jp} replaced by $\tilde{\omega}_{jp}$ (Eq. 2.47). The horizontal dashed line corresponds to $\theta_{12} = 0.68$ rad. 28

- 2.7 Sample evolution of “two-planet + perturber” system using N-body integrations. From top to bottom, the y-axis shows e_1 , e_2 , and θ_{12} . From left to right are three different scenarios corresponding to the stable, unstable and nonlinear (Lidov-Kozai-like oscillation) regimes. The red curve shows results based on secular integration while the blue curve are from N-body integration using the same initial parameters. Left: an example where the secular hybrid algorithm matches closely with N-body integrations. For this particular model, a_1, a_2, a_p are 0.3, 0.39 and 1.6 au respectively, while $m_1 = m_2 = 3M_\oplus$ and $m_p = 3M_J$. The perturber has $e_p = a_p = 0.1$. Center: Same as left, except here $a_p = 1.26$ au. This is an example of the inner two planets driven into dynamical instability, as a result of eccentricity excitation by the perturber. Right: An example of Kozai-like oscillations. Here, a_1, a_2, a_p are 0.3, 0.45, 1.94 au respectively, such that $\epsilon_{12} \simeq 1$. The planets have masses $m_1 = 0.6M_\oplus$, $m_2 = 3M_\oplus$ and $m_p = 3M_J$, and the perturber has $m_p = 3M_J$, $e_p = 0.02$ and $\theta_p = 0.4$ 34
- 2.8 RMS values of planet eccentricities and inclinations for a “2-planet + perturber” system with $a_1 = 0.3$ au, $a_2 = 0.5$ au, $m_1 = 0.6M_\oplus$ and $m_2 = 3M_\oplus$, perturbed by a $m_p = 5M_J$ planet. The panels, from left to right, represent three different perturber strengths ϵ_{12} , which is varied by adjusting a_p . The different colors are for different values of e_p , with red, blue and green corresponding to $e_p = 0.2, 0.3$, and 0.4 respectively. The solid curves are the results based on N-body integrations while the dashed curves are the results of hybrid secular equations. Systems that are stable during the integration were marked with a filled square for the solid curves, while those that were unstable with respect to orbit crossings are marked with a star. The dashed horizontal lines on the bottom panels corresponds to $\theta_{12} = 0.68$ rad. 35
- 2.9 Same as Fig. 2.8, except that $m_1 = m_2 = 3M_\oplus$ 36

- 2.10 Comparison of the RMS values of planet eccentricities and inclinations for a hypothetical 4-planet system under the influence of an inclined, eccentric perturber, computed from secular theory (solid and dashed curves) and N-body simulations ('x' and squares). The planets have masses $m_1 = m_2 = m_4 = 3M_\oplus$, and the 3rd planet is the 'dominant' one with $m_d = m_3$ equal to 3, 9, and $30M_\oplus$ for the red, green and blue curves respectively. The semi-major axes of the four inner planets are [0.1, 0.15, 0.25, 0.4] au, while \bar{e} is varied by varying a_p . Points that are marked with filled squares represent systems stable against orbit crossings, while systems that have undergone orbit crossings are marked with an 'x'. From the top panel, the y-axis is the RMS eccentricity averaged over all planets, as function of mean coupling parameter \bar{e} . The left panel represents a "linear" case with $e_p = \theta_p = 0.1$ while the right panel has $e_p = \theta_p = 0.4$. The colored dashed lines are given by the forced eccentricity only (Eq. 2.68), while the solid curves are analytical estimates based on linear theory, given by Eq. (2.67) on the left panel and using the mild e_p extension (Eq. 2.77) on the right panel. The bottom panels are similar to the top panels, except the mean pairwise mutual inclination σ_θ is plotted on the y-axis. The solid curves are obtained from Eq. (2.75) for the left panel, with the nonlinear extension Eq. (2.78) being used for the right panel. 40
- 2.11 RMS orbital eccentricity and mutual inclination (Eqs. 2.58 - 2.59) of the Kepler-11 system when being perturbed by a hypothetical misaligned and eccentric external companion. The top panels show the RMS eccentricity while the bottom panel shows the RMS mutual inclination. The perturber, whose coupling strength is parametrized by \bar{e} , has mass $3M_J$ and semi-major axis ranging from 1 - 3 au; its eccentricity is $e_p = 0.1$ for the left panels, and $e_p = 0.4$ for the right panels. The inner 6 planets are initially started on circular, co-planar orbits. The red, green and blue curves correspond to different values of $\theta_p = 0.1, 0.2, 0.4$ respectively. The solid lines are obtained from our hybrid secular theory (Eqs. 2.77 and 2.78 for the top and bottom panels respectively), while the points are obtained from N-body integrations over a period of 10^6 yrs; for the top panels only, the dashed curves were obtained under the "strong coupling" approximation using Eq. (2.68). Filled squares represent systems stable against orbit crossings, while stars are systems that have undergone orbit crossings (but not collisions or ejections) within 10^6 yrs. An 'x' marks an unstable systems where one or more planets have collided or been ejected. Systems marked by 'x' are arbitrarily placed on the solid curves for visual clarity as their RMS eccentricities and mutual inclinations can be ill-defined due to ejections and/or collisions. 48

2.12	The same as Fig. 2.11, but showing the RMS orbital eccentricities $\langle e_j^2 \rangle^{1/2}$ (top panels) and mutual inclinations between the Kepler-11b and the j -th planet $\langle \theta_{1j} \rangle^{1/2}$ (bottom panel). The left panels have $e_p = \theta_p = 0.1$ while the right panels have $e_p = \theta_p = 0.3$. The red, green, blue, magenta, yellow and cyan curves correspond to planets $b - g$ in the Kepler-11 system. The solid curves are obtained from the hybrid secular analytical theory, and given by Eqs. (2.77) and (2.78) for the top and bottom panels respectively.	49
3.1	A histogram of the final eccentricity of the remaining planet, for a system of two initial planets that have undergone an ejection event. The different colors correspond to various values of the mass ratio m_1/m_2 . Each histogram represents 600 simulations, with $k_0 \in [1.5, 2.0, 2.5]$ (where $k_0 \equiv (a_2 - a_1)/r_H$) and $m_1 \in [3.0, 1.0] M_J$. Runs with different m_1 were binned together as their distributions were indistinguishable statistically.	63
3.2	A histogram of the final inclination of the remaining planet (relative to the initial plane), for a system of two initial planets that have undergone an ejection event. The initial mutual inclination of the two planets is 3° . The different colors correspond to various values of the mass ratio m_2/m_1 . Each histogram represents 600 simulations, with $k_0 \in [1.5, 2.0, 2.5]$ and $m_1 = M_J$. Simulations with different k_0 were binned together as their distributions were approximately identical statistically.	65
3.3	Probability density distribution of N_{ej} from our two planet scattering simulations. The different colors represent different values of m_1 , with red, green and blue corresponding to $m_1 = 3, 1, 0.3 M_J$ respectively. For each histogram, we fix $m_2/m_1 = 1/10$ and $k_0 = 2.0$. The histograms are empirical results from our N-body simulations, while the solid curves are obtained using the theoretical model in Eq. (3.19), with b empirically determined using Eq. (3.22).	66
3.4	Same as Fig. 3.3, except we fix $m_1 = M_J$, while m_2/m_1 varies as indicated in the legend.	67
3.5	Same as Fig. 3.3, except we fix $m_1 = M_J$, while the initial separation parameter $k_0 = \Delta a/r_H$ varies as indicated in the legend.	68
3.6	The maximum likelihood estimate (MLE) estimate of b , as a function of m_1 , for various combinations of the planet mass ratio m_2/m_1 . The filled circles are the results of numerical N-body simulations, while the solid lines are given by Eq. (3.24). The errorbars are computed using the asymptotic variance of the MLE (Eq. 3.23).	69

3.7	Top: empirical values of $a_{2,\min}$ as function of m_2/m_1 . Each data point represents the global minimum over all simulations. The blue, green and red circles correspond to $m_1 = 10, 3, 1M_J$ respectively. The dashed lines are derived from minimizing a_2 under the constraints given by Eqs. (3.25) - (3.27) in the limit of $m_2/m_1 \ll 1$. We suppress error bars in the empirical results because it is unclear how to estimate the minimum of a set of observations without prior assumptions about the distribution of our data. The bottom panel is similar to the upper panel, except we plot $r_{2,\min} = \min[a_2(1 - e_2)]$ instead of $a_{2,\min}$	78
3.8	The final values of $e_{a,\infty}$ (top panels) and $\theta_{a,\infty}$ (in radians, bottom panels) as defined by Eqs. (3.38) - (3.39), as a function of N_{ej} , for a 1-planet inner system subject to the gravitational influence of two scattering giant planets. The masses of the outer planets are varied with $m_1 = 10, 3, 1$ or $0.3M_J$ (the red, green, blue and magenta points respectively), while the mass ratio $m_2/m_1 = 1/2, 1/5, 1/10$ for the filled circles, triangles and stars respectively. The initial semi-major axes of the outer planets are $a_1 = 6.0$ au and $a_2 = a_1 + k_0 r_H$ with r_H being the mutual Hill radius and k_0 chosen randomly from $[1.5, 2.0, 2.5]$; the value of k_0 matters little for the final results. The left panels show systems where the initial $a_a/a_1 = 1/20$, while the right panels have $a_a/a_1 = 1/10$	83
3.9	Same as the Fig. 3.8, except the eccentricities and inclinations are normalized by the “secular” expectation $e_{a,\text{sec}}$ and $\theta_{a,\text{sec}}$ given by Eqs. (3.40) - (3.41).	84
3.10	The value of γ_e^2 (Eq. 3.44) plotted as a function of $N_{\text{ej}}/N_{\text{sec}}$ (see Eq. 3.43) for our simulations. Here $a_a = 0.3$ au (corresponding to $a_a/a_1 = 1/20$). Red, green and blue points correspond to $m_1 = 3, 1, 0.3M_J$ respectively. The filled circles, triangles and stars correspond to $m_2/m_1 = 1/2, 1/5, 1/10$ respectively. The black solid line is given by $\gamma_e^2 = N_{\text{ej}}/N_{\text{sec}}$	87
3.11	Same as Fig. 3.10, except we show γ_θ^2 as defined by Eq. (3.45).	88
3.12	The average value of γ_e^2 , binned by $\log(N_{\text{ej}}/N_{\text{sec}})$ with 4 bins per logarithmic decade, as a function of $N_{\text{ej}}/N_{\text{sec}}$. For each of the points, $m_1 = M_J$ and $m_2/m_1 = 1/5$. The red, green, blue and magenta filled circles correspond to $a_a/a_1 = 1/20, 1/13, 1/10$ and $1/7$ respectively. The errorbars are given by the standard error, and the solid black line is given by $\langle \gamma_e^2 \rangle = N_{\text{ej}}/N_{\text{sec}}$	89
3.13	Same as Fig. 3.12, except that we fix $a_a/a_1 = 1/10$, and m_2/m_1 varies as indicated by the plot legend.	90
3.14	Same as Fig. 3.12, except that we fix $a_a/a_1 = 1/10$, and m_1 varies as indicated by the plot legend.	91

- 3.15 Distribution of $y_e \equiv \gamma_e \sqrt{N_{\text{sec}}/\langle N_{\text{ej}} \rangle_{\text{HM}}}$ (see Sec. 3.4.4). The histograms are empirical distributions obtained from our simulations, while the black line is the theoretical distribution given by Eq. (3.79) - (3.80). On the top panel, $m_2/m_1 = 1/5$ while m_1 and a_a/a_1 varies as shown in the legend. On the bottom panel, $a_a/a_1 = 1/10$ and $m_1 = 1M_J$, while m_2/m_1 varies as shown in the legend. 100
- 3.16 Similar to Fig. 3.10, except with 2 inner planets. We have $m_a = m_b = 3M_{\oplus}$, $a_a = a_1/20$ and $a_b = 1.5a_a$, while m_1 varies as shown on the plot legend and $m_2 = m_1/5$. The boost factor for the first inner planet $\gamma_{e,a}$ corresponds to the filled circles, while that for the second inner planet is shown as filled triangles. 104
- 3.17 Similar to Fig. 3.14, except the simulations have two inner planets. The system parameters are the same as those for Fig. 3.16. The top panel shows the eccentricity boost factor γ_e^2 while the bottom panel show the mutual inclination boost factor $\gamma_{\theta,ab}^2$ 105
- 4.1 The value of $e_{1,\text{forced}}/e_2$ (Eq. 4.40) of an inner planet with $m_1 = M_{\oplus}$ and $R_1 = R_{\oplus}$ as a function of a_1 for various values of a_2 and m_2 . The three thick curves correspond to different values of m_2 and a_2 as labeled. For the blue curve, we also show its limiting cases: the thin, solid blue curve corresponds to the approximation given by $e_{1,\text{forced}}/e_2 \simeq \nu_{12}/\omega_{12}$, the dash-dotted curve corresponds to $e_{1,\text{forced}}/e_2 \simeq \nu_{12}/\omega_{1,\text{gr}}$ and the thin dashed line corresponds to $e_{1,\text{forced}}/e_2 \simeq \nu_{12}/\omega_{1,\text{tide}}$ 127
- 4.2 Sample time evolution for a two-planet system with initial conditions $a_{1,0} = 0.03$ au, $a_2 = 0.08$ au and $e_{1,0} = 0$, $e_{2,0} = 0.15$. The left panels have planet masses $m_1 = M_{\oplus}$, $m_2 = 3M_{\oplus}$ while the right panels have $m_1 = M_{\oplus}$ and $m_2 = 30M_{\oplus}$. Note here we adopt a large value of $\Delta t_{L,1} = 10^5$ s in order to speed up numerical calculations. In the middle and bottom panels, the dashed curves show our approximate solution using Eq. (4.28) while the solid curves are obtained using a direct integration of Eqs. (4.2) and (4.14). On the left panels, the orbital decay of m_1 is limited by the amount of total angular momentum deficit, as the two modes decay away before substantial orbital decay can take place, whereas on the right panels, the planets have sufficient AMD to undergo substantial orbital decay, and is instead limited by the rate of orbital decay. 128

- 4.3 The critical eccentricity $e_{2,0}$ needed to meet the AMD (dashed curves) and tidal decay time constraints (solid curves) for USP formation in a two-planet system is plotted as a function of the companion semi-major axis a_2 . The inner planet has initial semi-major axis $a_{1,0} = 0.03$, mass $m_1 = M_\oplus$, radius $R_1 = R_\oplus$, and tidal lag time $\Delta t_{L,1} = 100$ s. The dashed curve are given by Eq. (4.46), corresponding to $a_{1,\min}/a_{1,0} = \frac{1}{2}$, while the solid curves are given by Eq. (4.47), corresponding to $|\dot{a}_1/a_1| \gtrsim 10^{-10}$ yr. The red, blue, green, magenta and cyan curves correspond to $m_2 = 7, 10, 15, 30$ and $300 M_\oplus$ respectively. For a given m_2 , in order for efficient orbital decay to occur, the outer planet's initial eccentricity must be above both curves of the corresponding color. 132
- 4.4 Planet eigenmode amplitudes B_α (top), eccentricities e_i (middle) and inner planet semi-major axis a_1 (bottom) as a function of scaled time for three different three-planet systems. Here, the time evolution is obtained from Eq. (4.28). The thick dashed, thin solid and thin dashed lines correspond to values of $\Delta t_{L,1} = 10^2, 10^3$ and 10^5 s respectively. The time is scaled as $\hat{t} \equiv (\Delta t_{L,1}/100\text{s}) t$. For the top three panels, the red, green and blue curves correspond to modes I, II and III respectively, while for the middle panels they correspond to e_1, e_2 and e_3 . The three columns have different values of a_2 (0.043, 0.059 and 0.089 au respectively, from left to right), but otherwise identical parameters. The planets have masses $m_1 = M_\oplus$ and $m_2 = m_3 = 17M_\oplus$ and initial semi-major axes $a_{1,0} = 0.03$ au and $a_3 = 0.10$ au. The inner planet's radius is $R_1 = R_\oplus$, and stellar dissipation is neglected ($\gamma_\star = 0$). The initial planet eccentricities are given by $e_{1,0} = 0$ and $e_{2,0} = e_{3,0} = 0.15$, with the initial longitude of pericenter for all three planets set to $\varpi_{i,0} = 0$ 135
- 4.5 Mode structure for the three different systems depicted in Fig. 4.4. The red, green and blue curves correspond to modes I, II and III respectively. For each of the three columns, the top panel shows the real component of the eigenfrequency of the α -th mode ω_α as a function of inner planet semi-major axis a_1 , while the middle-upper subpanel shows the imaginary component of the eigenvalue γ_α . The bottom-middle subpanel shows $\mathcal{E}_{\alpha 1}/\mathcal{E}_{\alpha 3}$ and the bottom subpanel shows $\mathcal{E}_{\alpha 2}/\mathcal{E}_{\alpha 3}$. For the bottom two panels, the solid lines represent positive values while dashed lines represent negative values on the log-axis plot. The columns from left to right show three different cases for mode crossings: In the left column, the modes are well-separated and no mixing occurs; in the middle column, modes I and II show a mixing around $a_1 \approx 0.027$ au and $a_1 \approx 0.014$ au; in the right column, modes II and III cross one another at $a_1 \approx 0.022$ au. 140

- 4.6 Eccentricities e_i and semi-major axis of the innermost planet a_1 as a function of time for the three-planet system corresponding to the right panels of Fig. 4.4 - 4.5, with $\Delta t_{L,1} = 100$ s; the dashed curves represent the results of our approximate method based on Eq. (4.28) while the solid lines are the results of a direct integration of Eq. (4.2). The thick dashed curve show the values of $\langle e_i^2 \rangle^{1/2}$ (Eq. 4.27) while the two thin dashed lines show the maximum and minimum eccentricities given by Eq. (4.30) - (4.31). Note that there is some disagreement between the maximum and minimum values of our approximate method and the brute force calculation due to the fact that the system has insufficient time to reach the theoretical long-term extrema due to the rapid orbital decay. 141
- 4.7 Similar to Fig. 4.3, except here the system has 3 planets. The semi-major axis of the 3rd planet is fixed at $a_3 = 0.10$ au in the top panel, and $a_3 = 0.15$ au in the bottom panel. The dashed curves (AMD constraint) are given by Eq. (4.49) while the solid curves (decay time constraint) are given by Eqs. (4.47) and (4.50), with the eigenvectors being solved numerically and assuming that $e_{2,0} = e_{3,0}$. The two dips in the solid curves correspond to the two resonant mode crossings discussed in section 4.4.2. For a given $m_2 = m_3$, in order for efficient orbital decay to occur, the outer planet's initial eccentricities must be above both curves of the corresponding color. Note that some values of a_2 may result in dynamically unstable systems. 144
- 4.8 The final value of $a_{1,f}$ after 10 Gyr of evolution in a three-planet system (solid curves) and its theoretical minimum dictated by the AMD constraint (dashed curves, Eq. 4.48), plotted as a function of a_2 . The inner planet has mass $m_1 = M_\oplus$, radius $R_1 = R_\oplus$ and tidal lag time $\Delta t_{L,1} = 100$ s, while the outer planets have $m_2 = m_3 = 13M_\oplus$. The three panels correspond to different initial values of $e_{2,0} = e_{3,0}$ (with initially aligned pericenters), as indicated. For each panel, the semi-major axis of the outer planet is fixed at $a_3 = 0.15$ au, while a_2 is varied; the red, blue, green and yellow curves correspond to $a_{1,0} = 0.025, 0.03, 0.035$ and 0.04 au respectively. Regions where the solid curves lie on top of the dashed curves indicate the system is AMD-constrained, while regions where the solid curve is well separated from the dashed curve correspond to tidal decay time-constrained systems. 145

- 4.9 Final values of the inner planet mutual inclination $\theta_{12,f}$ (top) and the spin-orbit angle $\theta_{1\star,f}$ (bottom) as a function of a_2 for a three-planet system with $m_1 = M_\oplus$, $m_2 = 7M_\oplus$ (green curves, left panels) or $17M_\oplus$ (blue curves, right panels) and $m_3 = 17M_\oplus$. The initial semi-major axes of the planets are $a_{1,0} = 0.03$ au and $a_3 = 0.10$ au, while a_2 is varied between 0.04 to 0.07 au. The stellar rotation period is set to $P_\star = 30$ days. The initial eccentricities are $e_{1,0} = 0$ and $e_{2,0} = e_{3,0} = 0.15$, such that the inner planet reaches $a_{1,f} \approx 0.017$ au after 10 Gyr of tidal decay (note that $a_{1,f}$ can be slightly different for different values of a_2). The initial inclination is given by $\mathcal{I}_{1,0} = \mathcal{I}_{2,0} = 0$ and $\mathcal{I}_{3,0} = 0.075$. The bolded curves are the final RMS values given by Eqs. (4.77) and (4.74) for the top and bottom panels respectively, while the two thin curves are their “instantaneous” maximum and minimum values given by Eqs. (4.75) - (4.76) and (4.78) - (4.79) for the bottom and top panels respectively. The top axis of each panel shows the initial value of $\epsilon_{12,0}$ (Eq. 4.80). The two thin vertical lines show the values of a_2 (or $\epsilon_{12,0}$) that lead to specific values of $\epsilon_{12,f}$ (as indicated). 149
- 4.10 Same as Fig. 4.9, except with the stellar spin period fixed at $P_\star = 1$ day. 150
- 4.11 Similar to the right panels of Fig. 4.9 (corresponding to $m_2 = 17M_\oplus$), except we fix the value of $a_2 = 0.055$ au, and instead vary the value of P_\star , which is fixed in time during the evolution. 152
- 4.12 Histogram of the initial and final period of the inner-most planet P_1 for systems with inner planet tidal lag time $\Delta t_{L,1} = 100$ s. The blue bars shows the initial distribution of P_1 , while the blue, green and red lines show the final USP period distribution for values of $Q'_\star = 10^6$, 10^7 and 10^8 respectively. The two solid black lines are given by the power-law distribution $dN/d \log P_1 \propto P_1^\alpha$, where $\alpha = 3.0$ for $P_1 \leq 1$ day and $\alpha = 1.5$ for $1 < P_1 < 8$ days; we also adopt the discontinuous “bump” at $P_1 = 1$ day corresponding to an excess of 50% more planets just below $P = 1$ day as proposed by Lee & Chiang (2017). The normalization of the black lines is chosen so that the total probability density integrates to unity. 161
- 4.13 Same as Fig. 4.12 except that we fix the value of $Q'_\star = 10^7$ and instead vary $\Delta t_{L,1} = 10, 100, 1000$ s, corresponding to tidal $Q_1 = 700, 70$, and 7 (at $P_1 = 1$ day), for the blue, green and red lines respectively. 162
- 4.14 Same as Fig. 4.12 except that we fix the value of $Q'_\star = 10^7$, $\Delta t_{L,1} = 100$ s and instead vary $m_1 = 0.5 \pm 0.25, 1.0 \pm 0.25$ and $2.0 \pm 0.25 M_\oplus$, for the blue, green and red lines respectively. 163
- 4.15 Same as Fig. 4.12 except that we fix the value of $Q'_\star = 10^7$, $\Delta t_{L,1} = 100$ s and instead vary the initial eccentricity $\bar{e} = 0.05 \pm 0.025, 0.1 \pm 0.025$, and 0.15 ± 0.025 for the blue, green and red lines respectively. 164

- 4.16 Same as Fig. 4.12 except that we fix the value of $Q'_\star = 10^7$, $\Delta t_{L,1} = 100$ s and instead vary $P_{\min} = 0.5, 1.0, 2.0$ and 3.0 days (the minimum period of the initial planet population), for the red, green, blue and magenta colors respectively. The solid bars show the initial period distribution for the four values of P_{\min} while the lines show the final distribution. . 165
- 4.17 PDF of the final RMS mutual inclination between the two inner planets after 10 Gyrs of integrations for all systems in our population synthesis. The blue line shows the mutual inclination for planets that became USPs, while the green line is for non-USPs. 166
- 4.18 PDF of the final initial and final period ratio of the inner planets P_2/P_1 distribution for systems in our population synthesis. The blue curve is the initial period ratio, while the green and blue curves are the final period ratios for systems that resulted in USPs and no USPs respectively. 167

CHAPTER 1

INTRODUCTION

The scientific study of the orbital evolution of systems of multiple planets has a history as long and old as Newton's *Principia* (Newton, 1999). Newton calculated the orbital trajectory of a single planet orbiting around its host star, but was unable to find a closed-form solution when the number of planets was extended to two. It turns out that when there is more than a single planet around the host star, the orbital evolution of the planets is 'chaotic': they are highly sensitive to the initial conditions and cannot be described by closed form expressions (see Stone and Leigh, 2019, for a recent advance on this problem). In certain scenarios, it is possible to solve the problem as a perturbation to the two-body problem (e.g. Laplace-Lagrange theory); in general, the problem must be solved numerically using N-body integrations.

Historically, research on the dynamical evolution of multi-planet systems had focussed on our own Solar System, and in particular its long-term stability (e.g. Sussman and Wisdom, 1988; Laskar and Gastineau, 2009; Batygin and Laughlin, 2008). This was due in no small part to the fact that the Solar System was hitherto the only multi-planet system known to astronomy. However, in recent years various observational approaches, in particular transit photometry and radial velocity methods have led to the discovery of large numbers of extra-solar planet systems. To date, over 5,000 planetary systems and system candidates have been discovered ¹. Particularly noteworthy is the success of NASA's Kepler mission, which has discovered over 3,000 planetary system candidates containing nearly 5,000 planet candidates using the transiting method, of which about 700 are multi-planet systems.

Most of the discovered exo-planetary systems bear little resemblance to our own Solar

¹From exoplanets.eu, as of June 1, 2020

System: Kepler planets are typically super-Earths or mini-Neptunes, and have orbital periods shorter than 200 days (e.g. Borucki et al., 2011; Lissauer et al., 2011). The discovery of such exoplanetary systems challenges existing understandings of planetary systems and exposed new fertile areas of research in planetary dynamics. This thesis presents three papers that study the dynamical evolution of these systems in the context of findings by Kepler. The unifying theme of the three papers is an attempt to use theoretical and heuristic approximations to gain physical insights about the dynamics of multi-planet systems in general; for each paper, I then discuss the insights and implications of these results on specific exoplanet systems of interest. A major tool of the papers in this thesis is orbit-averaged (“secular”) theory for calculating the orbital dynamics of planet systems. In the secular theory, gravitational interactions cause planets to exchange eccentricity and/or inclination with one another, but the semi-major axes of the planets remain constant; thus, it is appropriate for planet systems with well-separated orbits and/or low eccentricities that do not undergo hard scatterings.

The first two papers (Chapters 2 and 3) study the eccentricity and inclination evolution of multi-planet systems with external perturbers in the form of exterior planetary or stellar companions. Paper I (Chapter 2) has already been published (Pu and Lai, 2018) while paper II has been submitted to MNRAS.

The motivation for these works comes from Kepler’s discovery of a large number of highly compact planet systems. Such systems, sometimes referred to in the literature as ‘System of Tightly Packed Inner Planets’ (STIPs), contain up to half a dozen planets, typically super-Earths, all of which are within $a \lesssim 1$ AU of their host stars. A notable feature of STIPs is their dynamical “calmness”. Statistical analyses of STIPs have found that planet orbits in these systems tend to be nearly circular and co-planar, with mean orbital eccentricities and inclinations of 0.02 and 2 degrees respectively (Fang

and Margot, 2012; Tremaine et al., 2009; Fabrycky et al., 2014). I had shown earlier through numerical experiments that these compact systems are at the edge of a regime of meta-stability (Pu and Wu, 2015): If the planets were placed any closer, they would undergo close encounters within their lifetimes.

This property of STIPs stands in stark contrast to another population of Kepler planets: Those in systems with only a single transiting planet. Such ‘Kepler singles’ have large orbital eccentricities ($\bar{e} \sim 0.3$) (Van Eylen and Albrecht, 2015; Xie et al., 2016; Van Eylen et al., 2019) and other statistical deviations from typical Kepler systems (e.g. Wittenmyer et al., 2016).

The observation that there may be two distinct population of planet systems have led some to propose the ‘Kepler Dichotomy’ (Ballard and Johnson, 2016; Morton et al., 2016): Kepler systems may be divided into two different architecture, in somewhat equal proportions. This is supported by the fact that models with a single mutual inclination dispersion (e.g. in a Rayleigh distribution) fall short in explaining the large number of single-transit systems relative to multiple-transit systems by a factor of two or more (Lissauer et al., 2011; Johansen et al., 2012). Under the Kepler dichotomy, approximately half of planet systems are the aforementioned STIPs, while the other half consists of systems of mostly Kepler singles with large orbital eccentricities. Alternatively, it has been proposed that the ‘Kepler Dichotomy’ is less of a sharp distinction between two populations but rather a spectrum (e.g Tremaine et al., 2009; Zhu et al., 2018), with highly eccentric Kepler singles on one end, and highly compact multi-planet systems on the other; as planet multiplicity decreases, the planet spacing, orbital eccentricities and inclinations increases.

In recent years, increasing number of exterior giant planet companions (sometime referred to in the literature as Cold Jupiters or CJs) have been discovered around inner

planet systems (e.g. Huang et al., 2018b; Mills et al., 2019; Weiss et al., 2020; Herman et al., 2019). In fact, statistical analyses have shown an excess number of CJs around systems with inner Super-Earths, with as many as 30% of inner planet systems harboring exterior CJs (Zhu and Wu, 2018; Bryan et al., 2019). In comparison to the STIPs, these CJ companions tend to be much more ‘excited’ dynamically, typically having eccentricities of order $e \sim 0.3$ (Bryan et al., 2019). The CJs also tend to be mildly misaligned with their inner systems (Masuda et al., 2020).

As a result of these findings, the dynamical interactions between the inner systems and their external companions had become an active research topic as of late. In an earlier paper, Lai and Pu (2017) proposed that external companions mildly inclined relative to STIPs can excite the mutual inclinations of the inner planets, contributing to the Kepler dichotomy (see also Read et al., 2017; Becker and Adams, 2017; Huang et al., 2017; Hansen, 2017; Mustill et al., 2017b). Lai and Pu (2017) showed that the inclination evolution of an inner system of 2 planets under the influence of a misaligned perturber is governed by the dimensionless parameter ϵ_{12} , which decreases when the inner planets are spaced more tightly and when the perturber is less massive and farther away. In the limit that $\epsilon_{12} \ll 1$, the strong mutual gravitational interactions between the inner planets may allow the system as a whole to behave like a “rigid” disk, such that the planet orbital inclinations change in unison when perturbed by outside forces. This implies that tightly packed inner systems should much more easily maintain a low degree of mutual inclination, even under perturbations that would otherwise excite mutual misalignments.

In Chapter 2, I extend the earlier results of (Lai and Pu, 2017) to also consider the eccentricities of the inner planets. I present a comprehensive study on the evolution of the inner planetary system subject to the gravitational influence of an eccentric, misaligned outer perturber. I develop an approximate method for secular evolution that interpolates

between Laplace-Lagrange theory and multipole expansion; this method allows orbital evolution to be computed in most cases without having to perform N-body integrations. Analytic results are derived for the inner planet eccentricities (e_i) and mutual inclination (θ_{12}) of the “2-planet + perturber” system, calibrated with numerical secular and N-body integrations, as a function of the perturber mass m_p , semi-major axis a_p and inclination angle θ_p . We find that the dynamics of the inner system is determined by the dimensionless parameter ϵ_{12} , given by the ratio between the differential precession rate driven by the perturber and the mutual precession rate of the inner planets. When $\epsilon_{12} \ll 1$, the inner planets act as a “rigid” disc, and strongly resist excitation in orbital eccentricity by external perturbers. Loosely packed systems (corresponding to $\epsilon_{12} \gg 1$) are more susceptible to eccentricity/inclination excitations by the perturber than tightly packed inner systems (with $\epsilon_{12} \ll 1$) (or singletons), although resonance may occur around $\epsilon_{12} \sim 1$, leading to large e_i and θ_{12} . Dynamical instability may set in for inner planet systems with large excited eccentricities and mutual inclinations. I present a formalism to extend our analytical results to general inner systems with $N > 2$ planets and apply our results to constrain possible external companions to the Kepler-11 system. Eccentricity and inclination excitation by external companions may help explain the observational trend that systems with fewer transiting planets are dynamically hotter than those with more transiting planets.

Chapter 3 is an extension of the scenario laid out in Chapter 2. The scenario proposed in Chapter 2 supposes that CJ companions to inner planet systems are primordially misaligned with their inner systems and/or have mildly eccentric orbits. However, models of giant planet formation inside planetary disks do not generate giant planets with substantial eccentricities and/or orbital misalignment. It is most likely that these orbital properties are generated by hard gravitational scatterings between the giant planet and its neighboring planets, or possibly between multiple giant planets. These scatterings

typically result in all but the most massive planet being ejected from the planet system, leaving behind a single CJ with excited eccentricity and inclination. To what extent this outer scattering might influence a system of inner planets is not well known. Previous studies (e.g. Huang et al., 2017) had focused on performing large numbers of N-body simulations. Although these simulations can suggest the possible outcomes of this process, the end results are highly diverse and not well understood from a theoretical perspective.

In Chapter 3, I present a paper that studies the dynamical evolution of such inner systems subject to the gravitational effect of an unstable system of outer ($\gtrsim 1au$) giant planets, focussing on systems whose end configurations feature only a single remaining outer giant. In contrast to similar previous studies which tend to focus solely on N-body simulations with specific parameters or scenarios, I implement a novel hybrid algorithm which combines N-body simulations with secular dynamics with the aim of obtaining analytical understanding. I find that the dynamical evolution of the inner planet system depends crucially on N_{ej} , the number of mutual close encounters between the outer planets prior to eventual ejection/merger. When N_{ej} is small, the eventual evolution of the inner planets can be well described by secular dynamics. For larger values of N_{ej} , the inner planets gain orbital inclination, mutual inclination and eccentricity in a stochastic fashion analogous to Brownian motion. I develop a novel mathematical model based on Brownian motion and stochastic processes and calibrated by my suite of N-body simulations, that can model the effect of outer giant planet scatterings on inner planets. This model can reproduce the observed distribution of final inner planet system parameters *a priori*, without the need to perform costly N-body simulations. I then apply my results to the HAT-P-11 and Gliese 777 planet systems and comment on the likelihood that the existing inner system orbital properties can be explained by “N+2” scattering.

In the third paper of my thesis (Chapter 4, published in MNRAS as Pu and Lai 2019), I shift my attention from the outer system inwards, and study the origins of a population of small planets with periods shorter than 1 day. These planets, commonly referred to in the literature as Ultra-Short Period Planets (USPs), have statistical properties that differ from longer period Kepler planets.

Planets with $P \leq 1$ days appear to follow a different period distribution than planets above the one day cut-off: Lee and Chiang (2017) found that whereas transiting planets with $1 \leq P \leq 10$ days followed a power law $dN/d \log P \propto P^\alpha$ with $\alpha \simeq 1.5 - 1.7$ (see also Petigura et al., 2018; Weiss et al., 2018), USPs followed a steeper trend with $\alpha \sim 3.0$. In addition, the normalization of the period distribution may also be different: the planet occurrence rate is discontinuous across the $P = 1$ day boundary, with $\sim 50\%$ more planets with periods just below $P = 1$ days than just above. USPs have smaller radii, with the vast majority having $1R_\oplus \leq R \leq 1.4R_\oplus$ (Winn et al., 2018), a fact which may be attributed to photo-evaporation or ‘boil-off’ as the planets are intensely irradiated. Compared with the other *Kepler* planets, planet systems with USPs also appear to have higher mutual inclinations: Dai et al. (2018) found that transiting *Kepler* planets with a semi-major axis to stellar radius ratio $a/R_\star < 5$ had an inclination dispersion of $\Delta\theta \approx 6.7 \pm 0.7$ degrees, while planets with $5 < a/R_\star < 12$ had only $\Delta\theta \approx 2.0 \pm 0.1$ (consistent with the overall figures for Kepler multis, see e.g. Tremaine and Dong, 2012; Fang and Margot, 2012; Fabrycky et al., 2014). This observation is further corroborated by the fact that for FGK host stars, USPs feature a factor of ~ 8 fewer co-transiting external companions compared with their merely ‘short-period planet’ (SP) counterparts (Petrovich et al., 2018; Weiss et al., 2018), and when USPs do have external transiting companions, the period ratios between the USP and their closest companion is $P_2/P_1 \gtrsim 15$, a value that is nearly an order of magnitude above the typical period ratios of $1.3 - 4.0$ seen in *Kepler* multis (see also Steffen and Farr, 2013).

In Chapter 4, I formulate and study a "low-eccentricity" migration scenario for the formation of USPs, in which a low-mass planet with initial period of a few days maintains a small but finite eccentricity due to secular forcings from exterior companion planets, and experiences orbital decay due to tidal dissipation. USP formation in this scenario requires that the initial multi-planet system have modest eccentricities ($\gtrsim 0.1$) or angular momentum deficit. During the orbital decay of the inner-most planet, the system can encounter several apsidal and nodal precession resonances that significantly enhance eccentricity excitation and increase the mutual inclination between the inner planets. In order to efficiently compute the orbital dynamics of these systems, I develop an approximate method based on eccentricity and inclination eigenmodes to efficiently evolve a large number of multi-planet systems over Gyr timescales in the presence of rapid (as short as ~ 100 years) secular planet-planet interactions and other short-range forces. Through a population synthesis calculation, I demonstrate that the "low- e migration" mechanism can naturally produce USPs from the large population of *Kepler* multis under a variety of conditions, with little fine tuning of parameters. This mechanism favors smaller inner planets with more massive and eccentric companion planets, and the resulting USPs have properties that are consistent with observations.

CHAPTER 2

ECCENTRICITIES AND INCLINATIONS OF MULTIPLANET SYSTEMS WITH EXTERNAL PERTURBERS

2.1 Introduction

Recent advances in radial velocity and transit surveys have led to a large increase in the number of detected multi-planet systems, indicating that such systems are common in the Galaxy. Of particular interest are the compact multi-planet systems discovered by NASA’s *Kepler* mission (Mullally et al., 2015; Burke et al., 2015; Morton et al., 2016). Such systems generally feature multiple super-Earths or sub-Neptunes (with radii $1.2\text{--}3R_{\oplus}$) with periods inwards of 200 days. The orbital configurations of these systems suggest that they are generally “dynamically cold”, with eccentricities $e \sim 0.02$ (Lithwick et al., 2012; Van Eylen and Albrecht, 2015; Xie et al., 2016; Hadden and Lithwick, 2017), orbital mutual inclinations $\theta \sim 2^\circ$ (Lissauer et al., 2011; Fang and Margot, 2012; Figueira et al., 2012; Johansen et al., 2012; Tremaine and Dong, 2012; Fabrycky et al., 2014), and orbital spacings close to the limit of stability (Fang and Margot, 2013; Pu and Wu, 2015; Volk and Gladman, 2015).

What account for the origins of these orbital properties? One suggestion is that these planets have orbital configurations that reflect their formation environments (Hansen and Murray, 2013; Moriarty and Ballard, 2016) - with the “dynamically cold” population being an indicator of having formed in highly dissipative environments or vice-versa. Indeed, there is evidence for a correlation between planet compositions and orbits: planets with more gaseous envelopes tend to have dynamically “colder” orbits, consistent with a gaseous formation environment (Dawson et al., 2016).

Another possibility is that the orbital properties of such planets are driven by external perturbers, of either the planetary or stellar variety. Stellar companions to numerous Kepler systems have been detected in a wide range of separations (Baranec et al., 2016). There is evidence for a reduced occurrence of stellar companions to stars hosting multiple transiting planets: Wang et al. (2015) found that $5.2 \pm 5\%$ of Kepler multi’s have stellar companions at separation 1-100 au in comparison to the rate of 21 % for field stars, indicating that stellar companions may be disruptive to the formation or stability of cold multi-planet systems. Several proto-planetary disks have been observed to be misaligned with their binary companions (Jensen and Akeson, 2014; Brinch et al., 2016), therefore misaligned binary companions to planetary systems may be common.

On the other hand, a number of long-period giant planet companions to Kepler compact systems have been found using the transit method (Schmitt et al., 2014; Uehara et al., 2016) and the RV method (e.g., Kepler-48, Kepler-56, Kepler-68, Kepler-90, Kepler-454). A few non-Kepler “inner compact planets + giant companion” systems have also been discovered (e.g., GJ 832, WASP-47). Bryan et al. (2016) reported that about 50% of one and two-planet systems discovered by RV have companions in the 1-20 M_J and 5-20 au range. These results indicate that external ($\gtrsim 1$ au) giant planet companions are common around hot/warm ($\lesssim 1$ au) planets, and may significantly shape the architecture of the inner planetary systems.

The outer stellar or planetary companions can influence their inner systems in a variety of ways, changing their orbital properties and even making them dynamically unstable. The most common effects arise from secular gravitational perturbation. In general, a distant stellar companion may be on an inclined orbit relative to the inner planetary system because of its misaligned orbital angular momentum at birth. A giant planet may also have an inclined and eccentric orbit, as a result of strong scatterings

between multiple giants (Jurić and Tremaine, 2008; Chatterjee et al., 2008). Such misaligned external perturbers can induce mutual inclination oscillations amongst the inner planets, making the inner system dynamically hotter or even unstable (Lai and Pu, 2017; Hansen, 2017; Becker and Adams, 2017; Read et al., 2017; Jontof-Hutter et al., 2017). While mild inclination oscillations tend to preserve the integrity of the inner systems, they can nevertheless disrupt the co-transiting geometry of the inner planets and thereby reduce the number of transiting planets (e.g. Brakensiek and Ragozzine, 2016). In Lai and Pu (2017), we have derived approximate analytic expressions, calibrated with numerical calculations, for the mutual inclination excitations for various planetary systems and perturber properties; we have also identified a secular resonance mechanism that can generate large mutual inclinations even for nearly co-planar perturbers.

A more subtle effect of external perturbers on inner planetary systems is “evection resonance” (Touma and Sridhar, 2015; Xu and Lai, 2016). This occurs when the apsidal precession frequencies of the inner planets, driven by mutual gravitational interactions, match the orbital frequency of the external companion. Resonant eccentricity excitation in the inner planets may lead to disruption of the system under some conditions.

A more “violent” scenario involves two or more giant planets in an unstable configuration, leading to multiple close encounters and ejections/collisions of planets that finally end when a stable configuration is reached - usually with a single giant planet remaining (Chatterjee et al., 2008; Jurić and Tremaine, 2008). This “outer violence” can excite the eccentricities and inclinations of the inner systems, often to their demise - although the end result is highly variable, depending on the initial separations between the giants and inner planets (Matsumura et al., 2013; Carrera et al., 2016; Huang et al., 2017; Gratia and Fabrycky, 2017; Mustill et al., 2017b). One can view this ‘violent phase’ as the precursor of the “secular phase” mentioned above: Two or three giant

planets first form in nearly circular, co-planar configurations ; the planets then undergo strong scatterings. This is a natural mechanism of producing a misaligned giant planet that can induce further secular eccentricity/inclination excitations in the inner planetary system. Indeed, there is an interplay between the “violent” and “secular” phases of such planetary systems (Pu & Lai 2018, in prep); the results of this paper serves as a baseline for our forthcoming exploration on the eccentricity and inclination excitation during the “dynamical” phase.

In this paper, we study the evolution of multi-planet inner systems with a single eccentric, misaligned outer companion (star or giant planet). We develop tools based on secular perturbation theory, calibrated with N-body simulations, to predict the outcomes of inner planet orbital properties based on the perturber’s orbits. We extend our previous work (Lai and Pu, 2017) to treat the combined excitations of eccentricities and mutual inclinations. A major goal of our paper is to derive approximate analytic expressions and scaling formulae that can be adapted to various planetary and perturber parameters.

The framework of this paper is as follows. In Section 2.2, we apply linear Laplace-Lagrange theory to derive analytic expressions for the evolution of eccentricities and inclinations of planets in a “2-planets + perturber” system. In Section 2.3 (see also Appendix B), we develop an approximate procedure to extend our analytic results to the mildly non-linear regime (with the perturber’s inclination and eccentricity satisfying $\theta_p, e_p \lesssim 0.4$); within this regime, our analytic results agree robustly with numerical results based on integration of secular equations. In Section 2.4 we compare our theoretical results based on secular theory to N-body simulations. In Section 2.5 we extend our results to inner systems with $N > 2$ planets, and a prescription for evaluating the planet RMS eccentricities and mutual inclinations in a “N-planets + perturber” system is given in Appendix B. In Section 2.6 we illustrate our results by applying them to the

Kepler-11 system. We summarize our key findings in Section 2.7.

2.2 Eccentricity and Inclination Excitation in Linearized Secular Theory

Consider an inner system of planets with masses m_i ($i = 1, 2, 3, \dots, N$) and semi-major axes a_i ($a_1 < a_2 < \dots < a_N$). These inner planets are initially coplanar and have circular orbits, and are accompanied by a giant planet (or stellar) perturber with $m_p \gg m_i$, semi-major axis $a_p \gg a_i$, inclination angle θ_p and eccentricity e_p . How do the eccentricities and mutual inclinations of the inner planet system evolve?

In this Section we consider the regime where all eccentricities and inclinations are small ($e_p, e_i \ll 1$ and $\theta_p, \theta_i \ll 1$). In this regime, the evolutions of the eccentricities e_i and inclinations θ_i decouple, and are governed by the standard linearized Laplace-Lagrange planetary equations (Murray and Dermott, 1999). We present several analytical results that will be useful for the more general cases where e_p and θ_p are more modest.

We define the dimensionless eccentricity vector \mathbf{e}_j and dimensionless angular momentum vector \mathbf{j}_j of the j -th planet as

$$\mathbf{j}_j = \sqrt{1 - e_j^2} \hat{\mathbf{n}}_j, \quad \mathbf{e}_j = e_j \hat{\mathbf{u}}_j \quad (2.1)$$

where $\hat{\mathbf{n}}_j$ and $\hat{\mathbf{u}}_j$ are unit vectors, and note that $\mathbf{j}_j \simeq \hat{\mathbf{n}}_j$ since $e_j \ll 1$. The evolution equations for \mathbf{e}_j and \mathbf{j}_j (where $j = 1, 2, 3, \dots, N, p$, with the perturber included) are:

$$\frac{d\mathbf{e}_j}{dt} = - \sum_{k \neq j} \omega_{jk} (\mathbf{e}_j \times \mathbf{j}_k) - \sum_{k \neq j} \nu_{jk} (\mathbf{j}_j \times \mathbf{e}_k), \quad (2.2)$$

$$\frac{d\mathbf{j}_j}{dt} = \sum_{k \neq j} \omega_{jk} (\mathbf{j}_j \times \mathbf{j}_k). \quad (2.3)$$

The quantities ω_{jk} and ν_{jk} are the quadrupole and octupole precession frequencies of the j -th planet due to the action of the k -th planet, given by:

$$\omega_{jk} = \frac{Gm_j m_k a_{<}}{a_{>}^2 L_j} b_{3/2}^{(1)}(\alpha), \quad (2.4)$$

$$\nu_{jk} = \frac{Gm_j m_k a_{<}}{a_{>}^2 L_j} b_{3/2}^{(2)}(\alpha). \quad (2.5)$$

Here $a_{<} = \min(a_j, a_k)$, $a_{>} = \max(a_j, a_k)$, $\alpha = a_{<}/a_{>}$, $L_j \simeq m_j \sqrt{GM_* a_j}$ is the angular momentum of the j -th planet, and the $b_{3/2}^{(n)}(\alpha)$ are the Laplace coefficients defined by

$$b_{3/2}^{(n)}(\alpha) = \frac{1}{2\pi} \int_0^\pi \frac{\cos(nt)}{(\alpha^2 + 1 - 2\alpha \cos t)^{3/2}} dt. \quad (2.6)$$

Note that:

$$\omega_{jk} L_j = \omega_{jk} L_k. \quad (2.7)$$

For $\alpha \ll 1$, we have $b_{3/2}^{(1)}(\alpha) \simeq 3\alpha/4 + 43\alpha^3/32 + 525\alpha^5/256$ and $b_{3/2}^{(2)}(\alpha) \simeq 15\alpha^2/16 + 105\alpha^4/64$. Thus the ratio of the quadrupole and octupole frequencies is given by

$$\frac{\nu_{jk}}{\omega_{jk}} = \beta(\alpha) \equiv \frac{b_{3/2}^{(2)}(\alpha)}{b_{3/2}^{(1)}(\alpha)} \simeq 5\alpha/4 - 5\alpha^3/32. \quad (2.8)$$

It is usually sufficient to take $\beta(\alpha) \simeq 5\alpha/4$, as this is accurate to within 8% for $\alpha \leq 0.8$.

Note that $\beta(\alpha) < 1$ for all α ; in the limit that $\alpha \rightarrow 1$, we have $\beta(\alpha) \rightarrow 1$ from below.

For convenience, we introduce the variables \mathcal{I} and \mathcal{E} as the complex inclination and eccentricity:

$$\mathcal{I} \equiv |\mathcal{I}| \exp(i\Omega), \quad (2.9)$$

$$\mathcal{E} \equiv |\mathcal{E}| \exp(i\varpi), \quad (2.10)$$

where Ω and ϖ are the longitude of the ascending node and the longitude of pericenter, respectively.

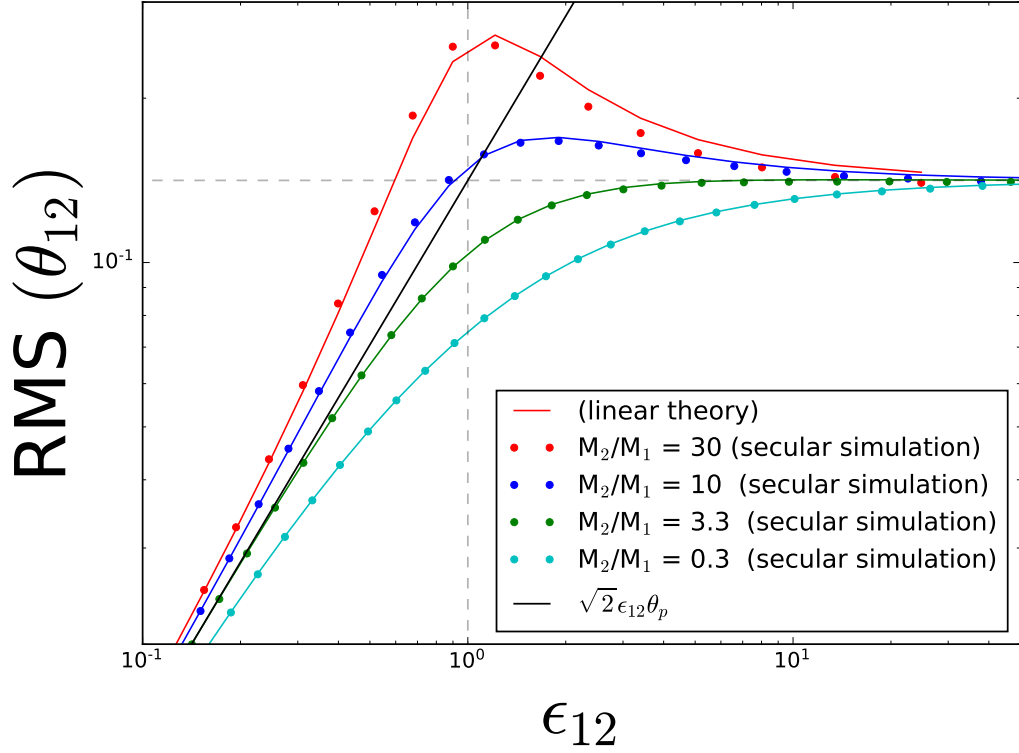


Figure 2.1: RMS values of the mutual inclination between the inner planets in a fiducial two-planet system under the influence of a mis-aligned perturber. The perturber has initial eccentricity $e_p = 0$ and inclination $\theta_p = 0.1$ rad. Planet 1 has a fixed mass at $m_1 = M_\oplus$ while the mass of planet 2 varies from $0.3M_\oplus$ to $30M_\oplus$ and are represented by different colors. The perturber has a mass of $m_p = 3M_J$ and its semi-major axis is varied to produce different ϵ_{12} , the coupling strength of the perturbation (Eq. 2.15). The solid colored points represent the results of numerical integrations using secular equations, while the solid colored curves are calculated using linearized theory. The dashed vertical line corresponds to $\epsilon_{12} = 1$, where a resonance feature occurs. Note that the resonance feature becomes sharper and more pronounced as the mass ratio m_2/m_1 increases. The horizontal dashed line corresponds to the weak-coupling limit $\text{RMS}(\theta_{12}) \simeq \sqrt{2}\theta_p$, which holds when $\epsilon_{12} \gg 1$. The solid black line is the prediction from secular theory, when the planets are strongly coupled ($\epsilon_{12} \ll 1$).

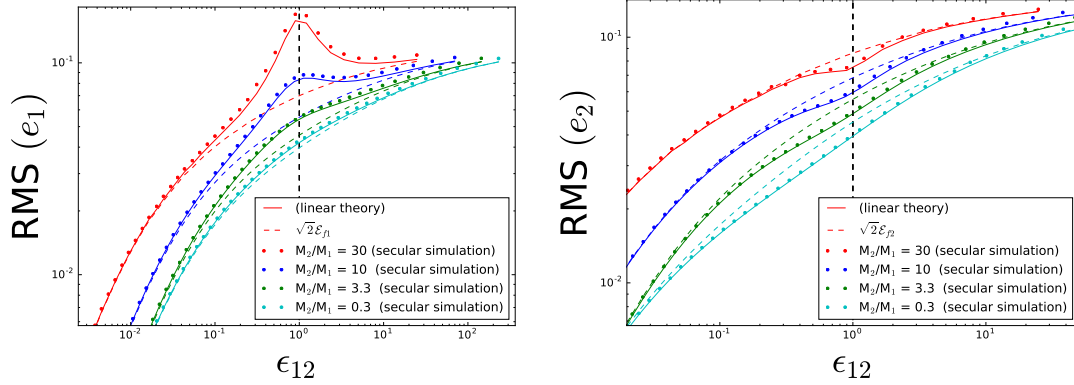


Figure 2.2: RMS values of the eccentricities of the planets in a fiducial two-planet system under the influence of an eccentric perturber. The perturber has initial eccentricity $e_p = 0.1$ and has an orbit co-planar with the inner system. The other parameters are the same as Fig. 2.1. The solid colored points represent the results of numerical integrations using secular equations, while the solid colored curves are calculated using linearized theory; the dashed colored lines show the forced eccentricity (Eq. 2.26). The dashed vertical line corresponds to $\epsilon_{12} = 1$.

2.2.1 “One Planet + Perturber” System: Eccentricity

In the limit $m_p \gg m_1$, the eccentricity vector of the inner planet evolves in time as

$$\mathcal{E}_1(t) = \frac{\nu_{1p}}{\omega_{1p}} \mathcal{E}_p [1 - \exp(i\omega_{1p}t)] \quad (2.11)$$

assuming $\mathcal{E}_1(t = 0) = 0$. The root-mean-square (RMS) value of the eccentricity is therefore

$$\langle e_1^2 \rangle^{1/2} = \langle |\mathcal{E}_1|^2 \rangle^{1/2} = \sqrt{2} \frac{\nu_{1p}}{\omega_{1p}} e_p \simeq \sqrt{2} \left(\frac{5}{4} \right) \left(\frac{a_1}{a_p} \right) e_p. \quad (2.12)$$

The maximal eccentricity reached by planet 1 is

$$(e_1)_{\max} = 2 \frac{\nu_{1p}}{\omega_{1p}} e_p \simeq \left(\frac{5}{2} \right) \left(\frac{a_1}{a_p} \right) e_p. \quad (2.13)$$

The above expressions assume $L_p \gg L_1$ and neglect the eccentricity evolution of

the perturber. For finite L_1/L_p , the RMS value of e_1 can be generalized to

$$\begin{aligned}\langle e_1^2 \rangle^{1/2} &= \frac{\sqrt{2}\nu_{1p}e_p}{\sqrt{(\omega_{1p} - \omega_{p1})^2 + 4\nu_{1p}\nu_{p1}}} \\ &\simeq \sqrt{2} \left(\frac{5}{4} \right) \left(\frac{a_1}{a_p} \right) e_p \left[\left(1 - \frac{L_1}{L_p} \right)^2 + \frac{25}{4} \left(\frac{L_1}{L_p} \right) \left(\frac{a_1}{a_p} \right)^2 \right]^{-1/2}.\end{aligned}\quad (2.14)$$

2.2.2 “Two Planets + Perturber” System: Mutual Inclination

In a previous paper (Lai and Pu, 2017), we have already studied the secular evolution of the mutual inclination angle between the inner planets in the presence of a misaligned outer companion. It was found that the evolution of the inner system depends critically on the ratio of the differential quadrupole precession frequency driven by the perturber and the mutual quadrupole precession frequency between the inner planets, succinctly described by the dimensionless parameter ϵ_{12} (note that we adopt a change of notation from the previous paper, Ω_{ip} is now ω_{ip}):

$$\begin{aligned}\epsilon_{12} &\equiv \frac{\omega_{2p} - \omega_{1p}}{\omega_{12} + \omega_{21}} \\ &\approx \left(\frac{m_p}{10^3 m_2} \right) \left(\frac{10a_2}{a_p} \right)^3 \left[\frac{3a_1/a_2}{b_{3/2}^{(1)}(a_1/a_2)} \right] \frac{(a_2/a_1)^{3/2} - 1}{1 + (L_1/L_2)}.\end{aligned}\quad (2.15)$$

When $\epsilon_{12} \gg 1$, the perturber is dominant and the inner planets behave as if they are independent of one another; when $\epsilon_{12} \ll 1$, the inner planets are tightly coupled and their angular momenta stay closely aligned, with a mutual inclination $\theta_{12} \sim \epsilon_{12}\theta_p$. In the regime where $\epsilon_{12} \sim 1$, a secular resonance feature exists and it is possible for the inner planets to have $\theta_{12} \gg \theta_p$.

The general expression for the mutual inclination, in the limit of $m_p \gg m_j$, is given

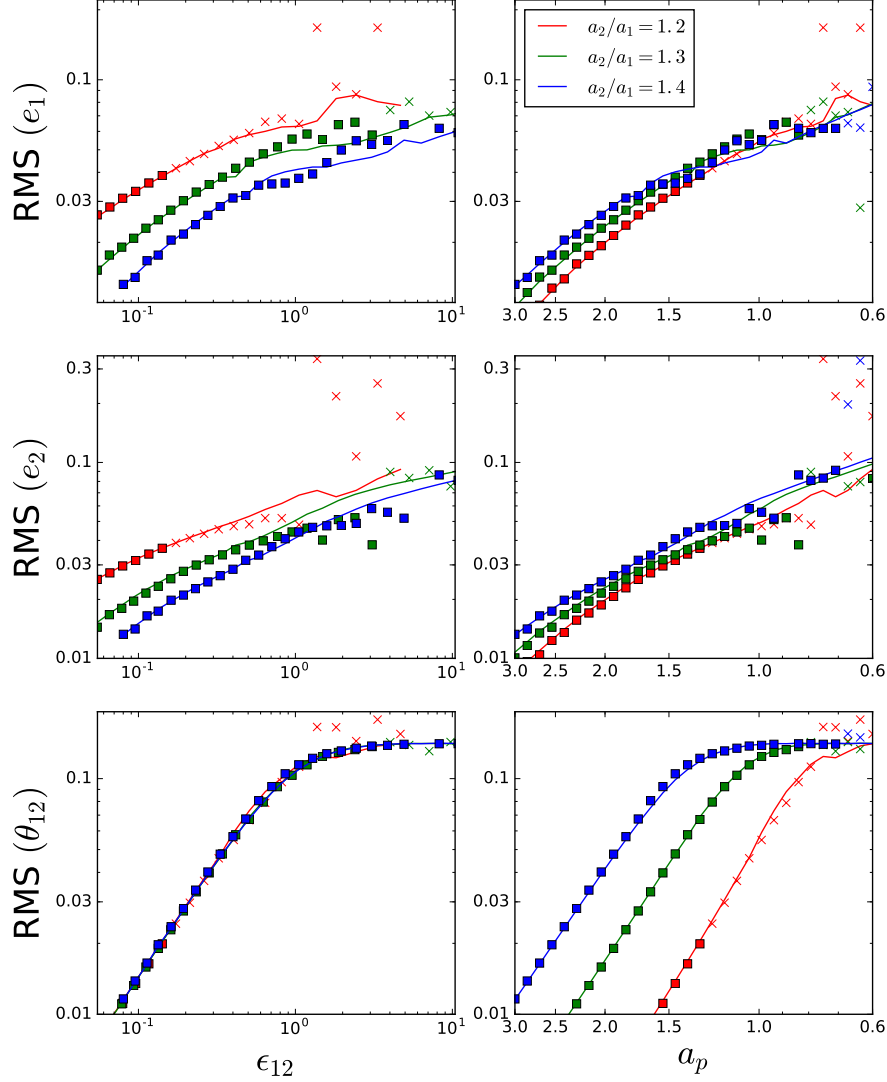


Figure 2.3: RMS values of e_1 , e_2 and θ_{12} (top to bottom) as a function of ϵ_{12} and a_p for a 2-planet system with different spacings a_2/a_1 . The solid curves are results of numerical integrations using the hybrid secular equations (Eqs. A.2 - A.5) while the results of N-body simulations are marked with an “x” if the system becomes gravitationally unstable with respect to orbit crossings within 10^5 yr, otherwise they are marked with a filled square. The different colored lines represent different values of a_2/a_1 , with red, green and blue being $a_2/a_1 = 1.2, 1.3, 1.4$ respectively. In each case, $a_1 = 0.3$ au, and a_p is varied from 0.6 to 3.0 au. The planet masses are $m_1 = m_2 = 3M_\oplus$ and $m_p = 3M_J$. The inner planets are initially on circular and co-planar orbits while the perturber has $e_p = 0.05$ and $\theta_p = 0.1$.

by:

$$\langle \sin^2 \theta_{12} \rangle^{1/2} = 2\theta_p \left(\frac{\omega_{2p} - \omega_{1p}}{\sqrt{(\omega_1 - \omega_2)^2 + 4\omega_{12}\omega_{21}}} \right), \quad (2.16)$$

where

$$\omega_1 = \omega_{12} + \omega_{1p}, \quad (2.17)$$

$$\omega_2 = \omega_{21} + \omega_{2p}. \quad (2.18)$$

It is clear that a resonance occurs when $\omega_1 = \omega_2$ ¹. At the resonance, we have

$$\langle \sin^2 \theta_{12} \rangle_{\text{res}}^{1/2} = \theta_p \sqrt{\frac{L_2}{L_1}} \left(1 - \frac{L_1}{L_2} \right). \quad (2.19)$$

In the weak coupling limit ($\epsilon_{12} \ll 1$) the mutual inclination is given by

$$\langle \sin^2 \theta_{12} \rangle^{1/2} \simeq \langle \theta_{12}^2 \rangle^{1/2} \simeq \sqrt{2}\theta_p. \quad (2.20)$$

In the above expression, we have neglected the back-reaction on the perturber by the inner planets. In the weak coupling regime, this feedback is of order L_2/L_p and we find

$$\langle \sin^2 \theta_{12} \rangle^{1/2} \simeq \langle \theta_{12}^2 \rangle^{1/2} \simeq \sqrt{2}\theta_p \left(1 + \frac{L_2}{L_p} \right)^{-1}. \quad (2.21)$$

In the strong coupling limit ($\epsilon_{12} \ll 1$), the back-reaction is always negligible, and we have

$$\langle \sin^2 \theta_{12} \rangle^{1/2} \simeq \langle \theta_{12}^2 \rangle^{1/2} \simeq \sqrt{2}\epsilon_{12}\theta_p. \quad (2.22)$$

The above results are summarized in Fig. 2.1, in which we show the root-mean-square (RMS) mutual inclination between the inner planets in a fiducial two-planet system under the influence of an external misaligned companion. The linearized analytic results (solid curves) are shown to be in excellent agreement with secular numerical integrations (dots).

¹Equation (2.16) is valid for $\theta_p \ll 1$. See Lai and Pu (2017) for the result and the property of the resonance when θ_p is not restricted to small values.

2.2.3 “Two Planets + Perturber” System: Eccentricity

The eccentricity vectors of the two inner planets are governed by

$$\begin{aligned} \frac{d}{dt} \begin{pmatrix} \mathcal{E}_1 \\ \mathcal{E}_2 \end{pmatrix} &= i \begin{pmatrix} \omega_1 & -\nu_{12} \\ -\nu_{21} & \omega_2 \end{pmatrix} \begin{pmatrix} \mathcal{E}_1 \\ \mathcal{E}_2 \end{pmatrix} - i \begin{pmatrix} \nu_{1p} \\ \nu_{2p} \end{pmatrix} \mathcal{E}_p \\ &\equiv i\mathbf{A} \begin{pmatrix} \mathcal{E}_1 \\ \mathcal{E}_2 \end{pmatrix} - i\mathbf{B} \mathcal{E}_p, \end{aligned} \quad (2.23)$$

where ω_1 and ω_2 are given by Eqs. (2.17) - (2.18).

The homogeneous equation of (2.23) (with $\mathcal{E}_p = 0$) has two modes, with eigenfrequencies

$$\lambda_{\pm} = \frac{1}{2} (\omega_1 + \omega_2 \pm \gamma) \quad \text{with } \gamma \equiv \sqrt{\Delta\omega^2 + 4\nu_{12}\nu_{21}}, \quad (2.24)$$

where $\Delta\omega \equiv (\omega_1 - \omega_2)$ (the “distance” from the resonance). Note γ is at a minimum at the resonance ($\Delta\omega = 0$). The corresponding eigenvectors are:

$$\mathbf{v}_{\pm} = \begin{pmatrix} \frac{\Delta\omega \pm \gamma}{2\nu_{21}} \\ 1 \end{pmatrix}. \quad (2.25)$$

The forcing term in Eq. (2.23) gives the inner planets a forced eccentricity

$$\begin{pmatrix} \mathcal{E}_{f1} \\ \mathcal{E}_{f2} \end{pmatrix} = \mathbf{A}^{-1} \mathbf{B} \mathcal{E}_p = \begin{pmatrix} F_{11} \\ F_{12} \end{pmatrix} e_p, \quad (2.26)$$

where

$$F_{11} = \frac{\nu_{1p}\omega_2 + \nu_{12}\nu_{2p}}{\omega_1\omega_2 - \nu_{12}\nu_{21}}, \quad (2.27)$$

$$F_{12} = \frac{\nu_{2p}\omega_1 + \nu_{21}\nu_{1p}}{\omega_1\omega_2 - \nu_{12}\nu_{21}}. \quad (2.28)$$

If the inner planets are on two initially circular orbits, the general solution to equation (2.23) is then

$$\begin{pmatrix} \mathcal{E}_1(t) \\ \mathcal{E}_2(t) \end{pmatrix} = \begin{pmatrix} \mathcal{E}_{f1} \\ \mathcal{E}_{f2} \end{pmatrix} + c_+ \mathbf{v}_+ \exp(i\lambda_+ t) + c_- \mathbf{v}_- \exp(i\lambda_- t), \quad (2.29)$$

where the coefficients c_{\pm} are determined by the initial conditions

$$c_+ = +\frac{v_{21}}{\gamma} \left(\frac{\mathcal{E}_{f2}(\Delta\omega + \gamma)}{2v_{21}} - \mathcal{E}_{f1} \right) \quad (2.30)$$

$$c_- = -\frac{v_{21}}{\gamma} \left(\frac{\mathcal{E}_{f2}(\Delta\omega - \gamma)}{2v_{21}} - \mathcal{E}_{f1} \right). \quad (2.31)$$

Note that $c_+ \mathbf{v}_+ + c_- \mathbf{v}_- = \mathcal{E}_f$. One can verify that Eq. (2.29) is equivalent to

$$\begin{pmatrix} \mathcal{E}_1(t) \\ \mathcal{E}_2(t) \end{pmatrix} = -c_+ \mathbf{v}_+ [1 - \exp(i\lambda_+ t)] + c_- \mathbf{v}_- [1 - \exp(i\lambda_- t)]. \quad (2.32)$$

The RMS value of the eccentricity is then given by

$$\langle e_j^2 \rangle^{1/2} = \sqrt{\mathcal{E}_{fi}^2 + c_+^2 (v_+)_j^2 + c_-^2 (v_-)_j^2}, \quad (2.33)$$

where $(v_{\pm})_j$ is the j -th component of vector \mathbf{v}_{\pm} (Eq. 2.25). The equation above can be simplified to give the explicit expressions for the RMS eccentricities of the two inner planets:

$$\langle e_1^2 \rangle^{1/2} = \sqrt{2} \left[\mathcal{E}_{f1}^2 + \frac{(-L_1 \mathcal{E}_{f1}^2 + L_2 \mathcal{E}_{f2}^2) v_{12}^2 - L_1 \mathcal{E}_{f1} \mathcal{E}_{f2} \Delta\omega v_{12}}{L_2 \Delta\omega^2 + 4L_1 v_{12}^2} \right]^{1/2}, \quad (2.34)$$

$$\langle e_2^2 \rangle^{1/2} = \sqrt{2} \left[\mathcal{E}_{f2}^2 + \frac{(L_2 \mathcal{E}_{f1}^2 - L_1 \mathcal{E}_{f2}^2) v_{21}^2 - L_2 \mathcal{E}_{f1} \mathcal{E}_{f2} \Delta\omega v_{21}}{L_2 \Delta\omega^2 + 4L_1 v_{21}^2} \right]^{1/2}. \quad (2.35)$$

A comparison between the above expressions and the results of numerical integrations based on secular equations is shown in Fig. 2.2, where we plot the RMS values of the planet eccentricities of a fiducial 2-planet inner system under the influence of a co-planar,

eccentric giant perturber. As in the case of mutual inclinations, the eccentricities of the inner system fall into the three regimes characterized by strong inner planet coupling, resonance and weak inner planet coupling. We elaborate on these in the following subsections.

Resonance

When $\omega_1 \simeq \omega_2$ (note that this is approximately equivalent to the condition $\epsilon_{12} \sim 1$), a potential resonance feature arises where large eccentricities can be excited in the inner planets, even for small e_p . If we take $\omega_1 = \omega_2$, equations (2.34) and (2.35) becomes

$$\langle e_1^2 \rangle_{\text{res}}^{1/2} = \sqrt{2} \left[\frac{3L_1 \mathcal{E}_{f1}^2 + L_2 \mathcal{E}_{f2}^2}{4L_1} \right]^{1/2}, \quad (2.36)$$

$$\langle e_2^2 \rangle_{\text{res}}^{1/2} = \sqrt{2} \left[\frac{5L_2 \mathcal{E}_{f2}^2 - L_1 \mathcal{E}_{f2}^2}{4L_2} \right]^{1/2}. \quad (2.37)$$

We see that the eccentricity of planet 1 is boosted while the eccentricity of planet 2 is dampened near the resonance. The resonance feature is most pronounced when $L_2 \gg L_1$. To illustrate this, let $L_1 = 0$, then the forced eccentricity on the inner planet becomes

$$\mathcal{E}_{f1} = \left(\frac{\nu_{1p}}{\omega_1} + \frac{\nu_{2p}}{\omega_2} \right) \mathcal{E}_p, \quad (L_1 \ll L_2). \quad (2.38)$$

If the inner planets both have zero initial eccentricity, then their eccentricity evolution is given by:

$$\begin{aligned} \mathcal{E}_1(t) = & \left[\frac{\nu_{1p}}{\omega_1} + \frac{\nu_{12}\nu_{2p}}{(\omega_1 - \omega_2)\omega_1} \right] [1 - \exp(i\omega_1 t)] \mathcal{E}_p \\ & + \left[\frac{\nu_{12}\nu_{2p}}{(\omega_1 - \omega_2)\omega_2} \right] [1 - \exp(i\omega_2 t)] \mathcal{E}_p, \end{aligned} \quad (2.39)$$

$$\mathcal{E}_2(t) = \left(\frac{\nu_{2p}}{\omega_2} \right) [1 - \exp(i\omega_2 t)] \mathcal{E}_p, \quad (L_1 \ll L_2). \quad (2.40)$$

In this limiting case, according to the linear theory, at $\epsilon_{12} \simeq 1$ the eccentricity of the inner planet can become arbitrarily large, even for small initial values of e_p . In reality, the linear theory breaks down as e_1 becomes too large, and higher order terms will keep e_1 to a modest value.

An illustration of the resonance behavior can be seen in Fig. 2.2. Systems with larger ratios of m_2/m_1 tend to exhibit pronounced resonance features, whereas for systems with more comparable masses, the feature is notably reduced.

Strongly and Weakly Coupled Regime

In the case where the mutual precession rates of the inner planets dominates over the influence of the perturber (i.e. $\omega_{12} \gg \omega_{1p}$ and $\omega_{21} \gg \omega_{2p}$), the general expressions (2.34) and (2.35) can be significantly simplified; we refer to this as the strongly coupled regime. In this regime, the two planets attain very similar forced eccentricities ($\mathcal{E}_{f1} \simeq \mathcal{E}_{f2}$), and as a result Eqs. (2.34) and (2.35) are dominated by their first terms. Explicitly, in this regime the RMS eccentricities are approximately given by

$$\begin{aligned} \langle e_1^2 \rangle^{1/2} &\simeq \sqrt{2}\mathcal{E}_{f1} \simeq \sqrt{2}F_{11}e_p \\ &\simeq \frac{5\sqrt{2}e_p}{4} \left[\frac{\alpha_{12} + \beta_{12} \left(\frac{m_2}{m_1} \right) \alpha_{12}^{-2}}{1 - \beta_{12}^2} \right] \left[\frac{3\alpha_{12}}{b_{3/2}^{(1)}(\alpha_{12})} \right] \left(\frac{m_p}{m_2} \right) \left(\frac{a_2}{a_p} \right)^4 \end{aligned} \quad (2.41)$$

$$\begin{aligned} \langle e_2^2 \rangle^{1/2} &\simeq \sqrt{2}\mathcal{E}_{f2} \simeq \sqrt{2}F_{12}e_p \\ &\simeq \frac{5\sqrt{2}e_p}{4} \left[\frac{\beta_{12}\alpha_{12} + \left(\frac{m_2}{m_1} \right) \alpha_{12}^{-2}}{1 - \beta_{12}^2} \right] \left[\frac{3\alpha_{12}}{b_{3/2}^{(1)}(\alpha_{12})} \right] \left(\frac{m_p}{m_2} \right) \left(\frac{a_2}{a_p} \right)^4, \end{aligned} \quad (2.42)$$

where $\alpha_{12} = (a_1/a_2)$ and $\beta_{12} = \beta(a_1/a_2)$ (see Eq. 2.8). In the other limiting case (i.e. weak coupling), when the precession rates of the inner planets driven by the perturber dominate their mutual precession rates (i.e. $\nu_{1p} \gg \omega_{12}$ and $\nu_{2p} \gg \omega_{21}$), the terms of

order ν_{12}/ω_{1p} and ν_{21}/ω_{2p} in Eqs. (2.34) - (2.35) can be dropped, and the final inner planets' RMS eccentricities are again given by $\sqrt{2}\mathcal{E}_f$. In this case, the planets precess independently of one another, and their eccentricities are given by Eqs. (2.11) and (2.12), i.e.

$$\langle e_1^2 \rangle^{1/2} \simeq \sqrt{2} \left(\frac{5}{4} \right) \left(\frac{a_1}{a_p} \right) e_p, \quad (2.43)$$

$$\langle e_2^2 \rangle^{1/2} \simeq \sqrt{2} \left(\frac{5}{4} \right) \left(\frac{a_2}{a_p} \right) e_p. \quad (2.44)$$

Note that the criterion for the eccentricities of the inner planets to be strongly coupled or weakly coupled is related to the parameter ϵ_{12} (see Eq. 2.15). For distant perturbors (i.e. $a_2 \ll a_p$), we generally have that $\nu_{1p} \sim \nu_{2p} \lesssim (\omega_{2p} - \omega_{1p})$. Therefore, the condition for strong eccentricity coupling is approximately $\max(\nu_{1p}, \nu_{2p}) \sim (\omega_{2p} - \omega_{1p}) \lesssim (\omega_{12} + \omega_{21})$, which is the same as $\epsilon_{12} \ll 1$.

Similarly, $\epsilon_{12} \gg 1$ implies that $\omega_{2p} - \omega_{1p} \gg \omega_{12} + \omega_{21}$. Since $\omega_{1p}, \omega_{2p} > (\omega_{2p} - \omega_{1p})$ while $\omega_{12}, \omega_{21} < (\omega_{12} + \omega_{21})$, we find that $\epsilon_{12} \gg 1$ corresponds to the weak eccentricity coupling condition that $\omega_{2p} \gg \omega_{21}$ and $\omega_{1p} \gg \omega_{12}$. Although the correspondence between ϵ_{12} and the strong/weak coupling regimes is not exact, it serves as a useful dimensionless parameter for describing the dynamical evolution of the inner planet eccentricities.

The colored dashed curves in Fig. 2.2 compare the strong coupling and weak coupling approximations with both the full linearized theory (solid curves) as well as numerical secular integrations (dots). One can see that as ϵ_{12} approaches either very small or very large values, the limiting expression $\langle e_j^2 \rangle^{1/2} \simeq \sqrt{2}\mathcal{E}_{fj}$ becomes an increasingly more robust approximation for the full secular dynamics of the inner system.

Qualitatively, for $\epsilon_{12} \ll 1$, the inner planets are tightly coupled and their eccentricity vectors precess in tandem, and the eccentricity excitations are greatly muted; in this

regime, $e_i \propto e_p m_p / a_p^4$. In the weak coupling regime ($\epsilon_{12} \gg 1$), $e_i \sim e_p (a_i / a_p)$. Note that in either limit, the scaling of e_j is suppressed by factor a_p^{-1} compared to the scaling for θ_{12} ; this is due to eccentricity oscillations being driven by the octupole (as opposed to the quadrupole) potential of the perturber.

However, there is one important difference between the eccentricity and inclination excitations for highly compact inner systems. As the inner planets become increasingly compact ($a_1/a_2 \rightarrow 1$), $\epsilon_{12} \rightarrow 0$ and the inner systems become essentially rigid and the mutual inclination induced by any perturber approaches zero. On the other hand, for highly compact planets even as $(a_2/a_1) \rightarrow 1$ the induced eccentricity approaches a finite value that scales with (m_p/a_p^4) . In other words, extremely compact systems that are strongly protected from mutual inclination excitations can still be somewhat susceptible to excitations in eccentricity.

This effect is shown in Fig. 2.3, where the inner planet mutual inclinations and eccentricities are plotted for different values of a_2/a_1 . We find that with a_1, a_p fixed, as $(a_2/a_1) \rightarrow 1$, even a small decrease in (a_2/a_1) leads to significant decreases in the inner planet mutual inclination excitations. For instance, as (a_2/a_1) decreases from 1.3 to 1.2, θ_{12} decreases by a factor of ~ 3 , whereas the changes in e_1 and e_2 are only $\sim 8\%$.

2.3 Extension to Moderately Inclined and Eccentric Perturbers

When both e_p and θ_p are significant, the linearized secular theory breaks down and one must resort to secular or N-body numerical integrations. However, note that for inner planets in the strong coupling regime, the planets maintain small eccentricities and mutual inclinations. As a result, for this region of parameter space the evolution is non-linear only in the variables e_p and θ_p . This allows us to extend the regime of

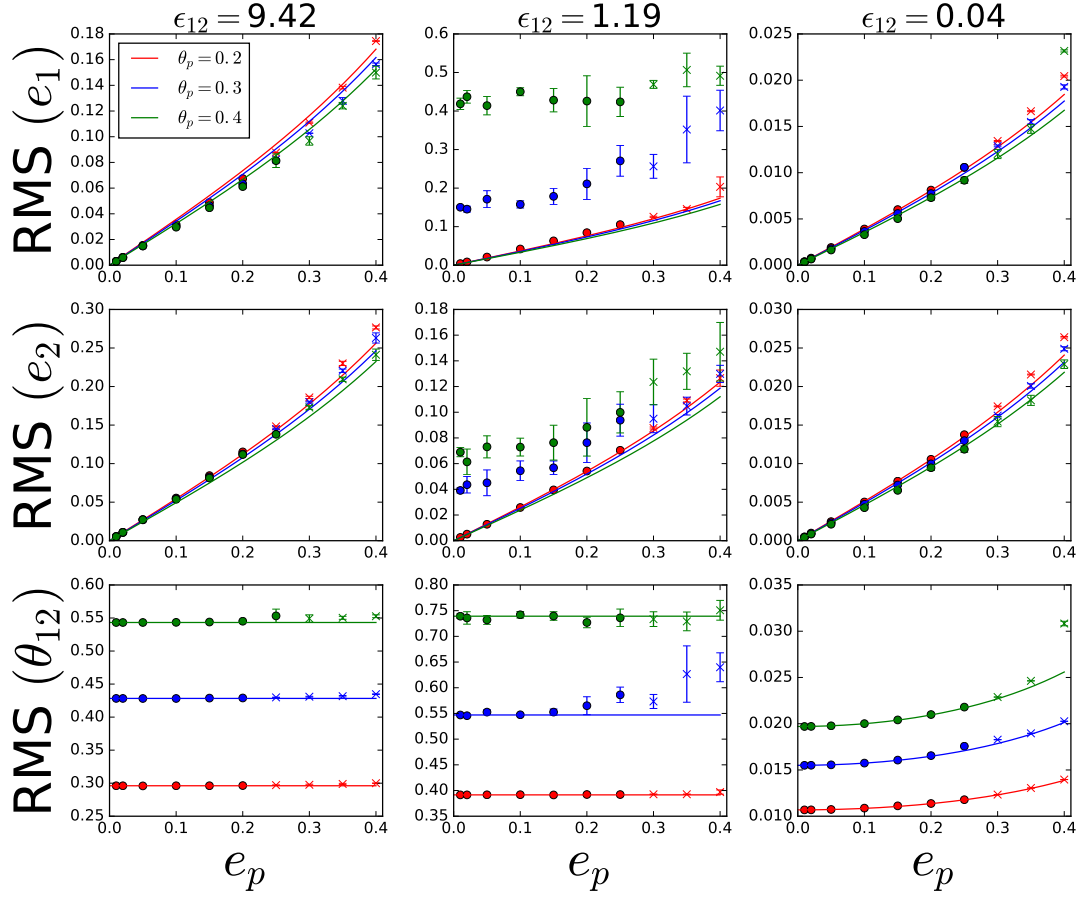


Figure 2.4: RMS values of the inner planet eccentricities e_1, e_2 and their mutual inclination θ_{12} as a function of e_p for a “2-planet plus perturber system” with $a_1 = 0.3$ au, $a_2 = 0.5$ au, $m_1 = 3M_\oplus$ and $m_2 = 5m_1$, perturbed by a $m_p = 5M_J$ planet. The panels, from left to right, represent three different perturber strengths ϵ_{12} , which is varied by adjusting a_p . The different colors are for different values of θ_p , with red, blue and green being $\theta_p = 0.2, 0.3, 0.4$ respectively. The points are the results of numerical secular equation integrations using Eqs. (A.2) - (A.5) while the solid lines are analytical results based on non-linear extensions to linear secular theory (Sec. 2.2). For the left and center panels where $\epsilon_{12} > 1$, we obtain the solid curves from Eqs. (2.54) - (2.56), while for the right panel they were obtained from Eqs. (2.51) - (2.53). A point is marked with an ‘o’ if the inner system is stable, and ‘x’ if it is unstable with respect to the stability criterion (Eq. 2.57). Each point represents 3 different numerical secular simulations with otherwise identical initial parameters, except with the initial longitude of ascending node and longitude of perihelion sampled randomly in the interval $[0, 2\pi]$.

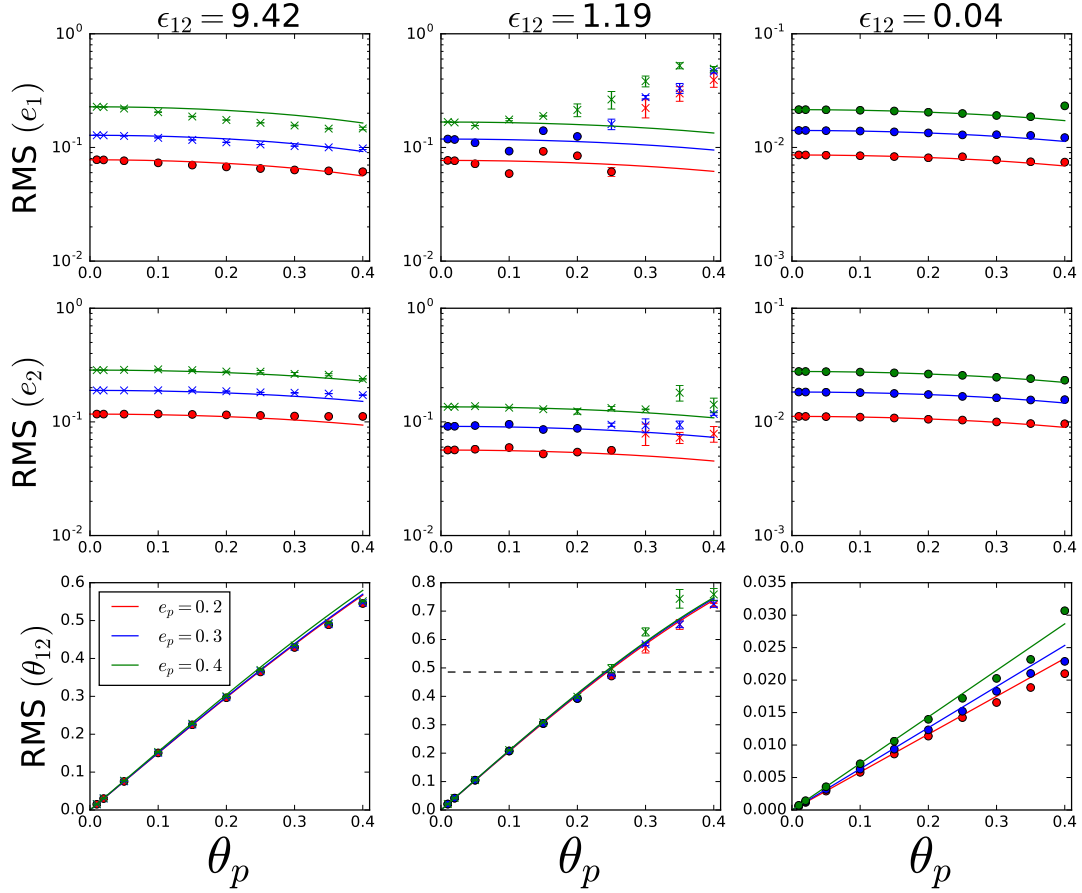


Figure 2.5: Same as Fig. 2.4, except that the results are plotted as a function of θ_p . The different colors are for different values of e_p with red, blue and green being $e_p = 0.2, 0.3, 0.4$ respectively. The dashed line in the center bottom panel corresponds to $\theta_{12} = 0.68$ rad. (39°), the Lidov-Kozai critical angle. Note that when $\theta_{12} \leq 0.68$ rad., the inner planets experience mutual Lidov-Kozai oscillations leading to large excitation of e_1 (see the middle column).

validity of the result based on linearized secular theory by substituting the linear scalings of e_p, θ_p with the appropriate non-linear scalings.

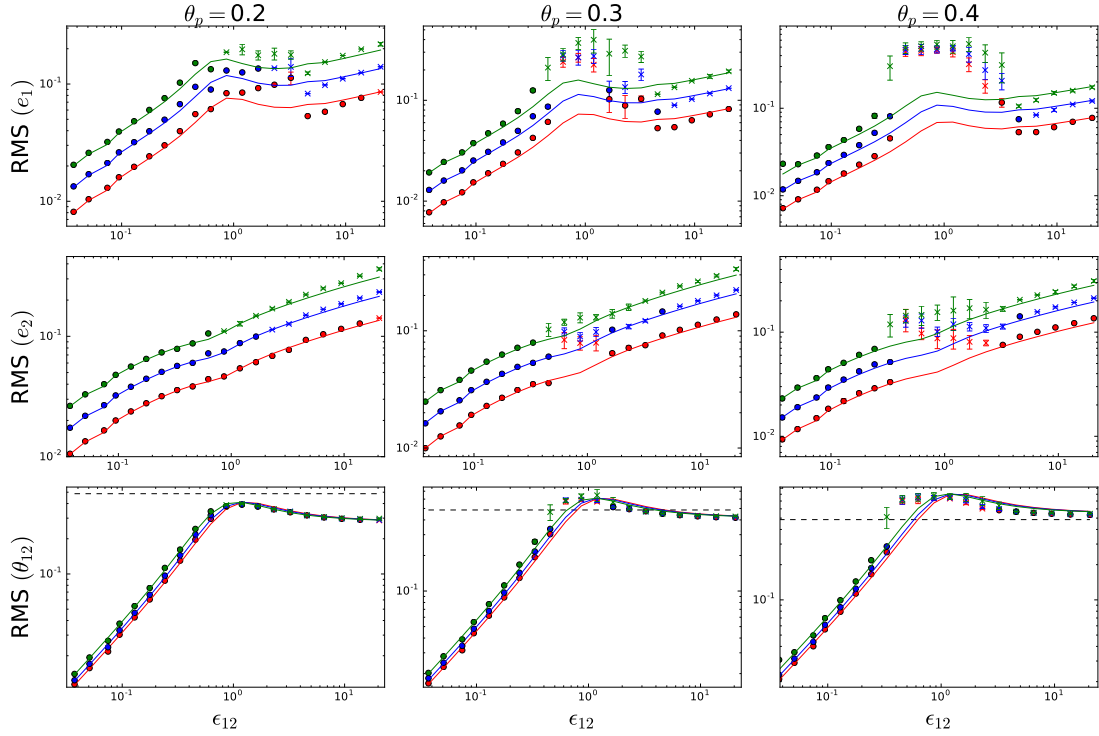


Figure 2.6: Same as Fig. 2.4, except that the results are plotted as a function of ϵ_{12} . The variation of ϵ_{12} is achieved by fixing $m_p = 5M_J$ while varying a_p . The different colors are for different values of e_p , with red, blue and green being $e_p = 0.2, 0.3, 0.4$ respectively. The panels from left to right have different values of $\theta_p = 0.2, 0.3, 0.4$ respectively. For the bottom three panels, the solid lines are derived from Eq. (2.16), but with ω_{jp} replaced by $\tilde{\omega}_{jp}$ (Eq. 2.47). The horizontal dashed line corresponds to $\theta_{12} = 0.68$ rad.

2.3.1 Secular Equations

The secular evolution multi-planet systems can be studied using different approaches, each having its own regime of validity. The standard Laplace-Lagrange theory (see Murray and Dermott, 1999, the vector form is used in Section 2.2) assumes small eccentricities and inclinations for all planets (and perturbers), but allows arbitrary ratio of semi-major axes between planets, as long as the system is dynamically stable. On the other hand, for hierarchical systems, one can expand the interaction potential between

planets (and perturbers) in terms of the (small) ratio of semi-major axes, while allowing for arbitrary eccentricities and inclinations – this multipole expansion approach has a long history (e.g. Lidov, 1962; Kozai, 1962; Ford et al., 2000; Laskar and Boué, 2010). We derive our results from the secular equations based on full, doubly-averaged multipole expansion of the disturbing potential up to the octupole order. We use the vector form of the secular equations of motion (Liu et al. 2015; see also Boué and Fabrycky 2014a, Petrovich 2015a), expressed in terms of the dimensionless angular momentum vector \mathbf{j}_j and eccentricity vector \mathbf{e}_j of each planet (see Eq. 2.1). While these equations of motion accurately account for the interaction between a planet in the inner system and the distant perturber, they become a poor approximation when describing the interaction between the inner, closely spaced planets. We therefore use a modified version of the equations of motion that hybridizes the Lagrange-Laplace theory with the multipole expansion results by introducing appropriate Laplace coefficients in place of the usual $a_{<}^n/a_{>}^{n+1}$ terms in the multipole expansion (see Appendix A).

While our hybrid equations of motion are formally nonlinear in terms of the eccentricities and inclinations of all planets, they are valid only when the inner planets have small eccentricities and mutual inclinations. For systems where the inner planets are strongly packed and e_p, θ_p of the external perturber are modest (e.g. $\lesssim 0.4$), the inner planet eccentricities and mutual inclinations will be small, and the equations are nonlinear only in e_p and θ_p . (In the case when the inner planets develop large eccentricities and/or mutual inclinations, dynamical instability is likely to set in and the secular theory breaks down.) As a result, we can treat the inner planets as behaving linearly, but subject to external forcing with a non-linear dependence on e_p, θ_p .

To the leading order, the evolution of $\mathbf{j}_j, \mathbf{e}_j$ of an inner planet due to the perturber is

given by (see Eqs. A.2 - A.3)

$$\left(\frac{d\mathbf{j}_j}{dt}\right)_p \simeq \frac{\omega_{jp} \cos \theta_{jp}}{(1 - e_p^2)^{3/2}} (\mathbf{j}_j \times \hat{\mathbf{n}}_p), \quad (2.45)$$

$$\begin{aligned} \left(\frac{d\mathbf{e}_j}{dt}\right)_p &\simeq \frac{\omega_{jp}}{(1 - e_p^2)^{3/2}} [\cos \theta_{jp} (\mathbf{e}_j \times \hat{\mathbf{n}}_p) - 2(\mathbf{e}_j \times \mathbf{j}_j)] \\ &\quad - \frac{5\nu_{jp}}{4(1 - e_p^2)^{5/2}} \left[\cos^2 \theta_{jp} - \frac{1}{5} \right] (\mathbf{j}_j \times \mathbf{e}_p) \\ &\simeq -\frac{\omega_{jp} \cos \theta_{jp}}{(1 - e_p^2)^{3/2}} (\mathbf{e}_j \times \hat{\mathbf{n}}_p) \\ &\quad - \frac{5\nu_{jp}}{4(1 - e_p^2)^{5/2}} \left[\cos^2 \theta_{jp} - \frac{1}{5} \right] (\mathbf{j}_j \times \mathbf{e}_p), \end{aligned} \quad (2.46)$$

where in the last equation we have replaced the term $(\mathbf{e}_j \times \mathbf{j}_j)$ with its time-average by taking $\mathbf{j}_j \approx \langle \mathbf{j}_j(t) \rangle = \cos \theta_{jp} \hat{\mathbf{n}}_p$. The terms proportional to $(\mathbf{e}_j \times \hat{\mathbf{n}}_p)(\mathbf{j}_j \times \hat{\mathbf{n}}_p)$ were dropped as they are proportional to e_j which is assumed to be small. We now define:

$$\tilde{\omega}_{jp} \equiv \omega_{jp} \left[\frac{\cos \theta_{jp}}{(1 - e_p^2)^{3/2}} \right], \quad (2.47)$$

$$\tilde{\nu}_{jp} \equiv \nu_{jp} \left[\frac{5 \cos^2 \theta_{jp} - 1}{4(1 - e_p^2)^{5/2}} \right]. \quad (2.48)$$

We then obtain a modified version of the Laplace-Lagrange evolution equations for the eccentricity vector \mathbf{e}_j and unit angular momentum vector \mathbf{j}_j (with $k = 1, 2, 3 \dots N$, not including the perturber):

$$\frac{d\mathbf{e}_j}{dt} = - \sum_{k \neq j} \omega_{jk} (\mathbf{e}_j \times \mathbf{j}_k) - \sum_{k \neq j} \nu_{jk} (\mathbf{j}_j \times \mathbf{e}_k) - \tilde{\omega}_{jp} (\mathbf{e}_j \times \mathbf{j}_p) - \tilde{\nu}_{jp} (\mathbf{j}_j \times \mathbf{e}_p), \quad (2.49)$$

$$\frac{d\mathbf{j}_j}{dt} = \sum_{k \neq j} \omega_{jk} (\mathbf{j}_j \times \mathbf{j}_k) + \tilde{\omega}_{jp} (\mathbf{j}_j \times \mathbf{j}_p). \quad (2.50)$$

The above equations are analogous to the linearized Laplace-Lagrange theory (Eq. 2.2 and 2.3), except with modified quadrupole and octupole precession frequencies $\tilde{\omega}_{jp}$ and $\tilde{\nu}_{jp}$.

2.3.2 Results for “Two Planets + Perturber” System

We can now extend the analytical results of Section 2.2 to finite e_p and θ_p . Specifically, the mutual inclination θ_{12} of the “two planets + perturber” system can be obtained using Eq. (2.16), except with ω_{1p} and ω_{2p} replaced by $\tilde{\omega}_{1p}$ and $\tilde{\omega}_{2p}$, respectively. Similarly, the inner planet eccentricities can be computed using Eqs. (2.34) - (2.35), except with ω_{jp} and ν_{jp} replaced by $\tilde{\omega}_{jp}$ and $\tilde{\nu}_{jp}$ for $j \in \{1, 2\}$.

When the inner planets are strongly coupled ($\epsilon_{12} \ll 1$), the extension to mildly eccentric and misaligned perturbers can be simplified even further. Substituting the frequencies from Eqs. (2.47) - (2.48) into Eqs. (2.16), (2.34) and (2.35), and making an expansion to second order in θ_p we have

$$\langle e_1^2 \rangle^{1/2}(e_p, \theta_p) \simeq \left[\frac{1 - 5\theta_p^2/4}{(1 - e_p^2)^{5/2}} \right] \langle e_1^2 \rangle_{\text{lin}}^{1/2}, \quad (2.51)$$

$$\langle e_2^2 \rangle^{1/2}(e_p, \theta_p) \simeq \left[\frac{1 - 5\theta_p^2/4}{(1 - e_p^2)^{5/2}} \right] \langle e_2^2 \rangle_{\text{lin}}^{1/2}, \quad (2.52)$$

$$\langle \theta_{12}^2 \rangle^{1/2}(e_p, \theta_p) \simeq \left[\frac{1 - \theta_p^2/2}{(1 - e_p^2)^{3/2}} \right] \langle \theta_{12}^2 \rangle_{\text{lin}}^{1/2}, \quad (2.53)$$

where the “linear” expressions for $\langle e_1^2 \rangle_{\text{lin}}^{1/2}$, $\langle e_2^2 \rangle_{\text{lin}}^{1/2}$ and $\langle \theta_{12}^2 \rangle_{\text{lin}}^{1/2}$ are given by Eqs. (2.12), (2.35) and (2.16), respectively.

When the inner planets are weakly coupled ($\epsilon_{12} \gg 1$), a similar simplification can be made. However, we caution that the underlying assumptions that e_j and θ_{jk} are small may no longer be valid in this regime, and the non-linear extensions in this case may not

be fully justified. Nonetheless, we include them below for completeness:

$$\langle e_1^2 \rangle^{1/2}(e_p, \theta_p) \simeq \left(\frac{1 - 3\theta_p^2/4}{1 - e_p^2} \right) \langle e_1^2 \rangle_{\text{lin}}^{1/2}, \quad (2.54)$$

$$\langle e_2^2 \rangle^{1/2}(e_p, \theta_p) \simeq \left(\frac{1 - 3\theta_p^2/4}{1 - e_p^2} \right) \langle e_2^2 \rangle_{\text{lin}}^{1/2}, \quad (2.55)$$

$$\langle \theta_{12}^2 \rangle^{1/2}(e_p, \theta_p) \simeq \langle \theta_{12}^2 \rangle_{\text{lin}}^{1/2}, \quad (2.56)$$

where the “linear” expressions for $\langle e_j^2 \rangle_{\text{lin}}^{1/2}$ are given by Eq. (2.12), and $\langle \theta_{12}^2 \rangle_{\text{lin}}^{1/2}$ is given by Eq. (2.20).

Our results are summarized in Figs. 2.4 - 2.6, in which we show the RMS values of the inner planet eccentricities e_1 and e_2 and mutual inclination θ_{12} as a function of e_p , θ_p and a_p (varied by varying ϵ_{12}) respectively. In each figure, we compare the results of our non-linear extension to linear theory (solid curves) with numerical secular integrations (points). The linear theory extension to mild θ_p and e_p appears to agree well with numerical secular integrations up to values of e_p and $\theta_p \sim 0.4$. One case where our analytical expressions agree poorly with secular integrations occur when $m_1 \ll m_2$, $\epsilon_{12} \simeq 1$ and $\theta_{12} \geq 39^\circ$, seen most prominently for the green points in the middle panels of Figs. 2.4 and 2.5 and the top panels of Fig. 2.6. We elaborate on this feature in the next subsection.

2.3.3 Resonance Feature and Internal Lidov-Kozai Oscillations

In cases with mild e_p, θ_p , for certain parameters the previously noted resonance at $\epsilon_{12} \simeq 1$ takes on a richer behavior (see Section 2.2.3). We find that for systems with $\epsilon_{12} \simeq 1$, whenever θ_p is sufficiently large such that the inner planets attain the critical mutual inclination angle for Lidov-Kozai oscillations ($\theta_{12} \geq 0.68 \text{ rad.} = 39^\circ$) (see Lidov, 1962; Kozai, 1962), the inner planets can experience dramatic growth in eccentricity regardless

of the value of e_p , in a fashion analogous to secular oscillations first described by Lidov (1962) and Kozai (1962). This is most clearly seen in the middle column of Fig. 2.5. The rise in $\langle e_1^2 \rangle^{1/2}$ coincides with the inner planets obtaining a mutual inclination greater than 39° . This behavior is not predicted by the linearized secular theory, which always yields $e_1 \lesssim e_p$ for $e_p \ll 1$.

In order for the Lidov-Kozai-like oscillations between the inner planets to occur, we find the three following criteria are required: The innermost planet should be less massive than the outer one (i.e. $m_1 \lesssim m_2$); the “2 planets plus perturber” system should be near the secular resonance, with $\epsilon_{12} \simeq 1$; the misalignment angle θ_p should be smaller than the Kozai critical angle ($\theta_p \lesssim 0.68$ rad.), but sufficiently large to induce the inner pair to have a mutual misalignment greater than the Lidov-Kozai critical angle ($\theta_{12} \simeq 0.68$ rad.)².

In our numerical investigations, we find that both our hybrid secular numerical algorithm and N-body calculations exhibit this behavior, although the N-body results deviate somewhat from our secular predictions. We find that such mutual Lidov-Kozai cycles generally require larger θ_p in the N-body simulations and take on milder behaviors (see Section 2.4).

2.4 Comparison with N-body Integrations

We compare our results based on secular equations with N-body simulations by computing the same systems with REBOUND, using the WHFast integrator (Rein and Liu, 2012a; Rein and Tamayo, 2015). We chose $a_1 = 0.3$ au and $a_2 = 0.5$ au, with a_p

²Note that for $\theta_p \gtrsim 0.68$ rad., the perturber will drive the inner planets into conventional Lidov-Kozai oscillations, resulting in close encounters and/or collisions between the inner planets as their orbits would eventually cross.

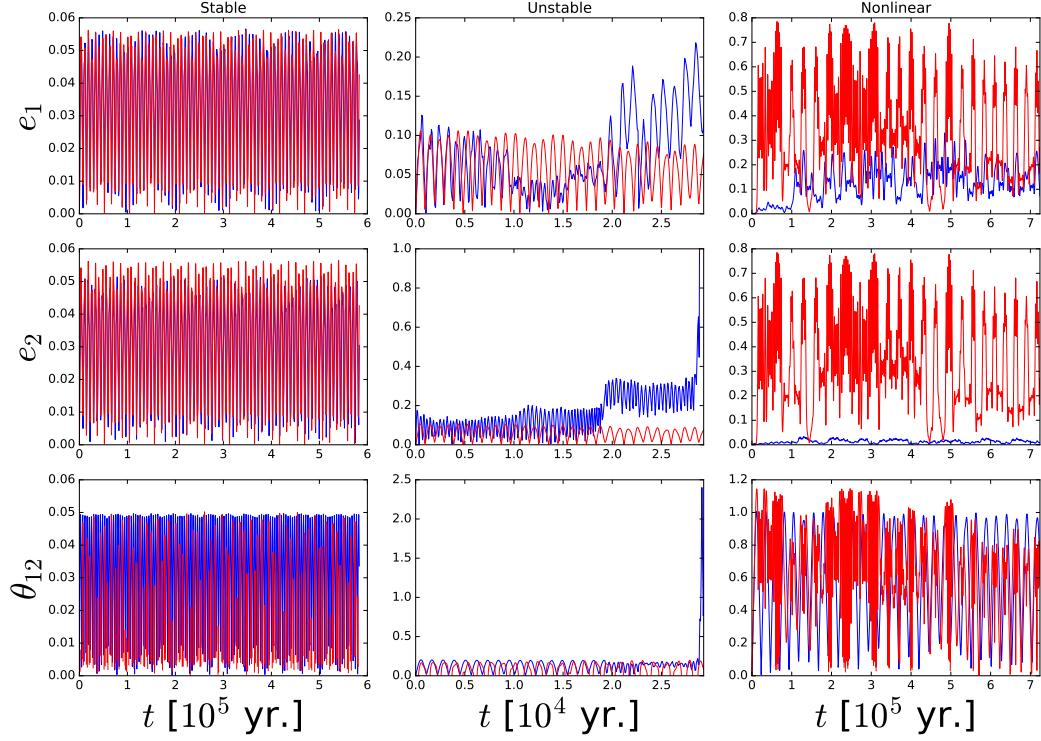


Figure 2.7: Sample evolution of “two-planet + perturber” system using N-body integrations. From top to bottom, the y-axis shows e_1 , e_2 , and θ_{12} . From left to right are three different scenarios corresponding to the stable, unstable and nonlinear (Lidov-Kozai-like oscillation) regimes. The red curve shows results based on secular integration while the blue curve are from N-body integration using the same initial parameters. Left: an example where the secular hybrid algorithm matches closely with N-body integrations. For this particular model, a_1, a_2, a_p are 0.3, 0.39 and 1.6 au respectively, while $m_1 = m_2 = 3M_\oplus$ and $m_p = 3M_J$. The perturber has $e_p = a_p = 0.1$. Center: Same as left, except here $a_p = 1.26$ au. This is an example of the inner two planets driven into dynamical instability, as a result of eccentricity excitation by the perturber. Right: An example of Kozai-like oscillations. Here, a_1, a_2, a_p are 0.3, 0.45, 1.94 au respectively, such that $\epsilon_{12} \simeq 1$. The planets have masses $m_1 = 0.6M_\oplus$, $m_2 = 3M_\oplus$ and $m_p = 3M_J$, and the perturber has $m_p = 3M_J$, $e_p = 0.02$ and $\theta_p = 0.4$.

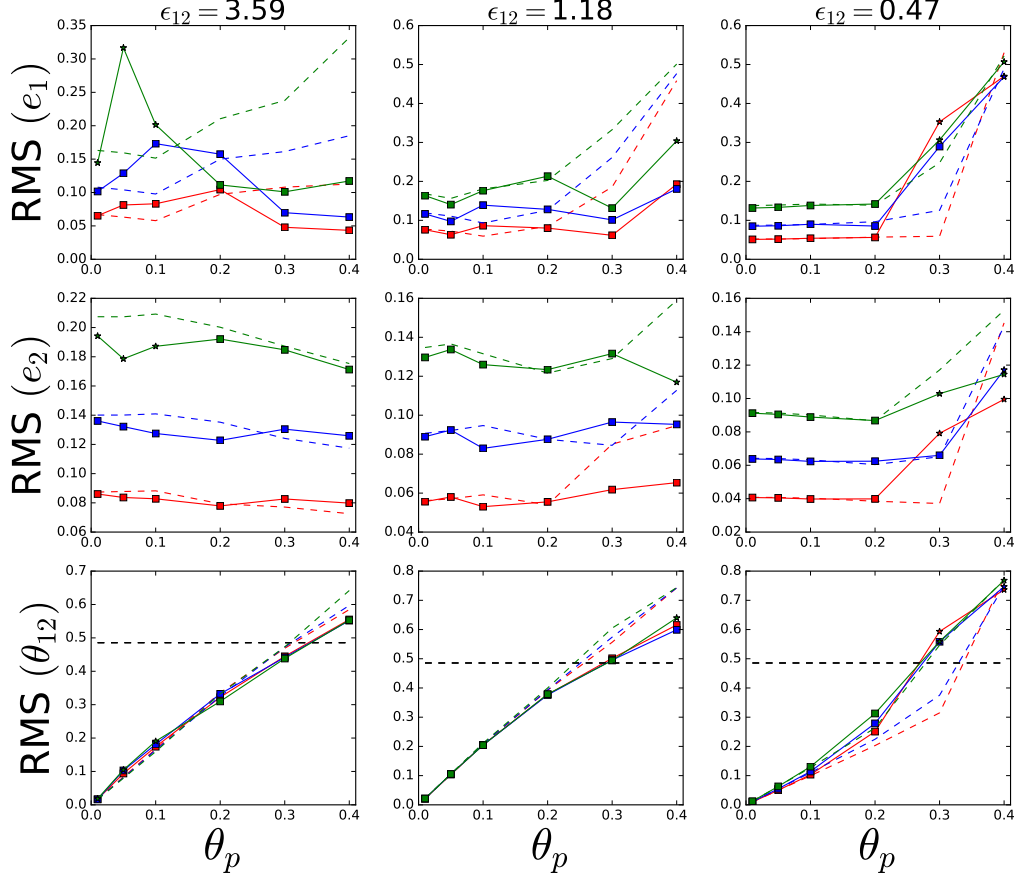


Figure 2.8: RMS values of planet eccentricities and inclinations for a “2-planet + perturber” system with $a_1 = 0.3$ au, $a_2 = 0.5$ au, $m_1 = 0.6M_\oplus$ and $m_2 = 3M_\oplus$, perturbed by a $m_p = 5M_J$ planet. The panels, from left to right, represent three different perturber strengths ϵ_{12} , which is varied by adjusting a_p . The different colors are for different values of e_p , with red, blue and green corresponding to $e_p = 0.2$, 0.3 , and 0.4 respectively. The solid curves are the results based on N-body integrations while the dashed curves are the results of hybrid secular equations. Systems that are stable during the integration were marked with a filled square for the solid curves, while those that were unstable with respect to orbit crossings are marked with a star. The dashed horizontal lines on the bottom panels corresponds to $\theta_{12} = 0.68$ rad.

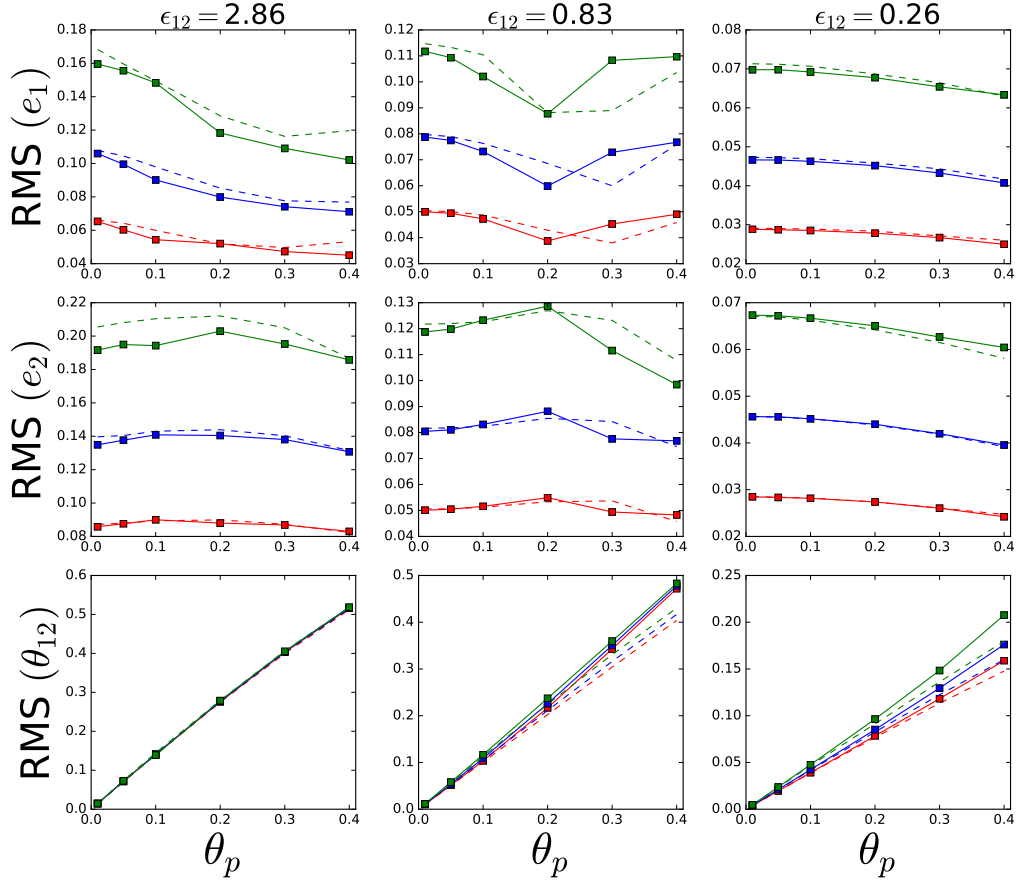


Figure 2.9: Same as Fig. 2.8, except that $m_1 = m_2 = 3M_\oplus$.

varying between 0.9 – 6 au. We select our timestep such that dt is equal to 1/40 of the orbital periods of the innermost planet, and we integrate our systems up to 10^6 yr or until one of the planets is ejected. The planets were taken to be point masses and physical collision were ignored. The planet masses are $m_2 = 3M_\oplus$, $m_p = 5M_J$ and m_1 was either 0.5 or $3.0M_\oplus$. The first case (with $m_1 = 0.5M_\oplus$) represents a scenario where the secular resonance feature can significantly boost e_1 and θ_{12} . We start the integration with the inner planets in circular, co-planar orbits while the perturber has inclinations and eccentricities taken from the set $[0.01, 0.02, 0.05, 0.1, 0.2, 0.3, 0.4]$. The RMS eccentricities and inclinations are calculated over the timespan from the start until the end of the simulation.

The results of our comparison between N-body integrations and hybrid secular equation integrations are shown in Figs. 2.7 - 2.9. These results can be generally divided into three regimes, corresponding to the three columns of Fig. 2.7:

- In the first regime (left panels of Fig. 2.7), the inner planets undergo steady oscillations in their eccentricities and mutual inclinations; we call this the “stable” regime. The planet eccentricities and mutual inclinations (e_1 , e_2 , θ_{12}) tend to remain small in this regime, and there is excellent agreement between the results of our hybrid secular equations and N-body integrations. Note that while the oscillation amplitudes of the planet eccentricities and inclinations agree between the two methods, there is also a notable difference in the phase of the oscillations; this is in agreement with other studies and tends to usually be the case for systems in the stable regime.

- In the second regime (middle column of Fig. 2.7), the perturber drives the inner system into gravitational instability, leading to close encounters and/or orbit crossings between planets that are not captured by secular dynamics; we call this the ‘unstable’ regime. This regime typically corresponds to systems with $\epsilon_{12} > 1$ and modest e_p . In this scenario, whereas the hybrid secular integrations show stable oscillations for the planet eccentricities and mutual inclinations, the N-body simulations feature sudden and drastic growth in the eccentricities and mutual inclinations of the planets, eventually leading to planet collisions or ejections. Such planet systems would appear to be stable in our integrations based on secular equations, but are in reality unstable in the long-term.

Since secular methods are unsuitable for the study of these unstable systems, we caution that some of our secular results which leads to systems that undergo close encounters may produce misleading results. One way to filter out such potentially unstable systems is to use a stability criterion based on orbital parameters to identify systems that are gravitationally unstable. Petrovich (2015b) found empirically that the

criterion for a pair of planets on somewhat co-planar orbits ($\theta_{12} \lesssim 39^\circ$) to be stable for all time is given by:

$$\frac{a_1(1 - e_1)}{a_2(1 + e_2)} \leq 1.2. \quad (2.57)$$

Note that the above criterion was based on ensembles of numerical N-body integrations with planet ratios $\mu \equiv m/M_*$ between $10^{-2} - 10^{-4}$, and therefore is an overestimate for the stability criterion for planets with masses more comparable to super-Earths ($\mu \sim 10^{-5}$); nevertheless, we adopt it as a conservative estimate. In this study we adopt the above stability criterion for 2-planet systems and check our secular integrations for instability against this criteria. We found that for some of our numerical secular equations integrations, an external perturber could indeed excite the inner planets into instability for large enough ϵ_{12} and e_p . The parameters leading to this instability are marked with an ‘ \times ’ in Figs. 2.4 - 2.6. We caution that secular theory cannot adequately describe the dynamics of these systems and one should resort to full N-body simulations.

- A third regime of final outcomes occurs when the inner planets undergo Lidov-Kozai-like oscillations (right column of Fig 2.7), discussed in Section 2.3.3. In this regime, the results of secular integrations tend to be qualitatively similar to the N-body integrations, but with qualitative differences in the oscillation amplitudes of the planet eccentricities e_1 and e_2 . In comparison to the secular integrations, N-body integrations generally feature far milder eccentricity growth in the inner planets. In the example shown on the right of Fig. 2.7, whereas the secular integrations predict e_1 and e_2 to reach values of ~ 0.8 and ~ 0.14 respectively, the N-body integrations showed much smaller values of $e_1 \sim 0.15$ and $e_2 \sim 0.02$ respectively. The overall trend is most clearly seen in the middle column of Fig. 2.8, where even though both the secular integrations and N-body integrations show a steep increase in $\langle e_1^2 \rangle^{1/2}$ as θ_{12} increases beyond 39° , the magnitude of $\langle e_1^2 \rangle^{1/2}$ seen in N-body integrations is generally smaller than the secular integrations. The discrepancy is likely due to the presence of higher order corrections to

the secular equations, which were not captured by our expansion up to octupole order.

Figs. 2.8 and 2.9 show a comparison of the final RMS planet eccentricities and mutual inclinations obtained from our hybrid secular equations (dashes) versus N-body simulations (stars and filled squares); planet systems that became unstable in the N-body simulations due to the effect of the perturber were marked with a star, otherwise they were marked by filled squares. For Fig. 2.8, the planet masses were chosen to allow for resonance features and Lidov-Kozai-like oscillations to occur, by setting $m_1 = 0.6M_\oplus$ and $m_2 = 3M_\oplus$. The columns represent different coupling regimes, with the left, center and right panels corresponding to weak, resonant and strong coupling respectively, while the different colors represent different perturber eccentricities (with red, blue and green being $e_p = 0.2, 0.3, 0.4$ respectively). When ϵ_{12} , e_p and θ_p are small, there is good agreement between the results of hybrid secular equations and N-body integrations as the inner planets remain in the stable regime. For the case of $\epsilon_{12} \gtrsim 1$, the inner planets can be driven into the unstable regime (see, e.g. the green curve on the left-side panels), and there are more substantial deviations between our hybrid secular equations and N-body integrations. When the inner planets achieve $\theta_{12} \leq 0.68$ rad. (delineated by the dashed line on the bottom panels), Lidov-Kozai-like oscillations develop and the agreement between hybrid secular equations and N-body simulations become poor.

In Fig. 2.9, we show the same comparisons as Fig. 2.8, except with the inner planets having equal masses ($m_1 = m_2 = 3M_\oplus$) to prevent the development of resonance effects or Lidov-Kozai-like oscillations. In this case, we find strong agreements between the hybrid secular equations and N-body integrations across the range of parameters.

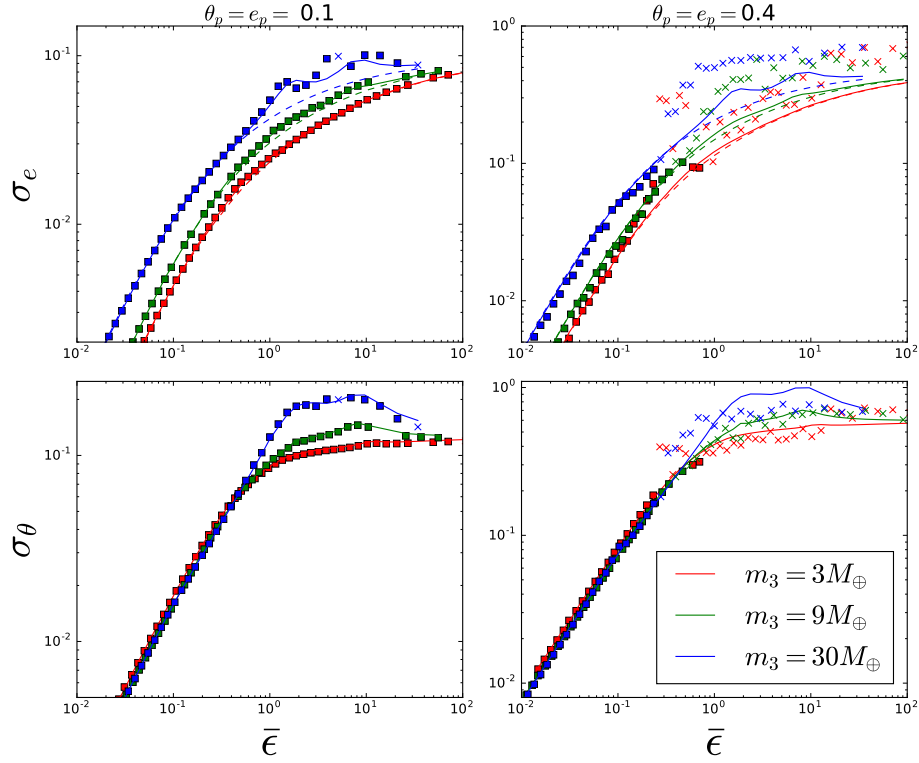


Figure 2.10: Comparison of the RMS values of planet eccentricities and inclinations for a hypothetical 4-planet system under the influence of an inclined, eccentric perturber, computed from secular theory (solid and dashed curves) and N-body simulations (‘ \times ’ and squares). The planets have masses $m_1 = m_2 = m_4 = 3M_\oplus$, and the 3rd planet is the ‘dominant’ one with $m_d = m_3$ equal to 3, 9, and $30M_\oplus$ for the red, green and blue curves respectively. The semi-major axes of the four inner planets are [0.1, 0.15, 0.25, 0.4] au, while $\bar{\epsilon}$ is varied by varying a_p . Points that are marked with filled squares represent systems stable against orbit crossings, while systems that have undergone orbit crossings are marked with an ‘ \times ’. From the top panel, the y-axis is the RMS eccentricity averaged over all planets, as function of mean coupling parameter $\bar{\epsilon}$. The left panel represents a “linear” case with $e_p = \theta_p = 0.1$ while the right panel has $e_p = \theta_p = 0.4$. The colored dashed lines are given by the forced eccentricity only (Eq. 2.68), while the solid curves are analytical estimates based on linear theory, given by Eq. (2.67) on the left panel and using the mild e_p extension (Eq. 2.77) on the right panel. The bottom panels are similar to the top panels, except the mean pairwise mutual inclination σ_θ is plotted on the y-axis. The solid curves are obtained from Eq. (2.75) for the left panel, with the nonlinear extension Eq. (2.78) being used for the right panel.

2.5 $N > 2$ Inner Planets + Perturber

The results of the above sections, applicable for inner systems with $N = 2$ planets, can be generalized to systems with more than two inner planets. Consider a system of $N > 2$ inner planets of masses m_i ($i = 1, 2, 3, \dots, N$) and semi-major axes a_i ($a_1 < a_2 < \dots < a_N$), accompanied by a giant planet (or stellar) perturber (with $m_p \gg m_i$, semi-major axis $a_p \gg a_i$, inclination angle θ_p and eccentricity e_p). The evolution equations for the eccentricity and inclination vectors of the j -th planet \mathbf{e}_j and \mathbf{j}_j are given by Eqs. (A.2) - (A.5). Given an inner system, how do the inner planet eccentricities and mutual inclinations change as a function of e_p , θ_p , m_p and a_p ?

For systems with many planets it is useful to consider the averaged dynamical quantities of all planets. We define σ_θ as the RMS time-averaged mis-alignment angle between all planet pairs:

$$\sigma_\theta \equiv \sin^{-1} \left[\left(\frac{1}{N(N-1)} \sum_j \sum_{k \neq j} \langle |\hat{\mathbf{n}}_j \times \hat{\mathbf{n}}_k|^2 \rangle \right)^{1/2} \right]. \quad (2.58)$$

We also define σ_e as the RMS time-averaged eccentricity of all planets:

$$\sigma_e \equiv \left(\frac{1}{N} \langle \sum_j |e_j|^2 \rangle \right)^{1/2}. \quad (2.59)$$

It is also useful to consider an “averaged” coupling parameter, analogous to ϵ_{12} for the $N = 2$ case. We define the “dominant” planet (labeled “d”) in the system as whichever planet in the system that has the largest mass. If all planets share the same mass, a good approximation is to let the planet with the median semi-major axis be the “dominant” one. Lai and Pu (2017) found a good choice for an averaged coupling parameter $\bar{\epsilon}$ to be

$$\bar{\epsilon} \equiv \left(\frac{1}{N-1} \langle \sum_{j \neq d} |\epsilon_{jd}|^2 \rangle \right)^{1/2}. \quad (2.60)$$

2.5.1 Multi-planet Eccentricity Evolution : Linear Theory

For $e_p \ll 1$, it is suitable to use the Laplace-Lagrange theory. The evolution of the eccentricity vector of each planet is given by Eq. (2.2), and we start by first casting this equation into matrix form:

$$\frac{d\mathcal{E}}{dt} = i\mathbf{A}\mathcal{E} - i\mathbf{B}e_p, \quad (2.61)$$

where \mathcal{E} is an N-dimensional vector with element \mathcal{E}_j given by the complex eccentricity (see Eq. 2.10). The matrix \mathbf{A} is given by:

$$\mathbf{A} = \begin{pmatrix} \omega_1 & -\nu_{12} & \cdots & -\nu_{1N} \\ -\nu_{21} & \omega_2 & \cdots & -\nu_{2N} \\ \vdots & \vdots & \ddots & \vdots \\ -\nu_{N1} & -\nu_{N2} & \cdots & \omega_N \end{pmatrix} \quad (2.62)$$

with ω_j defined as the sum of “quadrupole” frequencies from all other planets acting on planet j ,

$$\omega_j \equiv \sum_{k \neq j}^N \omega_{jk} + \omega_{jp}. \quad (2.63)$$

The vector \mathbf{B} is an N-dimensional vector representing the forcing term given by $B_j = \nu_{jp}$ (where $j = 1, 2, 3 \dots N$).

Let \mathbf{V} be the N×N matrix of eigenvectors for \mathbf{A} , and λ_n be the eigenvalue associated with the n -th eigenvector \mathbf{V}_n . Then the eccentricity evolution of the j -th planet is given by:

$$\mathcal{E}_j(t) = \mathcal{E}_{fj} + \sum_n^N b_n (\mathbf{V}_n)_j \exp(i\lambda_n t). \quad (2.64)$$

where $(\mathbf{V}_n)_j$ is the j -th component of vector \mathbf{V}_n , and \mathcal{E}_{fj} is the forced eccentricity on the j -th planet given by

$$\mathcal{E}_{fj} = (\mathbf{A}^{-1}\mathbf{B})_j e_p. \quad (2.65)$$

The coefficient b_n can be obtained by matching Eq. (2.64) to the initial condition. Since the inner planet eccentricities are initially zero, we have that:

$$b_n = e_p \left(\mathbf{V}^{-1} \cdot \mathbf{A}^{-1} \cdot \mathbf{B} \right)_n. \quad (2.66)$$

The RMS eccentricity of planet j is then given by:

$$\langle e_j^2 \rangle^{1/2} = \left(\sum_n b_n^2 (\mathbf{V}_n)_j^2 + \mathcal{E}_{fj}^2 \right)^{1/2}. \quad (2.67)$$

Analogous to the $N = 2$ case, in either the strong-coupling limit ($\bar{\epsilon} \ll 1$) or the weak-coupling limit ($\bar{\epsilon} \gg 1$), the forced eccentricity term dominates over the other modes, and a good approximation is

$$\langle e_j^2 \rangle^{1/2} = \sqrt{2} \mathcal{E}_{fj}. \quad (2.68)$$

The RMS eccentricity of the system σ_e is then given by

$$\sigma_e \approx \sqrt{\frac{2}{N}} |\mathbf{A}^{-1} \mathbf{B}| e_p. \quad (2.69)$$

Note that in the strong coupling limit, σ_e and $\langle e_j^2 \rangle^{1/2}$ both scale proportionally to m_p/a_p^4 , since in this limit $\omega_{jk} \gg \omega_{jp}$ for all $j, k \in \{1, 2, \dots, N\}$, and \mathbf{A}^{-1} is a linear combination of ω_{jk} , while \mathbf{B} is determined by $(v_{1p}, v_{2p}, \dots, v_{Np})$. Therefore, the quantity $(\mathbf{A}^{-1} \mathbf{B})$ can be written as a vector whose entries are a linear combination of v_{jp} divided by a linear combination of ω_{jk} (with various j and k). Similarly, in the weak coupling limit we have $\omega_j \simeq \omega_{jp}$, and σ_e and $\langle e_j^2 \rangle^{1/2}$ will scale with linear combinations of v_{jp}/ω_{jp} (with various j).

We illustrate our linear results on the top-left panel of Fig. 2.10, where we plot σ_e as a function of $\bar{\epsilon}$ (adjusted by adjusting a_p) for a 4-planet system under the influence of a $3M_J$ perturber with $e_p = \theta_p = 0.1$. The three different colored curves represent three different planet systems with different mass ratios between the dominant planet ($m_3 = m_d$) and

the other planets (which have equal masses). The solid and dashed curves are computed from Eqs. (2.67) and (2.68) respectively, while the filled squares and ‘×’ markers are obtained from N-body integrations with squares and crosses representing stable and unstable systems. Notice the excellent agreement between the theoretical and numerical results.

2.5.2 Multi-planet Inclination: Linear Theory

For $\theta_p \ll 1$, the evolution of the angular momentum vector of the j -th planet \mathbf{j}_j can be obtained using Laplace-Lagrange theory (Eq. 2.3). Again we start by first re-writing this equation into matrix form:

$$\frac{d}{dt}\mathcal{I} = i\mathbf{C}\mathcal{I} + i\mathbf{D}\theta_p. \quad (2.70)$$

The matrix \mathbf{C} is given by

$$\mathbf{C} = \begin{pmatrix} -\omega_1 & \omega_{12} & \cdots & \omega_{1N} \\ \omega_{21} & -\omega_2 & \cdots & \omega_{2N} \\ \vdots & \vdots & \ddots & \vdots \\ \omega_{N1} & \omega_{N2} & \cdots & -\omega_N \end{pmatrix} \quad (2.71)$$

where ω_j is given by Eq. (2.63) and the vector \mathbf{D} is an N-dimensional vector representing the forcing term given by $D_j = \omega_{jp}$.

Let \mathbf{Y} be the $N \times N$ matrix of eigenvectors for \mathbf{C} , and λ_n be the eigenvalue associated with the n -th eigenvector \mathbf{Y}_n . Then the inclination evolution of the j th planet is given by:

$$\mathcal{I}_j(t) = \mathcal{I}_p + \sum_n^N c_n (\mathbf{Y}_n)_j \exp(i\lambda_n t). \quad (2.72)$$

The coefficients c_n are determined by from the initial conditions, and are given by

$$c_n = \theta_p (\mathbf{Y}^{-1} \cdot \mathbf{C}^{-1} \cdot \mathbf{D})_n. \quad (2.73)$$

The RMS mutual inclination between planet j and k is then given by

$$\langle \theta_{jk}^2 \rangle^{1/2} \simeq \sqrt{2} \sum_n^N c_n^2 [(\mathbf{Y}_n)_j - (\mathbf{Y}_n)_k]^2. \quad (2.74)$$

The RMS mutual inclination, RMS-averaged over all pairs of planets is given by:

$$\sigma_\theta \simeq \sqrt{2} \left(\sum_n^N c_n^2 \Theta_n \right)^{1/2}, \quad (2.75)$$

where Θ is the N-dimensional vector given by:

$$\Theta_n = \sum_j^N (\mathbf{Y}_n)_j^2 - \frac{1}{N} \left(\sum_j^N (\mathbf{Y}_n)_j \right)^2. \quad (2.76)$$

Note that in the strong coupling limit we have that $\omega_{jk} \gg \omega_{jp}$ for all $j, k \in \{1, 2, \dots, N\}$, and therefore \mathbf{C}^{-1} is given by some linear combinations of ω_{jk} , while \mathbf{D} is determined by $(\omega_{1p}, \omega_{2p}, \dots, \omega_{Np})$. Therefore, in this limit the RMS inclination scales as ω_{jp}/ω_{jk} for various combinations of j and k . On the other hand, in the weak coupling limit, we have $\omega_j \simeq \omega_{jp}$, and thus σ_θ is determined by by various combinations of ω_{jp}/ω_{kp} (for various j and k), and this combination approaches unity for $\bar{\epsilon} \gg 1$.

The above results are compared against numerical integrations in the bottom-left panel of Fig. 2.10, where we plot σ_θ as a function of $\bar{\epsilon}$ (adjusted by adjusting a_p) for a 4-planet system under the influence of a $3M_J$ perturber with $e_p = \theta_p = 0.1$. The three different colored curves represent three systems with different mass ratios between the dominant planet and the other planets (which have equal masses). The solid curves are computed from Eq. (2.75) while the filled squares and ‘ \times ’ markers represent N-body integrations with stable and unstable systems respectively. Again, we find our analytical results to agree with numerical integrations.

2.5.3 Extension to Modest Eccentricities and Inclinations

The results in Sections 2.5.1 and 2.5.2 are derived under the assumption of e_p and $\theta_p \ll 1$. For systems with modest values of e_p and θ_p (up to ~ 0.4), we can extend the results to include the effect of finite e_p and θ_p . The derivation is analogous to the case of two inner planets as discussed in Section 2.3.1. The results of Eqs. (2.64) - (2.68) and (2.74) - (2.75) remain valid for modest values of e_p and θ_p as long as one uses the modified frequencies $\tilde{\omega}_{jp}$ and $\tilde{\nu}_{jp}$ (see Eqs. 2.47 - 2.48) instead of ω_{jp} and ν_{jp} .

For a system of $N > 2$ inner planets in the strong coupling regime ($\bar{\epsilon} \ll 1$) the extension to modest e_p and θ_p can be further simplified (analogous to Eqs. (2.51) - (2.53) for the $N = 2$ case):

$$\langle e_j^2 \rangle^{1/2}(e_p, \theta_p) \simeq \langle e_j^2 \rangle_{\text{lin}}^{1/2} \left[\frac{1 - 5\theta_p^2/4}{(1 - e_p^2)^{5/2}} \right], \quad (2.77)$$

$$\langle \theta_{jk}^2 \rangle^{1/2}(e_p, \theta_p) \simeq \langle \theta_{jk}^2 \rangle_{\text{lin}}^{1/2} \left[\frac{1 - \theta_p^2/2}{(1 - e_p^2)^{3/2}} \right], \quad (2.78)$$

where $\langle e_j^2 \rangle_{\text{lin}}^{1/2}$ and $\langle \theta_{jk}^2 \rangle_{\text{lin}}^{1/2}$ are the expressions obtained from the linear theory, and are given by Eqs. (2.67) and (2.74) respectively. We omit the scaling for the weak coupling limit ($\bar{\epsilon} \gg 1$) here since weakly coupled $N > 2$ systems with modest e_p are generally unstable.

The right panels of Fig. 2.10 show a comparison of the above analytical results with the results from numerical N-body integrations (the left panels show a case with $e_p = \theta_p = 0.1$ where the linear theory is approximately valid; the right panels show a set-up with more significant values of $e_p = \theta_p = 0.4$). We find that for the $e_p = \theta_p = 0.4$ case, our analytical results agreed well with the N-body simulations up to $\bar{\epsilon} \sim 1$, at which point the system generally becomes unstable and the planets attain eccentricities much larger than predicted from the secular theory.

Combined with the results of Sections 2.5.1 and 2.5.2, Eqs. (2.77) - (2.78) present a way to rapidly compute analytically the RMS planet eccentricities and mutual inclinations in a “N-planets + perturber” system without resorting to numerical integrations. A short summary for the steps to carry out this computation is given in Appendix B.

2.6 Application to the Kepler-11 System

In this section, we apply our results to Kepler-11, a system with 6 tightly packed super-Earths. Previous works have used the co-planarity of the 6 planets to constrain the presence of any misaligned external companions (Jontof-Hutter et al., 2017). Due to the highly compact nature of this system, secular integrations were thought to be unsuitable and Jontof-Hutter et al. (2017) relied on N-body simulations. Here we show that the secular theory based on our hybrid secular equations can robustly reproduce N-body orbital eccentricities and mutual inclinations of Kepler-11 under the influence of a companion for a wide range of parameter space.

We consider the Kepler-11 system (with parameters as described in Lissauer et al., 2011) with the addition of a $3M_J$ companion ranging from 1.2 - 3 au. Planets b through g are given semi-major axes [0.091, 0.107, 0.155, 0.195, 0.250, 0.466] au, masses [1.9, 2.9, 7.3, 8.0, 2.0, 25] M_\oplus and radii [1.8, 2.87, 3.12, 4.19, 2.49, 3.33] R_\oplus respectively. Their initial orbital eccentricities and inclinations are set to zero while the perturber has its eccentricity and inclination set to range from 0.1 to 0.4. We integrate this system using the HERMES integrator from REBOUND (Rein et al 2015, Silburt & Rein unpublished) instead of the WHFast integrator used in Sec. 2.4 as it offers superior accuracy over repeated close encounters between planets. The HERMES “ R_{Hill} switch factor” is set to 1 and physical collisions between planets were assumed to be perfect mergers, an

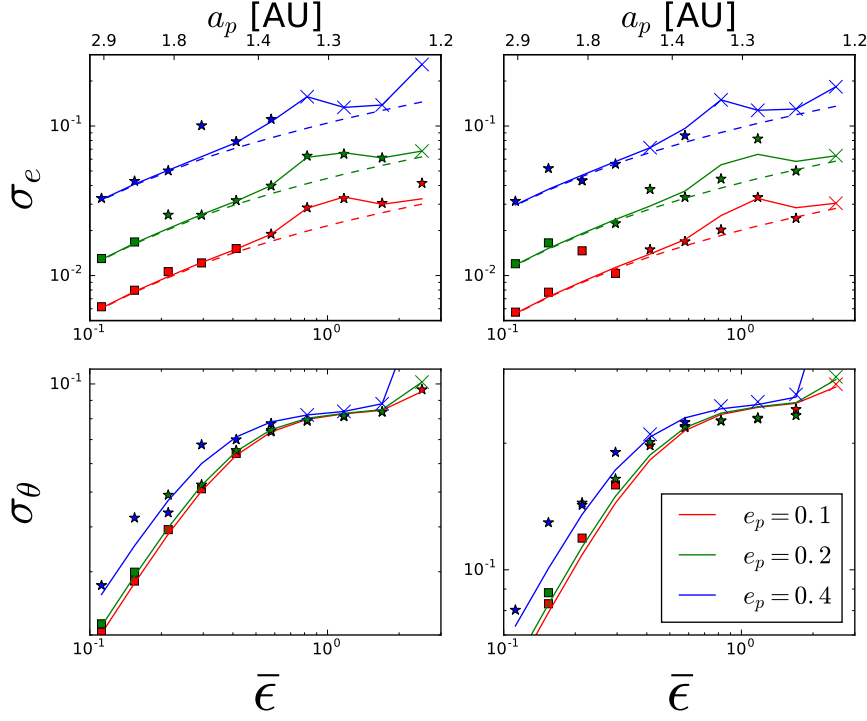


Figure 2.11: RMS orbital eccentricity and mutual inclination (Eqs. 2.58 - 2.59) of the Kepler-11 system when being perturbed by a hypothetical mis-aligned and eccentric external companion. The top panels show the RMS eccentricity while the bottom panel shows the RMS mutual inclination. The perturber, whose coupling strength is parametrized by $\bar{\epsilon}$, has mass $3M_J$ and semi-major axis ranging from 1 - 3 au; its eccentricity is $e_p = 0.1$ for the left panels, and $e_p = 0.4$ for the right panels. The inner 6 planets are initially started on circular, co-planar orbits. The red, green and blue curves correspond to different values of $\theta_p = 0.1, 0.2, 0.4$ respectively. The solid lines are obtained from our hybrid secular theory (Eqs. 2.77 and 2.78 for the top and bottom panels respectively), while the points are obtained from N-body integrations over a period of 10^6 yrs; for the top panels only, the dashed curves were obtained under the “strong coupling” approximation using Eq. (2.68). Filled squares represent systems stable against orbit crossings, while stars are systems that have undergone orbit crossings (but not collisions or ejections) within 10^6 yrs. An ‘x’ marks an unstable systems where one or more planets have collided or been ejected. Systems marked by ‘x’ are arbitrarily placed on the solid curves for visual clarity as their RMS eccentricities and mutual inclinations can be ill-defined due to ejections and/or collisions.

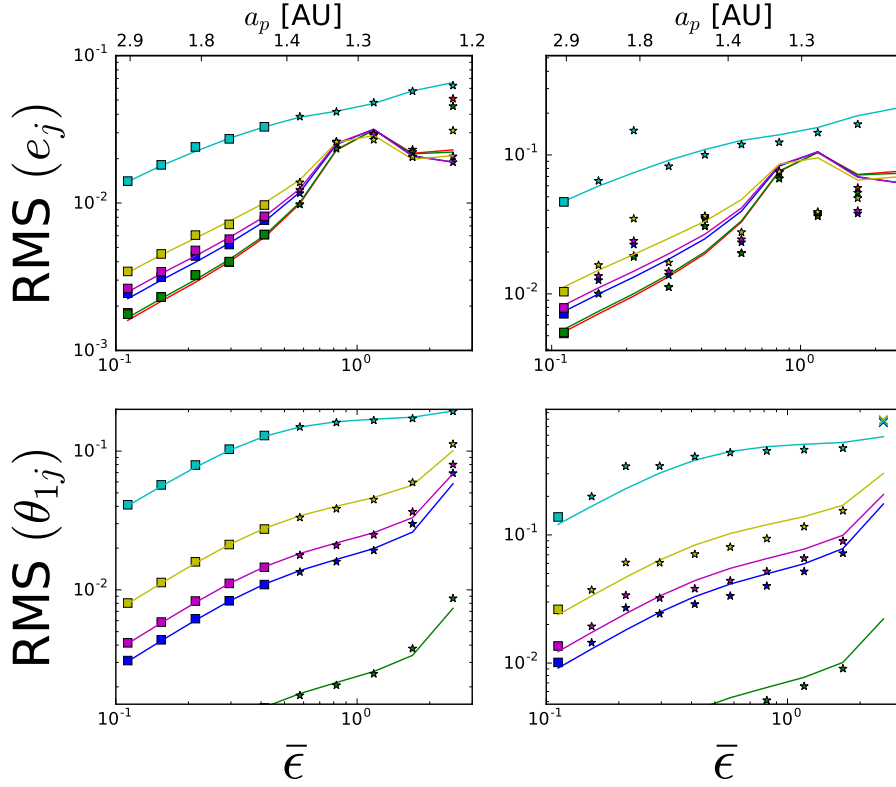


Figure 2.12: The same as Fig. 2.11, but showing the RMS orbital eccentricities $\langle e_j^2 \rangle^{1/2}$ (top panels) and mutual inclinations between the Kepler-11b and the j -th planet $\langle \theta_{1j} \rangle^{1/2}$ (bottom panel). The left panels have $e_p = \theta_p = 0.1$ while the right panels have $e_p = \theta_p = 0.3$. The red, green, blue, magenta, yellow and cyan curves correspond to planets $b - g$ in the Kepler-11 system. The solid curves are obtained from the hybrid secular analytical theory, and given by Eqs. (2.77) and (2.78) for the top and bottom panels respectively.

assumption that is reasonable for planets above $1M_{\oplus}$ (see Mustill et al., 2017a).

We then compute the RMS orbital eccentricities and mutual inclinations obtained from the N-body integrations and compare them to the secular analytical results described in Section 5 (shown in Figs. 2.11 and 2.12). In Fig. 2.11, the left and right panels represent two different inclinations for the perturber ($\theta_p = 0.1$ and 0.4). The squares, stars and crosses represent systems that are stable, meta-stable and unstable respectively,

with ‘meta-stable’ referring to systems having undergone orbit crossings but not physical collisions and/or ejections with-in 1 Myr, while ‘unstable’ refers to systems that have undergone collisions and/or ejection events. We see that so long as the system is not ‘unstable’, our hybrid secular theory shows excellent agreement with N-body simulations, even for mild values of $e_p = \theta_p = 0.4$. In Fig. 2.12, we show the RMS values of e_j and θ_{1j} (the mutual inclination between Kepler-11b and each of the other Kepler-11 planets) for all the individual planets of Kepler-11. The left and right panel represent two different perturber eccentricities and inclinations, with the left panel having $e_p = \theta_p = 0.1$ and the right panel having $e_p = \theta_p = 0.3$. For the case with $e_p = \theta_p = 0.1$ (left panels) we found our theoretical results to agree excellently with N-body simulations, while for the case with $e_p = \theta_p = 0.3$ our results agreed qualitatively with N-body simulations, with an average deviation of $\sim 30\%$ and a maximum deviation of $\sim 100\%$.

In summary, we find that a hypothetical, nearly co-planar $3M_J$ perturber with $e_p = 0.1$ would drive the inner system into instability if it is closer than $a_p \approx 1.5$ au; the condition becomes $a_p \approx 2.3$ au if the perturber instead has $e_p = 0.2$.

2.7 Summary and Discussion

We have studied the excitation of orbital eccentricities and mutual inclinations in compact multi-planet systems induced by the gravitational influence of eccentric and/or misaligned external planetary or stellar companions. Our major goal is to derive analytical expressions and scaling relations for the excited eccentricities/inclinations of the inner system as functions of the parameters the external perturber (mass m_p , semi-major axis a_p , eccentricity e_p and inclination θ_p), so that the impact of the perturber can be evaluated without resorting to computationally intensive N-body integrations for a

variety of systems. We provide a summary of our main results and guide to key equations and figures as follows.

- For $e_p, \theta_p \ll 1$, we used the linear Laplace-Lagrange theory to obtain explicit analytic expressions for the RMS mutual inclination θ_{12} (Eq. 2.16) and eccentricities e_1, e_2 (Eqs. 2.34-2.35) of two inner planets perturbed by an external companion (Section 2.2).

In general, the dynamics of a “2-planet + perturber” system is determined by the dimensionless parameter ϵ_{12} (Eq. 2.15), given by the ratio of the differential precession frequency of the inner planets (driven by the perturber) and their mutual coupling frequency (see also Lai & Pu 2017). When the two inner planets are weakly coupled ($\epsilon_{12} \gg 1$), they are more susceptible to inclination and eccentricity excitations, with

$$\theta_{12} \sim \theta_p \quad (2.79)$$

$$e_j \sim (a_j/a_p)e_p \quad (2.80)$$

(see Eqs. 2.20, 2.43 and 2.44). In contrast, a strongly coupled planet pair ($\epsilon_{12} \ll 1$) experiences reduced inclination/eccentricity excitations, with

$$\theta_{12} \sim \epsilon_{12}\theta_p \propto (m_p/a_p^3)\theta_p \quad (2.81)$$

$$e_1, e_2 \propto (m_p/a_p^4)e_p \quad (2.82)$$

(see Eqs. 2.22, 2.41 and 2.42). This indicates that a pair of planets in a compact configuration are more resistant to perturbations by a misaligned and/or eccentric external companion, as compared to a more loosely packed planet pair or a single planet. There may be observational support for this trend: Xie et al. (2016) found that taken as a group, transiting Kepler singles have systematically larger eccentricities than Kepler multis (with $\bar{e} \sim 0.3$ for Kepler singles and $\bar{e} \sim 0.04$ for Kepler multis). Our results suggest that perturbations by outer companions can be one contributing factor to this

observational trend.

For the case of $\epsilon_{12} \sim 1$, a resonance feature occurs if the innermost planet is the least massive one (i.e. $m_1 \lesssim m_2$), and the mutual inclinations and eccentricities of the inner planets can be boosted to values much larger than θ_p and e_p respectively (Eqs. 2.36 - 2.37).

- We extended our linear results to perturbers with ‘modest’ e_p and θ_p by developing ‘hybrid’ secular equations of motion (Eqs. A.2 - A.5) that interpolates between Laplace-Lagrange theory and multi-pole expansion (Section 2.3). We derived analytical results for the inner planet eccentricities (Eqs. 2.49, 2.51 - 2.52 and 2.54 - 2.55) and inclinations (Eqs. 2.50, 2.53 and 2.56). Comparing with numerical integrations of hybrid secular equations and N-body simulations (see Figs. 2.4-2.6 and Section 2.4), we found that our analytical results are valid for general values of θ_p and e_p (up to $\theta_p, e_p \approx 0.4$), provided that the resulting e_j and θ_{12} are small. In particular, for the cases where $\epsilon_{12} \sim 1$ and $\theta_{12} \geq 0.68$ rad. (39°), the inner planets can develop Kozai-Lidov-like oscillations in their eccentricities and inclinations, leading to rapid growth in e_1 and e_2 even for small values of e_p , a feature that is not captured by our secular theory.

- We extended our analysis to inner systems with more than two planets (Section 2.5). In the linear theory, the inner planet eccentricities are given by Eqs. (2.64) - (2.68), and the mutual inclinations are given by Eqs. (2.74)-(2.75). For strongly coupled inner systems, we extend our linear results to modest values of e_p and θ_p in Eqs. (2.77) and (2.77). A comparison of these results are shown against N-body simulations for a hypothetical “4-planet + perturber” system in Fig. 2.9. The results of our linear theory agree robustly with N-body simulations, as long as the inner system is not made unstable by the external perturber.

- We applied our hybrid secular equations to Kepler-11, a tightly packed 6-planet system. We examined the impact of a hypothetical external giant planet companion on the observed system, and compared the results of ‘hybrid’ secular equation integrations with N-body simulations, the results of which are shown in Figs. 2.10 and 2.11. We found our hybrid secular theory to agree closely with N-body simulations as long as the Kepler-11 system is not rendered unstable against collisions and/or ejections within the integration timescale. For example, using on hybrid secular equations, we can rule out the presence of a $\sim 3M_J$ companion to Kepler-11 with eccentricity $e_p = 0.1$ out to $a_p = 1.4$ au, and $e_p = 0.2$ out to $a_p = 2.5$ au.

In this work we have focused on evolution of an inner multi-planet system with initially circular, co-planar orbits subject to an eccentric and/or misaligned external companion. How might such a companion be generated is a pertinent question that lies outside the scope of this work. In the case of distant stellar companions, the eccentricity and inclination of the perturber is simply a product of star/binary formation process in a turbulent molecular cloud. In the case of giant planet companions, the eccentricity and inclination may be generated as the end-product of a violent scattering process in an unstable system of primordial giant planets that underwent violent close encounters and scatterings until only a single planet remained. In this scenario, the assumption that such inner systems have initially circular and co-planar is likely to be incorrect, as the violent process itself may generate inner planet eccentricities and mutual inclinations larger than than the results found in this work. Nevertheless, the secular results studied in this paper provide a benchmark of the eccentricity/inclination excitation by the external companions. In chapter 4 we will study the scenario involving primordial giant planet scatterings, and present a model for the inner planet eccentricity and mutual inclinations excitation during the violent giant-planet scattering phase.

CHAPTER 3

ON THE SCATTERING OF COLD JUPITERS AND ITS INFLUENCE ON
INNER PLANET SYSTEMS: THEORY AND SIMULATION

3.1 Introduction

Exoplanets with masses and radii between that of the Earth and Neptune, commonly referred to as “super-Earths” or “mini-Neptunes”, have been discovered in large quantities in recent years. Indeed, such planets appear to be ubiquitous in the Galaxy: about 30% of Sun-like stars host super-Earth planets, with each system containing an average of 3 planets (Zhu et al., 2018). The observed super-Earth systems have compact orbits, with periods typically less than 200 days. In recent years, an increasing number of such systems have been found to host long-period giant planet companions (i.e. “Cold Jupiters” or CJs). Zhu et al. (2018) analysed a sample of ground-based radial velocity (RV) observations of super-Earth systems and an independent sample of *Kepler* transiting Super-Earths with RV follow-up, and found that cold Jupiters are three times more common around hosts of super-Earths than around field stars: about 30% the inner super-Earth systems have cold Jupiter companions, and the fraction increases to 60% for metal-rich stars. Bryan et al. (2019) found a similar result, and gave the estimated occurrence rate of $39 \pm 7\%$ for companions between $0.5\text{--}20M_J$ and $1 - 20$ au. There is evidence that stars with cold Jupiters or with high metallicities have smaller multiplicity of inner Super-Earths, suggesting that cold Jupiters have influenced the inner planetary system. Masuda et al. (2020) found that these CJ companions are typically mildly misaligned with their inner systems with a mutual of $\Delta\theta \sim 12$ deg. These mild inner-outer misalignments could potentially explain the apparent excess of *Kepler* single-transit Super-Earth systems (Lai and Pu, 2017).

The question of how low-mass inner planet systems may be influenced by the presence of one or more external giant planets has attracted recent attention (e.g. Carrera et al., 2016; Gratia and Fabrycky, 2017; Lai and Pu, 2017; Huang et al., 2017; Mustill et al., 2017b; Hansen, 2017; Becker and Adams, 2017; Read et al., 2017; Jontof-Hutter et al., 2017; Pu and Lai, 2018; Denham et al., 2018). This paper is the third in a series where we systematically investigate the effect of outer companions on the architecture of inner super-Earth systems. In (Lai and Pu, 2017) and (Pu and Lai, 2018) we study the secular evolution of an inner multi-planet system perturbed by an inclined and/or eccentric external companion. Combining analytical calculations and numerical simulations (based on secular and N-body codes), we quantify to what extent eccentricities and mutual inclinations can be excited in the inner system for different masses and orbital parameters of super-Earths and cold Jupiter. When the perturber is sufficiently strong compared to the mutual gravitational coupling between the inner planets, the inner system becomes dynamically hot and may be unstable. Even for milder perturbers that do not disrupt integrity of the inner system, the small/modest excitation of mutual inclinations can nevertheless disrupt the co-transiting geometry of the inner planets and thereby reduce the number of transiting planets (e.g. Brakensiek and Ragozzine, 2016). Other related works can be found in Boué and Fabrycky (2014a); Hansen (2017); Becker and Adams (2017); Read et al. (2017); Jontof-Hutter et al. (2017); Denham et al. (2018) (see also Boué and Fabrycky, 2014b; Lai et al., 2018; Anderson and Lai, 2018, for the effect of external companion on the stellar obliquity relative to the inner planets).

In this paper we study the dynamical evolution of inner planet systems under the influence of a pair of external giant planets with initially unstable orbits. A number of previous works (based on N-body simulations) have already investigated this problem, illustrating that the strong scatterings of unstable giant planets can affect the orbits of the inner planets in different ways (e.g. Matsumura et al., 2013; Carrera et al., 2016;

Gratia and Fabrycky, 2017; Huang et al., 2017; Mustill et al., 2017b). For example, the outer scatterings can send a giant planet inward, sweeping up all the inner planets along its wake and totally destroying the inner system. Also, the scattering events can excite the eccentricities and mutual inclinations of the inner planets beyond the threshold of their stability, causing the inner system to also undergo scattering events of their own, resulting in a pared down inner system. In this paper we attack this problem more systematically, going beyond previous works in several ways. Our rationales are: (i) Previous works were restricted to small number of numerical examples, often considering specific orbital parameters. As such, it is difficult to obtain a quantitative understanding or scaling relations (even approximate) in order to know “what systems lead to what outcomes”. (ii) Previous works often considered systems where the inner planets are not too detached from the outer planets. This was adopted for numerical reason: If the inner planets have too small a semi-major axis compared to the outer planets, their dynamical times would be much shorter than the outer planets, and it would be difficult to simulate the whole system over a long time or simulate a large number of systems. As a result, previous works tended to over-emphasize the more “disruptive” events. In reality, for sufficiently hierarchical systems, the scattering events may only mildly excite the eccentricities and mutual inclinations of the inner planets; in this case, the super-Earths themselves are preserved, but their mutual inclinations may be large enough to “hide” the inner planets from simultaneously transiting their host stars – such “mild” systems or events may be most relevant to the currently observed super-Earths with cold Jupiter companions. (iii) Most importantly, there is a wide range of “ejection times” associated with the evolution of the unstable giant planets (e.g., for some systems, the lighter cold Jupiter may be ejected very quickly, while for others the ejection may take place over much longer time). As we show in this paper, the degree of influences on the inner system from the outer planets is directly correlated with the

ejection time of the unstable giant planets. Thus, numerical studies that only consider restricted examples would not capture the whole range of dynamical behaviors of the “inner planets + outer giants” system.

Thus, the goal of this paper is to systematically examine how strong scatterings of outer giant planets influence the inner super-Earth system. We aim at obtaining an understanding of the whole range of different outcomes and deriving relevant scaling relations for different systems (with various planet masses and orbital parameters) and different ejection times. Of particular interest are the “mild” systems where the inner planets survive the “outer violence”. We elucidate the connections between the “violent” phase and the ensuing “secular” phase studied in our previous papers (Lai and Pu, 2017; Pu and Lai, 2018). As mentioned above, because of the hierarchy of dynamical timescales, it is difficult to study the systems where the inner super-Earths and outer giants are well separated using brute-force N -body simulations, especially when the ejection time of giant planet is large – and yet such systems are most relevant to the observed super-Earths with cold Jupiter companions. To this end, we developed a hybrid algorithm, combining N -body simulations of outer giant planets undergoing strong scatterings with secular forcing on the inner planets, to compute the evolution of the inner planets throughout the “violent” phase.

A major part of this paper is devoted to the dynamics of strong scatterings between two giant planets (section 2 and section 3). Although there have been many previous studies on giant planet scatterings (e.g. Rasio and Ford, 1996; Weidenschilling and Marzari, 1996; Lin and Ida, 1997; Ford et al., 2000; Ford and Rasio, 2008; Chatterjee et al., 2008; Jurić and Tremaine, 2008; Matsumura et al., 2013; Petrovich et al., 2014; Freikh et al., 2019; Anderson et al., 2020; Li et al., 2020), they all focused on the final outcomes of the unstable giant planets (e.g., the eccentricity distribution of the remaining planets),

and did not investigate the timescale (“ejection time”) of violent phase. As noted above, this “ejection time” directly influences the perturbations the inner planets receive from the “outer violence”. In addition to obtaining the “ejection time” distribution, we also obtain a number of new analytic and scaling results for strong scatterings between two giant planets.

We then develop a theoretical model for the “violent” phase of the scattering process, and model the inner planet’s secular evolution as a linear stochastic differential equation. We obtain analytic estimates for both the expectation values and the distributions of the final orbital parameters of the inner planets, and test these results against direct numerical integrations. A major achievement of this work is the derivation for the marginalized “violent-phase” boost factor γ , which summarizes the entire dynamics of the “1+2” scattering process in a single, dimensionless parameter. We derive an analytical expression for the distribution of γ , which agrees robustly with numerical simulations over a wide range of initial system parameters.

This paper is structured as follows. In Sec. 3.2, we study the scattering process between two unstable giant planets using N-body simulations, focusing in particular on the planet ejection timescale. through N-body simulations. In Sec. 3.3, we outline our hybrid N -body and secular algorithm to study the effect of giant planet scatterings on the inner super-Earth system. In Sec. 3.4, we present the results of these simulations, as well as theoretical scaling results for the final outcome of these systems. These results are extended to systems with more than one inner planets in Sec. 3.5. We provide a summary of our results, and apply them to several “Super-Earth + CJ” systems of interest in Sec. 3.6, as well as providing suggestions for further studies.

3.2 Gravitational Scatterings of Two Giant Planets

The topic of gravitational scatterings between two or more giant planets on unstable orbits is a classic one and has been the subject of numerous previous studies (e.g. Rasio and Ford, 1996; Weidenschilling and Marzari, 1996; Lin and Ida, 1997; Ford et al., 2000; Jurić and Tremaine, 2008; Ford and Rasio, 2008; Chatterjee et al., 2008; Ida et al., 2013; Matsumura et al., 2013; Petrovich et al., 2014; Frelikh et al., 2019; Anderson et al., 2020; Li et al., 2020). These studies focused on the final states of unstable systems, such as the eccentricity distribution of the remaining planets. We return to this topic to re-focus our attention on the scattering/ejection timescale t_{ej} , a quantity that plays a key role in the interaction between the scattering CJs and the inner super-Earth system, but hitherto ignored by previous studies (but see Fig. 1 of Anderson et al. 2020 and Fig. 7 of Li et al. 2020). In particular, we seek to understand the distribution of t_{ej} and how the ejection outcome may scale with various system parameters, in particular the planet masses and spacing. In this section, we present our numerical results (based on N -body simulations) – these empirical findings serve as the basis for our theoretical model and analytical understanding discussed in Section 3.

Consider a pair of planets with masses m_1 and m_2 , radii R_1 and R_2 and semi-major axes a_1 and a_2 orbiting a star with mass M_\star . We assume the planets are initially on circular orbits and have a mutual inclination $0 < \theta_{12} \ll 1$. The planets are stable against close encounters for all time if the condition

$$|a_2 - a_1| > 2\sqrt{3}r_H \quad (3.1)$$

is satisfied (Gladman, 1993), where the mutual Hill radius r_H is given by:

$$r_H \equiv \left(\frac{a_1 + a_2}{2} \right) \left(\frac{m_1 + m_2}{3M_\star} \right)^{1/3}. \quad (3.2)$$

If this condition is not satisfied, the resulting system is gravitationally unstable and will

inevitably undergo mutual close encounters. The results of previous studies show that generally, such an unstable system will result in either the merger of two planets or the ejection of one of the planets. The exact prevalence depends on the initial system parameters, and planetary systems with smaller semi-major axes and/or larger planetary radii are more likely to result in collisions/mergers rather than planet ejections. For gas giant planets with semi-major axes beyond a few au's, the most likely outcome appears to be eventual ejection of the least massive planet from the system (see, e.g. Li et al., 2020). Appendix D presents a simple theoretical model for why this is the case. We focus on such ejection events in this section.

3.2.1 Numerical Set-Up

We perform N-body simulations of the orbital evolution of giant planets orbiting a solar mass star, using the IAS15 integrator included as part of the REBOUND N-body software (Rein and Liu, 2012b; Rein and Spiegel, 2015). IAS15 is a 15th-order integrator based on Gauss-Radau quadrature with automatic time-stepping that is capable of achieving machine precision; it is well suited for problems involving close encounters and high-eccentricity orbits.

We performed an array of N-body simulations involving the scattering of hypothetical unstable 2-planet systems. Each system had an inner planet with semi-major axis $a_1 = 5$ au, with the outer planet's semi-major axis given by $a_2 = a_1 + k_0 R_H$, with $k_0 \in [1.5, 2.0, 2.5]$. The inner planet had mass $m_1 \in [10.0, 3.0, 1.0, 0.3] M_J$ while the outer planet's mass is m_2 , with the mass ratio m_2/m_1 chosen from $[1, 2/3, 1/2, 1/3, 1/5, 1/10]$. Note that in our simulations, the outer planet is less massive than the inner planet, although our analytic results apply to cases with the inner planet being more massive

as well. The planets were treated as point particles (their radius were set to zero), and the possibility for collisions between planets were not considered. Both planets were started on initially circular orbits, and their initial orbital mutual inclination is set to be $\theta_{12,0} = 3^\circ$. The initial mean anomaly f , longitude of the ascending node Ω and longitude of pericenter ϖ were each drawn from uniform distributions on $[0, 2\pi]$. We computed each system for up to 3×10^7 orbits of the inner planet, terminating simulations once an ejection has occurred (i.e. the orbit of one of the planets becomes unbounded). For each combination of k_0 , m_1 and m_2/m_1 we performed computations until 200 systems that resulted in ejected systems were obtained. The reason we perform such large numbers of simulations is to have sufficient data to test various statistical hypotheses that will arise later in the paper. The results of these simulations are summarized in the following sections.

3.2.2 Final Outcomes of Scatterings: Orbital Parameters

After the scattering process has completed, we are interested in the final semi-major axis, eccentricity and inclination (relative to either the initial plane or the ejected planet) of remaining planet, which we denote as $a_{1,\text{ej}}$, $e_{1,\text{ej}}$ and $\theta_{1,\text{ej}}$ respectively, with the subscripts “0” and “ej” denoting the quantity being at time zero and at the final time immediately after the ejection of the final planet. Although these results have been known and presented previously in various contexts (e.g. Weidenschilling and Marzari, 1996; Ford et al., 2000; Jurić and Tremaine, 2008; Chatterjee et al., 2008; Ida et al., 2013; Matsumura et al., 2013; Petrovich et al., 2014; Frelikh et al., 2019; Anderson et al., 2020; Li et al., 2020), our results explore a broader range of planet masses and mass ratios.

1. **Final semi-major axis $a_{1,\text{ej}}$:** We find the final semi-major axis to be well determined by the conservation of energy, given by

$$E_{\text{tot}} = -\frac{GM_{\star}m_1}{2a_{1,0}} - \frac{GM_{\star}m_2}{2a_{2,0}} \simeq -\frac{GM_{\star}m_1}{2a_{1,\text{ej}}}, \quad (3.3)$$

which gives a final semi-major axis of

$$a_{1,\text{ej}} = a_{1,0} \left(1 + \frac{a_{1,0}m_2}{a_{2,0}m_1} \right)^{-1} \quad (3.4)$$

for the remaining, non-ejected planet.

We find that given the same set of initial planet masses and semi-major axes, the final distribution of the semi-major axis is determined by Eq. (3.4) to within 1%. This is a consequence of the diffusive nature of the ejection process, which proceed over many orbits through a series of energy exchanges, each exchange shifting the ejected planet's orbital energy by an amount $\delta E_{12} \ll E_{2,0}$. At ejection, the ejected planet deposits all its initial energy into planet 1, and the scatter in its final (positive) orbital energy is of order δE_{12} and is negligible compared to the total energy lost $E_{2,0}$.

2. **Final eccentricity $e_{1,\text{ej}}$:** We find that the final eccentricity of the remaining planet depends strongly on the mass ratio m_2/m_1 , and weakly on the initial separation of the two planets. Figure 3.1 shows a plot of the distribution density of e_1 as a function of the mass ratio m_2/m_1 for a system with $m_1 = 1M_J$. For $m_2 \ll m_1$ with initial separation of order r_H , a good empirical scaling for the typical value of $e_{1,\text{ej}}$ is

$$\langle e_{1,\text{ej}} \rangle \approx 0.7m_2/m_1. \quad (3.5)$$

The spread in the value of $e_{1,\text{ej}}$ increases with the mass ratio of the planet: for the case where $m_2/m_1 \ll 1$ (i.e. m_2 being a test particle), the standard deviation

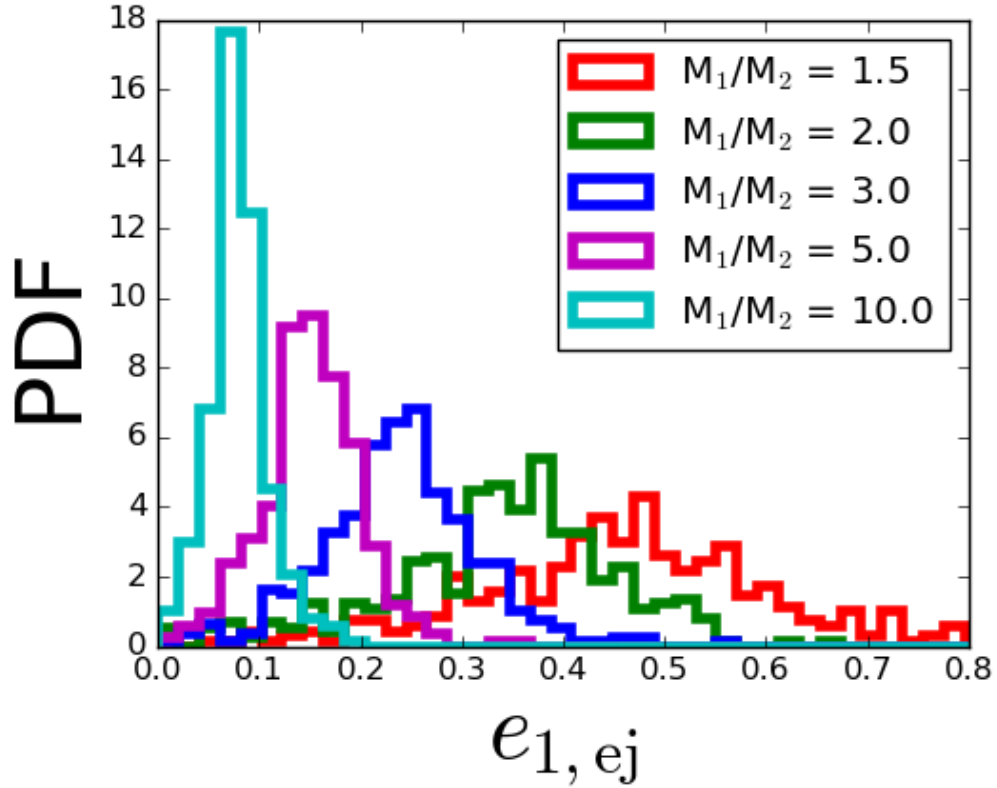


Figure 3.1: A histogram of the final eccentricity of the remaining planet, for a system of two initial planets that have undergone an ejection event. The different colors correspond to various values of the mass ratio m_1/m_2 . Each histogram represents 600 simulations, with $k_0 \in [1.5, 2.0, 2.5]$ (where $k_0 \equiv (a_2 - a_1)/r_H$) and $m_1 \in [3.0, 1.0] M_J$. Runs with different m_1 were binned together as their distributions were indistinguishable statistically.

$\sigma(e_{1,ej})$ is of order $\sim 0.25\langle e_{1,ej} \rangle$, while for the case of $m_2/m_1 \sim 0.5$ the standard deviation is $\sim 0.5\langle e_{1,ej} \rangle$.

The scaling of eccentricity can be understood as a consequence of the conservation of angular momentum:

$$m_1 \sqrt{GM_\star a_1 (1 - e_1^2)} + m_2 \sqrt{GM_\star a_2 (1 - e_2^2)} = \text{const.} \quad (3.6)$$

We make the approximation that the apsis of the outer planet and the periapsis of

the inner planet change much more slowly than their eccentricities and semi-major axes during close encounters, i.e.

$$p_1 \equiv a_1(1 + e_1) = a_{1,0} \simeq \text{const.} \quad (3.7)$$

$$q_2 \equiv a_2(1 - e_2) = a_{2,0} \simeq \text{const.} \quad (3.8)$$

Combining Eqs. (3.7) - (3.8) with Eq. (3.6) and substituting a final value of $e_2 = 1$, we have

$$\sqrt{1 - e_{1,f}} \simeq 1 + (1 - \sqrt{2})m_2/m_1\alpha_0^{-1/2}, \quad (3.9)$$

where α_0 is the initial value of the semi-major axis ratio a_1/a_2 . In the limit that $(m_2/m_1) \ll 1$, Eq. (3.9) reduces to

$$e_{1,\text{ej}} \approx 0.8(m_2/m_1). \quad (3.10)$$

3. Final inclination of planet 1 $\theta_{1,\text{ej}}$ (relative to initial plane): We find $\theta_{1,\text{ej}}$ to be determined most strongly by the mass ratio m_2/m_1 , and somewhat independent of the other parameters. Fig. 3.2 shows our empirical results for the distribution of the inclination as a function of m_2/m_1 . We find that $\theta_{1,\text{ej}}$ is well-fit by a Rayleigh distribution with scale parameter $\sigma \sim 0.7\theta_{12,0}$. This can be understood as a consequence of angular momentum conservation. Since the ejected planet picks up a change in its angular momentum about the z-axis of order $\sin \theta_{12,0}L_{2,0}$, angular momentum conservation requires the remaining planet to gain angular momentum in equal and opposite direction. As a result, planet 1 will pick up an inclination relative to its original plane of order

$$\theta_{1,\text{ej}} \sim (L_{2,0}/L_{1,0}) \sin \theta_{12,0} \sim (m_2/m_1) \sin \theta_{12,0}. \quad (3.11)$$

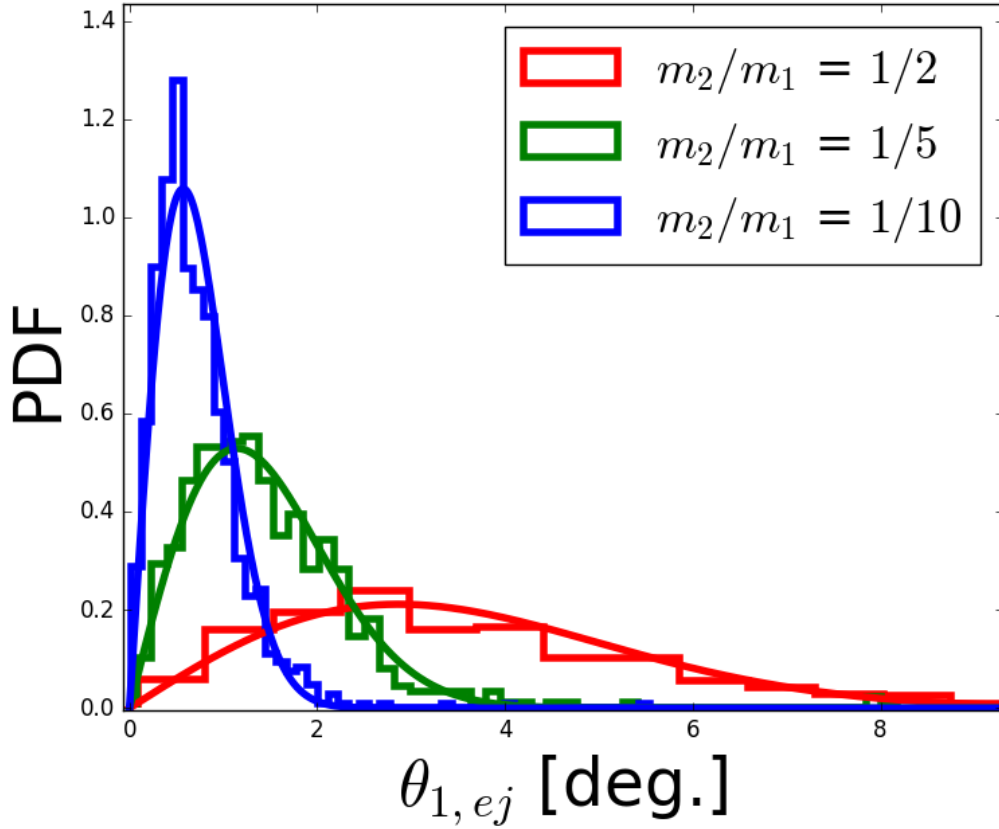


Figure 3.2: A histogram of the final inclination of the remaining planet (relative to the initial plane), for a system of two initial planets that have undergone an ejection event. The initial mutual inclination of the two planets is 3° . The different colors correspond to various values of the mass ratio m_2/m_1 . Each histogram represents 600 simulations, with $k_0 \in [1.5, 2.0, 2.5]$ and $m_1 = M_J$. Simulations with different k_0 were binned together as their distributions were approximately identical statistically.

3.2.3 Timescale to Ejection

An important quantity in the dynamical evolution of inner planet systems with scattering CJs is the timescale required to finally eject one of the planets. We present our empirical results on the scaling and dependence of the ejection timescale with system parameters. However, before proceeding, there are some caveats with regards to the correct metric to

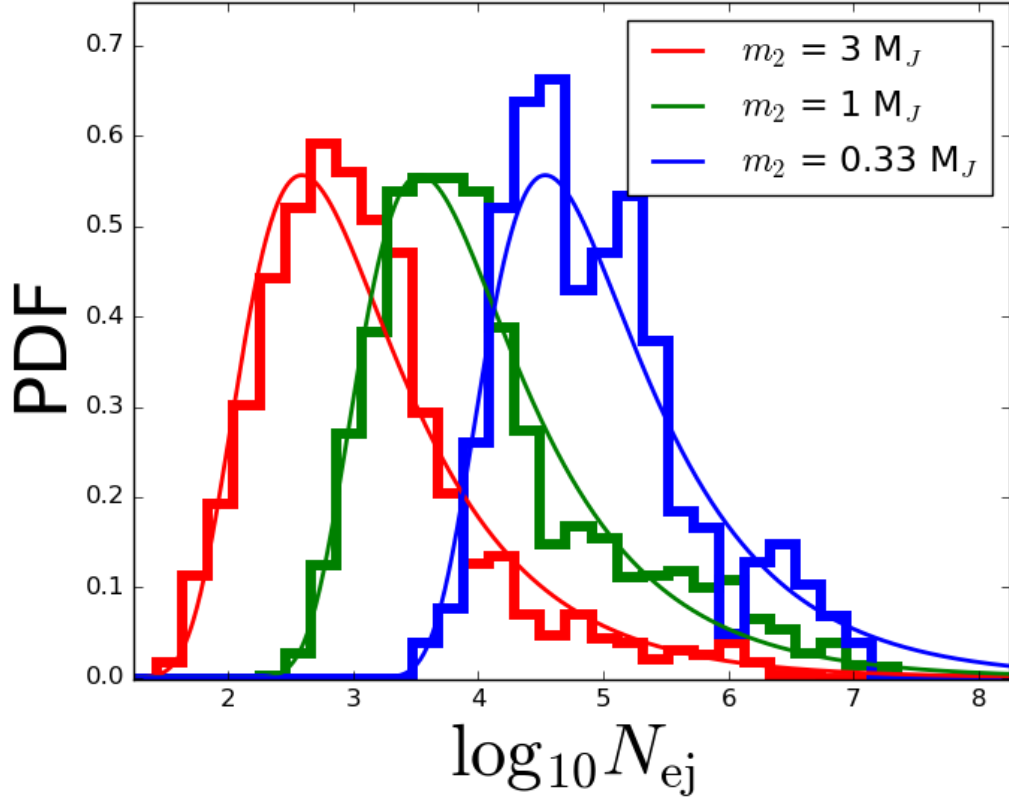


Figure 3.3: Probability density distribution of N_{ej} from our two planet scattering simulations. The different colors represent different values of m_1 , with red, green and blue corresponding to $m_1 = 3, 1, 0.3 M_J$ respectively. For each histogram, we fix $m_2/m_1 = 1/10$ and $k_0 = 2.0$. The histograms are empirical results from our N-body simulations, while the solid curves are obtained using the theoretical model in Eq. (3.19), with b empirically determined using Eq. (3.22).

use for the ejection timescale.

Firstly, an unstable pair of planets on initially circular orbits will first pass through a meta-stable phase where the eccentricities of both planets ramp up gradually, without the planets undergoing violent close encounters. This ramp-up phase is called the ‘instability timescale’ t_{inst} in other contexts and its length depends on the parameters of the system. The scaling dependence of t_{inst} has been the subject of many studies, the results of which show that generally the instability timescale scales exponentially with the planet

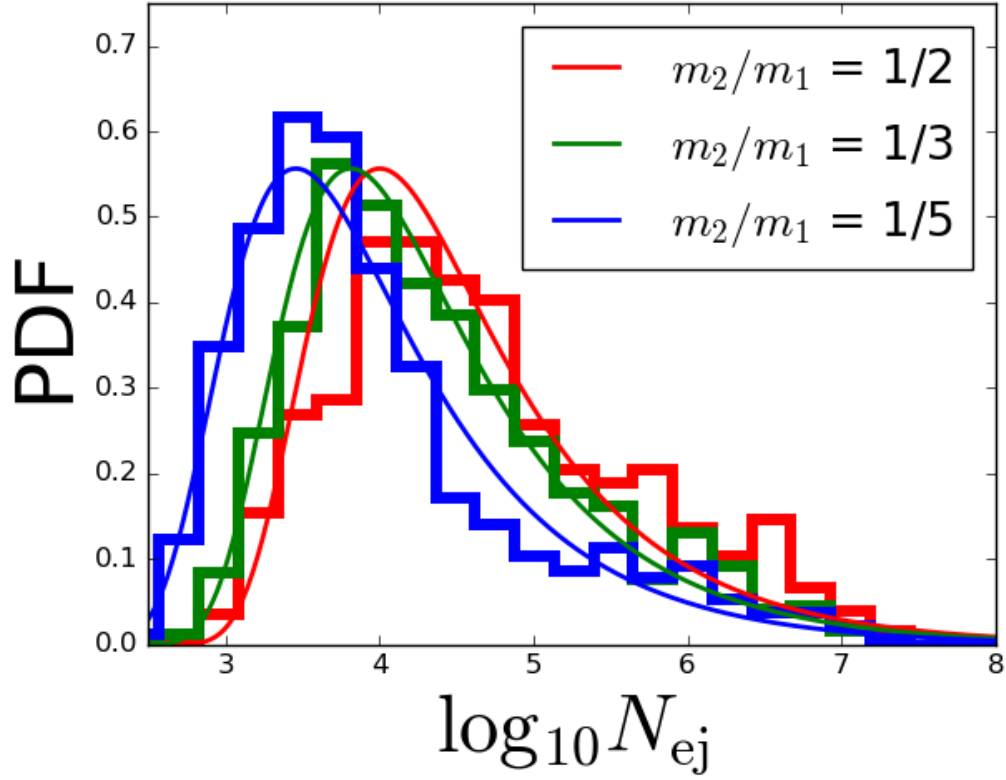


Figure 3.4: Same as Fig. 3.3, except we fix $m_1 = M_J$, while m_2/m_1 varies as indicated in the legend.

spacing, i.e. $\ln t_{\text{inst}} \propto \Delta a$. In this study we are interested in the timescale required for an initially unstable system to finally eject one of the planets, a process which only occurs after t_{inst} has already been reached. Therefore, it is convenient to separate the ramp-up phase from the ejection timescale by counting time only after the first close encounter. We do so by starting our count of the passage of time for planet ejections only after the planets 1 and 2 have orbits that are separated by a Hill radius or less, i.e. when $a_2(1 - e_2) - a_1(1 + e_1) \leq r_H$ is satisfied.

We define t_{ej} and N_{ej} respectively as the time and the number of pericenter passages the ejected planet (planet 2) takes between the first Hill-sphere crossing event and the final ejection event. Note that we use the number of orbits of the ejected planet as

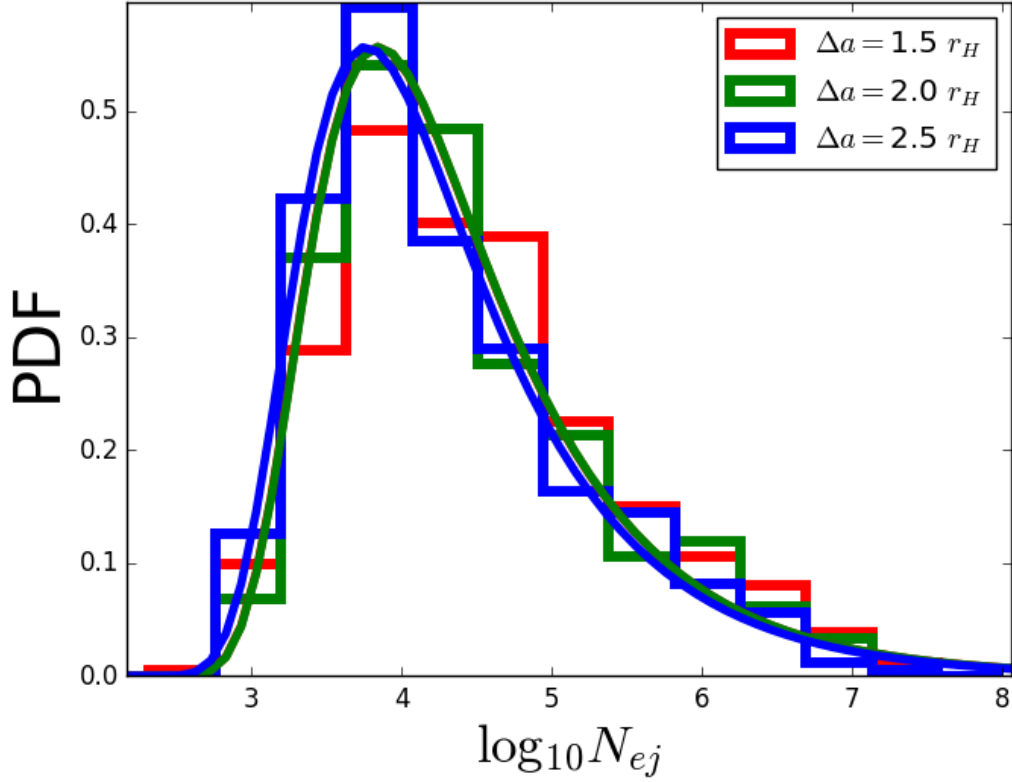


Figure 3.5: Same as Fig. 3.3, except we fix $m_1 = M_J$, while the initial separation parameter $k_0 = \Delta a/r_H$ varies as indicated in the legend.

opposed to the number of synodic periods, because at higher eccentricities the energy exchange mainly occurs at pericenter passages and not orbital conjunctions. N_{ej} and t_{ej} can be converted from each other using the transformations

$$N(t) \simeq \frac{1}{2\pi} \int_0^t \left(\frac{GM_*}{a^3(t)} \right)^{1/2} dt \quad (3.12)$$

$$t(N) \simeq 2\pi \int_0^N \left(\frac{GM_*}{a^3(N)} \right)^{-1/2} dN. \quad (3.13)$$

We focus on N_{ej} below, as it is the more physically relevant quantity in the scattering and ejection process. The results of our numerical simulations are shown in Figs. 3.3 - 3.6. We summarize the key results below:

1. **Dependence on m_1 :** We find a strong dependence in our simulations of N_{ej} on the

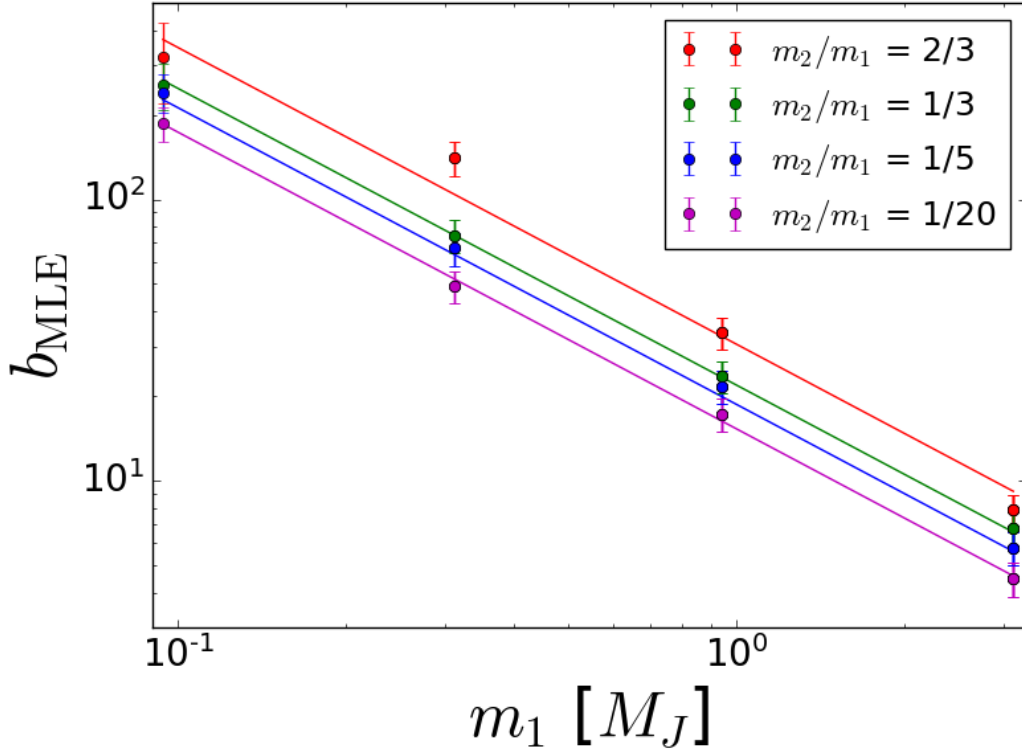


Figure 3.6: The maximum likelihood estimate (MLE) estimate of b , as a function of m_1 , for various combinations of the planet mass ratio m_2/m_1 . The filled circles are the results of numerical N-body simulations, while the solid lines are given by Eq. (3.24). The errorbars are computed using the asymptotic variance of the MLE (Eq. 3.23).

mass of the more massive planet m_1 . The histograms in Fig. 3.3 show the different probability density distributions of N_{ej} for systems with various m_1 ranging from $3M_J$ to $0.3M_J$. In our simulations, while systems with $m_1 = 3M_J$ have $N_{\text{ej}} \sim 10^3$, the same system with a $m_1 = 0.3M_J$ had a typical ejection timescale that is nearly a hundred times greater. We find that the scaling is very close to $N_{\text{ej}} \propto m_1^{-2}$.

2. **Dependence on m_2/m_1 :** For a given m_1 , N_{ej} generally depends on m_2/m_1 . When $m_2/m_1 \ll 1$, there is little dependence on m_2 . On the other hand, as m_2 increases to be of similar order as m_1 , the ejection timescale starts to increase significantly. Fig. 3.4 shows the density distribution of N_{ej} for a system with all other parameters fixed,

except the ratio m_2/m_1 , which is varied from $1/5 - 1/2$. We find that in comparison to the test-particle limit ($m_2/m_1 \ll 1$), a mass ratio of $1/2$ results in an ejection timescale that is ~ 10 times larger. We find a scaling of $N_{\text{ej}} \propto (1 + m_2/m_1)^{4.0}$, the functional form being somewhat arbitrary.

3. **Variance of N_{ej} :** in our simulations, we find significant variance in the distribution of N_{ej} for systems that have different initial orbital phases but otherwise identical orbital parameters. This can be seen clearly in Figs. 3.3 and 3.4, where similar systems can have ejection timescales that range 4-5 orders of magnitude. We find that the standard deviation of $\log_{10} N_{\text{ej}}$ is approximately 0.9; this variance is empirically independent of the other system parameters such as planet masses.
4. **Dependence on k_0 :** We found that the initial planet spacing $\Delta a = k_0 r_H$ plays little role in determining the final ejection timescale, as long as the initial ramp-up period of meta-stability is accounted for. Fig. 3.5 shows a comparison in the density distribution of N_{ej} for systems with otherwise identical parameters, except with k_0 varying from 1 to 2.5.
5. **Relation between N_{ej} and ejection time t_{ej} :** Since the semi-major axis of the planet increases as it is being ejected, the ejection time t_{ej} is usually significantly larger than the naive estimate $t_{\text{ej}} \sim N_{\text{ej}} P_{2,0}$ where $P_{2,0}$ is the initial orbital period. The discrepancy grows larger when m_1 is smaller, due to the fact that the to-be-ejected planet can maintain larger semi-major axes before finally being ejected. We find a best-fit power-law with the form:

$$t_{\text{ej}} \sim 8 P_{2,0} N_{\text{ej}}^{0.7} \left(\frac{m_1}{M_\star} \right)^{0.46}. \quad (3.14)$$

3.2.4 Theoretical Model for CJ Scattering

We present a simple theoretical model for the process of CJ scattering to explain our empirical results of Section 3.2.3. As we shall demonstrate in this section, by assuming that the planet orbital energy undergo a random walk during the scattering process, this model can explain both the distribution and the scaling of the ejection time of CJ scatterings.

Consider the limiting case of a pair of planets with $m_1 \gg m_2$. The two planet orbits are ‘unstable’ such that their orbits come very close to each other and experience repeated crossings. At larger orbital distances it is common for the two planets to remain orbit-crossing for extended periods of time without physically colliding. Since $m_1 \gg m_2$, we assume the orbital parameters of m_1 stay constant during the scattering process.

At every pericenter passage (or apocenter passage if $a_2 < a_1$), planet 2 exchanges a certain amount of orbital energy with planet 1. The amount of energy exchanged, δE_{12} depends on the orbital properties of the two planets. We hypothesize that δE_{12} can be approximated as follows:

$$\delta E_{12} \sim \left(\frac{G m_1 m_2}{a_1} \right) F(a_2, f_{12}), \quad (3.15)$$

where F is a dimensionless function, and f_{12} is the difference of the two planets’ true longitudes at time of pericenter passage of planet 2. Note that in general, F should depend on e_2 as well. However, given some a_2 , the possible values of e_2 is narrowly constrained due to conservation laws (see Sec. 3.2.5 below), so to a first order approximation, it is sufficient to know only a_2 .

Due to symmetry, for a fixed value of a_2 the function F is odd with respect to f_{12} , i.e. the energy exchange is equally likely to be positive and negative, and averaging over f_{12} gives $\langle F(a_2, f_{12}) \rangle = 0$. As a result, even though at each close approach between planet

1 and planet 2 there is a finite amount of energy exchange, in the limit that $|\delta E_{12}| \ll E_2$, the long-term energy exchange is small, since f_{12} is sampled almost periodically and uniformly. On the other hand, if $|\delta E_{12}| \sim E_2$, then each close encounter changes the period of planet 2 materially, such that the value of f_{12} on the next approach is randomized. It is this randomization of the relative phase that causes energy exchange at iterative encounters to behave chaotically, resulting in a drift in orbital energy of planet 2 (a similar phenomenon occurs when highly eccentric binaries experiences chaotic tides; see, e.g. Vick and Lai, 2018).

In general, the amount of random diffusion in E_2 scales inversely proportional to the timescale in which the relative orbital phases f_{12} at successive encounters can be randomized, so the energy exchange is most efficient at large values of a_2 , and suppressed when a_2 is small. When eventually E_2 drifts to a positive value, the planet is ejected and the process terminates.

Now we study the question of for how long this process occurs, i.e. the mean value and distribution of N_{ej} . To do this, we make use of a Brownian motion approximation in E_2 (for a recent application of this idea in a different context, see Mushkin and Katz, 2020).

Suppose we are able to find the RMS value of the function $F(a_2, f_{12})$ over the course of two-planet scattering, weighted by the likelihood of each a_2 occurring during the scattering process. We call this quantity $\bar{\delta}(m_1, m_2, a_1, a_{2,0})$, which depends on the initial separations, i.e.,

$$\bar{\delta} \equiv \left(\frac{1}{2\pi} \int_0^{2\pi} \int_0^\infty F^2(a_2, f_{12}) f(a_2) da_2 df_{12} \right)^{1/2}, \quad (3.16)$$

where $f(a_2)$ is the (unknown) probability density function of a_2 over the course of the scattering event. Then we may assume that the distribution of energy exchanges over the scattering process can be approximated as a Gaussian distribution with a mean of zero

and width of $\bar{\delta}$. We do not attempt to compute $F(a_2, f_{12})$ or $f(a_2)$ explicitly; instead, we constrain them statistically from our N-body simulations by measuring the related parameter b , which is the ratio of the initial orbital energy and the RMS energy exchange and is given by

$$b \equiv |E_{2,0}| \left(\frac{Gm_1m_2\bar{\delta}}{a_1} \right)^{-1}. \quad (3.17)$$

In the limit of many successive passages, each giving a kick in energy that is small relative to the initial orbital energy $|E_{2,0}|$ (i.e. $N \gg 1$ and $b \gg 1$), the probability density distribution in $\Delta E_2/E_{2,0}$ after N orbits is given by

$$f(\Delta E_2/|E_{2,0}|) = \frac{1}{\sqrt{2\pi N}} \exp \left(-\frac{(\Delta E_2/E_{2,0})^2}{2Nb^2} \right). \quad (3.18)$$

N_{ej} is the lowest value of N such that $\Delta E_2/|E_{2,0}| = 1$; it is known as the ‘stopping time’ of the Weiner process and its probability density distribution is given by the Levy distribution (see, e.g. Borodin and Salminen, 2002):

$$f(N_{\text{ej}}|b) = \frac{b}{\sqrt{2\pi N_{\text{ej}}^3}} \exp(-b^2/2N_{\text{ej}}). \quad (3.19)$$

The distribution in Eq. (3.19) is long-tailed since $f(N_{\text{ej}}) \propto N_{\text{ej}}^{-3/2}$ for $N_{\text{ej}} \gg b^2$, and all of its moments including the arithmetic mean diverge. The geometric mean is $\langle N_{\text{ej}} \rangle_{\text{GM}} = \exp(2\gamma_{\text{EM}})b^2 \approx 3.17b^2$ (where $\gamma_{\text{EM}} \approx 0.57$ is the Euler-Mascheroni constant) and its mode is equal to $b^2/3$. Another useful quantity is the harmonic mean, given by

$$\langle N_{\text{ej}} \rangle_{\text{HM}} \equiv \langle 1/N_{\text{ej}} \rangle^{-1} = b^2. \quad (3.20)$$

The standard deviation of the quantity $\ln N_{\text{ej}}$ is $\text{Var}(\ln N_{\text{ej}}) = \pi/\sqrt{2} \approx 2.2$, regardless of the value of b , and the 68% and 95% quantile ranges are $N_{\text{ej}} \in [0.25b^2, 13b^2]$ and $[0.1b^2, 500b^2]$, respectively. In short, N_{ej} is distributed with a long tail at larger values and its distribution can easily span several orders magnitude.

The next step is to empirically determine the value of b from the results of our numerical simulations, given the set of system parameters (m_1 , m_2 , $a_{2,0}$, etc.). To do so, we make use of the maximum likelihood estimate (MLE). The likelihood function for K observations of $N_{\text{ej},i}$, $i \in [1, 2, \dots, K]$ is given by

$$L(b) = \prod_i^K \frac{b}{\sqrt{2\pi N_{\text{ej},i}^3}} \exp(-b^2/2N_{\text{ej},i}). \quad (3.21)$$

Maximizing $\ln L$ with respect to b , we have

$$b_{\text{MLE}} = \underset{b}{\operatorname{argmax}} L(b) = \sqrt{K} \left(\sum_i^K N_{\text{ej},i}^{-1} \right)^{-1/2}. \quad (3.22)$$

Its variance is given by the asymptotic variance of the MLE:

$$\operatorname{Var}(b_{\text{MLE}}) = \left(K \frac{\partial^2 L(b)}{\partial b^2} \right)^{-1}_{b=b_{\text{MLE}}} = -2b_{\text{MLE}}^2/K. \quad (3.23)$$

In Fig. 3.6 we show the empirical values of b_{MLE} estimated using Eq. (3.22) as functions of m_1 and m_2/m_1 . We find that b can be well-approximated by

$$b \approx c_1 \left(\frac{m_1}{M_\star} \right)^{c_2} \left(1 + \frac{m_2}{m_1} \right)^{c_3} \left(\frac{a_{1,0}}{a_{2,0}} \right)^{c_4}, \quad (3.24)$$

with $c_1 = 0.06 \pm 0.02$, $c_2 = -0.98 \pm 0.03$, $c_3 = 2.14 \pm 0.07$ and $c_4 = -1.4 \pm 0.5$; the above model has a value of $R^2 = 0.99$ when fitted against the empirical values of b (as estimated by MLE).

This empirical scaling is in fact consistent with the results of past studies, which showed that for comets with $a_2 \gg a_1$ and $(1 - e_2) \ll 1$, the RMS energy exchange per pericenter passage is of order $\delta E_{12} \sim Gm_1m_2/a_1$ (see, e.g. Wiegert and Tremaine, 1999; Fouchard et al., 2013). This result would imply that $c_2 = c_4 = -1$, which is in agreement with our empirical results.

Eqs. (3.19) and (3.24) provides a very accurate description of the distribution for N_{ej} as long as $m_2/m_1 \lesssim 1/3$. However, this model breaks down in the comparable

mass regime ($m_1 \sim m_2$), where N_{ej} is usually much larger than predicted by Eq. (3.24). This is because for planets of comparable mass, as a_2 increases a_1 will decrease by a comparable value. As a result, the energy exchange becomes much less efficient as a_2 increases since the planet can only come close to one another when planet 1 and planet 2 are simultaneously at their apocenter and pericenter respectively. A theoretical model for this strong scattering process at comparable masses is an intriguing question in its own right, and necessary for further refinements on the results presented here, but beyond the scope of this paper.

3.2.5 Scattering into inner system

Aside from the orbital parameters and ejection timescale, another quantity we are interested in is the minimum approach distance a planet might have with its host star. Since planet ejections occur gradually in a random walk-like manner, the ejected planet may first meander a significant amount inwards before being eventually ejected. If the to-be-ejected giant planet at some point comes too close to the inner system, it can undergo non-secular interactions with the inner system, causing our semi-secular approximation (see Section 3.3) to break down. Therefore, it is important to quantify the extent to which the giant planet might first move inward.

First, due to conservation laws, there is a limit to how deeply inwards a planet can meander during the scattering process. If we assume the planet orbits remain (approximately) co-planar, then the 4 relevant variables are a_1 , a_2 , e_1 and e_2 , which satisfy the constraints

- Energy conservation:

$$\sum_j m_j / a_{j,0} = \sum_j m_j / a_j. \quad (3.25)$$

- Angular momentum conservation:

$$\sum_j m_j \sqrt{a_{j,0}(1 - e_{j,0}^2)} = \sum_j m_j \sqrt{a_j(1 - e_j^2)}. \quad (3.26)$$

- Second law of thermodynamics: The system must not spontaneously ‘scatter’ itself into a state that is indefinitely stable, even if this is permitted by the conservation laws. In general, the stability criterion for 2 planets with general masses, eccentricities and inclinations is complicated (see, e.g. Petrovich, 2015b). In the limit of co-planar orbits with $m_1 \gg m_2$, we find that requiring planets to follow the criterion below results in best agreement with the empirical results:

$$\frac{a_2(1 - e_2)}{a_1(1 - e_1)} \lesssim 1 + 2(m_1/3M_\star)^{1/3}. \quad (3.27)$$

The above constraint asserts that the maximal planet separation should not exceed 2 Hill radii at all times.

The above 3 constraints reduce the degree of freedom to 1, which means that given any one variable, the other 3 variables are uniquely determined. One can then optimize for the lowest allowed values of a_2 and $a_2(1 - e_2)$. This then produces a theoretical lower limit on a_2 during the scattering process. However, it is not a given that this minimum can always be reached, for two reasons: Firstly, since ΔE_2 undergoes an approximate Brownian motion, it is likely to spend large fractions of time being positive, such that a_2 is never much below its initial value. Secondly, energy exchange becomes less efficient as a_2 decreases, since the timescale for the randomization of the relative orbital phase becomes larger.

We show these limits for a_2 and $r_2 \equiv a_2(1 - e_2)$, compared with empirical results from our simulations, in Fig. 3.7. We see that generally, $a_{2,\min} \sim 1/2$, and decreases with increasing m_1 . The theoretical constraints agreed well with empirical results when $m_2/m_1 \ll 1$, but breaks down when $m_2/m_1 \gtrsim 0.2$. We also find that $r_{2,\min}$ decreases strongly with increasing m_2/m_1 , and can reach $r_{2,\min}/a_{1,0} \lesssim 0.05$ for $m_2 \sim m_1$.

3.3 Semi-Secular Algorithm for “N+2” Scatterings

We now consider how an inner low-mass planet system respond to an outer pair of giant planets undergoing strong scatterings. We label the inner planets as $j \in [a, b, c, \dots]$, while the outer planets are labeled $p \in [1, 2]$. In Sec. 3.4 we focus on inner systems with only one planet, and we extend our results to cases with 2 inner planets in Sec. 3.5, although our method can work for a general number of inner and outer planets. We imagine the inner system to be consistent with those discovered by Kepler, i.e. the planets have semi-major axes typically between 0.02 – 0.5 au and are super-Earths in mass ($m_j \sim 3 - 20M_\oplus$). We have a system of outer planets with semi-major axes beyond $\sim 2 - 3$ au that are gravitationally unstable ($k_0 \leq 2\sqrt{3}$), and at least one of the planets have a fairly large mass ($\geq 100M_\oplus$), although m_2 may be more comparable to super-Earths in size. We assume that the inner system is well-separated from the outer system ($a_j \ll a_1, a_2$), such that the inner planets do not participate directly in the outer scattering process.

As noted in Section 3.1, to address the question of how the inner planets are affected by the outer scattering, a direct approach based on N-body simulations is inadequate. The issue lies in the differing time-scales involved: The inner planets have short orbits on the timescale of days, which forces the time-step of the N-body simulation to not

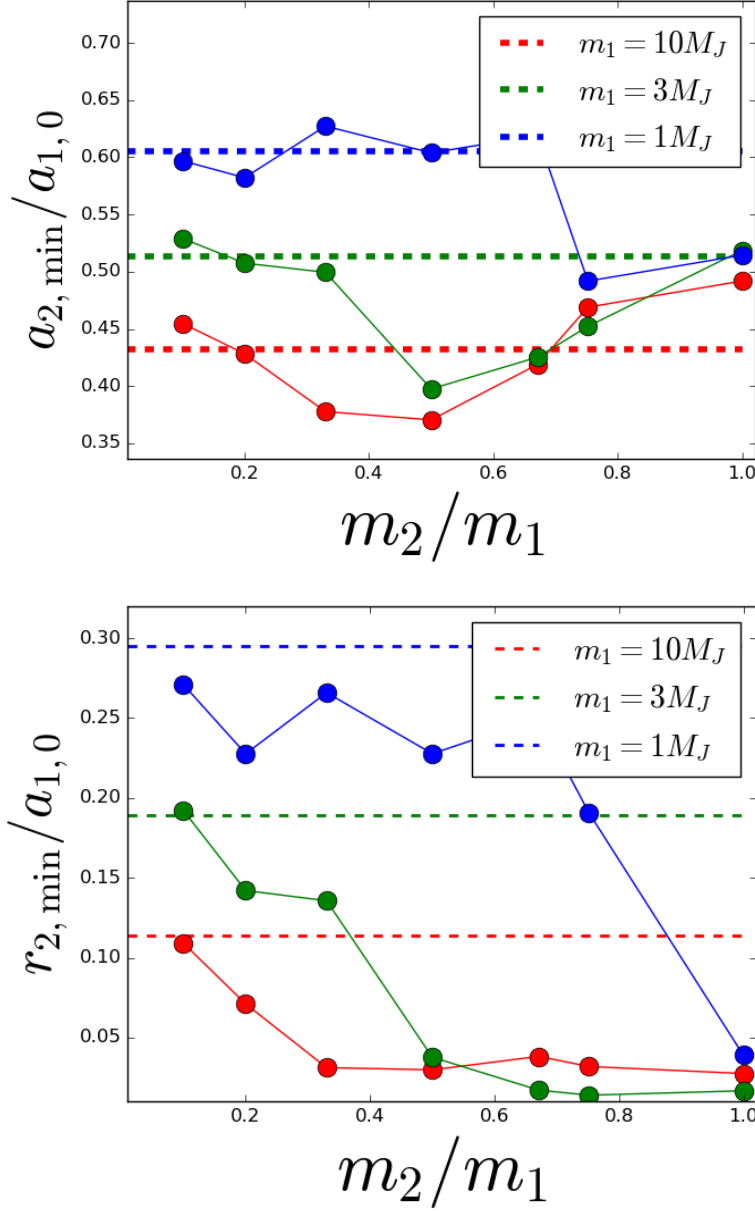


Figure 3.7: Top: empirical values of $a_{2,\min}$ as function of m_2/m_1 . Each data point represents the global minimum over all simulations. The blue, green and red circles correspond to $m_1 = 10, 3, 1M_J$ respectively. The dashed lines are derived from minimizing a_2 under the constraints given by Eqs. (3.25) - (3.27) in the limit of $m_2/m_1 \ll 1$. We suppress error bars in the empirical results because it is unclear how to estimate the minimum of a set of observations without prior assumptions about the distribution of our data. The bottom panel is similar to the upper panel, except we plot $r_{2,\min} = \min[a_2(1 - e_2)]$ instead of $a_{2,\min}$.

more than a few hours. On the other hand, the outer planets have periods of ~ 10 years and an ejection timescale of potentially hundreds of Myrs. To make matters even worse, the prospect of scattering events driven constantly by close encounters between planets preclude the use of fast and efficient symplectic integrators (e.g. the Wisdom-Holman mapping).

Here, we develop a hybrid method to evaluate the dynamical evolution of an inner system perturbed by a system of unstable outer CJs. In this method, we decouple the timescale of the inner planets and outer planets by computing their orbital evolutions separately. This is possible because we can safely neglect the back-reaction on the outer planets by the inners: since the inner planets are much less massive compared to their outer companions, the gravitational influence of the inner planets on the outer planets is negligible in comparison with the outer planets' own violent scatterings. Furthermore, since the inner planets are sufficiently far from the outer planets as to avoid direct scattering interactions, the gravitational influence by the outer planets is well described by secular dynamics (Matsumura et al., 2013).

Our algorithm is as follows. First, we evolve the gravitational interaction between the outer planets, in the absence of any inner planets. We then obtain a timeseries of the position-velocity vectors of each of the outer planets from beginning until final ejection. In the case of two giant planets, we have $\mathbf{r}_p(t)$ and $\mathbf{v}_p(t)$ for $p = 1, 2$. These will be used as forcing terms to calculate the evolution of the inner planets, as follows.

Define \mathbf{j} and \mathbf{e} as a planet's dimensionless angular momentum and eccentricity vectors:

$$\mathbf{j} = \sqrt{1 - e^2} \hat{\mathbf{n}}, \quad \mathbf{e} = e \hat{\mathbf{u}} \quad (3.28)$$

where $\hat{\mathbf{n}}$ and $\hat{\mathbf{u}}$ are unit vectors, $\hat{\mathbf{n}}$ is in the direction normal to the orbital plane and $\hat{\mathbf{u}}$ is pointed along the pericenter. We compute the time evolution of these vectors for the

outer planet p using

$$\mathbf{j}_p(t) = \frac{1}{(GM_\star a_p)^{1/2}} [\mathbf{r}_p(t) \times \hat{\mathbf{v}}_p(t)] \quad (3.29)$$

$$\mathbf{e}_p(t) = \frac{1}{GM_\star} [\hat{\mathbf{v}}_p(t) \times (\mathbf{r}_p(t) \times \hat{\mathbf{v}}_p(t))]. \quad (3.30)$$

According to Laplace-Lagrange theory (e.g. Murray and Dermott, 1999), the evolution equations for the eccentricity vector \mathbf{e}_j and unit angular momentum vector \mathbf{j}_j on the planet j due to the action of planet k , in the limit that e_j, e_k, θ_{jk} are small, are given by:

$$\left(\frac{d\mathbf{e}_j}{dt} \right)_k = -\omega_{jk}(\mathbf{e}_j \times \mathbf{j}_k) + \nu_{jk}(\mathbf{e}_k \times \mathbf{j}_j), \quad (3.31)$$

$$\left(\frac{d\mathbf{j}_j}{dt} \right)_k = \omega_{jk}(\mathbf{j}_j \times \mathbf{j}_k). \quad (3.32)$$

The quantities ω_{jk} and ν_{jk} are the quadrupole and octupole precession frequencies of the j -th planet due to the action of the k -th planet, given by:

$$\omega_{jk} = \frac{Gm_j m_k a_{<}}{a_{>}^2 L_j} b_{3/2}^{(1)}(\alpha), \quad (3.33)$$

$$\nu_{jk} = \frac{Gm_j m_k a_{<}}{a_{>}^2 L_j} b_{3/2}^{(2)}(\alpha). \quad (3.34)$$

Here $a_{<} = \min(a_j, a_k)$, $a_{>} = \max(a_j, a_k)$, $\alpha = a_{<}/a_{>}$, $L_j \simeq m_j \sqrt{GM_\star a_j}$ is the angular momentum of the j -th planet, and the $b_{3/2}^{(n)}(\alpha)$ are the Laplace coefficients defined by:

$$b_{3/2}^{(n)}(\alpha) = \frac{1}{2\pi} \int_0^\pi \frac{\cos(nt)}{(\alpha^2 + 1 - 2\alpha \cos t)^{3/2}} dt. \quad (3.35)$$

Laplace-Lagrange theory breaks down for more general values of e_j and θ_{jk} , and therefore, in this work we instead adopt a set of modified secular equations that interpolates between Laplace-Lagrange theory and secular multipole expansion. The equations are given in Eqs. (A2)-(A5) in (Pu and Lai, 2018) and have better performance than Eqs. (3.31 - 3.32) when e_j and θ_{jk} are large but $(a_a/a_1) \ll 1$. Thus we use these hybrid equations from (Pu and Lai, 2018) in place of Eqs. (3.31) - (3.32) to compute the

gravitational influence of the outer planets on the inner planets. Note that the adopted equations employ orbital averaging over both the inner planet and outer planet orbits. Even though the outer planet orbits vary on orbital timescales due to the strong mutual scatterings, the use of secular orbital averaging is appropriate since the interactions between the outer and inner planets are secular and accumulate over large number of orbits, the orbit-to-orbit variations can be ignored so long as the orbital period of outer planets is much shorter than the secular timescale.

In summary, we compute the evolution of the inner planets $j \in [a, b, c\dots]$, by the action of other inner planets $k \in [a, b, c\dots]$ as well as outer planets $p \in [1, 2]$ as follows:

$$\frac{d\mathbf{j}_j}{dt} = \sum_{k=a,b\dots} \left(\frac{d\mathbf{j}_j}{dt} \right)_k + \sum_{p=1,2} \left(\frac{d\mathbf{j}_j}{dt} \right)_p, \quad (3.36)$$

$$\frac{d\mathbf{e}_j}{dt} = \sum_{k=a,b\dots} \left(\frac{d\mathbf{e}_j}{dt} \right)_k + \sum_{p=1,2} \left(\frac{d\mathbf{e}_j}{dt} \right)_p. \quad (3.37)$$

The results of the calculations are discussed in Sec. 3.4.

3.4 1+2 Scattering

We consider a single inner planet ("a") with two outer CJs. Planet a has mass $3M_\oplus$ and semi-major axis chosen from $a_a \in \{0.1, 0.15, 0.2, 0.25, 0.375, 0.5, 0.75, 1.0\}$, these are much smaller than the initial semi-major axes (≥ 5 au) of the outer planets so that planet a typically does not participate directly in the scattering between planets 1 and 2. We assume all planets have initially circular and co-planar orbits, except that $\theta_{2,0} = 3$ degrees. We integrate this system using the semi-secular algorithm described in Sec. 3.3. A simulation is halted if any pair of planets undergo orbit crossings, or if planet a attains an eccentricity greater than 0.99. We discuss the results of these simulations below.

3.4.1 Empirical Results

In our simulations we find a wide range of the final possible values of the inner planet eccentricity e_a , inclination θ_a measured relative to the original orbital plane of planet a (note the orbits of planets a and the remaining CJ are initially aligned), and mutual inclination θ_{a1} between the inner planet and the remaining CJ. As mentioned earlier, the evolution has two phases: the first phase is when the system has 3 planets total, with the outer two planets (planets 1 and 2) undergoing scattering and the inner planet (planet a) interacting secularly with both planets. At some point, an outer planet is ejected, and the inner planet interacts with only the remaining CJ, whose orbital properties remain a constant in time.

We define the eccentricity and inclination of the inner planet at the time of ejection as $e_{a,\text{ej}}$ and $\theta_{a,\text{ej}}$ respectively. After ejection, the inner planet still undergoes secular oscillations in eccentricity and inclination due to interactions with the remaining CJ. We thus define the time-averaged RMS eccentricity and inclination at infinity as

$$e_{a,\infty} \equiv \left(\lim_{t \rightarrow \infty} \frac{1}{t - t_{\text{ej}}} \int_{t_{\text{ej}}}^t e_a^2(t) dt \right)^{1/2}, \quad (3.38)$$

$$\theta_{a,\infty} \equiv \left(\lim_{t \rightarrow \infty} \frac{1}{t - t_{\text{ej}}} \int_{t_{\text{ej}}}^t \theta_a^2(t) dt \right)^{1/2}. \quad (3.39)$$

These quantities can be easily evaluated using secular theory (see, e.g. Pu and Lai, 2018). For the mutual inclination, θ_{a1} remains constant once ejection has occurred, thus $\theta_{a1,\infty} = \theta_{a1,\text{ej}}$. We focus on $e_{a,\infty}$ and $\theta_{a,\infty}$ as they are more representative of the long-term post-scattering dynamics of the inner planet.

Since the final value of $\theta_{1,\text{ej}}$ is small (see Sec. 3.2.2), in general $\theta_{a1,\text{ej}} \approx \theta_{a,\infty}$. Thus in this section we focus on $\theta_{a,\infty}$ instead of the mutual inclination. Fig. 3.8 shows the values of $e_{a,\infty}$ and $\theta_{a,\infty}$ for a subset of our simulations. According to Fig. 3.8, $e_{a,\infty}$ and

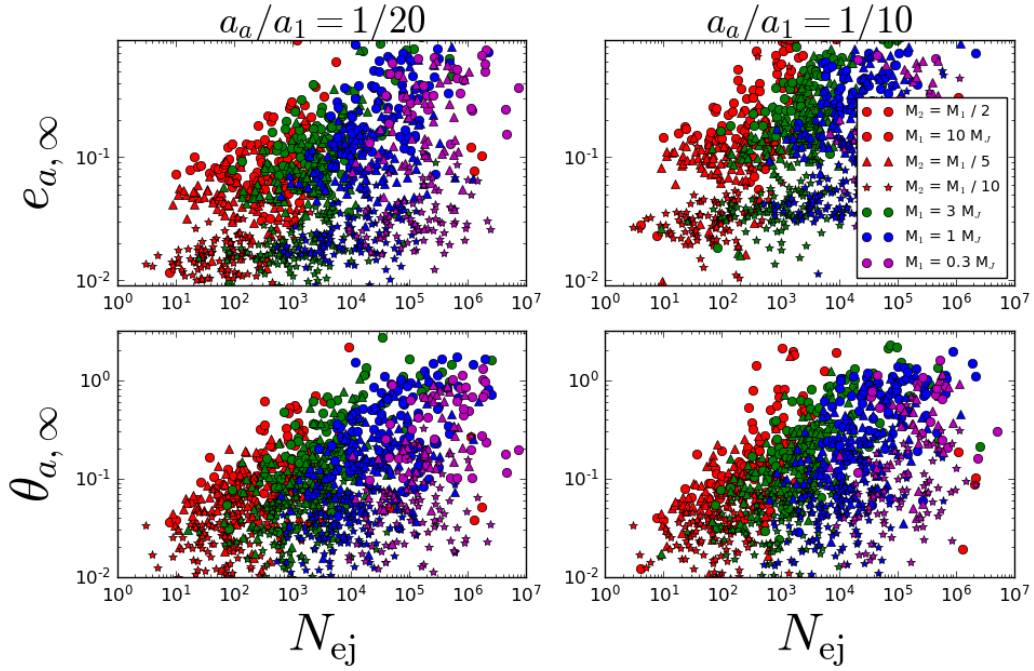


Figure 3.8: The final values of $e_{a,\infty}$ (top panels) and $\theta_{a,\infty}$ (in radians, bottom panels) as defined by Eqs. (3.38) - (3.39), as a function of N_{ej} , for a 1-planet inner system subject to the gravitational influence of two scattering giant planets. The masses of the outer planets are varied with $m_1 = 10, 3, 1$ or $0.3M_J$ (the red, green, blue and magenta points respectively), while the mass ratio $m_2/m_1 = 1/2, 1/5, 1/10$ for the filled circles, triangles and stars respectively. The initial semi-major axes of the outer planets are $a_1 = 6.0$ au and $a_2 = a_1 + k_0 r_H$ with r_H being the mutual Hill radius and k_0 chosen randomly from $[1.5, 2.0, 2.5]$; the value of k_0 matters little for the final results. The left panels show systems where the initial $a_a/a_1 = 1/20$, while the right panels have $a_a/a_1 = 1/10$.

$\theta_{a,\infty}$ tends to increase roughly as $\sqrt{N_{\text{ej}}}$. We provide a theoretical model for this behavior in Sec. 3.4.2. Secondly, we find a strong dependence of the final values of $e_{a,\infty}$ and $\theta_{a,\infty}$ on the planet mass ratio m_2/m_1 , with outer planet pairs having comparable masses leading to much higher values of $e_{a,\infty}$ and $\theta_{a,\infty}$ compared with cases where $m_1 \gg m_2$. The main reason is that these final values increase as the mass ratio m_2/m_1 increases, and more eccentric/inclined perturbbers tend to drive stronger perturbations on the inner planet.

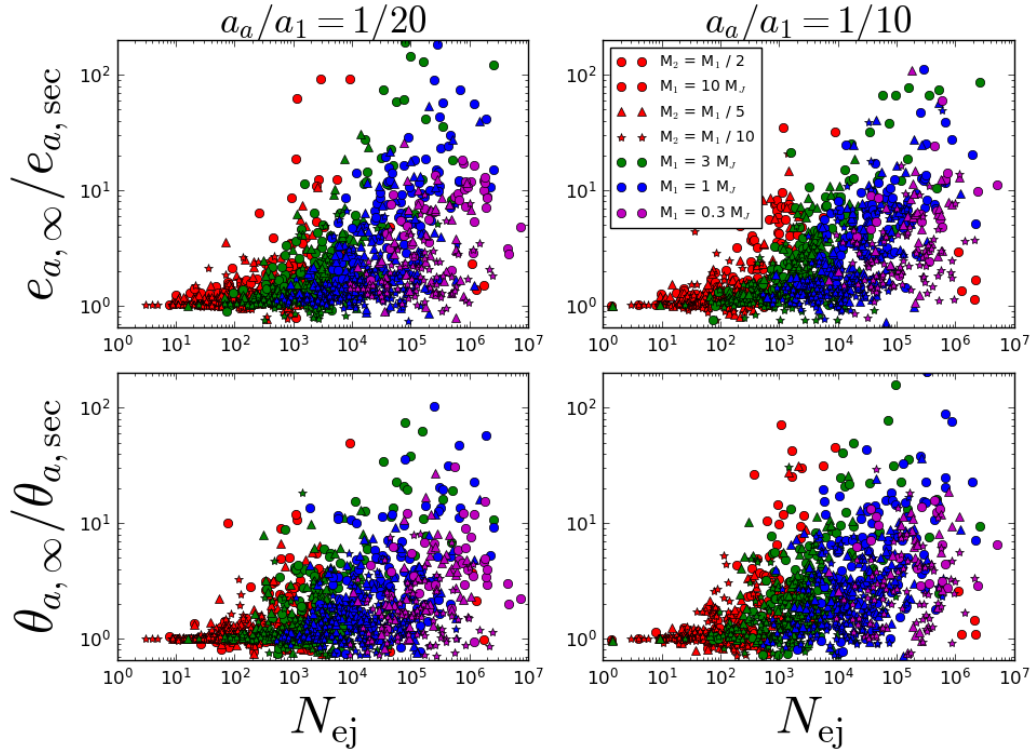


Figure 3.9: Same as the Fig. 3.8, except the eccentricities and inclinations are normalized by the “secular” expectation $e_{a,\text{sec}}$ and $\theta_{a,\text{sec}}$ given by Eqs. (3.40) - (3.41).

How to understand the diversity of final results in this parameter space? The picture becomes clearer if we normalize the results by the “scattering-free” theoretical expectations. We introduce these “scattering-free” quantities as the “secular” eccentricity and inclination $e_{a,\text{sec}}$ and $\theta_{a,\text{sec}}$ that are the (RMS) eccentricities and inclinations that would be expected on planet a , if the dynamical history of the two-planet scattering were to be ignored, and the inner planets started their orbital evolution with m_1 at its final orbital state and m_2 removed. In other words, $e_{a,\text{sec}}$ and $\theta_{a,\text{sec}}$ are RMS eccentricity and inclination that planet “a” would finally obtain, if it started on an initially circular, non-inclined orbit under the influence of the perturber planet “1” with initial eccentricity

and inclination $e_1 = e_{1,\text{ej}}$, $\theta_a = \theta_{a,\text{ej}}$. For $L_a \ll L_1$, we have (e.g. Pu and Lai, 2018):

$$e_{a,\text{sec}} = \frac{5\sqrt{2}a_a e_{1,\text{ej}}}{4a_1(1 - e_{1,\text{ej}}^2)} \quad (3.40)$$

$$\theta_{a,\text{sec}} = \sqrt{2}\theta_{1,\text{ej}} \quad (3.41)$$

$$\theta_{a1,\text{sec}} = \theta_{1,\text{ej}} \quad (3.42)$$

(note that $\theta_{1,\text{ej}}$ is the inclination of planet 1 measured relative to its initial orbital plane).

Fig. 3.9 shows our numerical results of Fig. 3.8 for the final RMS values of $e_{a,\infty}$ and $\theta_{a,\infty}$, normalized by the secular expectations $e_{a,\text{sec}}$ and $\theta_{a,\text{sec}}$. We find that the scaling for the final values of $e_{a,\infty}$ and $\theta_{a,\infty}$ can be divided into two regimes. In the case where N_{ej} is small, $e_{a,\infty}$ and $\theta_{a,\infty}$ reduce to their “secular” expectations. In the case that N_{ej} is large, the ratio $e_{a,\infty}/e_{a,\text{sec}}$ and $\theta_{a,\infty}/\theta_{a,\text{sec}}$ can be either larger or smaller than 1, and is bounded from below by $\sqrt{2}/2$; the average values scale proportionally to $\sqrt{N_{\text{ej}}}$, albeit with a large spread. The transition between the two regimes occur approximately at $N_{\text{ej}} \sim N_{\text{sec}}$, with N_{sec} given by

$$N_{\text{sec}} \equiv \left(\frac{\omega_{a1,0} P_{1,0}}{2\pi} \right)^{-1} = \frac{1}{2\pi} \left(\frac{m_1}{M_\star} \right)^{-1} \left(\frac{a_a}{a_1} \right)^{-3/2}, \quad (3.43)$$

where $\omega_{a1,0}$ is the (initial) secular quadrupolar precession frequency of planet a driven by planet 1 (see Eq. 3.33) and $P_{1,0}$ is the initial orbital period of planet 1. This boundary is consistent with the inner planet a being driven by stochastic secular forcing from planets 1 and 2 during the ejection process: When $N_{\text{ej}} \ll N_{\text{sec}}$, the ejection occurs much more quickly than the timescale of secular interactions, and the dynamical history of the ejection can be ignored. On the other hand, when $N_{\text{ej}} \gg N_{\text{sec}}$, the stochastic ‘forcing’ on planet a driven by the scattering perturbors will cause e_a and θ_a to undergo a random walk of its own, with the value of $e_{a,\infty}$ and $\theta_{a,\infty}$ scaling proportionally to $\sqrt{N_{\text{ej}}}$.

The final results can be summarized most succinctly if we consider the deviation of

the final values of e_a and θ_a from their secular predictions and define the “boost factors”:

$$\gamma_e^2 \equiv \frac{|e_{a,\infty}^2 - e_{a,\text{sec}}^2|}{e_{a,\text{sec}}^2} \quad (3.44)$$

$$\gamma_\theta^2 \equiv \frac{|\theta_{a,\infty}^2 - \theta_{a,\text{sec}}^2|}{\theta_{a,\text{sec}}^2} \quad (3.45)$$

$$\gamma_{\theta a1}^2 \equiv \frac{|\theta_{a1,\infty}^2 - \theta_{a1,\text{sec}}^2|}{\theta_{a1,\text{sec}}^2}. \quad (3.46)$$

Figs. 3.10 and 3.11 show the comparison of our numerical results for the values of γ_e and γ_θ for a subset of our numerical integrations. We find that across a wide range of parameters for a_a , a_1 , m_a , m_1 and m_2 , the quantities γ_e , γ_θ have a universal scaling given by (shown as the solid black line in Figs. 3.10 and 3.11):

$$\gamma_e \sim \gamma_\theta \sim \sqrt{N_{\text{ej}}/N_{\text{sec}}}. \quad (3.47)$$

The boost factor for the mutual inclination also shows the same scaling, but with different normalization. We find that $\gamma_{\theta,a1} \sim 1.4\gamma_\theta$; we provide a theoretical explanation for this in Sec. 3.4.3.

To make this scaling even clearer, and to show its robustness over a range of system parameters, in Figs 3.12 - 3.14 we show the mean square values of γ_e^2 , binned by logarithmic increments of $N_{\text{ej}}/N_{\text{sec}}$ for various combinations of a_a , m_1 and m_2 . We see that the approximate scaling given by Eq. (3.47) agrees very well with the simulations for values of a_a/a_1 ranging from $1/7 - 1/20$, m_1 from $3 - 0.3M_J$, and m_2/m_1 from $1/10$ to $1/2$, although there is a trend of increasing deviation from Eq. (3.47) when $N_{\text{ej}}/N_{\text{sec}} \gg 1$. We explore a possible reason for this deviation, and present a more accurate analytic formula for $\langle \gamma^2 \rangle$ in Sec. 3.4.2. In general, the above scaling is accurate for $m_2/m_1 \lesssim 1/2$ and $a_a/a_1 \lesssim 1/5$. When $m_1 \sim m_2$ and/or $a_a/a_{1,0} \gtrsim 1/5$, it is often the case that the ejected planet can come very close to the orbit of planet a , resulting in strong non-secular interactions that causes γ_e , γ_θ to be much greater than predicted by Eq. (3.47).

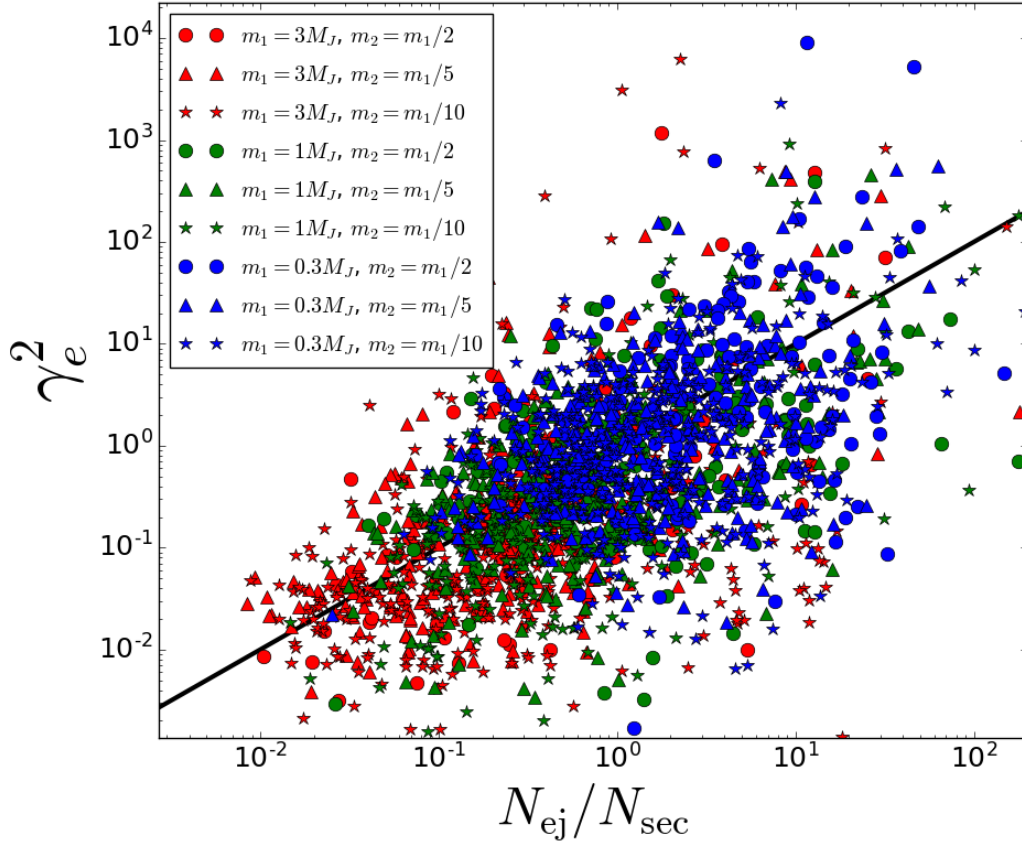


Figure 3.10: The value of γ_e^2 (Eq. 3.44) plotted as a function of N_{ej}/N_{sec} (see Eq. 3.43) for our simulations. Here $a_a = 0.3$ au (corresponding to $a_a/a_1 = 1/20$). Red, green and blue points correspond to $m_1 = 3, 1, 0.3M_J$ respectively. The filled circles, triangles and stars correspond to $m_2/m_1 = 1/2, 1/5, 1/10$ respectively. The black solid line is given by $\gamma_e^2 = N_{ej}/N_{sec}$.

The simple universal scaling $\sqrt{N_{ej}}$ can in fact be derived from the first principles using secular Laplace-Lagrange theory, as we discuss below.

3.4.2 Analytic Model for “1+2” Secular Evolution: Eccentricity

We model the dynamical evolution of an inner planet a subject to the gravitational influence of a pair of outer perturbers undergoing gravitational scattering as a linear

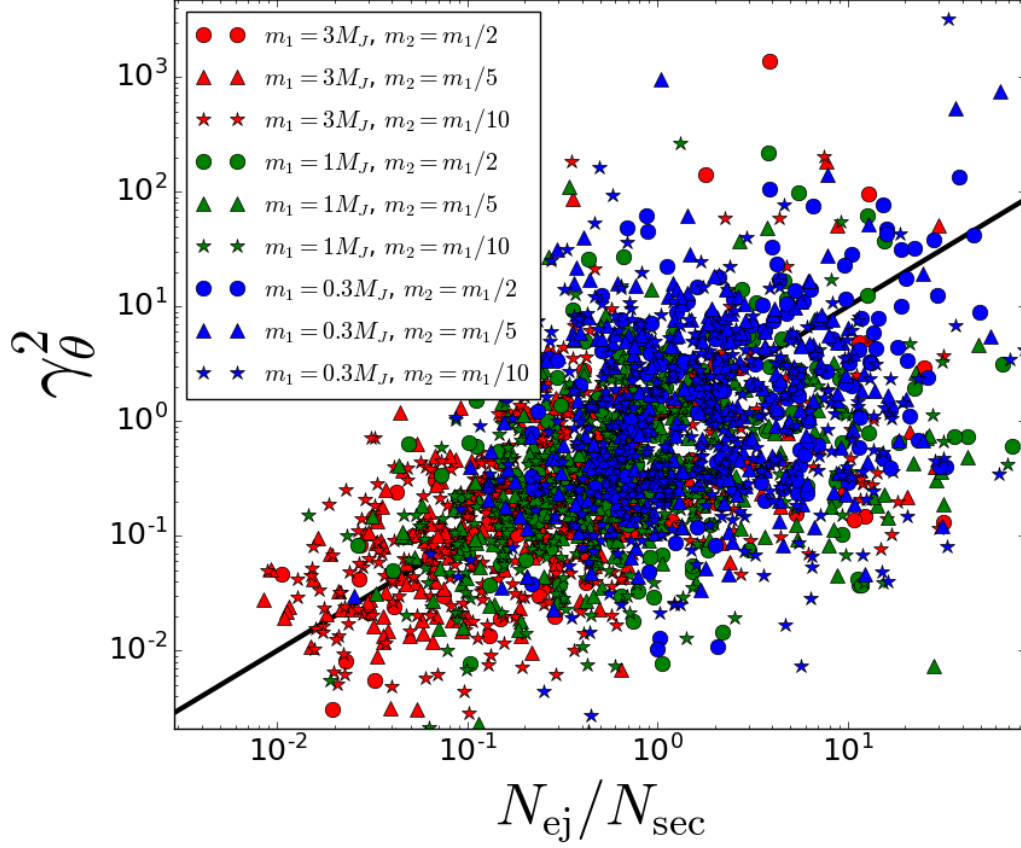


Figure 3.11: Same as Fig. 3.10, except we show γ_θ^2 as defined by Eq. (3.45).

stochastic differential equation (SDE). We define $\mathcal{E} \equiv e \exp(i\varpi)$ and $\mathcal{I} \equiv \theta \exp(i\Omega)$ as the complex eccentricity and inclination respectively. Note that $e = |\mathcal{E}|$ and $\theta = |\mathcal{I}|$. In the discussion below we will focus on the eccentricity evolution and derive the boost factor γ_e , although the inclination is completely analogous and will have the same scaling as γ_θ .

First, consider an inner planet m_a with initial eccentricity $\mathcal{E}_{a,0}$ undergoing secular evolution with an external planet $m_1 \gg m_a$ that has a constant eccentricity \mathcal{E}_1 . For simplicity, we ignore for now the secular interaction between planet a and 2. The

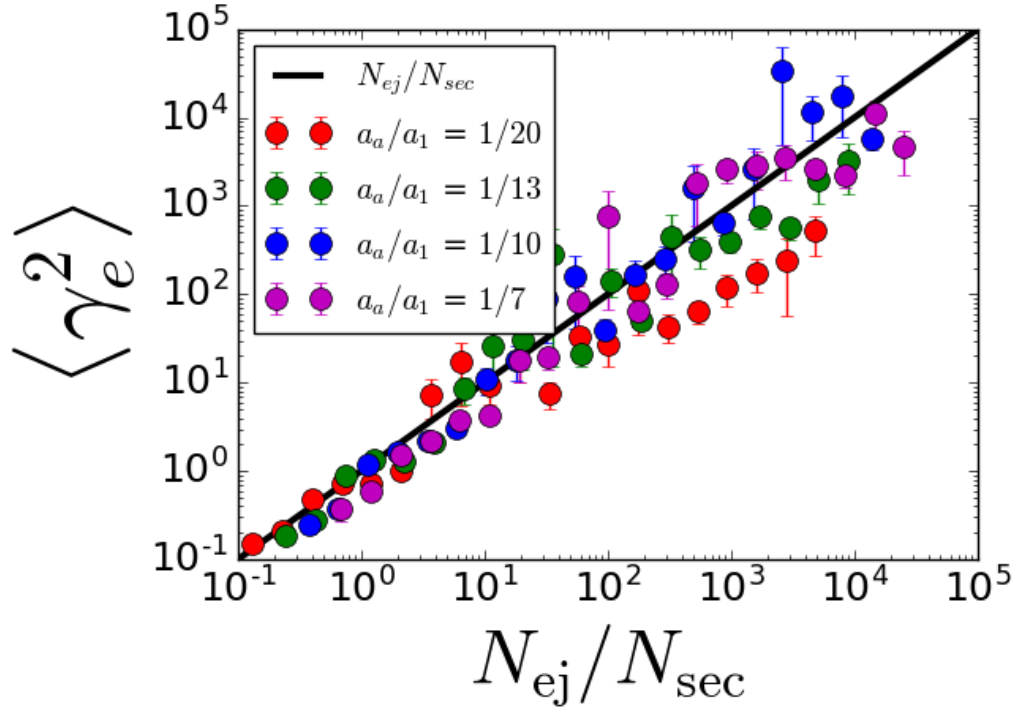


Figure 3.12: The average value of γ_e^2 , binned by $\log(N_{ej}/N_{sec})$ with 4 bins per logarithmic decade, as a function of N_{ej}/N_{sec} . For each of the points, $m_1 = M_J$ and $m_2/m_1 = 1/5$. The red, green, blue and magenta filled circles correspond to $a_a/a_1 = 1/20, 1/13, 1/10$ and $1/7$ respectively. The errorbars are given by the standard error, and the solid black line is given by $\langle \gamma_e^2 \rangle = N_{ej}/N_{sec}$.

evolution of $\mathcal{E}_a(t)$ is governed by the ODE

$$\frac{d\mathcal{E}_a(t)}{dt} = i\omega_{a1}\mathcal{E}_a(t) - i\nu_{a1}\mathcal{E}_1(t), \quad (3.48)$$

where ω_{a1}, ν_{a1} are given by Eqs. (3.33)-(3.34). The solution to the above equation is given by

$$\mathcal{E}_a(t) = \mathcal{E}_{a,\text{free}}(t) \exp(i\omega_{a1}t) + \mathcal{E}_{a,\text{forced}}, \quad (3.49)$$

where

$$\mathcal{E}_{a,\text{forced}} = \frac{\nu_{a1}}{\omega_{a1}} \mathcal{E}_1, \quad (3.50)$$

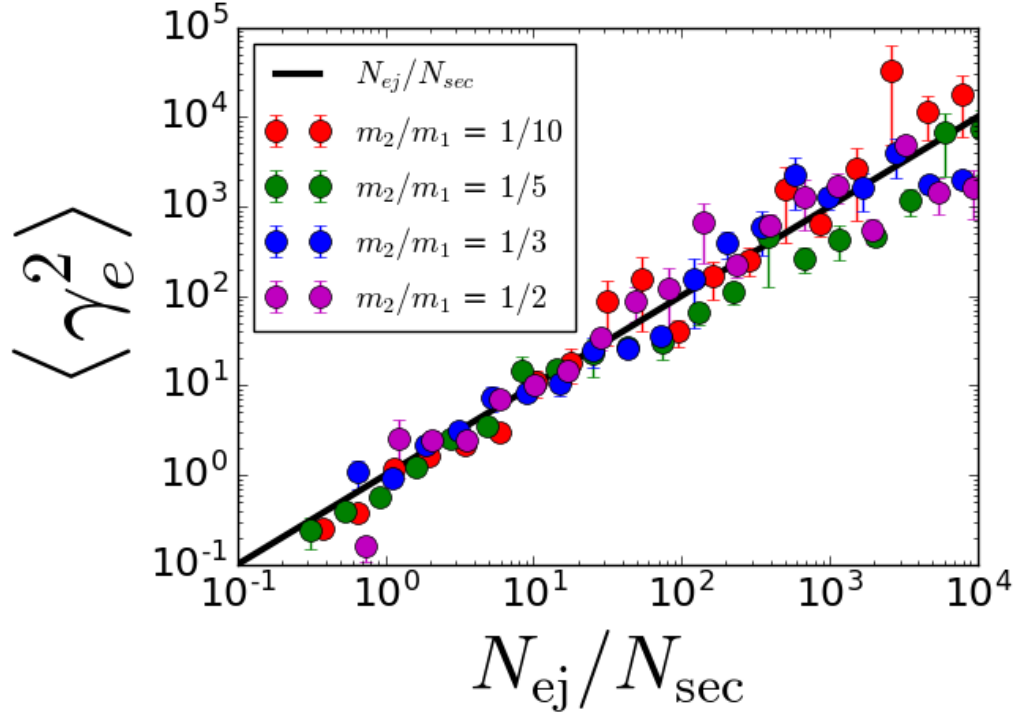


Figure 3.13: Same as Fig. 3.12, except that we fix $a_a/a_1 = 1/10$, and m_2/m_1 varies as indicated by the plot legend.

and

$$\mathcal{E}_{a,\text{free}} = \mathcal{E}_{a,0} - \mathcal{E}_{a,\text{forced}}. \quad (3.51)$$

Applying Eq. (3.48) to the secular evolution of planet a after the ejection of planet 2, we have that $\mathcal{E}_{a,0} = \mathcal{E}_{a,\text{ej}}$ (where $\mathcal{E}_{a,\text{ej}} = \mathcal{E}_a(t_{\text{ej}})$), and the RMS eccentricity $|\mathcal{E}_{a,\infty}|$ is given by

$$\begin{aligned} |\mathcal{E}_{a,\infty}|^2 &= |\mathcal{E}_{a,\text{free}}|^2 + |\mathcal{E}_{a,\text{forced}}|^2 \\ &= |\mathcal{E}_{a,\text{ej}}|^2 + 2|\mathcal{E}_{a,\text{forced}}|^2 - 2\text{Re}(\mathcal{E}_{a,\text{ej}}\mathcal{E}_{a,\text{forced}}^*). \end{aligned} \quad (3.52)$$

Note that $|\mathcal{E}_{a,\infty}|$ is what we termed $e_{a,\infty}$ in Sec. 3.4.1. If the initial eccentricity of planet a is zero, then the free eccentricity is equal to the forced eccentricity, and $e_{\text{sec}} = \sqrt{2}e_{\text{forced}}$.

Now we ask the question: What happens to $\mathcal{E}_a(t)$ if, instead of being a constant,

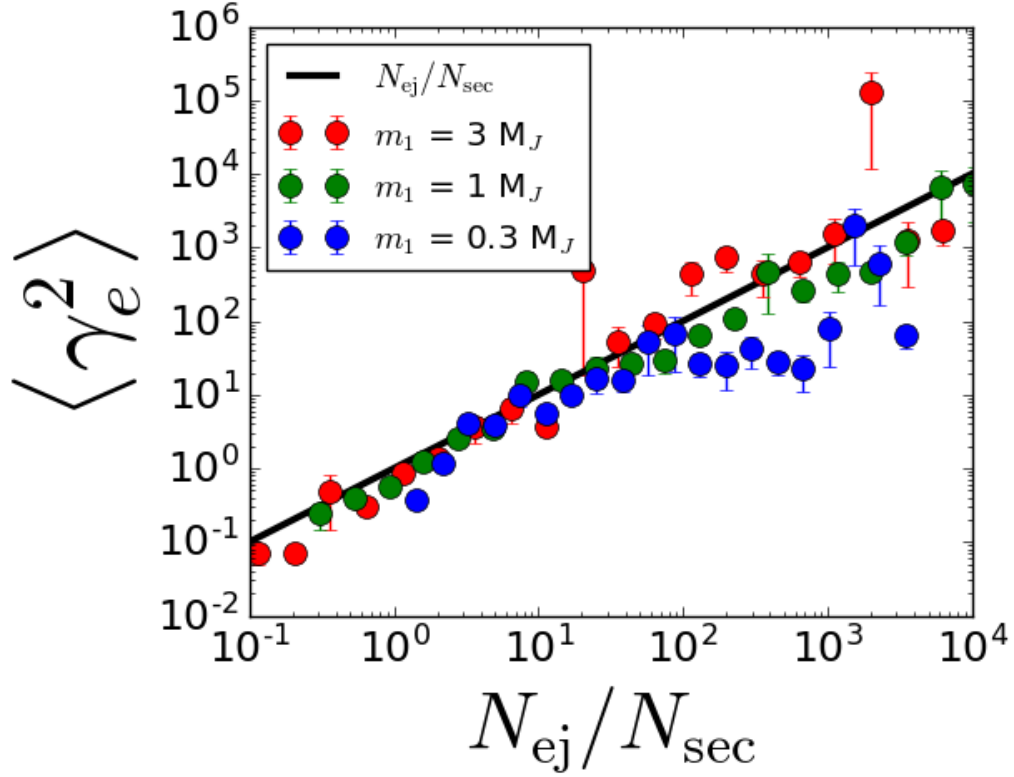


Figure 3.14: Same as Fig. 3.12, except that we fix $a_a/a_1 = 1/10$, and m_1 varies as indicated by the plot legend.

$\mathcal{E}_1(t)$ is a stochastically varying quantity, as is the case during the scattering process. We study a version of Eq. (3.48) with \mathcal{E}_1 being given by a Brownian motion stochastic process: $\mathcal{E}_1(t) = Z(t)$, where $Z(t)$ is a Brownian motion in the complex plane with diffusion constant equal to $\sigma_{\mathcal{E}_1}$, i.e. $Z(t) = X(t) + iY(t)$ where $X(t)$, $Y(t)$ are each given by a Gaussian distribution with mean $\langle X \rangle = \langle Y \rangle = 0$, variance $\text{Var}(X) = \text{Var}(Y) = \sigma_{\mathcal{E}_1}^2 t$, and covariance $\text{Cov}[X(s), X(t)] = \text{Cov}[Y(s), Y(t)] = \sigma_{\mathcal{E}_1}^2 \min(s, t)$.

The diffusion coefficient of the perturber eccentricity, $\sigma_{\mathcal{E}_1}$ is a constant that can either be calculated analytically or numerically, or derived empirically from the time series of scattering planet systems. We make a heuristic estimate of it here. Over the ejection timescale, the eccentricity of planet 1 changes from $e_1 = 0 \rightarrow e_{1,\text{ej}}$ (where $e_{1,\text{ej}}$ is the

eccentricity of planet 1 when planet 2 has been ejected; see Section 3.2). On average, this process takes $N_{\text{ej}} \sim t_{\text{ej}}/P_{1,0} \sim b^2$ orbits (see Eq. 3.18). Thus, one might surmise:

$$\langle e_{1,\text{ej}}^2 \rangle \sim 2\sigma_{\mathcal{E}1}^2 b^2 P_{1,0}, \quad (3.53)$$

where $\langle e_{1,\text{ej}}^2 \rangle \sim (m_2/m_1)$ (see Sec. 3.2.2). This yields

$$\sigma_{\mathcal{E}1}^2 \sim \langle e_{1,\text{ej}}^2 \rangle / (2P_{1,0}b^2). \quad (3.54)$$

We would like to know what are the mean, variance and distributions of $\mathcal{E}_a(t)$ given the initial conditions and parameters. Note that the value of $\mathcal{E}_a(t)$ at ejection is not the ultimate quantity of interest here, since planet a still undergoes secular coupling with planet 1 after ejection. Our final goal is to derive the expectation, and if possible the distribution of $\mathcal{E}_{a,\infty}$.

To proceed, note that Eq. (3.48), with $\mathcal{E}_1(t) = Z(t)$, has the solution

$$\mathcal{E}_a(t) = -i\nu_{a1} e^{i\omega_a t} \int_0^t e^{-i\omega_a s} Z(s) ds, \quad (3.55)$$

where we have assumed $\mathcal{E}_a(0) = 0$. The statistical property of $\mathcal{E}_a(t)$ as determined by Eq. (3.55) depends on whether the final value of $\mathcal{E}_1(t_{\text{ej}}) = \mathcal{E}_{1,\text{ej}}$ is known (empirically measured, or otherwise constrained by conservation laws). If $\mathcal{E}_{1,\text{ej}}$ is unconstrained, then $Z(s)$ is the classic 2-D Brownian motion. If $\mathcal{E}_{1,\text{ej}}$ is known *a priori*, then $Z(s)$ is not a Brownian motion but rather a Brownian bridge, which is given by a different density distribution that has a reduced variance towards the end of the stochastic process. We consider both cases below. In this study, since the final values of perturber properties are known, case 2 is the more appropriate one. We deal with case 1 first as a stepping stone.

Case 1: Unknown $\mathcal{E}_{1,\text{ej}}$

We study the expected value and distribution of \mathcal{E}_a at the time of ejection, $\mathcal{E}_{a,\text{ej}} = \mathcal{E}_a(t_{\text{ej}})$. First, since $\langle Z(s) \rangle = 0$ for all s , the integral in Eq. (3.55) has expectation $\langle \mathcal{E}_a(t) \rangle = 0$

for all t . The variance and covariances of interest can be computed using the linearity of expectation. The variance of the final eccentricity is given by (see Appendix C)

$$\langle |\mathcal{E}_{a,\text{ej}}|^2 \rangle = 4 \left(\frac{\nu_{a1}}{\omega_a} \right)^2 \left[1 - \frac{\sin(\omega_{a1} t_{\text{ej}})}{\omega_{a1} t_{\text{ej}}} \right] \sigma_{\mathcal{E}1}^2 t_{\text{ej}}, \quad (3.56)$$

while the covariance between the final eccentricity and its forced amount (see Eq. 3.50) is

$$\langle \text{Re}(\mathcal{E}_{a,\text{ej}} \mathcal{E}_{a,\text{forced}}^*) \rangle = 2 \left(\frac{\nu_{a1}}{\omega_{a1}} \right)^2 \left[1 - \frac{\sin(\omega_{a1} t_{\text{ej}})}{\omega_{a1} t_{\text{ej}}} \right] \sigma_{\mathcal{E}1}^2 t_{\text{ej}}. \quad (3.57)$$

The expectation of the forced eccentricity is

$$\langle |\mathcal{E}_{a,\text{forced}}|^2 \rangle = 2 \left(\frac{\nu_{a1}}{\omega_a} \right)^2 \sigma_{\mathcal{E}1}^2 t_{\text{ej}}. \quad (3.58)$$

From Eqs. (3.52)-(3.54), the RMS eccentricity of planet a is

$$\langle |\mathcal{E}_{a,\infty}|^2 \rangle = 4 \left(\frac{\nu_{a1}}{\omega_a} \right)^2 \sigma_{\mathcal{E}1}^2 t_{\text{ej}} \sim \frac{25 a_a^2 \langle e_{1,\text{ej}} \rangle^2 N_{\text{ej}}}{8 a_1^2 b^2}. \quad (3.59)$$

We see that $\langle |\mathcal{E}_{a,\infty}|^2 \rangle \propto N_{\text{ej}}$. However, in this unconstrained case, it is also the case that $|\mathcal{E}_{a,\text{forced}}|^2 \propto N_{\text{ej}}$, so that the scaling for the boost factor is $\gamma_e = \text{const.}$, which is contrary to our empirical results. This contradiction arises because we have not taken into account the fact that $\mathcal{E}_{1,\text{ej}}$ is a known quantity and not a random variable. Only when we place a constraint on the Brownian motion at t_{ej} can the desired scaling be derived.

Case 2: $\mathcal{E}_{1,\text{ej}}$ is known or constrained

When the final value of \mathcal{E}_1 at $t = t_{\text{ej}}$ is known, the evolution $\mathcal{E}_a(t)$ is qualitatively similar, but the statistical properties change due to the Brownian motion in \mathcal{E}_1 being “tied down” at the final time, giving it a lower variance. To recognise that this process is different from an unconstrained Brownian motion, we label it $B(t)$ instead of $Z(t)$. At $t = 0$, we have $\mathcal{E}_1 = B(0) = 0$, while at $t = t_{\text{ej}}$, $\mathcal{E}_1 = B(t_{\text{ej}}) = \mathcal{E}_{1,\text{ej}}$. In between this time,

$B(t)$ executes a (complex) Brownian motion and is normally distributed, with mean and variance (Borodin and Salminen, 2002)

$$\langle B(t) \rangle = \left(\frac{t}{t_{\text{ej}}} \right) \mathcal{E}_{1,\text{ej}} \quad (3.60)$$

$$\text{Var}[B(t)] \equiv \langle B^2(t) \rangle - \langle B(t) \rangle^2 = \frac{2t(t_{\text{ej}} - t)\sigma_{\mathcal{E}1}^2}{t_{\text{ej}}}. \quad (3.61)$$

Another relevant quantity is the covariance of a Brownian bridge with itself at a different time, which (without loss of generality, assuming $s < t$) is given by

$$\text{Cov}[B(s), B(t)] \equiv \langle B(s)B^*(t) \rangle = \frac{2s(t_{\text{ej}} - t)\sigma_{\mathcal{E}1}^2}{t_{\text{ej}}}. \quad (3.62)$$

We can now calculate the expectation of $\mathcal{E}_{a,\text{ej}}$. Unlike the unconstrained case, the mean is non-zero:

$$\langle \mathcal{E}_{a,\text{ej}} \rangle = i\mathcal{E}_{1,\text{ej}} \left(\frac{\nu_{a1}}{\omega_{a1}} \right) \left(\frac{e^{i\omega_{a1}t_{\text{ej}}} - i\omega_{a1}t_{\text{ej}} - 1}{\omega_{a1}t_{\text{ej}}} \right), \quad (3.63)$$

and the square of the mean eccentricity is

$$|\langle \mathcal{E}_{a,\text{ej}} \rangle|^2 = \left(\frac{\nu_{a1}}{\omega_{a1}} \right)^2 |\mathcal{E}_{1,\text{ej}}|^2 \times \left[1 + 2 \left(\frac{1 - \cos(\omega_{a1}t_{\text{ej}}) - \omega_{a1}t_{\text{ej}} \sin(\omega_{a1}t_{\text{ej}})}{\omega_{a1}^2 t_{\text{ej}}^2} \right) \right]. \quad (3.64)$$

The variance of the eccentricity is given by

$$\langle |\mathcal{E}_{a,\text{ej}}|^2 \rangle - |\langle \mathcal{E}_{a,\text{ej}} \rangle|^2 = 2\sigma_{\mathcal{E}1}^2 \left(\frac{\nu_{a1}}{\omega_{a1}} \right)^2 t_{\text{ej}} \left[1 - 2 \left(\frac{1 - \cos(\omega_{a1}t_{\text{ej}})}{\omega_{a1}^2 t_{\text{ej}}^2} \right) \right]. \quad (3.65)$$

In order to know the final RMS eccentricity $\mathcal{E}_{a,\infty}$, we also require the covariance between $\mathcal{E}_{a,\text{ej}}$ and $\mathcal{E}_{a,\text{forced}}$, which is given by

$$\langle \text{Re}(\mathcal{E}_{a,\text{ej}} \mathcal{E}_{a,\text{forced}}^*) \rangle = |\mathcal{E}_{a,\text{forced}}|^2 \left[\frac{\cos(\omega_{a1}t_{\text{ej}}) - 1}{\omega_{a1}t_{\text{ej}}} \right]. \quad (3.66)$$

Combining these expressions with Eq. (3.52), the RMS eccentricity at infinity is given by

$$\begin{aligned} \langle |\mathcal{E}_{a,\infty}|^2 \rangle = & 2 \left(\frac{\nu_{a1}}{\omega_{a1}} \right)^2 \left(\sigma_{\mathcal{E}1}^2 t_{\text{ej}} \left[1 - 2 \left(\frac{1 - \cos(\omega_{a1} t_{\text{ej}})}{\omega_{a1}^2 t_{\text{ej}}^2} \right) \right] \right. \\ & \left. + |\mathcal{E}_{1,\text{ej}}|^2 \left[\frac{3}{2} + \frac{1 - \cos(\omega_{a1} t_{\text{ej}}) - \sin(\omega_{a1} t_{\text{ej}})}{\omega_{a1} t_{\text{ej}}} + \frac{1 - \cos(\omega_{a1} t_{\text{ej}})}{\omega_{a1}^2 t_{\text{ej}}^2} \right] \right). \end{aligned} \quad (3.67)$$

In the above equation, when $\omega_{a1} t_{\text{ej}} \ll 1$, the second term of the RHS dominates and we have $|\mathcal{E}_{a,\infty}|^2 \propto t_{\text{ej}}$. On the other hand, when $\omega_{a1} t_{\text{ej}} \gg 1$, the first term dominates and we also have $|\mathcal{E}_{a,\infty}|^2 \propto t_{\text{ej}}$. In order words, for all t_{ej} we have $\langle |\mathcal{E}_{a,\infty}|^2 \rangle \propto t_{\text{ej}}$, in agreement with our numerical results. Since $e_{a,\text{sec}}^2 = 2|\mathcal{E}_{a,\text{forced}}|^2$, the ensemble RMS of the boost factor $\langle \gamma_e^2 \rangle$ is given by

$$\begin{aligned} \langle \gamma_e^2 \rangle = & \frac{\langle |\mathcal{E}_{a,\infty}|^2 \rangle - 2|\mathcal{E}_{a,\text{forced}}|^2}{2|\mathcal{E}_{a,\text{forced}}|^2} \simeq Ax \left[1 - 2 \left(\frac{1 - \cos(x)}{x^2} \right) \right] \\ & + \frac{1 - \cos(x) - \sin(x)}{x} + \frac{1 - \cos(x)}{x^2} + \frac{1}{2}, \end{aligned} \quad (3.68)$$

where we have defined $x \equiv \omega_a t_{\text{ej}} \sim 2\pi N_{\text{ej}}/N_{\text{sec}}$, and A is the dimensionless constant

$$A \equiv \frac{\sigma_{\mathcal{E}1}^2}{\omega_{a1} |\mathcal{E}_{1,\text{ej}}|^2} \sim \frac{1}{\omega_{a1} b^2 P_{1,0}} \sim 2\pi \left(\frac{\langle N_{\text{ej}} \rangle_{\text{HM}}}{N_{\text{sec}}} \right), \quad (3.69)$$

and $\langle N_{\text{ej}} \rangle_{\text{HM}} = b^2$ (Eq. 3.24) is the harmonic mean of N_{ej} . Here we have made use of the fact that the final eccentricity is well constrained by conservation laws, so $\langle e_{1,\text{ej}} \rangle^2 \approx |\mathcal{E}_{1,\text{ej}}|^2$.

Eq. (3.68) has two regimes: when $x \ll 1$, $\gamma_e \simeq \sqrt{x/2}$, while when $x \gg 1$, we have $\gamma_e \simeq \sqrt{Ax}$. The transition between the two regimes occurs when $x \sim \pi$. Using our earlier estimates for b (Eq. 3.24), A is of order

$$A \sim 7 \left(\frac{m_1}{M_\star} \right) \left(\frac{a_a}{a_1} \right)^{-3/2} \left(1 + \frac{m_2}{m_1} \right)^4 \left(\frac{a_{1,0}}{a_{2,0}} \right)^{-2}. \quad (3.70)$$

For the typical range of parameters relevant to Kepler planets ($m_1 \sim 10^{-3}$ and $a_a/a_1 \sim 1/10$) one obtains $A \sim 0.3$. Given the inherent scatter in the simulation results, the

difference between the two regimes in Eq. (3.68) is too subtle for us to empirically measure A in this study. Thus in this paper we simply adopt the approximation $\gamma_e \sim \sqrt{N_{\text{ej}}/N_{\text{sec}}}$ which agrees well with the empirical results.

Having computed the mean value $\langle \gamma_e^2 \rangle$ we now comment on its distribution. The Brownian bridge has a distribution that is normally distributed over an ensemble of simulations, and any linear transformation of normally distributed variables is also normally distributed. From Eq. (3.44) and Eq. (3.52), the boost factor can be written as

$$\gamma_e^2 = \frac{\left| |\mathcal{E}_{a,\text{ej}}|^2 - 2\text{Re}(\mathcal{E}_{a,\text{ej}}\mathcal{E}_{a,\text{forced}}^*) \right|}{|\mathcal{E}_{a,\text{forced}}|^2}. \quad (3.71)$$

The quantities $\mathcal{E}_{a,\text{ej}}$ and $\mathcal{E}_{a,\text{forced}}$ are normally distributed complex variables with zero mean. In the limit that $N_{\text{ej}} \gg N_{\text{sec}}$, we have that $|\mathcal{E}_{a,\text{ej}}|^2 \gg 2\text{Re}(\mathcal{E}_{a,\text{ej}}\mathcal{E}_{a,\text{forced}}^*)$, and γ_e is then the length of a 2-D vector whose components are normally distributed with zero mean; such a quantity has approximately a Rayleigh distribution. We define $\bar{\gamma}_e \equiv \langle \gamma_e^2 \rangle^{1/2}$ (see Eq. 3.68), then the distribution of γ_e in this limit is given by

$$f(\gamma_e) = \frac{\gamma_e}{\bar{\gamma}_e^2} \exp\left(\frac{-\gamma_e^2}{2\bar{\gamma}_e^2}\right). \quad (3.72)$$

Empirically, we find that Eq. (3.72) is a good approximation for the distribution of γ_e even when it is not the case that $N_{\text{ej}} \gg N_{\text{sec}}$.

3.4.3 Inclination Evolution

In the above analysis we have considered the eccentricity evolution of planet a subject to a stochastic forcing by the outer perturber. The evolution of the inclination can be derived in the same manner as the eccentricity, except, whenever appropriate, replacing the complex eccentricities \mathcal{E} with the corresponding complex inclinations \mathcal{I} , and replacing

$\omega_{a1} \rightarrow -\omega_{a1}$ and $\nu_{a1} \rightarrow -\omega_{a1}$. The forced inclination is given by Eq. (3.41). One will eventually find that the scaling for γ_e and γ_θ is the same:

$$\langle \gamma_e^2 \rangle = \langle \gamma_\theta^2 \rangle. \quad (3.73)$$

In addition, the probability density distribution for γ_θ is also the same as γ_e , and is given by Eq. (3.72) (note that $\bar{\gamma}_e = \bar{\gamma}_\theta$). Since γ_e , γ_θ have the same distribution, and $\bar{\gamma}_e = \bar{\gamma}_\theta$, we hereafter refer to the distribution of either quantity as γ (although note that γ_e and γ_θ are uncorrelated and independently distributed).

Having computed the distribution of θ_a , we now derive the boost factor for the mutual inclination $\gamma_{\theta,a1}$. We have that

$$\begin{aligned} \theta_{a1,\infty}^2 &= \theta_{a1,\text{sec}}^2 = |\mathcal{I}_{a,\text{ej}} - \mathcal{I}_{1,\text{ej}}|^2 \\ &= |\mathcal{I}_{a,\text{ej}}|^2 + |\mathcal{I}_{1,\text{ej}}|^2 - 2\text{Re}(\mathcal{I}_{a,\text{ej}}\mathcal{I}_{1,\text{ej}}^*). \end{aligned} \quad (3.74)$$

From Eq. (3.52) (but replacing $\mathcal{E} \rightarrow \mathcal{I}$), we thus have that

$$\theta_{a1,\infty}^2 = \theta_{a,\infty}^2 - \theta_{1,\text{ej}}^2. \quad (3.75)$$

Recall that $\theta_{a1,\text{sec}} = \theta_{a,\text{sec}} / \sqrt{2}$, thus from Eq. (3.45) - (3.46) we find

$$\gamma_{\theta,a1} = \sqrt{2}\gamma_\theta. \quad (3.76)$$

The above equation assumes that θ_{a1} , $\theta_a \ll 1$ and ignores the contribution from planet 2. In reality, $\gamma_{\theta,a1}$ will deviate from Eq. (3.76), although the above scaling still holds on average. Once we know the value of γ_θ , we can convert it to the corresponding value of $\gamma_{\theta,a1}$ to obtain the mutual inclination boost factor, and vice versa.

3.4.4 Marginal Distribution of the Boost Factor

The distributions we have derived so far for γ_e , γ_θ are contingent on N_{ej} , which is not an observable quantity. However, since we have some understanding of the distribution

of N_{ej} , we can now marginalize over it and only deal with observable quantities. First, combining Eq. (3.19) and Eq. (3.72) we can write the joint distribution for N_{ej} and γ as

$$f(N_{\text{ej}}, \gamma) = \frac{b\gamma}{\bar{\gamma}^2 \sqrt{2\pi N_{\text{ej}}^3}} \exp\left(\frac{-b^2}{2N_{\text{ej}}}\right) \exp\left(\frac{-\gamma^2}{2\bar{\gamma}^2}\right). \quad (3.77)$$

Now, from Eq. (3.47) we have that $\bar{\gamma}^2 \sim N_{\text{ej}}/N_{\text{sec}}$. Substituting into Eq. (3.77), and integrating over N_{ej} we thus obtain the distribution for γ in terms of observable quantities only:

$$\begin{aligned} f(\gamma) &= \int_0^\infty b\gamma N_{\text{sec}} \sqrt{\frac{1}{2\pi N_{\text{ej}}^5}} \exp\left(\frac{-b^2 - \gamma^2 N_{\text{sec}}}{2N_{\text{ej}}}\right) dN_{\text{ej}} \\ &= \frac{b\gamma N_{\text{sec}}}{(b^2 + N_{\text{sec}}\gamma^2)^{3/2}}. \end{aligned} \quad (3.78)$$

Now, if we define $y \equiv \gamma \sqrt{N_{\text{sec}}/\langle N_{\text{ej}} \rangle_{\text{HM}}}$ (recall that $b^2 = \langle N_{\text{ej}} \rangle_{\text{HM}}$), then we have the rather elegant expression for the scaled boost factor y :

$$f(y) = \frac{y}{(1 + y^2)^{3/2}}. \quad (3.79)$$

Just like the distribution for N_{ej} (Eq. 3.19), the distribution $f(y)$ is a long-tailed one, such that all its higher moments (e.g. mean, variance) fail to exist. Its mode occurs at $y = 1/\sqrt{2}$, its geometric mean is $\langle y \rangle_{\text{GM}} = 2$, its harmonic mean is $\langle y \rangle_{\text{HM}} = 1$ and its median is $y = \sqrt{3}$. The 68% and 95% confidence intervals are $y \in [0.65, 6.2]$ and $y \in [0.23, 40]$ respectively. Assuming that $a_{2,0} \sim a_{1,0}$, the harmonic mean of γ is given by the following scaling:

$$\langle \gamma \rangle_{\text{HM}} = \sqrt{\langle N_{\text{ej}} \rangle_{\text{HM}}/N_{\text{sec}}} \sim 1.1 \left(\frac{m_1}{M_\star}\right)^{-1/2} \left(\frac{a_a}{a_{1,0}}\right)^{3/4} \left(1 + \frac{m_2}{m_1}\right)^2. \quad (3.80)$$

Note that this scaling applies equally to γ_e and γ_θ . Thus, we see that the effect of CJ scatterings on inner planets is the greatest if the CJ scatters are lower in mass, have semi-major axes more comparable to the inner planets, and have comparable masses.

In Fig. 3.15 we show a comparison between our theoretical distribution given by Eq. (3.79) for the normalized eccentricity boost factor y_e and the empirical distribution

from our suite of simulations. We find that for $m_2/m_1 \lesssim 1/3$, the theoretical distribution agrees well with the empirical one over a range of different masses and a_a/a_1 . The empirical distribution starts to deviate somewhat from Eq. (3.79) for more comparable masses: in particular, the distribution becomes even more heavy-tailed, with significant fraction having $y \gg 1$, although the empirical mode and harmonic mean still agreed with Eq. (3.80) to within a factor of a few.

3.4.5 Theoretical Model: Simplifications and Refinements

In developing our stochastic model for “1+2” scattering, we have made several simplifying assumptions. A more careful treatment can yield refinements to the model and more accurate estimates for the distribution of final parameters. We discuss the most crucial simplifications and suggest possible ideas for refinement below.

- **Secular forcing by planet 2:** In our theoretical model we have ignored the secular interaction between the inner planet and planet 2 as it is being ejected from the system. This can be justified in the limit that $m_2/m_1 \ll 1$. However, for more comparable masses, m_2 can have an equal or even greater effect than m_1 on the secular evolution of the inner system. Our simplification of ignoring planet 2 is the main reason why our estimate from Eq. (3.68) becomes less accurate when $m_2 \sim m_1$. Since at the end of the ejection process, the secular forcing by m_2 vanishes, one way to incorporate the influence of m_2 is to absorb it into the variance of the Brownian bridge, i.e. by replacing $\sigma_{\mathcal{E}1} \rightarrow \sigma_{\mathcal{E}1}(1 + \varepsilon_{12})$, where ε_{12} is a dimensionless ratio that depends on m_2/m_1 (and possibly other quantities) that accounts for the added effect of secular perturbations by m_2 .

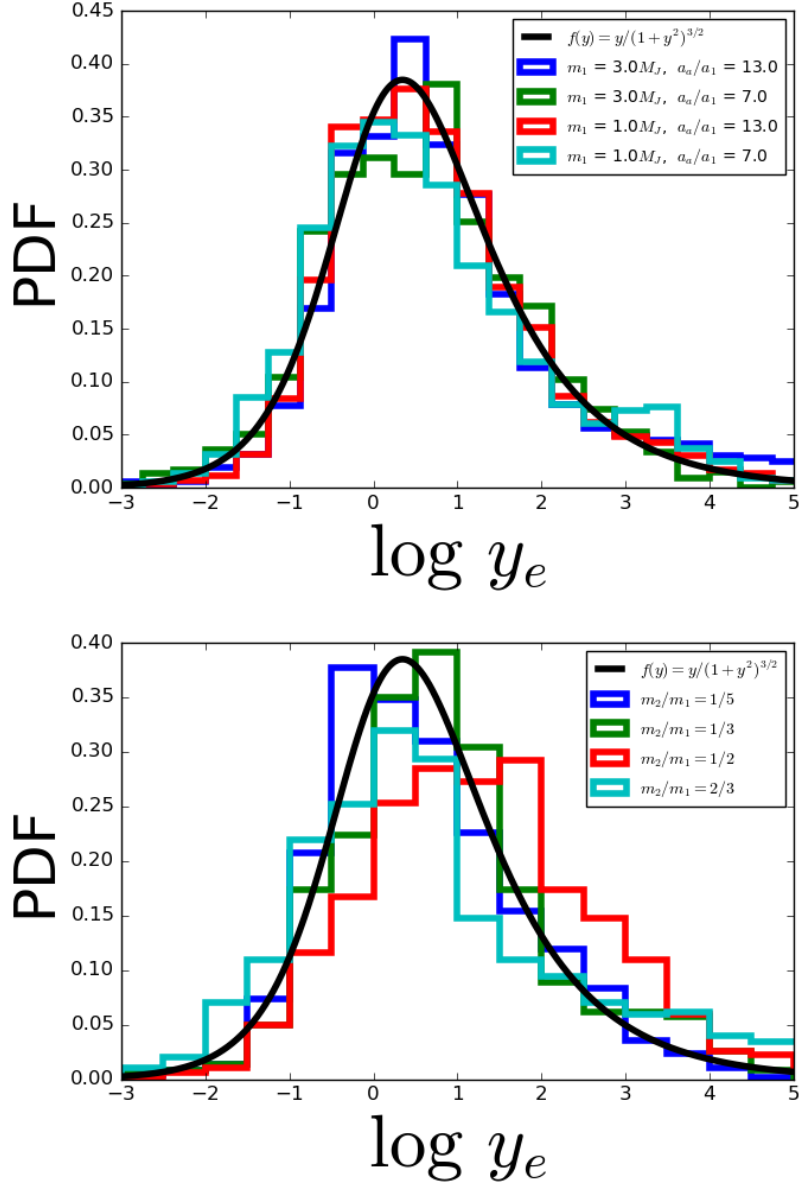


Figure 3.15: Distribution of $y_e \equiv \gamma_e \sqrt{N_{\text{sec}}/\langle N_{\text{ej}} \rangle_{\text{HM}}}$ (see Sec. 3.4.4). The histograms are empirical distributions obtained from our simulations, while the black line is the theoretical distribution given by Eq. (3.79) - (3.80). On the top panel, $m_2/m_1 = 1/5$ while m_1 and a_a/a_1 varies as shown in the legend. On the bottom panel, $a_a/a_1 = 1/10$ and $m_1 = 1 M_J$, while m_2/m_1 varies as shown in the legend.

- **Linearity in \mathcal{E} , \mathcal{I} :** In our theoretical model we have assumed that the secular evolution in eccentricity and inclination is linear. Note however that our hybrid algorithm (Sec. 3.3) allows for the possibility of larger growths in eccentricity due to non-linear Lidov-Kozai oscillations, and that such oscillations are indeed possible when θ_a grows to large values. Unfortunately differential equations with such stochastic terms become intractable when stochasticity is involved, and one would have to resort to numerical integrations in this regime.
- **Constancy of a_1 :** In our theoretical model we have also assumed that a_1 (and therefore ω_a , ν_{a1}) is constant, which is approximately the case when $m_2 \ll m_1$ but breaks down at more comparable mass ratios. In reality, a_1 changes randomly as a_2 undergoes strong scatterings, and its final value can decrease by as much as $a_{1,\text{ej}}/a_{1,0} = 1/2$ in the limit that $m_2 = m_1$. There are two ways to refine our model to incorporate this: First, one can absorb the stochastic changes in ν_{a1} as additional variance in $\sigma_{\mathcal{E}1}$, i.e. by replacing $\sigma_{\mathcal{E}1} \rightarrow \sqrt{\sigma_{\mathcal{E}1}^2 + \sigma_{\nu1}^2}$, where $\sigma_{\nu1}^2$ is the RMS change in ν_{a1} per unit time. In addition, one should replace ω_a with its expectation, i.e.

$$\langle \omega_a(t) \rangle = \omega_{a,0} + (\omega_{a,\text{ej}} - \omega_{a,0})(t/t_{\text{ej}}). \quad (3.81)$$

The above addition still allows for an analytic estimate for the final eccentricity and inclination, while incorporating the non-constancy of a_1 , although the resulting final expressions are much less elegant.

3.5 Extension to More Inner Planets

Having understood the dynamics of “1+2” scattering we now generalize our results to the case with more than one inner planets. The parameter space is vast when additional

planets are considered, but as we shall demonstrate, the universal scalings given by Eqs. (3.47) and (3.79) - (3.80) remain valid.

3.5.1 Two inner planets

For each of our N-body simulations, we consider inner systems with $a_a = a_1/20$ and $a_b = 1.5a_a$, and $m_a = m_b = 3M_\oplus$. The initial eccentricities and inclinations of the inner planets are set to zero. In our simulations, the inner planets effect each other secularly, and are influenced by the outer perturbers through secular interactions, as described by Sec. 3.3.

For systems with 2 inner planets and an external perturber, the dynamics of the system depends crucially on the dimensionless coupling parameter ϵ_{ab} (Lai and Pu, 2017; Pu and Lai, 2018), given by

$$\epsilon_{ab} \equiv \frac{\omega_{b1} - \omega_{a1}}{\omega_{ab} + \omega_{ba}} \approx \left(\frac{m_1}{m_b}\right) \left(\frac{a_b}{a_1}\right)^3 \left[\frac{3a_a/a_b}{b_{3/2}^{(1)}(a_a/a_b)} \right] \frac{(a_b/a_a)^{3/2} - 1}{1 + (L_a/L_b)}, \quad (3.82)$$

where $L_i \equiv m_i \sqrt{GM_\star a_i}$ is the circular angular momentum of the planet, and $b_{3/2}^{(1)}(a_a/a_b)$ is the Laplace coefficient given by Eq. (3.35).

In the parameter regime that we study in this work, the two inner planets are invariably in the “strong coupling” regime ($\epsilon_{ab} \ll 1$). In this limit, assuming initially circular and co-planar orbits for planets a and b , the “secular” eccentricities and mutual inclinations

are given by (see Pu and Lai, 2018)

$$e_{a,\text{sec}} = \sqrt{2} \left(\frac{\nu_{a1}\omega_b + \nu_{ab}\nu_{b1}}{\omega_a\omega_b - \nu_{ab}\nu_{ba}} \right) e_{1,\text{ej}}, \quad (3.83)$$

$$e_{b,\text{sec}} = \sqrt{2} \left(\frac{\nu_{b1}\omega_a + \nu_{ba}\nu_{a1}}{\omega_a\omega_b - \nu_{12}\nu_{21}} \right) e_{1,\text{ej}}, \quad (3.84)$$

$$\theta_{a1,\text{sec}} = \theta_{b1,\text{sec}} \approx \theta_{1,\text{ej}}, \quad (3.85)$$

$$\theta_{ab,\text{sec}} = 2 \left(\frac{\omega_{a1} - \omega_{b1}}{\sqrt{(\omega_a - \omega_b)^2 + 4\omega_{ab}\omega_{ba}}} \right) \theta_{1,\text{ej}}, \quad (3.86)$$

where $\omega_a = \omega_{ab} + \omega_{a1}$ and $\omega_b = \omega_{ba} + \omega_{b1}$ respectively. From these “secular” values, we compute the values of $\gamma_{e,a}$, $\gamma_{e,b}$ and $\gamma_{\theta,ab}$ analogous to Sec. 3.4.1. We show the results of our simulations in Figs. 3.16 - 3.17. We see that in the “2+2” case the boost factor is still consistent with the scaling law Eq. (3.47), even though the values of ω_a , ω_b and the forced eccentricities and inclinations are given by very different expressions.

3.5.2 3 or More Inner Planets

Having briefly studied the “2+2” scattering we make some remarks on extending our theory to systems with 3 or more inner planets. The numerical algorithm described in Sec. 3.3 works for a general number of inner (and outer) planets, so long as the inner and outer systems are sufficiently detached that the outer planets do not come in close contact with the inner planets. However, the theoretical model in Sec. 3.4.2, and in particular Eq. (3.68) must be modified if there are additional of more inner planets, due to the more complex secular coupling between the inner planets. In particular, one should deal with the amplitudes of the planet eccentricity and inclination secular eigenmodes, and the secular precession frequency should be replaced with the mode frequencies. The (complex) eigenmode amplitude of the α -th mode should scale as

$$\mathcal{E}_{\alpha,\text{ej}} \propto \mathcal{I}_{\alpha,\text{ej}} \propto \sqrt{N_{\text{ej}}/N_{\alpha,\text{sec}}}, \quad (3.87)$$

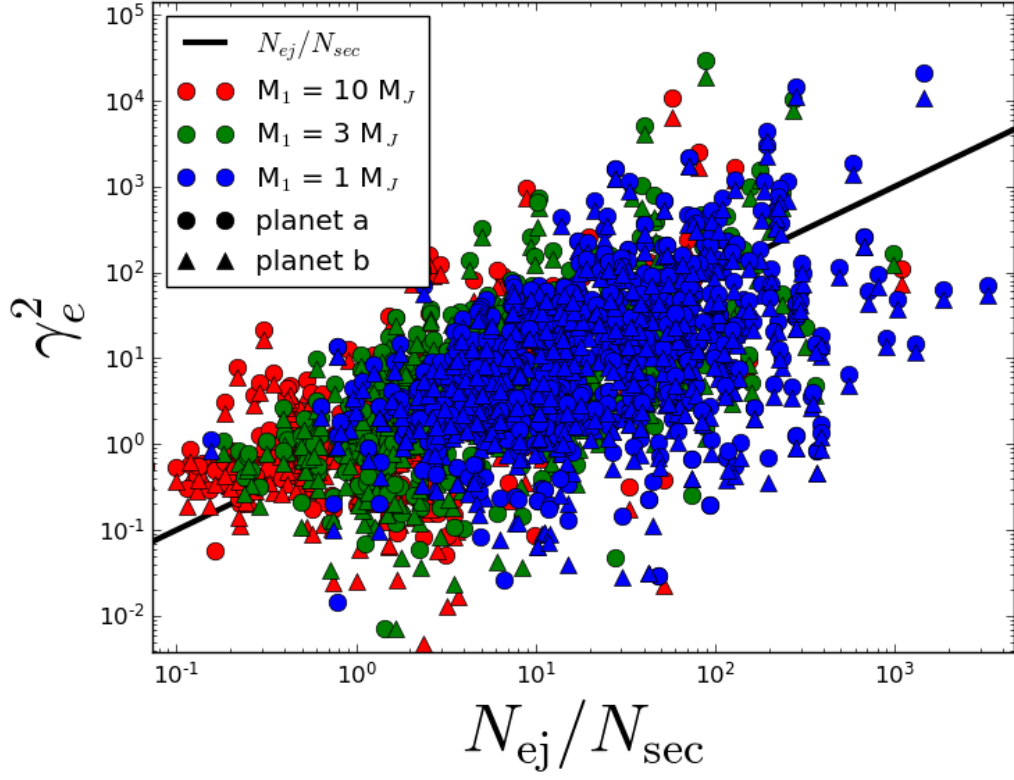


Figure 3.16: Similar to Fig. 3.10, except with 2 inner planets. We have $m_a = m_b = 3M_\oplus$, $a_a = a_1/20$ and $a_b = 1.5a_a$, while m_1 varies as shown on the plot legend and $m_2 = m_1/5$. The boost factor for the first inner planet $\gamma_{e,a}$ corresponds to the filled circles, while that for the second inner planet is shown as filled triangles.

where $\mathcal{E}_{\alpha, \text{ej}}$, $\mathcal{I}_{\alpha, \text{ej}}$ are the complex amplitude of the α -th eccentricity and inclination eigenmodes respectively, and

$$N_{\alpha, \text{sec}} \equiv \left(\frac{\omega_{\alpha, 0} P_{1, 0}}{2\pi} \right)^{-1}, \quad (3.88)$$

where $\omega_{\alpha, 0}$ is the initial eigenfrequency of the α -th eigenmode. An empirical test of the above scaling is beyond the scope of this work, but is promising ground for further research.

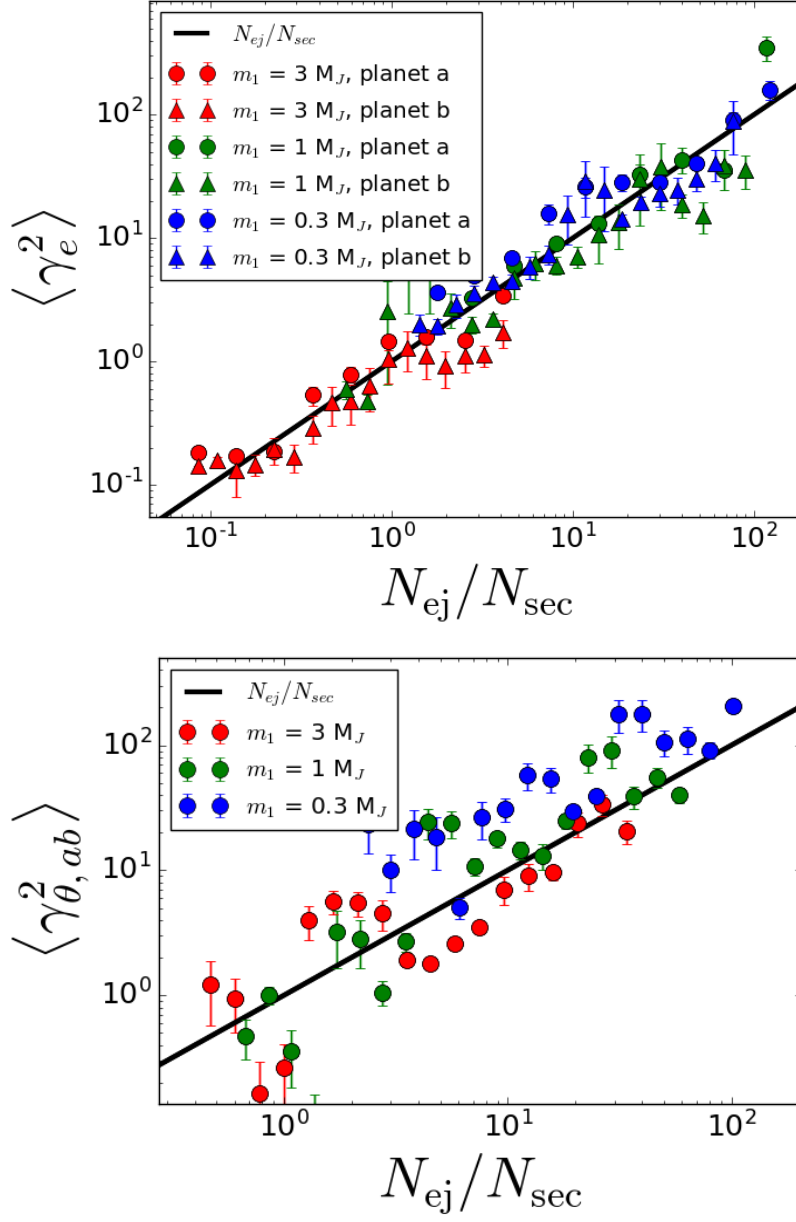


Figure 3.17: Similar to Fig. 3.14, except the simulations have two inner planets. The system parameters are the same as those for Fig. 3.16. The top panel shows the eccentricity boost factor γ_e^2 while the bottom panel show the mutual inclination boost factor $\gamma_{\theta,ab}^2$.

3.6 Summary and Discussion

3.6.1 Summary

In this work we have studied CJ scatterings and their effect on inner planet systems. The main results of this work are summarized below.

- **Final outcome of CJ scattering:** We have re-examined final outcomes of strong scatterings between two CJs on gravitationally unstable orbits. At the semi-major axis of a few au or larger, the most likely outcome of such scatterings is ejection of the less massive planet (see also Li et al., 2020). The remaining planet, which we call planet 1, has a final semi-major axis that is consistent with orbital energy conservation. The final eccentricity and inclination of the planet is $e_{1,\text{ej}} \sim 0.7m_2/m_1$ and $\theta_{1,\text{ej}} \sim 0.7\theta_{2,0}m_2/m_1$ for $m_2/m_1 \lesssim 0.5$, where m_2 is the mass of the ejected planet and $\theta_{2,0}$ is the initial mutual inclination of the two planets.
- **Ejection timescale:** The timescale from the first planet-planet Hill sphere crossing to the final ejection of planet 2 can be understood as the stopping time of a Brownian motion. We empirically measure the normalized dimensionless RMS energy exchange ($|\delta E_{12}/E_{2,0}|$) per pericenter passage b over an ensemble of N-body simulations, and present a best-fit law for it in Eq. (3.24). Given b , the distribution of N_{ej} (the number of orbits of m_2 prior to ejection) agrees well with Eq. (3.19).
- **Minimum a_2 of ejected planet:** We find that the possible values of a_2 during the strong scattering and ejection is constrained by energy conservation, angular momentum conservation, and the requirement that the system cannot spontaneously

scatter itself into an indefinitely stable state. Fig. 3.7 shows our empirical results for the minimum value of a_2 and r_2 over the course of ejection. We find that generally, $a_{2,\min} \sim a_{1,0}/2$, and for $m_2/m_1 \ll 1$ we have $r_{2,\min} \sim a_{1,0}/4$, although $r_{2,\min}$ decreases strongly as m_2/m_1 increases.

- **“1+2” Scattering - Numerical Results:** For well-separated inner super-Earth and outer CJ systems, the effect of CJ scatterings on the inner planet is secular. We develop a hybrid algorithm to simulate such systems efficiently, by computing two CJ scatterings and then simulating their effects on the inner planet via. secular evolution. We have performed such numerical integrations for “1+2” systems over a wide range of parameters. We find that the eccentricity and inclination of the inner planet induced by CJ scatterings can be much larger than the secular values (Eqs. 3.40 - 3.41) generated by the remaining giant planet, and the enhancement increases with N_{ej} (see Figs. 3.8 - 3.9). Despite diversity of initial parameters and final outcomes, the dynamics of the system can be succinctly summarized by the dimensionless “boost” factor γ (Eqs. 3.44 - 3.45). In the range of parameters we considered we find that Eq. (3.47) provided an universal scaling law for the final eccentricity and inclination of the inner planet, as a function of the system parameters (see Figs. 3.10 - 3.14).
- **“1+2” scattering - Theoretical model:** We develop a theoretical model to explain the empirical scaling law in Eq. (3.47), by modelling the “1+2” scattering process as a linear stochastic differential equation. We compute analytically the expected moments and distributions for the final inner planet eccentricity and inclination in terms of the boost factors, which are given by Eqs. (3.68) - (3.72). We calculate the distribution of γ , averaged over all possible N_{ej} , to derive a universal distribution function for the boost factor in terms of observable quantities only (Eq. 3.79); this analytical distribution agrees well with empirical results (see Fig. 3.15).

- **Extension to “2+2” systems:** We have extended our empirical investigation to “2+2” systems. We find that analogous to “1+2” systems, Eq. (3.47) is still valid for describing the dynamics of the system, although the final values of eccentricities and inclinations are substantially different due to strong secular coupling between the inner planets. We also describe how the theoretical model in Sec. 3.4.2 can be extended to inner systems with 3 or more planets.

3.6.2 Caveats

In our analysis we have considered the “clean” cases. Several important physical effects were neglected, and we comment on them below.

- **Physical collisions between CJs:** We have assumed that all scatterings between CJs resulted in ejection of the less massive planet. A small fraction of systems will undergo collisional mergers instead. If the final values of e_1 , θ_1 are known, then our theoretical model in Sec. 3.4.2 applies equally to systems that result in collisions and ejections. However, the collisional case is far less interesting, because the collisional timescale tends to be much shorter due to collisional probabilities being highest at the initial time when planet eccentricities are low (Nakazawa et al., 1989; Ida and Nakazawa, 1989). In addition, the final eccentricity e_1 and inclination θ_1 of the merger product tend to be low, due to collisions between CJs being highly inelastic (see Li et al., 2020). Typically, one can assume that the scattering history is unimportant for systems that result in collisions (i.e. the boost factor $\gamma \ll 1$).
- **Spin-orbit coupling:** We have neglected the coupling between the planets and stellar spin. In reality, the stellar spin and the inner planets can exchange angular

momentum, resulting in rich and complex behavior (see, e.g. Lai et al., 2018), which can change the inclination of the inner planet. Incorporating such evolution into our theoretical model is beyond the scope of this work, but is a promising area for future study.

- **Short-range forces:** In this study we assumed that the inner planets are effected by secular forces from other planets only. In particular, we have ignored the effects of short-ranged forces, such as general relativistic (GR) apsidal precession, tidal precession, and tidal dissipation (a discussion for the relative importance of these effects is given in Pu and Lai, 2019). The most important such effect is GR apsidal precession, whose angular frequency (in the limit that $e_j \ll 1$)

$$\omega_{j,\text{GR}} = \frac{3GM_\star}{c^2 a_j} n_j \approx 6 \times 10^{-6} \left(\frac{M_\star}{M_\odot} \right)^{3/2} \left(\frac{a_j}{0.1 \text{ au}} \right)^{-5/2} \text{ yr}^{-1}. \quad (3.89)$$

The main effect of this additional precession is to suppress eccentricity generation. We define $\epsilon_{j1,\text{GR}}$ as the ratio between $\omega_{j,\text{GR}}$ and the apsidal precession frequency due to secular coupling (between planets j and 1):

$$\epsilon_{j1,\text{GR}} \equiv \frac{\omega_{j,\text{GR}}}{\omega_{j1}} = \frac{3GM_\star^2 a_1^3}{a_j^4 c^2 m_1}. \quad (3.90)$$

In the “1+2” case, the secular frequency of planet a is thus changed from ω_{a1} to

$$\omega_a = \omega_{a1} (1 + \epsilon_{a1,\text{GR}}). \quad (3.91)$$

Now the forced eccentricity on planet a is proportional to $e_{a,\text{forced}} \propto (1 + \epsilon_{a1,\text{GR}})^{-1}$, at the same time we also have $N_{\text{sec}} \propto (1 + \epsilon_{a1,\text{GR}})^{-1}$. Since on average $e_{a,\infty} \sim e_{a,\text{forced}} \sqrt{2\langle N_{\text{ej}} \rangle_{\text{HM}} / N_{\text{sec}}}$ (see Eq. 3.68), the final eccentricity raised on planet a after scattering scales as $e_{a,\infty} \propto (1 + \epsilon_{a1,\text{GR}})^{-1/2}$.

In comparison, in the purely “secular” scenario without scattering events, the final eccentricity raised is proportional to $e_{a,\text{forced}} \propto (1 + \epsilon_{a1,\text{GR}})^{-1}$. Thus we see that in the stochastic forcing case, short ranged forces such as GR apsidal precession still

suppresses eccentricity generation, but the suppression factor is only proportional to the inverse square root of the strength of the short-ranged force.

3.6.3 Application to Specific Systems

We discuss our results in the context of a few specific planet systems of interest. These systems feature an inner planet well separated from an exterior CJ with high orbital eccentricities and/or mutual inclinations. Such eccentric CJs are a natural consequence of strong scatterings between CJs. We evaluate if the observed orbital properties of these inner-outer systems can be explained using our model.

- **HAT-P-11** is a system with a transiting inner mini-Neptune (HAT-P-11b, $m_a = 23.4 \pm 1.5 M_\oplus$, $a_a = 0.0525 \pm 0.0007$ au.) first discovered by photometry (Bakos et al., 2010) and an outer CJ (HAT-P-11c) with $m_1 \sin \theta = 1.6 \pm 0.1 M_J$ and $a_1 = 4.13 \pm 0.3$ au. RV measurements report values of $e_a = 0.218 \pm 0.03$ and $e_1 = 0.6 \pm 0.03$ for the two planets. The orbit of HAT-P-11c is highly misaligned relative to the stellar spin $\lambda_1 \sim 100$ deg.; Yee et al. (2018) argued that such a misalignment can be explained if the two planets are also highly mutually inclined with $\theta_a \gtrsim 50$ deg.

Due to the very tight orbit of HAT-P-11b, GR apsidal precession is important, with $\epsilon_{a1,GR} \approx 133$. Note that despite the large inclination between HAT-P-11b and HAT-P-11c, Kozai-Lidov oscillations are suppressed due to the strong GR effect, and the forced eccentricity is very small ($e_{a,forced} \sim 1.1 \times 10^{-4}$), and the required eccentricity boost factor is $\gamma_e \sim 2000$. The observed value of e_a is thus highly incompatible with pure secular interactions without scattering history.

Since $e_1 = 0.6$, if the observed eccentricity is the result of strong scattering

between HAT-P-11c and an ejected planet, it is most likely that $m_2 \sim m_1$ (see Sec. 3.2). Thus, applying Eq. (3.80) we have $\sqrt{\langle N_{\text{ej}} \rangle_{\text{HM}} / N_{\text{sec}}} \sim 40$. The observed value of γ_e is therefore larger than its typical value by a factor of $y = \gamma_e / \langle \gamma_e \rangle_{\text{HM}} \sim 50$. According Eq. (3.79), the likelihood of seeing such a boost factor is $P(y \geq 50) = 0.02$. However, Eq. (3.79) underestimates y at larger values when $m_2 \sim m_1$ (see Fig. 3.15); from our empirical results we find that for $m_2/m_1 \gtrsim 0.7$, $P(y \geq 50) \sim 0.09$. In other words, there is a 9% chance to have $e_a \gtrsim 0.2$ as a result of “1+2” scattering as given by the currently observed parameters.

Now turning to the mutual inclination, since the nodal precession is not affected by GR precession, we have $\sqrt{\langle N_{\text{ej}} \rangle_{\text{HM}} / N_{\text{sec}}} \sim 3.5$. On the other hand, the ‘forced’ mutual inclination depends on $\theta_{12,0}$, the initial misalignment angle between HAT-P-11c and the ejected planet. The observed value of y is given by $y \sim \theta_a / (3.5 \sqrt{2} \theta_{12,0}) - 1$ (recall that the factor $\sqrt{2}$ arises due to the boost factor being larger for the mutual inclination; see Sec. 3.4.3). If we take $\theta_a = 50$ deg. and $\theta_{12,0} = 3$ deg., then $y \sim 3$ and $P(y \geq 3) \sim 0.4$, i.e. there is a 40% chance for the observed mutual inclination to be as large as 50 degrees. The probability decreases if $\theta_{12,0}$ is smaller: for $\theta_{12,0} = 1$ deg., the p-value decreases to $P(y \geq 9) \sim 0.1$. Note again that the empirical value of P is greater than predicted by Eq. (3.79) due to the fact that $m_1 \sim m_2$.

We conclude that for the HAT-P-11 system, the observed eccentricity of the inner planet is marginally consistent with “1+2” scattering with a p-value of $P \sim 0.1$ for the observed eccentricity boost factor, while the observed inclination is consistent with “1+2” scattering (at $P = 0.1$ level) for $\theta_{12,0} \gtrsim 1$ degree.

- **Gliese 777 A** is a two-planet system detected by RV with an inner planet with $m_a \sin \theta_a = 18 \pm 2 M_{\oplus}$ and $a_a = 0.13 \pm 0.008$ au., and an outer CJ with $m_1 \sin \theta_1 =$

$1.56 \pm 0.13 M_J$ and $a_1 = 4 \pm 0.2$ au, orbiting around a yellow subgiant with $M_\star = 0.82 \pm 0.17 M_\odot$ (Wright et al., 2009). RV measurements report $e_a \approx 0.24 \pm 0.08$ and $e_1 \approx 0.31 \pm 0.02$.

The value of $\epsilon_{a1,GR} \sim 3$ which gives a forced eccentricity of 3.5×10^{-3} and boost factor $\gamma_e \sim 57$, thus the value of e_a cannot be explained by pure secular forcing alone. Hypothesizing that the current value of e_1 is due to scattering with an ejected planet, the value of $e_1 \approx 0.3$ suggests that $m_2/m_1 \sim 0.4$, which gives $\sqrt{\langle N_{ej} \rangle_{HM}/N_{sec}} \sim 8$ and $y \sim 7$. Evaluating Eq. (3.79), we find that $P(y \geq 7) \approx 0.14$. Thus, even though the observed value of e_a is much greater than the amount predicted by pure secular forcing, it is still consistent with “1+2” scattering theory.

- **π Men** is a two-planet system with an inner transiting super-Earth ($m_a = 4.8 M_\oplus$, $a_a = 0.0684$ au) discovered by TESS (Huang et al., 2018a) and an external companion discovered by RV with $a_1 = 3.3$ au and $m_1 \approx 12.9 M_J$. The host-star is G type with $M_\star = 1.11 M_\odot$. Follow-up surveys have shown a significant orbital misalignment between m_1 and m_a , with $49 \text{ deg.} < \theta_{a1} < 131 \text{ deg.}$ at 1σ level (Xuan and Wyatt 2020; see also Damasso et al. 2020; Kunovac Hodžić et al. 2020; Rosa et al. 2020). The external companion has an eccentric orbit of $e_1 \approx 0.642$ while the inner planet has $e_a \approx 0.15$ (Damasso et al., 2020).

For this system $\epsilon_{a1,GR} = 1.21$, and $e_{a,forced} = 0.013$, thus $\gamma_e \approx 11$, which shows the current value of e_a is inconsistent with pure secular forcing from m_1 alone. If the current value of e_1 is due to strong scattering, the ejected planet likely has $m_2 \sim m_1$, corresponding to $\sqrt{\langle N_{ej} \rangle_{HM}/N_{sec}} \sim 3.3$ when GR precession is taken into account. Thus $y_e \sim 3.3$, which is consistent with “1+2” scattering with $p(y \geq 3.3) \sim 0.3$. Thus we conclude that the observed value of e_1 is highly compatible with “1+2” scattering.

Now turning to the mutual inclination, we have that $\sqrt{\langle N_{\text{ej}} \rangle_{\text{HM}} / N_{\text{sec}}} \sim 2.3$. Taking a fiducial value of $\theta_{a1} \approx 90$ deg., we have $y = 90 \text{ deg.} / (2.3 \sqrt{2} \theta_{12,0}) - 1$. If $\theta_{12,0} = 3$ deg., then $y_\theta \sim 8$ and $P(y \geq 8) \sim 0.2$. On the other hand, if $\theta_{12,0} = 1$ deg., then $y_\theta \sim 27$, corresponding to $P(y \geq 27) \sim 0.12$. Recall that we are using empirical values for $P(y)$ derived from simulations, since Eq. (3.79) breaks down when $m_1 \sim m_2$. To conclude, the observed mutual inclination in the system can be easily generated by “1+2” scattering if $\theta_{12,0} \gtrsim 3$ deg., and is still possible with $P \sim 0.12$ probability for $\theta_{12,0} \sim 1$ degree.

CHAPTER 4

LOW-ECCENTRICITY MIGRATION OF ULTRA-SHORT PERIOD PLANETS IN MULTIPLANET SYSTEMS

4.1 Introduction

The existence of ultra-short period planets (USPs), defined to be small planets ($R \leq 2R_{\oplus}$), with sub-day periods (i.e. $P \leq 1$ day) is one of the major surprises in exoplanetary astrophysics. The first example of such planets, CoRoT-7b, was discovered in 2009 (Léger et al., 2009); since then, about a hundred USPs have been found by various transit surveys (Sanchis-Ojeda et al., 2014), and the overall occurrence rate of USPs sits at $\sim 1\%$, a figure that is similar to the census of hot Jupiters, i.e. giant planets with $P \leq 10$ days (Cumming et al., 2008; Wright et al., 2012). A few notable USPs have received special attention: 55 Cnc e (Dawson and Fabrycky, 2010) with $P = 0.74$ days was the first discovered Super-Earth, Kepler-10b with $P = 0.83$ days (Batalha et al., 2011a) was the first terrestrial planet discovered by *Kepler*, and Kepler-78b (Sanchis-Ojeda et al., 2013) with $P = 0.36$ days is the current record holder amongst planets known with the shortest orbital period. Kepler-32 and Kepler-80 are another pair of unusually interesting systems: both contain a USP with an additional set of three or four exterior transiting planets that are potentially locked in mean-motion resonances (Swift et al., 2013; MacDonald et al., 2016). A recent review on the detection and population statistics of USPs is provided by Winn et al. (2018).

Historically, the choice of the one day cut-off for the definition of USPs was not astrophysically motivated; it was chosen because the number of planets discovered below such period was rare at the time (Winn et al., 2018). However, recent evidence has emerged that USPs may in fact be a statistically distinct population. Planets with

$P \leq 1$ days appear to follow a different period distribution than planets above the one day cut-off: Lee and Chiang (2017) found that whereas transiting planets with $1 \leq P \leq 10$ days followed a power law $dN/d \log P \propto P^\alpha$ with $\alpha \simeq 1.5 - 1.7$ (see also Petigura et al., 2018; Weiss et al., 2018), USPs followed a steeper trend with $\alpha \sim 3.0$. In addition, the normalization of the period distribution may also be different: the planet occurrence rate is discontinuous across the $P = 1$ day boundary, with $\sim 50\%$ more planets with periods just below $P = 1$ days than just above.

In addition to their period distribution, USPs have other statistical properties that differentiate them from longer-period planets. USPs have smaller radii, with the vast majority having $1R_\oplus \leq R \leq 1.4R_\oplus$ (Winn et al., 2018), a fact which may be attributed to photo-evaporation or ‘boil-off’ as the planets are intensely irradiated. Compared with the other *Kepler* planets, planet systems with USPs also appear to have higher mutual inclinations: Dai et al. (2018) found that transiting *Kepler* planets with a semi-major axis to stellar radius ratio $a/R_\star < 5$ had an inclination dispersion of $\Delta\theta \approx 6.7 \pm 0.7$ degrees, while planets with $5 < a/R_\star < 12$ had only $\Delta\theta \approx 2.0 \pm 0.1$ (consistent with the overall figures for *Kepler* multis, see e.g. Tremaine and Dong, 2012; Fang and Margot, 2012; Fabrycky et al., 2014). This observation is further corroborated by the fact that for FGK host stars, USPs feature a factor of ~ 8 fewer co-transiting external companions compared with their merely ‘short-period planet’ (SP) counterparts (Petrovich et al., 2018; Weiss et al., 2018), and when USPs do have external transiting companions, the period ratios between the USP and their closest companion is $P_2/P_1 \gtrsim 15$, a value that is nearly an order of magnitude above the typical period ratios of $1.3 - 4.0$ seen in *Kepler* multis (see also Steffen and Farr, 2013).

The statistical distinctness of USPs and their unusual locations so close to their host stars defy conventional understandings of planet formation, and the origins of these

planets remains a mystery. USPs may sit in the short-period tail of the distribution of close-in rocky planets that formed in-situ through core accretion (Chiang and Laughlin, 2013), or they may have migrated to their current locations from initially more distant orbits (Ida and Lin, 2004; Schlaufman et al., 2010; Terquem, 2014). In the latter scenario, they (like most of their SP brethren) likely would have begun their lives as Super-Earths/Mini-Neptunes with a gaseous H/He envelope that was subsequently lost to photo-evaporation (Valencia et al., 2010; Owen and Wu, 2013). To shove the planets very close to their host stars, some form of disk migration and/or tidal dissipation is required. Lee and Chiang (2017) considered stellar tides raised by the planet, treating the stellar tidal quality factor Q'_\star as a free parameter; since the orbital decay rate is proportional to the planet mass, the required Q'_\star value to induce significant decay of small planets would make hot Jupiters at $P \sim 1$ day “disappear” on a short timescale. In the case of planetary tides, the proto-USP must maintain a finite eccentricity in order to undergo orbital decay. Petrovich et al. (2018) examined a high-eccentricity migration scenario in which a proto-USP attains large eccentricity due to secular chaos in a hierarchical system with $N > 3$ planets, followed by orbital circularization due to planetary tides. They also briefly explored the possibility of forming USPs through secular interactions with eccentric giant planet companions, but dismissed the possibility as unlikely: they found that producing USPs usually required eccentric giant planet companions with $P \leq 10$ days, a requirement at odds with the observation that the presence of USPs do not seem to be correlated with the stellar host metallicity, and therefore by proxy the occurrence of giant planet companions (Winn et al., 2017). In short, although these previous ideas indeed may produce ultra-short period planets under some conditions or assumptions, there is yet no firm evidence that USP formation can be completely accounted for by any one of the aforementioned scenarios.

Indeed, the formation mechanism of USPs remains unclear and this is the question

we aim to address. The main thesis of this work is that the combination of secular interactions and tidal dissipation in multi-planet systems is likely be the most natural and efficient way to generate USPs. This mechanism requires small, rocky planets to be born at moderate eccentricities (i.e. $e \gtrsim 0.1$) in multi-planet ($N \geq 3$) systems, but otherwise requires little fine tuning of planet parameters. Empirical studies suggest the orbital eccentricities of Kepler multis have a dispersion of $\sigma_e \sim 0.05$ (Xie et al., 2016; Van Eylen and Albrecht, 2015; Van Eylen et al., 2019), so USP formation in this mechanism would occur at the tail end of the eccentricity distribution. However, note that the currently observed eccentricity distribution has been damped over Gyrs by tidal dissipation (Hansen and Murray, 2015), and the primordial eccentricities may be much larger.

Certainly, the idea of secular forcings coupled with tidal dissipation is not a new one; it has already been applied to short-period exoplanet systems in various contexts (e.g. Wu and Goldreich, 2002; Mardling, 2007, 2010; Batygin et al., 2009; Hansen and Zink, 2015; Petrovich et al., 2018), although this work is the first to tackle the problem in the context of USP formation in multi-planet systems. The mechanism studied in this paper has some similarity to the secular chaos mechanism proposed by Petrovich et al. (2018), but with important differences: Whereas Petrovich et al. (2018) rely on secular chaos driving small planets to attain large eccentricities (e.g. $1 - e \ll 1$) and thereby small pericenter distances to achieve USP formation, our mechanism requires the inner planet (initially at $P = 1 - 3$ days) to achieve only mild initial eccentricities ($e \sim 0.1$) through secular interactions; although the mechanism proposed by Petrovich et al. (2018) allows for a more diverse proto-USP period, it also requires the presence of several well-separated exterior planets, whereas in our mechanism, the initial proto-USP period is more constrained, but the external planet companions are allowed more lee-way in terms of their spacing. In light of this fact, we call our proposed formation mechanism

the ‘low- e migration’ of USPs.

In this paper, we present an investigation on the prospects of generating USPs through ‘low- e migration’. The structure of the paper is as follows. In section 4.2, we present the mathematical formalism for the eccentricity and orbital evolution of a multi-planet system undergoing secular interactions and tidal dissipation. As we discuss below, a brute-force approach to this problem is impractical, and we derive the evolution equations in the framework of eigenmodes in section 4.2.1. In section 4.3, we apply our formalism to the case of 2-planet systems, deriving semi-analytical results for the eccentricity and mode evolution; in section 4.3.2 we discuss the criterion for USP formation to occur in such 2-planet systems. We then extend these results to the case of 3-planet systems in section 4.4, and show that such systems allow for successful low- e secular migration under reasonable conditions. In section 4.5 we consider the inclination evolution of the planets, taking into account planet-planet coupling as well as interactions with stellar spin. The results of the preceding sections are synthesized into a population model in section 4.6 - readers who are most interested in observational implications of our results may skip to this section. In section 4.7, we discuss the feasibility of low- e secular migration and compare it against other proposed mechanisms. Finally, a summary of our work is provided in section 4.8.

4.2 Eccentricity Evolution and Orbital Decay: Formalism

Consider a N -planet system with individual planet mass m_i , semi-major axis a_i , initial orbital eccentricity e_i , longitude of periapsis ϖ_i , inclination θ_i and longitude of the ascending node Ω_i , where $i \in [1, N]$ is the planet index, orbiting a host star with mass M_\star and radius R_\star . We assume that the host-star is Sun-like, i.e. $M_\star = M_\odot$

and $R_\star = R_\odot$. The planet's semi-major axis is related to the orbital period by $a \simeq 0.0196(P/\text{day})^{2/3}(M_\star/M_\odot)^{1/3}$ au. The dynamical evolution of the system is governed by the interplay of several effects: planet-planet secular perturbations, General Relativistic (GR) periastron advance, spin-orbit coupling due to stellar oblateness, planetary tides and stellar tides. We define $\mathcal{E}_i \equiv e_i \exp(i\varpi_i)$ to be the complex eccentricity of the i -th planet, and define the eccentricity vector of the N -planet system as

$$\vec{\mathcal{E}} = \begin{pmatrix} \mathcal{E}_1 \\ \mathcal{E}_2 \\ \vdots \end{pmatrix}. \quad (4.1)$$

In the linear (Laplace-Lagrange) theory, the time evolution of $\vec{\mathcal{E}}$ is governed by the equation

$$\frac{d}{dt}\vec{\mathcal{E}}(t) = i\mathbf{H}(t)\vec{\mathcal{E}}(t), \quad (4.2)$$

where the coefficients of the time-varying $N \times N$ matrix $\mathbf{H}(t)$ is given by

$$H(t) = \begin{pmatrix} \tilde{\omega}_1 & -\nu_{12} & \cdots & -\nu_{1N} \\ -\nu_{21} & \tilde{\omega}_2 & \cdots & -\nu_{2N} \\ \vdots & \vdots & \ddots & \vdots \\ -\nu_{N1} & -\nu_{N2} & \cdots & \tilde{\omega}_N \end{pmatrix}. \quad (4.3)$$

Here the complex “frequencies” $\tilde{\omega}_i$ (taking into account the eccentricity damping due to tidal dissipation in the i -th planet) is defined as

$$\tilde{\omega}_i \equiv \omega_i + i\gamma_i = \sum_{j \neq i} \omega_{ij} + \omega_{i,\text{gr}} + \omega_{i,\text{tide}} + i\gamma_i. \quad (4.4)$$

The quantities ω_{ij} and ν_{ij} are the quadrupole and octupole precession frequencies of the i -th planet driven by the actions of the j -th planet, given by

$$\begin{aligned}\omega_{ij} &= \frac{Gm_i m_j a_{<}}{4a_{>}^2 L_i} b_{3/2}^{(1)}(\alpha) \\ &\simeq 4.0 \times 10^{-4} \left(\frac{M_\star}{M_\odot} \right)^{-1/2} \left(\frac{m_j}{10M_\oplus} \right) \left(\frac{a_i}{0.02 \text{ au}} \right)^{3/2} \\ &\quad \times \left(\frac{a_j}{0.1 \text{ au}} \right)^{-3} \left(\frac{b_{3/2}^{(1)}(\alpha)}{3\alpha} \right) \text{yr}^{-1},\end{aligned}\tag{4.5}$$

and

$$\begin{aligned}\nu_{ij} &= \frac{Gm_i m_j a_{<}}{4a_{>}^2 L_i} b_{3/2}^{(2)}(\alpha) \\ &\simeq 1.0 \times 10^{-4} \left(\frac{M_\star}{M_\odot} \right)^{-1/2} \left(\frac{m_j}{10M_\oplus} \right) \left(\frac{a_i}{0.02 \text{ au}} \right)^{3/2} \\ &\quad \times \left(\frac{a_j}{0.1 \text{ au}} \right)^{-3} \left(\frac{b_{3/2}^{(2)}(\alpha)}{15\alpha^2/4} \right) \text{yr}^{-1},\end{aligned}\tag{4.6}$$

where we have defined $a_{<} = \min(a_i, a_j)$, $a_{>} = \max(a_i, a_j)$, $\alpha = a_{<}/a_{>}$, $L_i = m_i \sqrt{GM_\star a_i}$ is the (circular) angular momentum of the i -th planet, and $b_{3/2}^{(n)}(\alpha)$ are the usual Laplace coefficients given by

$$b_{3/2}^{(n)}(\alpha) = \frac{1}{2\pi} \int_0^\pi \frac{\cos(nt)}{(\alpha^2 + 1 - 2\alpha \cos t)^{3/2}} dt.\tag{4.7}$$

In the limit $\alpha \ll 1$, the first-order expansion of the Laplace coefficients are $b_{3/2}^{(2)}(\alpha) \simeq 3\alpha$ and $b_{3/2}^{(1)}(\alpha) \simeq 15\alpha^2/4$.

The general relativistic apsidal precession frequency is given by (for $e_i \ll 1$):

$$\omega_{i,\text{gr}} = \frac{3GM_\star}{c^2 a_i} n_i \simeq 3.3 \times 10^{-3} \left(\frac{M_\star}{M_\odot} \right)^{3/2} \left(\frac{a_i}{0.02 \text{ au}} \right)^{-5/2} \text{yr}^{-1},\tag{4.8}$$

where n_i is the angular orbital frequency. The rate of periastron advance on the i -th

planet due to its tidal bulge is given by

$$\begin{aligned}
\omega_{i,\text{tide}} &= \frac{15}{2} k_{2,i} \frac{M_\star}{m_i} \left(\frac{R_i}{a_i} \right)^5 n_i \\
&= 2.44 \times 10^{-4} k_{2,i} \left(\frac{M_\star}{M_\odot} \right)^{1.5} \left(\frac{m_i}{M_\oplus} \right) \left(\frac{R_i}{R_\oplus} \right)^5 \\
&\quad \times \left(\frac{a_i}{0.02 \text{ au}} \right)^{-13/2} \text{ yr}^{-1},
\end{aligned} \tag{4.9}$$

with $k_{2,i}$ being the tidal Love number of the i -th planet; in this work, we adopt a value of $k_{2,i} = 1$. Generally, as the planet moves inwards, the GR and tidal forces become increasingly important, while farther out, planet-planet secular interactions tend to prevail.

We use the weak friction theory of equilibrium tides to describe tidal dissipation in the planet (Darwin, 1880; Alexander, 1973; Hut, 1981). The eccentricity damping rate of the i -th planet due to tidal dissipation is

$$\begin{aligned}
\left(\frac{\dot{e}_i}{e_i} \right)_{\text{tide}} &\equiv -\gamma_i = -\frac{21}{2} k_{2,i} \Delta t_{L,i} \frac{M_\star}{M_\odot} \left(\frac{R_i}{a_i} \right)^5 n_i^2 \\
&= -2.4 \times 10^{-6} \times k_{2,i} \left(\frac{\Delta t_{L,i}}{100\text{s}} \right) \left(\frac{M_\star}{M_\odot} \right)^2 \\
&\quad \times \left(\frac{m_i}{M_\oplus} \right)^{-1} \left(\frac{R_i}{R_\oplus} \right)^5 \left(\frac{a_i}{0.02 \text{ au}} \right)^{-8} \text{ yr}^{-1},
\end{aligned} \tag{4.10}$$

where $\Delta t_{L,i}$ is the tidal lag time of the i -th planet, and is related to the tidal quality factor Q_i by

$$Q_i = (2n_i \Delta t_{L,i})^{-1} = 70 \left(\frac{a_i}{0.02 \text{ au}} \right)^{3/2} \left(\frac{M_\star}{M_\odot} \right)^{-1/2} \left(\frac{\Delta t_{L,i}}{100\text{s}} \right)^{-1}. \tag{4.11}$$

Note that in this formalism, the value of Q_i is not constant and instead varies with the planet's semi-major axis. In the Solar System, values of Q range from 10 – 500 for terrestrial planets and satellites, but the gas giants have values of Q that are much larger (Goldreich and Soter, 1966; Ogilvie, 2014). We assume proto-USPs to be predominantly rocky and adopt values of Q_1 in the range between 70 and 700, while the exterior planets

are assumed to have H/He envelopes comprising a few percent of the planet's mass (but a large fraction of the radius) and therefore have much larger values of tidal Q_i .

Because the the outer planets ($i \geq 2$) have much larger values of a_i and Q_i , the effects of tidal dissipation are much weaker for these planets. Therefore, we simplify the problem by only considering tidal dissipation for the innermost planet (i.e. by setting $Q_i = \infty$ for $i \geq 2$) in sections 4.2 through 4.5; the effects of tidal dissipation in the outer planets are included in our population synthesis study in section 4.6.

To completely determine the time evolution of the system, Eq. (4.2) for $\vec{\mathcal{E}}$ should be supplemented by the evolution of the inner planet's semi-major axis a_1 :

$$\begin{aligned} \left(\frac{\dot{a}_1}{a_1}\right)_{\text{tide}} &= -2\gamma_1 e_1^2 = -1.9 \times 10^{-9} k_{2,1} \left(\frac{\Delta t_{L,1}}{100\text{s}}\right) \left(\frac{e_1}{0.02}\right)^2 \\ &\times \left(\frac{M_\star}{M_\odot}\right)^2 \left(\frac{m_1}{M_\oplus}\right)^{-1} \left(\frac{R_1}{R_\oplus}\right)^5 \left(\frac{a_1}{0.02 \text{ au}}\right)^{-8} \text{ yr}^{-1}. \end{aligned} \quad (4.12)$$

We also consider the orbital decay driven by dissipation of tides raised on the host star by the planet (Goldreich and Soter, 1966):

$$\begin{aligned} \left(\frac{\dot{a}_1}{a_1}\right)_{\text{tide}\star} &\equiv -\gamma_\star = -\frac{9}{2} \left(\frac{m_1}{M_\star}\right) \left(\frac{R_\star}{a_1}\right)^5 \frac{n_1}{Q'_\star} \\ &= -1.85 \times 10^{-9} \left(\frac{M_\star}{M_\odot}\right)^{-1/2} \left(\frac{R_\star}{R_\odot}\right)^5 \left(\frac{Q'_\star}{10^6}\right)^{-1} \\ &\times \left(\frac{m_1}{M_\oplus}\right) \left(\frac{a_1}{0.01 \text{ au}}\right)^{-13/2} \text{ yr}^{-1}, \end{aligned} \quad (4.13)$$

where $Q'_\star = 3Q_\star/(2k_{2,\star})$ is the reduced tidal quality factor of the star. Empirical measurements by Penev et al. (2018) suggest a value of $Q'_\star = 10^7$ at a tidal forcing frequency of 2 days^{-1} , decreasing to $Q'_\star = 10^5$ when the forcing frequency is 0.5 day^{-1} . Lee and Chiang (2017) treated Q'_\star as a free parameter, and considered values of Q'_\star in the range of $10^6 - 10^8$. Thus, in general, the orbital decay rate of the inner-most planet is given by

$$\dot{a}_1 = -2\gamma_1 |\mathcal{E}_1|^2 a_1 - \gamma_\star a_1. \quad (4.14)$$

In sections 4.2 - 4.5 we will focus on planetary tides and neglect the effect of stellar tides (i.e. by setting $Q'_\star = \infty$), although we will include stellar tides in our population synthesis study in section 4.6. We do this for two reasons: Firstly, for typical values of Q'_\star the effect of stellar tides is small over the lifetime of the system and only attains significance when an USP has already been produced (i.e. $a_1 \leq 0.02$ au.), therefore its role is orthogonal to the aims of this work. Secondly, the addition of stellar tidal dissipation destroys the conservation of orbital angular momentum, an otherwise desirable property of Eqs. (4.2) & (4.14), as we will demonstrate in section 4.3.2.

4.2.1 Eccentricity Evolution in the Framework of Eigenmodes

A brute-force integration of Eqs. (4.2) and (4.14) encounters difficulty: the relevant frequencies vary over many orders of magnitude with the orbital decay timescale ($|a_1/\dot{a}_1| \gtrsim 1$ Gyr) being much longer than the precession timescales ($2\pi/\omega_i \sim 10^3$ yrs); the “stiffness” of the equations make it impractical to integrate a large number of systems. Our approach is eschew calculating the phase of the eccentricity vector. We do this by decomposing the planet eccentricities into eigenmodes.

We define the eigenvalue λ_α and eigenvector $\vec{\mathcal{E}}_\alpha$ (with modes denoted using Roman Numerals $\alpha \in [\text{I}, \text{II}, \text{III} \dots]$) of the system as

$$\mathbf{H}(t)\mathcal{E}_\alpha(t) = \lambda_\alpha(t)\vec{\mathcal{E}}_\alpha(t), \quad (4.15)$$

where

$$\vec{\mathcal{E}}_\alpha = \begin{pmatrix} \mathcal{E}_{\alpha 1} \\ \mathcal{E}_{\alpha 2} \\ \vdots \end{pmatrix}. \quad (4.16)$$

Note that since $\mathbf{H}(t)$ depends on a_1 (the time evolution of $a_2, a_3 \dots$ are negligible), the eigenvalue $\lambda_\alpha(t)$ and eigenvector $\vec{\mathcal{E}}_\alpha(t)$ evolve in time as a_1 decreases. We now introduce the matrices $\mathbf{G}(t)$ and $\mathbf{V}(t)$ formed from the eigenvalues and eigenvectors of $\mathbf{H}(t)$:

$$\mathbf{G}(t) = \text{diag}(\lambda_{\text{I}}, \lambda_{\text{II}}, \dots, \lambda_{\text{N}}) \quad (4.17)$$

and

$$\mathbf{V}(t) = \begin{bmatrix} \vec{\mathcal{E}}_{\text{I}} & \vec{\mathcal{E}}_{\text{II}} & \dots & \vec{\mathcal{E}}_{\text{N}} \end{bmatrix}. \quad (4.18)$$

By definition, the matrices $\mathbf{G}(t)$ and $\mathbf{V}(t)$ satisfy the identity

$$\mathbf{G}(t) = \mathbf{V}^{-1}(t) \mathbf{H}(t) \mathbf{V}(t). \quad (4.19)$$

In general, the time evolution of $\vec{\mathcal{E}}$ can be written as a superposition of eigenmodes,

$$\vec{\mathcal{E}}(t) = \sum_{\alpha} A_{\alpha}(t) \vec{\mathcal{E}}_{\alpha}(t) = \mathbf{V}(t) \vec{A}(t), \quad (4.20)$$

where $\vec{A}(t) \in \mathbb{C}^N$ is the vector of eigenmode amplitudes:

$$\vec{A}(t) \equiv \begin{pmatrix} A_{\text{I}} \\ A_{\text{II}} \\ \vdots \end{pmatrix}. \quad (4.21)$$

The initial condition $\vec{A}(0)$ is given by

$$\vec{A}(0) = \mathbf{V}^{-1}(0) \vec{\mathcal{E}}(0). \quad (4.22)$$

Substituting Eq. (4.20) into Eq. (4.2), and using the identity $\mathbf{H}\mathbf{V}\vec{A} = \mathbf{V}\mathbf{G}\vec{A}$ (which follows from Eq. 4.19), we find

$$\frac{d\vec{A}}{dt} = [i\mathbf{G}(t) - \mathbf{V}^{-1}(t)\dot{\mathbf{V}}(t)]\vec{A}(t) \equiv \mathbf{W}(t)\vec{A}(t). \quad (4.23)$$

The above equation is exact, but still involves highly oscillatory complex mode amplitudes. To make further progress, we note that Eq. (4.23) yields the evolution equation for $|A_\alpha(t)|$:

$$\frac{d}{dt}|A_\alpha| = \frac{1}{|A_\alpha|} \text{Re} \left(\sum_{\beta} A_\alpha^* W_{\alpha\beta} A_\beta \right). \quad (4.24)$$

In general, A_α^* and A_β contain fast varying phases. We now adopt the ansatz that when averaging over timescales much longer than $|\lambda_\alpha - \lambda_\beta|^{-1}$ but shorter than the orbital evolution time $|a_1/\dot{a}_1|$,

$$\langle e^{i\phi_{\alpha\beta}} \rangle = \left\langle \frac{A_\alpha^* A_\beta}{|A_\alpha||A_\beta|} \right\rangle \simeq 0 \quad (\alpha \neq \beta). \quad (4.25)$$

With this ansatz, Eq. (4.24) reduces to

$$\frac{d}{dt}|A_\alpha| \simeq \text{Re}(W_{\alpha\alpha})|A_\alpha|, \quad (4.26)$$

and the magnitude of the planet eccentricity is given by

$$\langle e_i^2 \rangle = \left\langle \left| \sum_{\alpha} A_\alpha \mathcal{E}_{\alpha i} \right|^2 \right\rangle \simeq \sum_{\alpha} |A_\alpha|^2 |\mathcal{E}_{\alpha i}|^2. \quad (4.27)$$

If we define $B_\alpha(t) \equiv |A_\alpha(t)| \in \mathfrak{R}^+$ and let $\vec{B}(t)$ be the vector with components $B_\alpha(t)$, Eq. (4.26) can be written in matrix form as

$$\frac{d\vec{B}(t)}{dt} = \text{Re} [\text{Diag}(\mathbf{W})] \vec{B}(t). \quad (4.28)$$

Eq. (4.28) is much easier to solve numerically than the exact Eq. (4.23), because both the vector \vec{B} and the matrix \mathbf{W} are explicit functions of $\vec{a}_1(t)$, and only vary with t as $a_1(t)$ varies. In particular, we can evaluate \mathbf{W} from

$$\mathbf{W} = i\mathbf{G} - \mathbf{V}^{-1} \left(\frac{\partial \mathbf{V}}{\partial a_1} \right) \dot{a}_1, \quad (4.29)$$

with \dot{a}_1 given by Eq. (4.14).

We solve Eq. (4.28) combined with Eqs. (4.14) and (4.27) to obtain the time evolution of the RMS eccentricity and semi-major axis. Although our formalism above

does not capture the short-term oscillations in eccentricity, it is nonetheless possible to know the extent of these oscillations by computing the “instantaneous” maximum and minimum eccentricity. The instantaneous maximum eccentricity is given by

$$\max(e_i) = \sum_{\alpha} B_{\alpha} |\mathcal{E}_{\alpha i}|, \quad (4.30)$$

and the minimum eccentricity is given by

$$\min(e_i) = \sqrt{2\langle e_i^2 \rangle - [\max(e_i)]^2}. \quad (4.31)$$

In the above RMS-averaged formulation, the ansatz leading to Eq. (4.28) is equivalent to assuming that the mode amplitude evolves adiabatically as a_1 decreases, i.e. we assume that the cross-terms corresponding to the mixing between modes average out to zero due to their incoherent phases, and only diagonal terms remain. In reality, the assumption in Eq. (4.25) may not hold in the later stages of orbital decay, as certain pairs of modes may become locked in either alignment or anti-alignment depending on the configuration of eigenvectors. In practice, this turns out not to be an issue since all but one mode will have decayed away by this point, leaving the question of how to handle the cross-mode terms moot, and we have found excellent agreements across the board between the approximate RMS-averaged formulation and the exact treatment. Nonetheless, the approximation made in Eq. (4.25) is the main source of uncertainty in our approximate formulation and may lead to errors in edge cases when modes do not vary sufficiently rapidly relative to the orbital decay timescale.

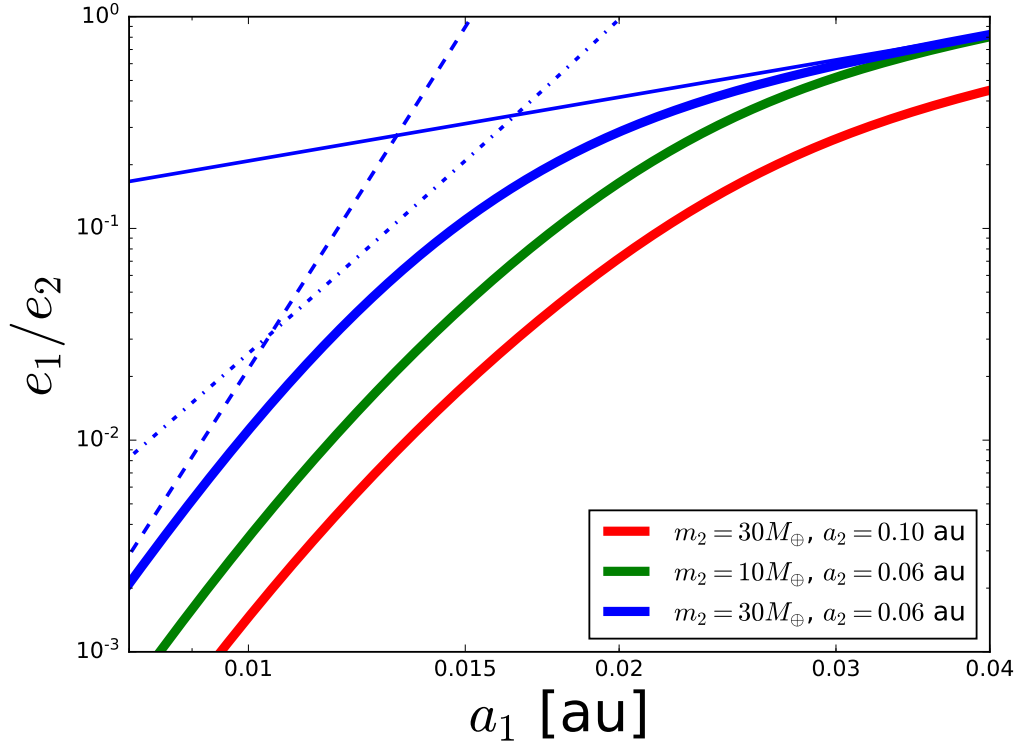


Figure 4.1: The value of $e_{1,\text{forced}}/e_2$ (Eq. 4.40) of an inner planet with $m_1 = M_\oplus$ and $R_1 = R_\oplus$ as a function of a_1 for various values of a_2 and m_2 . The three thick curves correspond to different values of m_2 and a_2 as labeled. For the blue curve, we also show its limiting cases: the thin, solid blue curve corresponds to the approximation given by $e_{1,\text{forced}}/e_2 \simeq \nu_{12}/\omega_{12}$, the dash-dotted curve corresponds to $e_{1,\text{forced}}/e_2 \simeq \nu_{12}/\omega_{1,\text{gr}}$ and the thin dashed line corresponds to $e_{1,\text{forced}}/e_2 \simeq \nu_{12}/\omega_{1,\text{tide}}$.

4.3 Two-Planet Systems

4.3.1 Mode Properties and General Evolution Behaviors

We demonstrate the application of the formalism presented in section 4.2.1 by considering 2-planet proto-USP systems. In this case, analytic expressions for the modes can be derived explicitly, providing useful insight into the more general multi-planet systems.

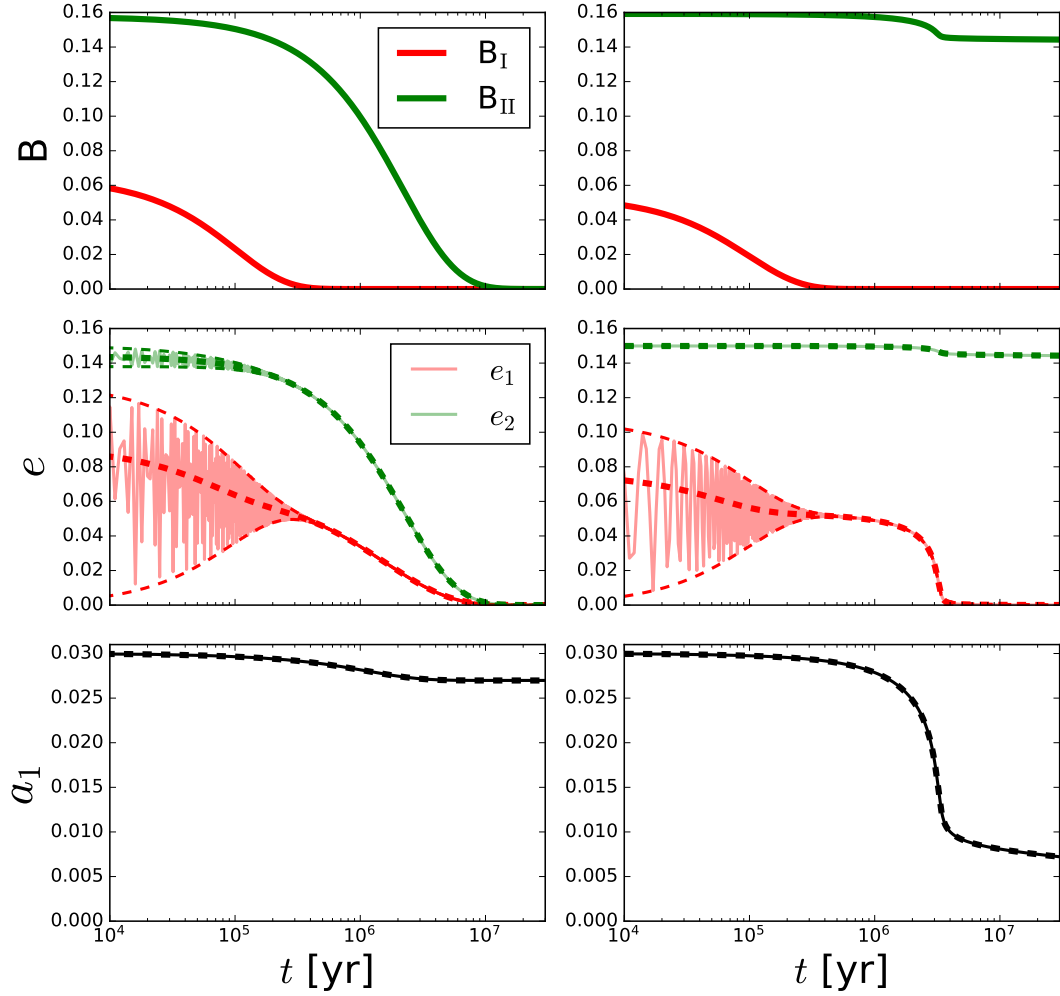


Figure 4.2: Sample time evolution for a two-planet system with initial conditions $a_{1,0} = 0.03$ au, $a_2 = 0.08$ au and $e_{1,0} = 0$, $e_{2,0} = 0.15$. The left panels have planet masses $m_1 = M_\oplus$, $m_2 = 3M_\oplus$ while the right panels have $m_1 = M_\oplus$ and $m_2 = 30M_\oplus$. Note here we adopt a large value of $\Delta t_{L,1} = 10^5$ s in order to speed up numerical calculations. In the middle and bottom panels, the dashed curves show our approximate solution using Eq. (4.28) while the solid curves are obtained using a direct integration of Eqs. (4.2) and (4.14). On the left panels, the orbital decay of m_1 is limited by the amount of total angular momentum deficit, as the two modes decay away before substantial orbital decay can take place, whereas on the right panels, the planets have sufficient AMD to undergo substantial orbital decay, and is instead limited by the rate of orbital decay.

The complex eigenfrequencies λ_I, λ_{II} (see Eq. 4.17) are given by

$$\lambda_I = \frac{1}{2} \left(\tilde{\omega}_1 + \tilde{\omega}_2 + \sqrt{\Delta \tilde{\omega}^2 + 4\nu_{12}\nu_{21}} \right) \quad (4.32)$$

$$\lambda_{II} = \frac{1}{2} \left(\tilde{\omega}_1 + \tilde{\omega}_2 - \sqrt{\Delta \tilde{\omega}^2 + 4\nu_{12}\nu_{21}} \right), \quad (4.33)$$

where $\Delta \tilde{\omega} \equiv \tilde{\omega}_1 - \tilde{\omega}_2$ (with $\tilde{\omega}_1 = \omega_1 + i\gamma_1$ and $\tilde{\omega}_2 \simeq \omega_2$), and the eigenvectors are

$$\begin{aligned} \vec{\mathcal{E}}_I &= \begin{pmatrix} \Delta \tilde{\omega} + \sqrt{\Delta \tilde{\omega}^2 + 4\nu_{12}\nu_{21}} \\ 2\nu_{21} \end{pmatrix}, \\ \vec{\mathcal{E}}_{II} &= \begin{pmatrix} \Delta \tilde{\omega} - \sqrt{\Delta \tilde{\omega}^2 + 4\nu_{12}\nu_{21}} \\ 2\nu_{21} \end{pmatrix}. \end{aligned} \quad (4.34)$$

In general, in order for the inner planet (m_1) to become an USP, one requires that $L_1 \ll L_2$ (where $L_i = m_i \sqrt{GM_\star a_i}$ is the circular angular momentum). In this limit the above expressions simplify considerably: Since $\omega_2, \nu_{12}, \nu_{21} \ll \omega_1$ (recall that $\omega_2 \simeq \omega_{21} = \omega_{12}L_1/L_2$), the eigenfrequencies become

$$\lambda_I \simeq \tilde{\omega}_1 \quad (4.35)$$

$$\lambda_{II} \simeq \tilde{\omega}_2 - \frac{\nu_{12}\nu_{21}}{\tilde{\omega}_1}. \quad (4.36)$$

The eigenvectors in this limit are given by

$$\mathcal{E}_I \simeq \begin{pmatrix} 1 \\ \frac{\nu_{21}}{\omega_1} \end{pmatrix}, \quad \mathcal{E}_{II} \simeq \begin{pmatrix} \frac{-\nu_{12}}{\tilde{\omega}_1} \\ 1 \end{pmatrix}. \quad (4.37)$$

Since $\nu_{21}/\omega_1 = (L_1/L_2)(\nu_{12}/\omega_1) \ll 1$, it is clear that the mode $\alpha = I$ (II) is associated with the free oscillation (apsidal precession) of the inner (outer) planet. The damping rate rate of the two modes are given by

$$\gamma_I \equiv \text{Im}(\lambda_I) \simeq \gamma_1 \quad (4.38)$$

$$\gamma_{II} \equiv \text{Im}(\lambda_{II}) \simeq \gamma_1 \frac{\nu_{12}\nu_{21}}{\omega_1^2} = \gamma_1 \left(\frac{\nu_{12}}{\omega_1} \right)^2 \frac{L_1}{L_2}. \quad (4.39)$$

Clearly, the decay of eigenmode II is substantially suppressed relative to mode I. It is therefore safe to assume that any initial oscillation along mode I is quickly damped out, and the system is locked into mode II. At this stage e_1 is given by the forced eccentricity:

$$e_1 = e_{1,\text{forced}} \simeq \frac{\nu_{12}}{\omega_1} e_2 = \frac{\nu_{12} e_2}{\omega_{12} + \omega_{1,\text{gr}} + \omega_{1,\text{tide}}}. \quad (4.40)$$

Figure 4.1 shows the ratio $e_{1,\text{forced}}/e_2$ as a function of a_1 for several values of m_2 and a_2 . We see that at large a_1 , $\omega_1 \simeq \omega_{12}$, and we have $e_{1,\text{forced}}/e_2 \simeq \nu_{12}/\omega_{12} \simeq 5a_1/4a_2$. As a_1 decreases, $\omega_{1,\text{gr}}$ begins to dominate; in this case we have $e_{1,\text{forced}}/e_2 \simeq \nu_{12}/\omega_{1,\text{gr}} \propto m_2 a_1^5/a_2^4$. When a_1 decreases even further, $\omega_{1,\text{tide}}$ becomes the most dominant term, and we have $e_{1,\text{forced}}/e_2 \simeq \nu_{12}/\omega_1 \propto m_1 a_1^9/a_2^4$.

Thus, for $t \gtrsim \gamma_1^{-1}$, the orbital evolution of the inner planet is governed by (neglecting stellar tides)

$$\frac{\dot{a}_1}{a_1} = -2\gamma_1 e_{1,\text{forced}}^2 = -2\gamma_1 \left(\frac{\nu_{12}}{\omega_1} \right)^2 e_2^2. \quad (4.41)$$

Comparing $|\dot{a}_1/a_1|$ with γ_{II} (Eq. 4.39), we see that the system may exhibit two possible outcomes, depending on the system parameters and initial conditions: (i) for $L_{1,0}/L_2 \lesssim 2e_{2,0}^2$ (where the subscript ‘0’ referring to the initial value), mode II does not experience significant damping (i.e. $e_2 \simeq e_{2,0}$), and the inner planet keeps undergoing orbital decay until its forced eccentricity is suppressed by GR and tides, dramatically slowing any further tidal decay. (ii) For $L_{1,0}/L_2 \gtrsim 2e_{2,0}^2$, both modes are eventually damped out, preventing further tidal decay and leaving behind two planets with circular orbits and fixed semi-major axes.

Figure 4.2 shows examples of time evolution for the two cases. The solid curves are direct integrations of Eq. (4.2) while the dashed curves utilize the approximate formulation in Eq. (4.28); to speed up the integration of Eq. (4.2) we have adopted an unphysical value of $\Delta t_{L,1} = 10^5$ s, corresponding to $Q_1 = 0.07$ (at $P_1 = 1$ day). Note

the excellent agreement between the exact treatment and our approximation. The left three panels of Fig. 4.2 shows an example of case (ii) - we see that in this case the mode amplitudes $\vec{B}(t)$ decay away to zero well before the nominal orbital decay timescale $|a_1/\dot{a}_1|$. In fact, this is a general barrier to USP formation: the planets must have sufficient initial eccentricities (i.e. angular momentum deficit or AMD, see below) in order to have substantial orbital decay prior to having all the mode amplitudes dissipated away.

The right three panels of Fig. 4.2 show an example of case (i). In this case the inner planet is able to undergo substantial decay to become an USP due to the greater amount of AMD stored in the more massive exterior planet, and substantial oscillation amplitude remains in mode II even after the inner planet has decayed to sub-day periods. We see that in this case the tidal decay is still self-limiting: As the inner planets decay further, the effects of short-range forces become important, which forces the inner planet to attain much lower $e_{1,\text{forced}}$ (see Eq. 4.40) that dramatically slows down the rate of tidal decay.

4.3.2 Criteria for Orbital Decay

The analysis and examples shown in Section 4.3 show that generally, two criteria must be met in order for the inner planet to undergo substantial tidal decay: (i) the total angular momentum deficit (AMD)¹ of the system $\text{AMD} \simeq L_2 e_{2,0}^2/2$ must be sufficiently large to allow the inner system to undergo orbital decay before all the eccentricities are decayed away. (ii) The inner planet must have sufficiently large forced eccentricity such that the orbital decay occurs within the lifetime of the system. The first criterion arises from the conservation of the total angular momentum. Indeed, for $e_i^2 \ll 1$, the

¹The AMD of a system is given by the difference between its total angular momentum if all planet orbits were circular and its actual angular momentum, i.e. $\text{AMD} \equiv \sum_i m_i \sqrt{GM_\star a_i} (1 - \cos \theta_i \sqrt{1 - e_i^2})$.

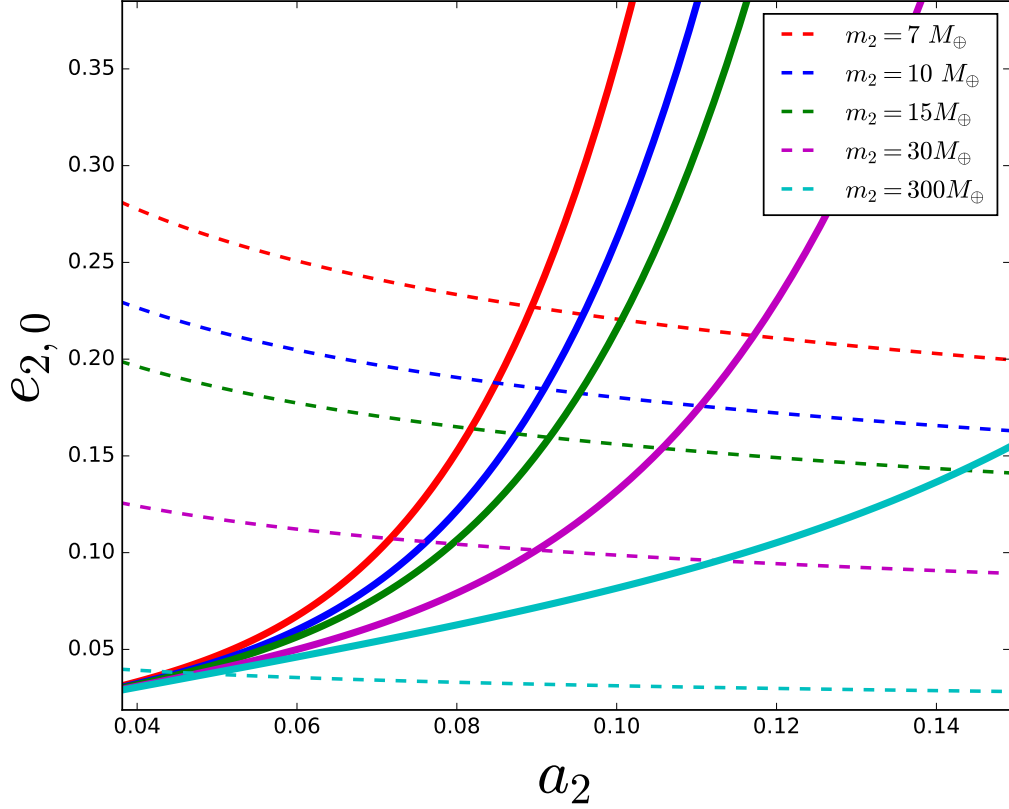


Figure 4.3: The critical eccentricity $e_{2,0}$ needed to meet the AMD (dashed curves) and tidal decay time constraints (solid curves) for USP formation in a two-planet system is plotted as a function of the companion semi-major axis a_2 . The inner planet has initial semi-major axis $a_{1,0} = 0.03$, mass $m_1 = M_\oplus$, radius $R_1 = R_\oplus$, and tidal lag time $\Delta t_{L,1} = 100$ s. The dashed curve are given by Eq. (4.46), corresponding to $a_{1,\min}/a_{1,0} = \frac{1}{2}$, while the solid curves are given by Eq. (4.47), corresponding to $|\dot{a}_1/a_1| \gtrsim 10^{-10}$ yr. The red, blue, green, magenta and cyan curves correspond to $m_2 = 7, 10, 15, 30$ and $300 M_\oplus$ respectively. For a given m_2 , in order for efficient orbital decay to occur, the outer planet's initial eccentricity must be above both curves of the corresponding color.

total angular momentum $L = \sum_i L_i \sqrt{1 - e_i^2} \simeq \sum_i L_i (1 - e_i^2/2)$ (with $L_i = m_i \sqrt{GM_\star a_i}$) evolves according to

$$\frac{dL}{dt} = L_1 \frac{\dot{a}_1}{2a_1} - \sum_i L_i \text{Re}(\dot{\mathcal{E}}_i \mathcal{E}^*), \quad (4.42)$$

where we have omitted the orbital decay of the other planets. Substituting Eqs. (4.2) - (4.3), and noting that $L_1 v_{12} = L_2 v_{21}$, we find that

$$\frac{dL}{dt} = -\frac{L_1}{2} \gamma_\star. \quad (4.43)$$

Thus L is constant when γ_\star is negligible (which is the case until a_1 is already reduced to a value well below 0.02 au by planetary tides). The semi-major axis of the inner planet decreases at the expense of the planet eccentricities, while keeping the total angular momentum constant. Assuming initially $e_{1,0} = 0$, we have

$$m_1 \sqrt{a_{1,0}} + m_2 \sqrt{a_2(1 - e_{2,0}^2)} = m_1 \sqrt{a_1(1 - e_1^2)} + m_2 \sqrt{a_2(1 - e_2^2)}. \quad (4.44)$$

For a given $a_{1,0}$, a_2 (= const.) and $e_{2,0}$, the minimum semi-major axis the inner planet can reach (after indefinite time) is given by

$$\frac{a_{1,\min}}{a_{1,0}} = \left[1 - \frac{m_2 \sqrt{a_2}}{m_1 \sqrt{a_{1,0}}} \left(1 - \sqrt{1 - e_{2,0}^2} \right) \right]^2 \simeq \left(1 - \frac{m_2 \sqrt{a_2} e_{2,0}^2}{2m_1 \sqrt{a_{1,0}}} \right)^2. \quad (4.45)$$

Thus, the critical initial eccentricity of m_2 required for significant semi-major axis decay ($a_{1,\min}/a_{1,0} \simeq \frac{1}{2}$) is given by

$$e_{2,\text{crit}} = \left(2 - \sqrt{2} \right)^{1/2} \left(\frac{m_1}{m_2} \right)^{1/2} \left(\frac{a_{1,0}}{a_2} \right)^{1/4} \simeq 0.77 \left(\frac{L_{1,0}}{L_2} \right)^{1/2}. \quad (4.46)$$

The second criterion pertains to the orbital decay timescale. In order for a_1 to decrease significantly within 10^{10} yrs, the inner planet must have (see Eq. 4.12)

$$\begin{aligned} e_1 &\gtrsim 4.6 \times 10^{-3} \left(\frac{\Delta t_{L,1}}{100s} \right)^{1/2} \left(\frac{M_\star}{M_\odot} \right) \\ &\times \left(\frac{m_1}{M_\oplus} \right)^{-1/2} \left(\frac{R_1}{R_\oplus} \right)^{5/2} \left(\frac{a_1}{0.02 \text{ au}} \right)^4. \end{aligned} \quad (4.47)$$

The above requirement is in fact overly conservative, since the rate of semi-major axis decay tends to accelerate as a_1 decreases until short-ranged forces become dominant (see Eq. 4.12). Using $e_1 \simeq e_{1,\text{forced}}$ (Eq. 4.51), Eq. (4.47) translates into another constraint on $e_{2,0}$ as a function of $a_2/a_{1,0}$.

Thus, in the 2-planet case, the formation of USPs is limited by two constraints given by Eq. (4.46) (the AMD constraint) and Eq. (4.47) (with $e_1 = e_{1,\text{forced}}$, the decay time constraint). These constraints are shown in Fig. 4.3. The combination of these two constraints make the formation of USPs from 2-planet progenitor systems a challenging prospect; one natural way around the two barriers is to consider the effects of an additional external planet - we examine the 3-planet case in section 4.4.

4.4 Three-Planet Systems

4.4.1 Set-up

In this section we perform a systematic study of USP formation in 3-planet systems. The goal here is to gain physical insights on the dynamical evolution of such systems. In section 4.6 we perform population synthesis model to assess whether our model can reproduce the observed USP demographics.

We consider a 3-planet systems where the proto-USP has an initial semi-major axis $a_{1,0}$ in the range between 0.02 and 0.04 au, corresponding roughly to a period of $P_{1,0} = 1 - 3$ days. The proto-USP is assumed to have an Earth-like composition with radius $R_1 \in [1, 1.4] R_\oplus$ with mass given by $m_1 = (R_1/R_\oplus)^4 M_\oplus$, a scaling consistent with purely rocky compositions (Zeng et al., 2016). The tidal lag time $\Delta t_{L,1}$ is taken to

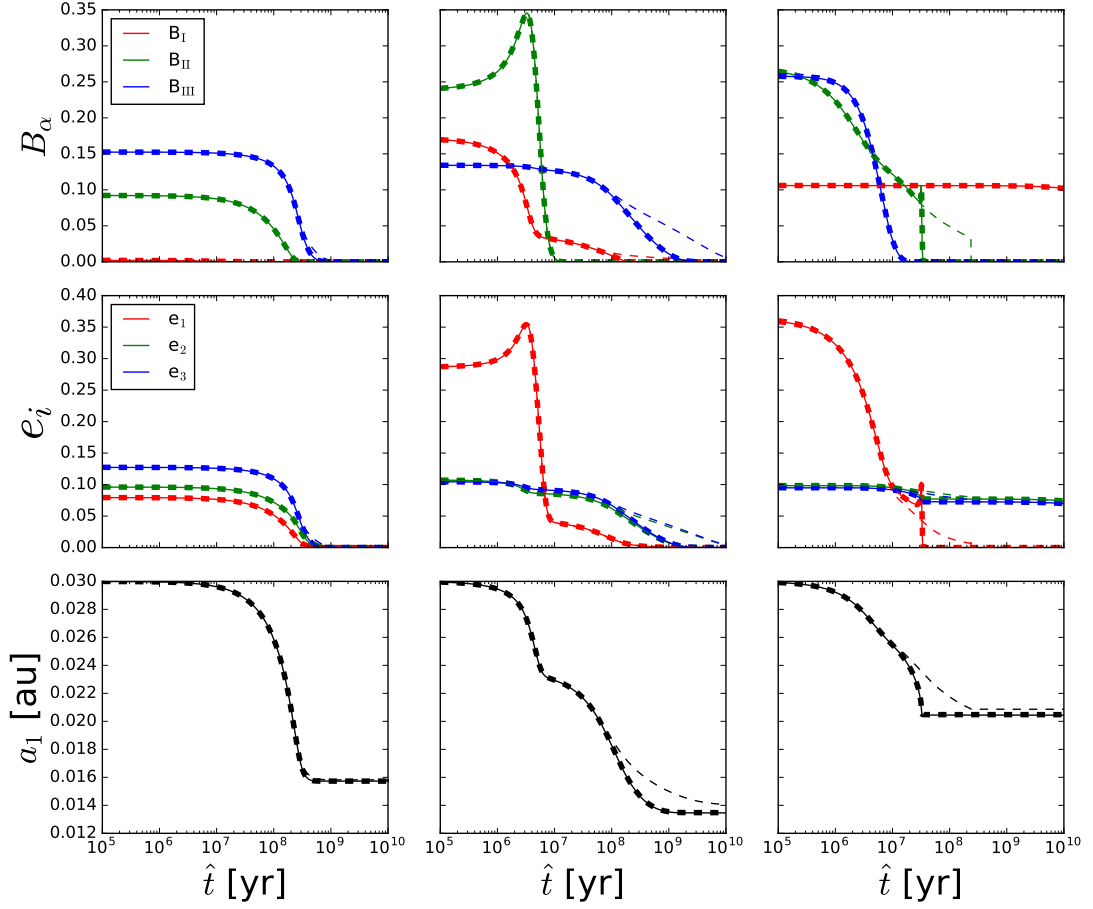


Figure 4.4: Planet eigenmode amplitudes B_α (top), eccentricities e_i (middle) and inner planet semi-major axis a_1 (bottom) as a function of scaled time for three different three-planet systems. Here, the time evolution is obtained from Eq. (4.28). The thick dashed, thin solid and thin dashed lines correspond to values of $\Delta t_{L,1} = 10^2, 10^3$ and 10^5 s respectively. The time is scaled as $\hat{t} \equiv (\Delta t_{L,1}/100\text{s}) t$. For the top three panels, the red, green and blue curves correspond to modes I, II and III respectively, while for the middle panels they correspond to e_1 , e_2 and e_3 . The three columns have different values of a_2 (0.043, 0.059 and 0.089 au respectively, from left to right), but otherwise identical parameters. The planets have masses $m_1 = M_\oplus$ and $m_2 = m_3 = 17M_\oplus$ and initial semi-major axes $a_{1,0} = 0.03$ au and $a_3 = 0.10$ au. The inner planet's radius is $R_1 = R_\oplus$, and stellar dissipation is neglected ($\gamma_\star = 0$). The initial planet eccentricities are given by $e_{1,0} = 0$ and $e_{2,0} = e_{3,0} = 0.15$, with the initial longitude of pericenter for all three planets set to $\varpi_{i,0} = 0$.

be 100 or 1000 s, corresponding to $Q_1 = 70$ and 7 (at $P_1 = 1$ day). The outer planets have semi-major axis $a_2, a_3 \in [0.04, 0.2]$ au, masses $m_2, m_3 \in [3, 30] M_\oplus$ and initial eccentricities $e_{2,0} = e_{3,0} \in [0.05, 0.3]$, and their tidal dissipation is neglected. Note that these system parameters are chosen expediently to showcase the evolution behavior when mode mixing occurs. Some of the illustrated systems may be dynamically unstable; to test for this possibility, we performed numerical N-body integrations for two of the example systems mentioned in Sec. 4.4.2. The implications of dynamical stability on USP generation at the population level is discussed in Sec. 4.6.

As discussed in section 4.2.1, due to the “stiffness” of Eqs. (4.2) and (4.14), we integrate Eq. (4.28) for all our systems. For comparison purposes, we also integrate the set of systems using Eq. (4.2), but with an enhanced value of $\Delta t_{L,1} = 10^5$ s, corresponding to an initial value of $Q_1 = 0.07$ (at $P = 1$ day); these integrations are compared to our approximate method (based on Eq. 4.28) using the same value of $\Delta t_{L,1}$. We find that our approximate formulation achieves excellent results across the entire parameter space we consider.

Note that the time evolution of systems with artificially reduced values of Q_1 cannot simply be considered time-scaled versions of systems with more realistic values of Q_1 : when $Q_1 \lesssim 1$, the presence of a large imaginary component to the matrix $\mathbf{H}(t)$ substantially modifies the structure of eigenmodes, causing the inner planet eccentricity to become quantifiably different. We demonstrate this in section 4.4.2.

4.4.2 Time Evolution & Mode Mixing

For the 3-planet case, the evolution in the framework of eigenmodes becomes considerably more complicated, and explicit analytic expressions are no longer possible.

Instead, one must resort to numerical solution for the eigenfrequencies and eigenmodes. Nonetheless, the general features from the 2-planet case carry over. The mode associated with the free eccentricity oscillation of the inner-most planet tends to be damped away rapidly, while the other two modes damp on much longer timescales. However, during the evolution the eigenvalues of the three modes may cross one another, leading to substantial mode mixing. Such mixings correspond to secular resonances, causing an enhancement in the eccentricity of the inner planet and potentially speeding up its orbital decay by orders of magnitude (see also Hansen and Murray, 2015). This effect is most prominent when L_1 is much less than L_2 or L_3 (Pu and Lai, 2018).

In Fig. 4.4, we depict some examples of the time-evolution of the mode amplitudes (B_I, B_{II}, B_{III}), the eccentricities (e_1, e_2, e_3) and the inner planet semi-major axis $a_1(t)$ for three hypothetical proto-USP systems. The three systems have the same parameters and initials conditions except for different values of a_2 . For each system, we consider three values of $\Delta t_{L,1} \in [10^2, 10^3, 10^5]$ s, corresponding to $Q_1 = [70, 7, 0.07]$ (at a period $P_1 = 1$ day). Notice that for the cases with $\Delta t_{L,1} = 10^2, 10^3$ s, the curves (with a scaled time axis) lie right on top of each other; this shows that as long as $Q_1 \gtrsim 1$, inner planets with different values of Q_1 will undergo identical time evolutions if the time is scaled as $\hat{t} = t(\Delta t_{L,1}/100\text{s})$. On the other hand, the case with $\Delta t_{L,1} = 10^5$ s (the thin dashed lines in Fig. 4.4), corresponding to an unphysical value of $Q_1 = 0.07$ (at $P = 1$ day), shows qualitatively different eccentricity and time evolutions. This demonstrates that for our parameter space, a naive approach of simply integrating Eq. (4.2) directly with re-scaled values of $Q_1 \ll 1$ would give rise to incorrect results.

We now focus on the two cases with physical values of $\Delta t_{L,1}$ (10^2 and 10^3 s), i.e. the thick dashed and thin solid lines of Fig. 4.4. In Fig. 4.5 we show the evolution of the eigenvalues and eigenmodes for the same systems. In the left column, the system

displays no mode mixing, each mode decays independently and the proto-USP reaches a final value of $a_{1,f} = 0.016$ au. In the middle column (with $a_2 = 0.059$ au), a resonance occurs between the two faster modes at $a_1 \simeq 0.027$ au (see Fig. 4.5), this causes e_1 to increase temporarily, followed by a rapid decrease in both e_1 and a_1 . After passing this resonance, the system continues to evolve, with each mode decaying independently until reaching a final value of $a_{1,f} \simeq 0.014$ au². In the right column (with $a_2 = 0.087$ au), the modes initially decay smoothly and independently of each other. A resonant mode crossing occurs at $a_1 \simeq 0.021$ au between the two slower modes. This causes e_1 to reverse course and increase sharply, followed by a rapid decrease in both e_1 and a_1 . The inner planet reaches a final $a_{1,f} \simeq 0.021$ au.

To show that our method accurately captures the evolution of a resonant system, in Fig. 4.6 we show a comparison of the right panels of Fig. 4.4 - 4.5 with the result obtained by a brute force computation using the exact Eq. (4.2), a result which took 5 days to complete on a Ryzen 1700 processor. Overall, there is an excellent agreement between our approximate results and the results obtained by the brute-force integration of Eq. (4.2).

In order to rule out the potential for dynamical instability due to non-secular effects not captured by our method, we integrated the two systems corresponding to the left and central columns of Figs. 4.3 - 4.5 using the WHFast algorithm (Rein and Tamayo, 2015) from the REBOUND integrator (the example system in the right panels is unstable due to the orbits of planets 2 and 3 being too close). The systems were integrated for 10 Myr with a timestep of $dt = 5 \times 10^{-5}$ yr. The initial longitudes of periapsis ϖ_i and true anomaly f_i for each planet were chosen randomly between 0 and 2π . We found that both systems were stable at the end of the simulation; the semi-major axes of all the planets

²Note that a second resonance between the faster modes occurs at $a_1 \simeq 0.014$ au; however, this does not influence the evolution because both modes have decayed to very small amplitudes by this point.

stayed to within 10^{-4} of their original values, suggesting minimal non-secular effects. Planet eccentricities had decayed noticeably ($\gtrsim 5\%$) by this time, which suggests that further instabilities are highly unlikely.

Although the presence of the secular resonance can help to speed up tidal evolution of proto-USP systems, it is not a necessary condition to form USPs. In the next section, we discuss the conditions under which USPs may form in 3-planet systems.

4.4.3 Criteria for Orbital Decay

As in the 2-planet case (section 4.3), the formation of USPs is constrained by two factors: (i) The amount of the total AMD to sustain the orbital decay, and (ii) the amount of forced eccentricity of the proto-USP in order to have tidal decay occur within the lifetime of the system. Angular momentum conservation implies that the minimum semi-major axis that can be attained by the inner planet is (cf. Eq. 4.45)

$$\left(\frac{a_{1,\min}}{a_{1,0}}\right) \simeq \left(1 - \frac{\sum_{i \geq 2} \sqrt{a_i} m_i e_{i,0}^2}{2m_1 \sqrt{a_{1,0}}}\right)^2. \quad (4.48)$$

Therefore, to achieve $a_{1,\min}/a_{1,0} \lesssim \frac{1}{2}$, one requires (assuming $e_{2,0} \sim e_{3,0}$)

$$e_{2,0} \sim e_{3,0} \gtrsim 0.77 \left(\frac{m_1 \sqrt{a_{1,0}}}{\sum_{i \geq 2} \sqrt{a_i} m_i}\right)^{1/2}. \quad (4.49)$$

At the same time, analogous to the 2-planet case, to have efficient orbital decay within the lifetime of the system, Eq. (4.47) must be satisfied. In the case of 3 planets, the inner planet forced eccentricity can no longer be expressed in a simple expression; one must solve numerically the eigenvalues and eigenvectors; the forced eccentricity can be obtained from the amplitudes of the two slower decaying modes

$$e_{1,\text{forced}} = \left(\sum_{\alpha \geq \text{II}} |A_\alpha| |\mathcal{E}_{\alpha 1}| \right)^{1/2}. \quad (4.50)$$

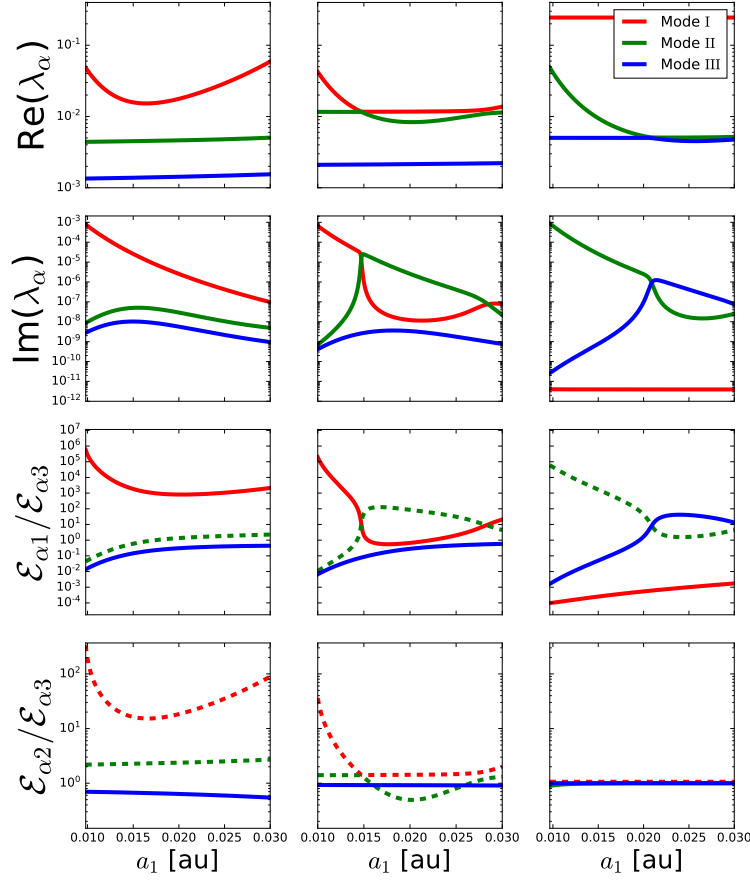


Figure 4.5: Mode structure for the three different systems depicted in Fig. 4.4. The red, green and blue curves correspond to modes I, II and III respectively. For each of the three columns, the top panel shows the real component of the eigenfrequency of the α -th mode ω_α as a function of inner planet semi-major axis a_1 , while the middle-upper subpanel shows the imaginary component of the eigenvalue γ_α . The bottom-middle subpanel shows $\epsilon_{\alpha 1}/\epsilon_{\alpha 3}$ and the bottom subpanel shows $\epsilon_{\alpha 2}/\epsilon_{\alpha 3}$. For the bottom two panels, the solid lines represent positive values while dashed lines represent negative values on the log-axis plot. The columns from left to right show three different cases for mode crossings: In the left column, the modes are well-separated and no mixing occurs; in the middle column, modes I and II show a mixing around $a_1 \approx 0.027$ au and $a_1 \approx 0.014$ au; in the right column, modes II and III cross one another at $a_1 \approx 0.022$ au.

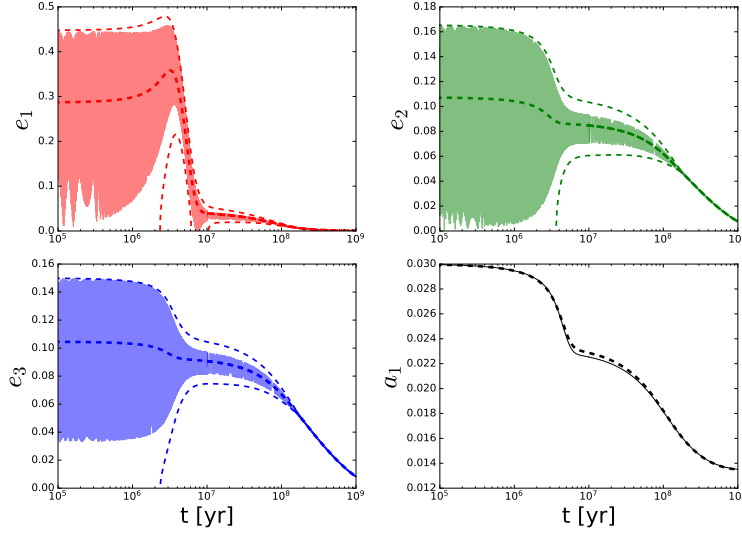


Figure 4.6: Eccentricities e_i and semi-major axis of the innermost planet a_1 as a function of time for the three-planet system corresponding to the right panels of Fig. 4.4 - 4.5, with $\Delta t_{L,1} = 100$ s; the dashed curves represent the results of our approximate method based on Eq. (4.28) while the solid lines are the results of a direct integration of Eq. (4.2). The thick dashed curve show the values of $\langle e_i^2 \rangle^{1/2}$ (Eq. 4.27) while the two thin dashed lines show the maximum and minimum eccentricities given by Eq. (4.30) - (4.31). Note that there is some disagreement between the maximum and minimum values of our approximate method and the brute force calculation due to the fact that the system has insufficient time to reach the theoretical long-term extrema due to the rapid orbital decay.

Since A_α is determined from the initial values of $e_{2,0}$ and $e_{3,0}$, the constraint on the inner planet eccentricity corresponds to a constraint on the external planet eccentricities. In the limit that $L_3 \gg L_2, L_1$, an approximate expression for the forced eccentricity is given by (see Pu and Lai, 2018)

$$e_1 \simeq e_{1,\text{forced}} = \left(\frac{\nu_{12}\omega_2 + \nu_{12}\nu_{23}}{\omega_1\omega_2 - \nu_{12}\nu_{21}} \right) e_3. \quad (4.51)$$

The above equation is more accurate when the planets are spaced evenly and well-separated, and does not fully capture the resonant mode crossings. In general, $e_{1,\text{forced}}$ tends to be greater than given by the expression above, due to the contribution of other

modes and aforementioned resonances.

In Fig. 4.7, we show the two constraints for USP formation in three-planet systems; this figure is analogous to Fig. 4.3, except with the addition of a third planet (with $m_3 = m_2$ and fixed a_3). We find two important differences between the constraints for two-planet systems (see Fig. 4.2) and three-planet systems: (i) *ceteris paribus*, the presence of an additional planet lowers the eccentricity values ($e_{2,0}, e_{3,0}$) required to meet the AMD constraint; (ii) the decay time constraint can be met by a larger set of values of a_2 and $e_{3,0}$, since the presence of two secular resonances makes it possible for $e_{1,\text{forced}}$ to be large even for smaller values of $e_{2,0}$ and $e_{3,0}$.

In general, for three-planet systems, the AMD constraint is more stringent than the decay time constraint. To illustrate this, we show the final value of $a_{1,f}$ reached after 10 Gyr of evolution as a function of a_2 in Fig. 4.8 for three-planet systems with varying initial values of $a_{1,0}$, with the planet masses, a_3 and $e_{2,0} = e_{3,0}$ fixed. The dashed curves in Fig. 4.8 correspond to the minimum possible value of $a_{1,f}$ given by the AMD constraint, while the solid curves are their actual values at the end of the evolution. For systems with $e_{3,0} \lesssim 0.1$, the solid curve comes very close to the dashed curve, indicating that the orbital decay of a_1 is being stalled by a lack of AMD. For systems with $e_{3,0} \gtrsim 0.15$, the orbital decay instead becomes time-limited.

The fact that USP production is more constrained by AMD has certain observational implications. One would expect USPs to be systematically lower in mass, as lower-mass inner planets are more likely to meet the AMD constraint (see Eq. 4.49). At the same time, we expect the external companions of USPs to have systematically larger masses, although giant planet companions are not required. To generate USPs efficiently, we also require the primordial planet eccentricities to be $e_{2,0} \sim e_{3,0} \gtrsim 0.1$, although their final values can be much lower due to tidal dissipation. The observational implications are

explored in more detail in section 4.6, where we develop a population model for USP generation.

In this section, we have explored USP formation from three-planet systems. At first glance, there is a tension between USP generation from multi-planet systems and the fact that observed USPs have a dearth of exterior transiting companions compared with their non-USP counterparts. This *prima facie* contradiction can be rectified when we consider the mutual inclination evolution of USP-forming systems, in section 4.5.

4.5 Inclination Evolution

We are interested in the inclination evolution of the proto-USP system because the evolution of the mutual inclination of planets determine the extent to which USPs will transit simultaneously with their companions, a quantity that can be observationally constrained (see Sec. 4.6). As we shall demonstrate in this section, there exists a secular mutual inclination ‘resonances’ that roughly coincides with the secular eccentricity resonance; systems that result in large excitations in eccentricity (and therefore forming USPs) should also expect large excitations in mutual inclination.

The inclination evolution of the proto-USP system proceeds in an analogous fashion as the eccentricity evolution. We define the complex variable $\mathcal{I}_j = \theta_j \exp(i\Omega_j)$ for each planet, where θ_j is the orbital inclination (relative to the initial orbital plane) and Ω_j is the longitude of the ascending node. The mutual inclination θ_{ij} between planets i and j is given by

$$\theta_{ij}(t) = |\mathcal{I}_i(t) - \mathcal{I}_j(t)|. \quad (4.52)$$

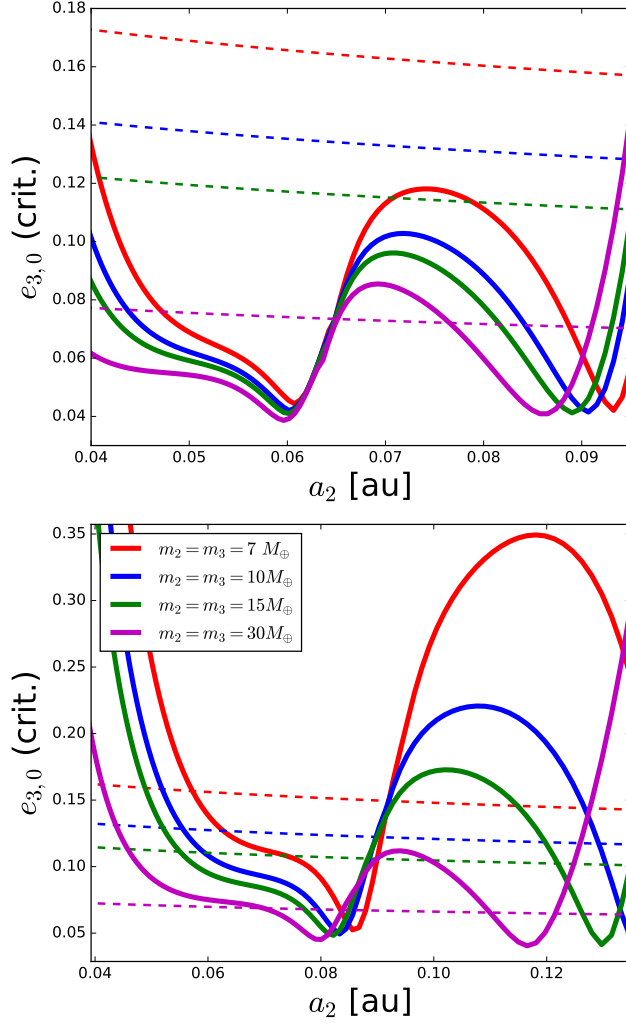


Figure 4.7: Similar to Fig. 4.3, except here the system has 3 planets. The semi-major axis of the 3rd planet is fixed at $a_3 = 0.10$ au in the top panel, and $a_3 = 0.15$ au in the bottom panel. The dashed curves (AMD constraint) are given by Eq. (4.49) while the solid curves (decay time constraint) are given by Eqs. (4.47) and (4.50), with the eigenvectors being solved numerically and assuming that $e_{2,0} = e_{3,0}$. The two dips in the solid curves correspond to the two resonant mode crossings discussed in section 4.4.2. For a given $m_2 = m_3$, in order for efficient orbital decay to occur, the outer planet's initial eccentricities must be above both curves of the corresponding color. Note that some values of a_2 may result in dynamically unstable systems.

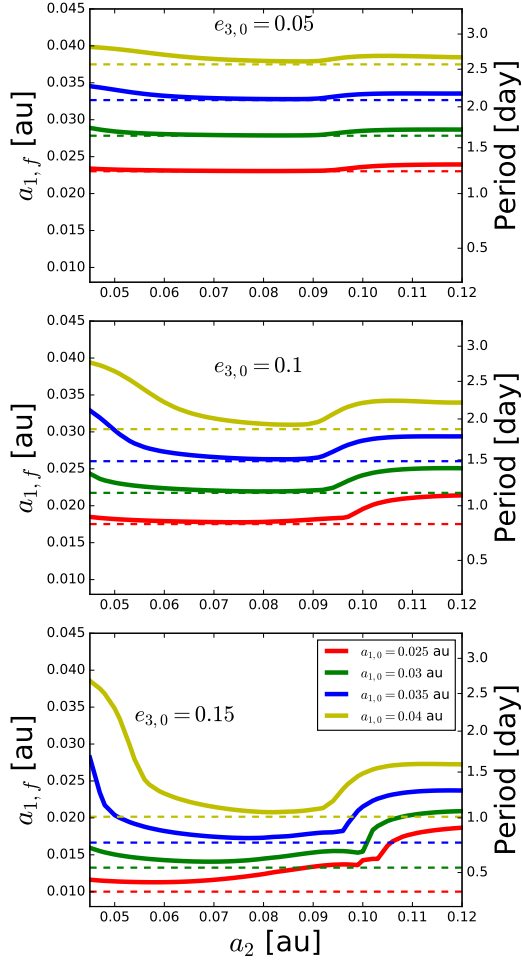


Figure 4.8: The final value of $a_{1,f}$ after 10 Gyr of evolution in a three-planet system (solid curves) and its theoretical minimum dictated by the AMD constraint (dashed curves, Eq. 4.48), plotted as a function of a_2 . The inner planet has mass $m_1 = M_\oplus$, radius $R_1 = R_\oplus$ and tidal lag time $\Delta t_{L,1} = 100$ s, while the outer planets have $m_2 = m_3 = 13M_\oplus$. The three panels correspond to different initial values of $e_{2,0} = e_{3,0}$ (with initially aligned pericenters), as indicated. For each panel, the semi-major axis of the outer planet is fixed at $a_3 = 0.15$ au, while a_2 is varied; the red, blue, green and yellow curves correspond to $a_{1,0} = 0.025, 0.03, 0.035$ and 0.04 au respectively. Regions where the solid curves lie on top of the dashed curves indicate the system is AMD-constrained, while regions where the solid curve is well separated from the dashed curve correspond to tidal decay time-constrained systems.

For convenience we define the inclination of the N-planet system as

$$\vec{\mathcal{I}} = \begin{pmatrix} \mathcal{I}_1 \\ \mathcal{I}_2 \\ \vdots \end{pmatrix}. \quad (4.53)$$

For small inclinations (i.e. $\theta_i \ll 1$) the time evolution of $\vec{\mathcal{I}}$ is governed by

$$\frac{d}{dt} \vec{\mathcal{I}}(t) = i \mathbf{H}'(t) \vec{\mathcal{I}}(t) + i \vec{\omega}_\star \mathcal{I}_\star, \quad (4.54)$$

where \mathcal{I}_\star is the complex obliquity of stellar spin. In Eq. (4.54), the first term in the RHS is due to secular planet-planet interactions, while the second term accounts for the nodal precession driven by the stellar spin; the vector $\vec{\omega}_\star$ is given by

$$\vec{\omega}_\star = \begin{pmatrix} \omega_{1\star} \\ \omega_{2\star} \\ \vdots \end{pmatrix}. \quad (4.55)$$

The $N \times N$ matrix $\mathbf{H}'(t)$ is given by

$$\mathbf{H}'(t) = \begin{pmatrix} -\omega'_1 & \omega_{12} & \cdots & \omega_{1N} \\ \omega_{21} & -\omega'_2 & \cdots & \omega_{2N} \\ \vdots & \vdots & \ddots & \vdots \\ \omega_{N1} & \omega_{N2} & \cdots & -\omega'_N \end{pmatrix} \quad (4.56)$$

where ω_{ij} is given by Eq. (4.5), and

$$\omega'_i = \sum_{j \neq i} \omega_{ij} + \omega_{i\star}. \quad (4.57)$$

We also need to account for the evolution of stellar spin, governed by

$$\frac{d\mathcal{I}_\star}{dt} = i \sum_j \omega_{\star j} \mathcal{I}_j. \quad (4.58)$$

The nodal precession rate of the i -th planet driven by the stellar spin-induced quadrupole is

$$\omega_{i\star} = \frac{3k_{q\star}}{2k_\star} \left(\frac{m_i}{M_\star} \right) \left(\frac{R_\star}{a_i} \right) \left(\frac{S_\star}{L_i} \right) \Omega_\star = 2.7 \times 10^{-5} \left(\frac{k_{q\star}}{0.01} \right) \times \left(\frac{a_i}{0.02\text{au}} \right)^{-7/2} \left(\frac{M_\star}{M_\odot} \right)^{-1/2} \left(\frac{R_\star}{R_\odot} \right)^5 \left(\frac{P_\star}{30\text{days}} \right)^{-2} \text{yr}^{-1}, \quad (4.59)$$

where M_\star , R_\star and $\Omega_\star = 2\pi/P_\star$ are the stellar mass, radius and angular rotation frequency respectively. The constants k_\star and $k_{q\star}$ are defined through the star's moment of inertia and quadrupole moment: $I_{\star 3} = k_\star M_\star R_\star^2$ and $I_{\star 3} - I_{\star 1} = k_{q\star} \hat{\Omega}_\star^2 M_\star R_\star^2$ where $\hat{\Omega}_\star^2 = \Omega_\star (GM_\star/R_\star^3)^{-1/2}$. Typical values for solar type stars are $k_\star \simeq 0.06$ and $k_{q\star} \simeq 0.01$ (e.g. Lai et al., 2018). The ratio of the stellar spin angular momentum $S_\star = I_{\star 3} \Omega_\star$ to the orbital angular momentum of the i -th planet L_i is

$$\frac{S_\star}{L_i} = 35 \left(\frac{k_\star}{0.06} \right) \left(\frac{m_i}{M_\oplus} \right)^{-1} \left(\frac{a_i}{0.02\text{au}} \right)^{-1/2} \left(\frac{M_\star}{M_\odot} \right)^{1/2} \left(\frac{R_\star}{R_\odot} \right)^2 \left(\frac{P_\star}{30\text{days}} \right)^{-1}, \quad (4.60)$$

The precession rate of the stellar spin driven by the i -th planet is

$$\omega_{\star i} = \omega_{i\star} \frac{L_i}{S_\star} = 7.7 \times 10^{-7} \left(\frac{6k_{q\star}}{k_\star} \right) \left(\frac{m_i}{M_\oplus} \right) \times \left(\frac{a_i}{0.02\text{au}} \right)^{-3} \left(\frac{M_\star}{M_\odot} \right)^{-1} \left(\frac{R_\star}{R_\odot} \right)^3 \left(\frac{P_\star}{30\text{days}} \right)^{-1} \text{yr}^{-1}. \quad (4.61)$$

For small planets ($m_1 \ll 35M_\oplus$) at $P_1 \sim 1$ day periods, the stellar spin angular momentum is much greater than the orbital angular momentum. Thus we can assume the stellar spin axis constantly points towards the \hat{z} -axis, i.e. $\mathcal{I}_\star \simeq 0$.

The rotation rate of the star Ω_\star decreases due to magnetic braking. According to Skumanich (1972), $\dot{\Omega}_\star \propto -\Omega_\star^3$, so that the time evolution of the spin rate is given by

$$\Omega_\star = \frac{\Omega_{\star,0}}{\sqrt{1 + \alpha_{\text{MB}} \Omega_{\star,0}^2 t}}, \quad (4.62)$$

where $\Omega_{\star,0}$ is the initial spin rate, and α_{MB} is a constant, calibrated such that the rotation period reaches ~ 30 days at an age ~ 5 Gyr. For this section, we adopt a constant value

of Ω_\star in lieu of the Skumanich law to better control for the effect of stellar spin; the effect of a time-dependent stellar spin period is left for section 4.6.

The above equations, coupled with the time-evolution of the planet eccentricities e_i and inner planet semi-major axis a_1 fully describes the inclination evolution of the system in the linear regime ($e_i, \theta_i \ll 1$). Analogous to the case of eccentricity evolution, Eq. (4.54) involves terms that oscillate rapidly compared with the timescale of orbital decay, leading to a ‘stiff’ set of equations that resists brute-force simulations. In section 4.5.1 we address this issue by recasting the problem in the framework of eigenmodes.

4.5.1 Inclination Evolution in the Framework of Eigenmodes

In the discussion below we assume that the stellar spin axis is always along the \hat{z} -axis.

In this case Eq. (4.54) simplifies to

$$\frac{d\vec{I}}{dt} \simeq i\mathbf{H}'\vec{I}. \quad (4.63)$$

We define the eigenvalue λ'_α and eigenvector \vec{I}_α with modes denoted using Roman Numerals ($\alpha \in [\text{I}, \text{II}, \text{III} \dots]$) of the system as

$$\mathbf{H}'\vec{I}_\alpha = \lambda'_\alpha\vec{I}_\alpha, \quad (4.64)$$

where we have define the vector eccentricity vector \vec{I} to be

$$\vec{I}_\alpha = \begin{pmatrix} I_{\alpha 1} \\ I_{\alpha 2} \\ \vdots \end{pmatrix}. \quad (4.65)$$

As in section 4.2.1, we introduce the matrices $\mathbf{G}'(t)$ and $\mathbf{V}'(t)$ constructed from the eigenvalues (λ'_α) and eigenvectors (\vec{I}_α) of $\mathbf{H}'(t)$:

$$\mathbf{G}'(t) = \text{diag}(\lambda'_{\text{I}}, \lambda'_{\text{II}}, \dots, \lambda'_{\text{N}}) \quad (4.66)$$

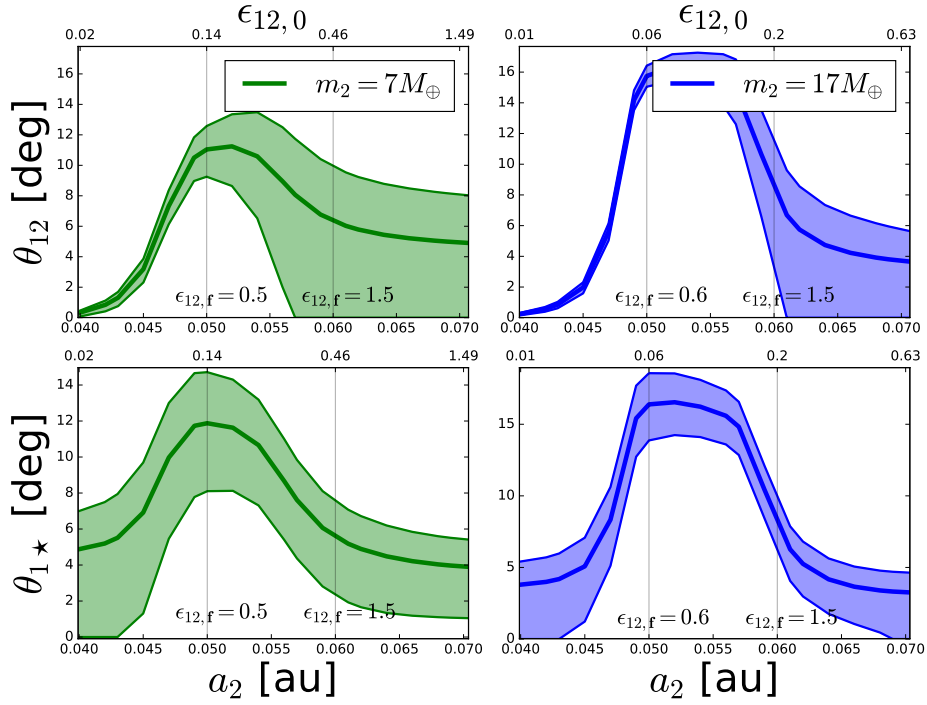


Figure 4.9: Final values of the inner planet mutual inclination $\theta_{12,f}$ (top) and the spin-orbit angle $\theta_{1\star}$ (bottom) as a function of a_2 for a three-planet system with $m_1 = M_{\oplus}$, $m_2 = 7M_{\oplus}$ (green curves, left panels) or $17M_{\oplus}$ (blue curves, right panels) and $m_3 = 17M_{\oplus}$. The initial semi-major axes of the planets are $a_{1,0} = 0.03$ au and $a_3 = 0.10$ au, while a_2 is varied between 0.04 to 0.07 au. The stellar rotation period is set to $P_{\star} = 30$ days. The initial eccentricities are $e_{1,0} = 0$ and $e_{2,0} = e_{3,0} = 0.15$, such that the inner planet reaches $a_{1,f} \approx 0.017$ au after 10 Gyr of tidal decay (note that $a_{1,f}$ can be slightly different for different values of a_2). The initial inclination is given by $I_{1,0} = I_{2,0} = 0$ and $I_{3,0} = 0.075$. The bolded curves are the final RMS values given by Eqs. (4.77) and (4.74) for the top and bottom panels respectively, while the two thin curves are their “instantaneous” maximum and minimum values given by Eqs. (4.75) - (4.76) and (4.78) - (4.79) for the bottom and top panels respectively. The top axis of each panel shows the initial value of $\epsilon_{12,0}$ (Eq. 4.80). The two thin vertical lines show the values of a_2 (or $\epsilon_{12,0}$) that lead to specific values of $\epsilon_{12,f}$ (as indicated).

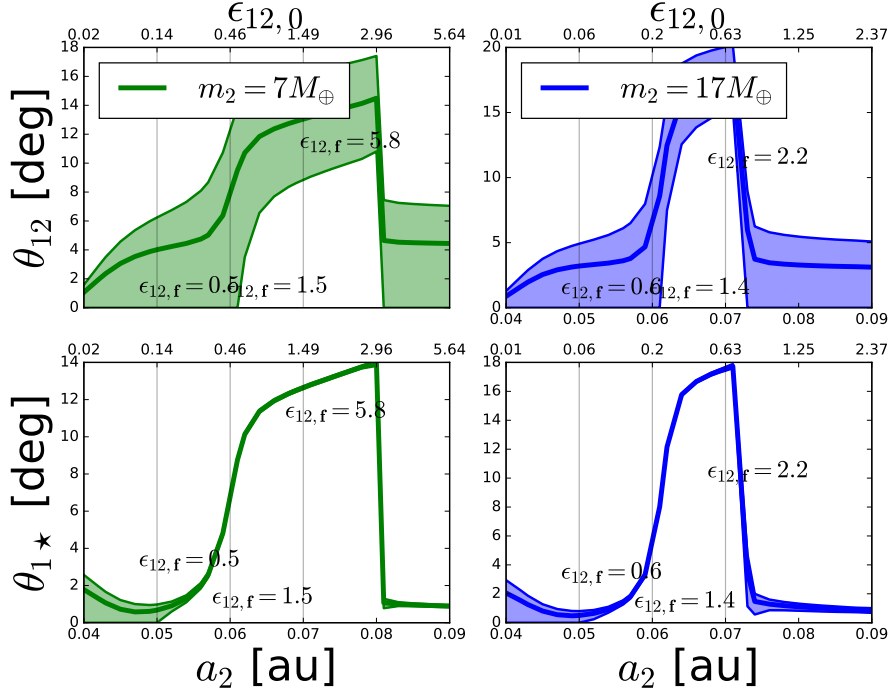


Figure 4.10: Same as Fig. 4.9, except with the stellar spin period fixed at $P_\star = 1$ day.

and

$$\mathbf{V}(t) = \begin{bmatrix} \vec{I}_I & \vec{I}_{II} & \dots & \vec{I}_N \end{bmatrix}. \quad (4.67)$$

The time evolution of \vec{I} can be written as a superposition of eigenmodes

$$\vec{I}(t) = \sum_{\alpha}^N C_{\alpha} \vec{I}_{\alpha} = \mathbf{V}'(t) \vec{C}(t), \quad (4.68)$$

where $\vec{C}(t)$ is the vector of eigenmode amplitudes:

$$\vec{C} \equiv \begin{pmatrix} C_I \\ C_{II} \\ \vdots \end{pmatrix} \quad (4.69)$$

whose initial value $\vec{C}(0)$ is

$$\vec{C}(0) = \mathbf{V}'^{-1}(0) \vec{I}(0). \quad (4.70)$$

The time evolution of \vec{C} is governed by

$$\frac{d\vec{C}}{dt} = [i\mathbf{G}'(t) - \mathbf{V}'^{-1}(t)\dot{\mathbf{V}}'(t)]\vec{C}(t) \equiv \mathbf{W}'(t)\vec{C}(t). \quad (4.71)$$

The above equation is exact. Similar to the case of the eccentricity evolution (section 4.2.1), we bypass the stiffness of the above equation by focusing only the evolution of $D_\alpha \equiv |C_\alpha|$, whose evolution is given by

$$\frac{d\vec{D}(t)}{dt} = -\text{Diag}[\mathbf{W}'(t)]\vec{D}(t). \quad (4.72)$$

Note here that $\mathbf{W}'(t)$ can also depend on the spin-down of the star, i.e.

$$\mathbf{W}' = i\mathbf{G}' - \mathbf{V}'^{-1} \left[\left(\frac{\partial \mathbf{V}'}{\partial a_1} \right) \dot{a}_1 + \left(\frac{\partial \mathbf{V}'}{\partial P_\star} \right) \dot{P}_\star \right]. \quad (4.73)$$

The instantaneous RMS inclination is given by

$$\langle \theta_i^2 \rangle = \left\langle \left| \sum_\alpha C_\alpha(t) \mathcal{I}_{\alpha i}(t) \right|^2 \right\rangle = \sum_\alpha D_\alpha^2(t) |\mathcal{I}_{\alpha i}(t)|^2. \quad (4.74)$$

The “instantaneous” maximum inclination is given by

$$\max(\theta_i) \simeq \sum_\alpha D_\alpha(t) |\mathcal{I}_{i,\alpha}(t)|, \quad (4.75)$$

while the minimum inclination is

$$\min(\theta_i) = \left[2\langle \theta_i^2 \rangle - \max(\theta_i)^2 \right]^{1/2}. \quad (4.76)$$

Using the mode solution, we can also obtain the mutual inclination between planets. The RMS mutual inclination between planets i and j is given by

$$\langle \theta_{ij}^2 \rangle^{1/2} = \sum_\alpha D_\alpha^2 |V'_{i,\alpha} - V'_{j,\alpha}|^2, \quad (4.77)$$

while the maximum and minimum mutual inclinations are respectively given by

$$\max(\theta_{ij}) = \sum_\alpha D_\alpha |V'_{i,\alpha} - V'_{j,\alpha}| \quad (4.78)$$

$$\min(\theta_{ij}) = \left[2\langle \theta_{ij}^2 \rangle - \max(\theta_{ij})^2 \right]^{1/2}. \quad (4.79)$$

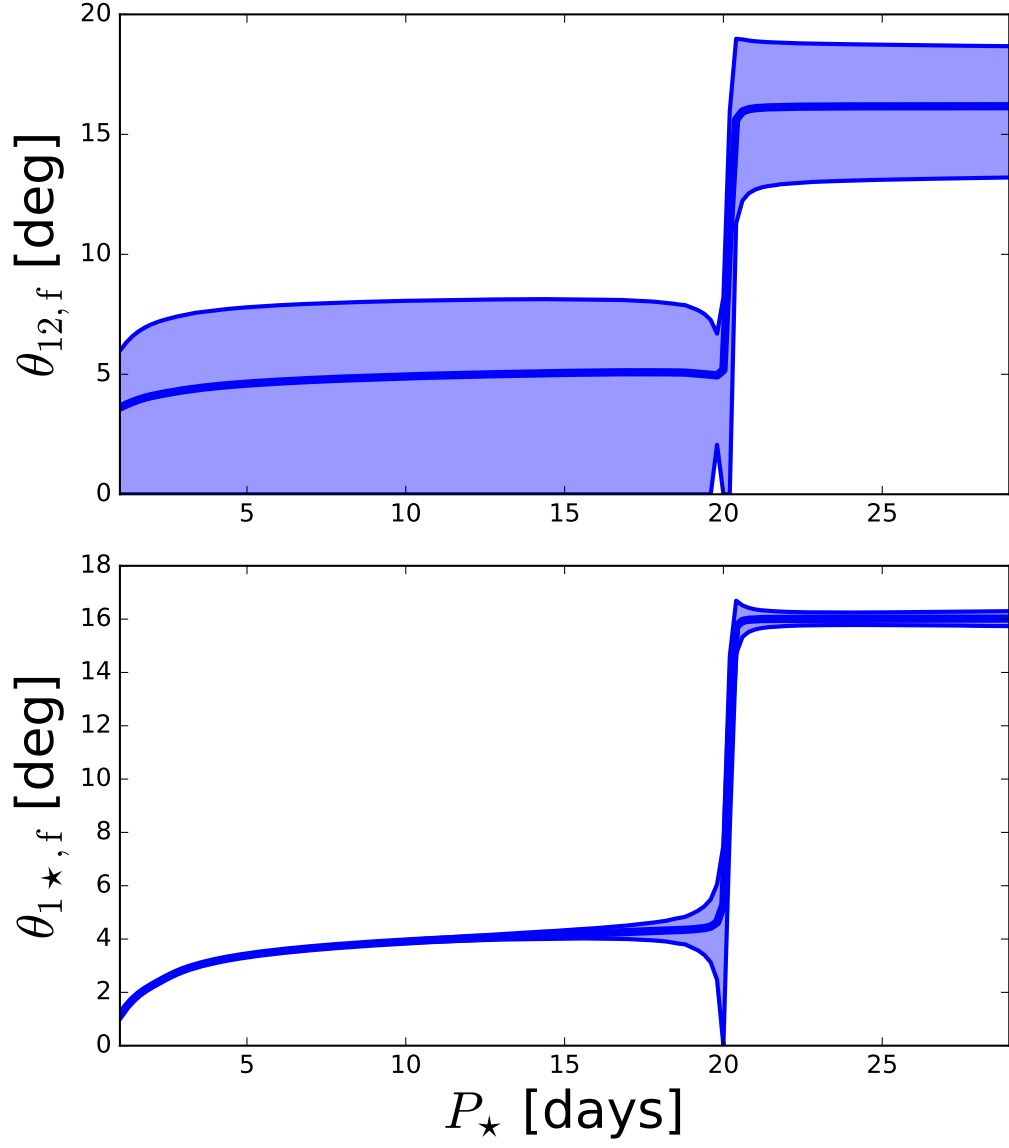


Figure 4.11: Similar to the right panels of Fig. 4.9 (corresponding to $m_2 = 17M_{\oplus}$), except we fix the value of $a_2 = 0.055$ au, and instead vary the value of P_{\star} , which is fixed in time during the evolution.

4.5.2 Resonance Crossing and Mutual Inclination Excitation

Significant mutual inclinations between the inner two planets can be excited when the planet system crosses a secular inclination resonance. When spin-orbit coupling is negligible (i.e. $\omega_{i\star}$ is small), and $L_3 \gg L_1, L_2$, the resonance occurs when the dimensionless “coupling parameter” ϵ_{12} , defined by

$$\epsilon_{12} \equiv \frac{\omega_{23} - \omega_{13}}{\omega_{12} + \omega_{21}} \quad (4.80)$$

is of order unity (see Lai and Pu, 2017). As the innermost planet decays in semi-major axis, the system may transition from $\epsilon_{12} \lesssim 1$ (strong coupling between the inner two planets) to $\epsilon_{12} \gtrsim 1$ (weak coupling), crossing the resonance and generating appreciable mutual inclination θ_{12} . If the orbits of m_1 and m_2 are initially co-planar, and m_3 is initially inclined with the inner two planets at an angle θ_3 , then the typical mutual inclination excited is of order (Pu and Lai, 2018)

$$\theta_{12,f} \sim \theta_3 \sqrt{\frac{L_1}{L_2}}. \quad (4.81)$$

To illustrate the possibility of resonance, in Fig. 4.9 we show the final values of the mutual inclination between the inner two planets ($\theta_{12,f}$), and the angle between the inner planet’s orbit and the spin axis of its host star ($\theta_{1\star,f}$)³ for a USP-forming three-planet system. Note that in the examples shown in Fig. 4.9, the stellar spin period is $P_\star = 30$ days, corresponding to a case where the spin-orbit coupling is negligible ($\omega_{i\star}$ is small). We find that indeed, when the system crosses $\epsilon_{12} \simeq 1$ during orbital decay, large mutual inclinations can be excited between the innermost planet and its companion. Moreover, this excitation is larger when the ratio $m_{1,0}/m_{2,0}$ (and thereby L_1/L_2) is smaller: we find that systems with $m_1 = M_\oplus$ and $m_2 = 17M_\oplus$ achieved a maximum value of $\langle \theta_{12,f}^2 \rangle^{1/2} \approx 16$ deg., compared to $\langle \theta_{12,f}^2 \rangle^{1/2} \approx 11$ deg. for the case of $m_2 = 7M_\oplus$.

³Since the stellar spin axis does not vary in our calculation, this angle is simply $\theta_{1,f}$, the final inclination angle of the planet’s orbit relative to the initial fiducial plane.

When there is more substantial spin-orbit coupling, the mutual inclination evolution is similar, except that the resonance occurs at higher values of ϵ_{12} . To illustrate this, in Fig. 4.10 we show the same examples as Fig. 4.9, except with the stellar spin period fixed at $P_\star = 1$ day, corresponding to strong spin-orbit coupling (large $\omega_{i\star}$). In this case, there is still a resonant excitation in the mutual inclination, except that it happens at much larger values of ϵ_{12} .

This shift of the mutual inclination resonance to higher values of ϵ_{12} can be understood if we consider that resonance occurs when

$$\omega'_1 = \omega_{12} + \omega_{13} + \omega_{1\star} \simeq \omega'_2 = \omega_{21} + \omega_{23} + \omega_{2\star}. \quad (4.82)$$

When spin-orbit coupling is negligible, $\omega_{i\star} \simeq 0$, and the resonance criterion corresponds to $\epsilon_{12} = (1 - L_1/L_2)/(1 + L_1/L_2)$, which is close to unity for $L_1 \ll L_2$. However, as the spin-orbit coupling becomes stronger, the resonance condition becomes $\epsilon_{12} \simeq (1 - L_1/L_2)/(1 + L_1/L_2) + \omega_{1\star}/(\omega_{12} + \omega_{21})$, so the critical ϵ_{12} increases as $\omega_{1\star}$ increases.

Another way to look at the role of spin-orbit coupling is to consider what happens when P_\star changes while fixing the other parameters. In Fig. 4.11, we show the final value of $\theta_{12,f}$ and $\theta_{1\star,f}$ as a function of the value of P_\star (fixed in time during the evolution) for a three-planet system undergoing low- e USP formation. The system has initial parameters chosen such that $\epsilon_{12,0} = 0.1$ and $\epsilon_{12,f} = 1.1$. We find that when $P_\star \geq 20$ days, the system indeed undergoes a secular inclination resonance, reaching a final value of $\langle \theta_{12,f}^2 \rangle^{1/2} \approx 16$ deg. However, as the stellar spin period decreases below $P_\star = 20$ days, there is a sudden transition and the final values of both $\langle \theta_{12,f}^2 \rangle^{1/2}$ and $\langle \theta_{1\star,f}^2 \rangle^{1/2}$ decrease to much lower values. In general, for systems with $\epsilon_{12,0} < 1$ and $\epsilon_{12,f} \sim 1$, the “transition” in Fig. 4.11 occurs when P_\star reaches a value such that $\omega_{1\star,f} \gtrsim \omega_{12,f}$ at the end of orbital decay. In other words, if $\omega_{1\star,f} \gtrsim \omega_{12,f}$, then spin-orbit coupling will suppress any resonant mutual inclination excitation between the innermost planets.

In real systems, the stellar rotation period increases over time, thus the importance of the spin-orbit coupling depends on the timescale of the proto-USP orbital decay: if the orbital decay occurs well within a Gyr, then spin-orbit coupling can be important. Otherwise, the star would have already spun down by the time the final USP semi-major axis is reached, and the effect of spin-orbit coupling is small.

4.6 Population Synthesis Model

We synthesize the results of sections 4.2 - 4.5 by performing a population synthesis calculation of USPs generated through the low-e migration mechanism. Given the inherent uncertainties in various population statistics (of both USPs and larger-period planets), the purpose of this study is not to accurately reproduce all the observed population of USPs. Instead, our goal is to illustrate the statistical trends that would be expected when USPs are generated by low-e migration.

The initial semi-major axis of the inner-most planet a_1 is drawn from a power-law distribution given by

$$\frac{dN}{d \log P_1} \propto P_1^{1.5} \quad (4.83)$$

in the interval $[P_{\min}, P_{\max}]$, with $P_{\max} = 8$ days and $P_{\min} = 0.5, 1.0, 2.0$ and 3.0 days in four separate experiments. The planet's mass m_1 is drawn from a log-uniform distribution between 0.5 and $3.0 M_{\oplus}$. The inner planet's composition is assumed to be Earth-like, with a radius of $R_1 = (m_1/M_{\oplus})^{1/4} R_{\oplus}$ (Zeng et al., 2016); its tidal lag time $\Delta t_{L,1}$ is chosen to be 1000, 100 or 10s, corresponding to $Q_1 = 7, 70$ and 700 for $P_1 = 1$ day. The outer planet masses are drawn from a log-uniform distribution between 3 and $20 M_{\oplus}$. We assign these outer planets ($i \geq 2$) a rocky compositions with a H/He envelope comprising a few percent of its mass, with radii given by $R_i = R_{i,\text{core}} + R_{i,\text{env}} = R_{\oplus}[(m_i/M_{\oplus})^{1/4} + 1.5]$,

and tidal lag times $\Delta t_{L,i} = 1$ or 10 sec, corresponding to $Q_i = 7 \times 10^3, 7 \times 10^4$ for $P_i = 10$ days. The initial semi-major axis of the outer planets are given by the ratios a_2/a_1 and a_3/a_2 , chosen independently on a log-uniform distribution between 1.41 and 3.0, corresponding to period ratios between 1.67 and 5.2. The initial eccentricities of all planets are equal to \bar{e} , which is chosen from a Rayleigh distribution with scale parameter $\sigma_e = 0.10$. The initial complex inclinations \mathcal{I}_j of each planet are chosen from a 2-D Gaussian distribution with mean $\mu = 0$ and variance $\sigma_\theta = \bar{e}/2$; the resulting ratio $e/\theta \simeq 2$ is consistent with equipartition of random velocities suggested by numerical simulations of accreting planetesimals (Kokubo and Ida, 2002). This choice of inclinations is equivalent to a Rayleigh distribution for $|\mathcal{I}_i|$ with scale parameter equal to $\bar{e}/2$ and with the complex argument uniformly distributed between 0 and 2π . We include the effect of tidal decay due to stellar tides, as given by Eq. (4.13). The value of Q'_\star is chosen to be $10^6, 10^7$ or 10^8 . We adopt an initial stellar spin of $P_{\star,0} = 8$ days, subject to the Skumanich law (Eq. 4.62) with $a_{\text{MB}} = 3.2 \times 10^{-14} \text{ yr}^{-1}$ such that the stellar spin period lengthens to $P_\star = 30$ days at $t = 5$ Gyr.

We account for the possibility of dynamically unstable systems. A system of N planets on initially circular orbits is stable up to $\tau \equiv t/P_1$ orbits if the spacing satisfies $(a_{i+1} - a_i) \geq k_c R_H$, where k_c is a parameter that depends on N and $\log \tau$, and R_H is the mutual Hill radius given by

$$R_H = \left(\frac{a_i + a_{i+1}}{2} \right) \left(\frac{M_i + M_{i+1}}{3M_\star} \right)^{1/3}. \quad (4.84)$$

For mildly eccentric systems, the same criterion as above can be applied, but instead of the semi-major axis difference $(a_{i+1} - a_i)$ one should use the pericenter-apocenter distance $a_{i+1}(1 - e_{i+1}) - a_i(1 - e_i)$ (Pu and Wu, 2015). We adopt a value of $k_c \sim 7$ (Smith and Lissauer, 2009), applicable for $N = 3$ and $\tau \sim 10^8$ (the typical eccentricity damping timescale); when systems fail to meet this stability criterion, they are regarded as potentially dynamically unstable. In addition, to account for the possibility that planet

systems may become unstable due to non-secular effects, we randomly select 100 USP-generating systems that were ‘stable’ according to the above criterion and integrate them using WHFast for 1 Myr (with the orbital elements ϖ , Ω and f selected uniformly between 0 and 2π). Only 1 of the 100 systems were unstable against orbit crossings by the end of the simulation. Although this result does not rule out the possibility of more systems becoming unstable beyond 1 Myr, it brings confidence that the above stability criterion is robust.

Using the above stability criterion, we find that systems can indeed become potentially dynamically unstable before forming USPs. 17.4% of systems that formed USPs and 6.3% of systems that did not form USPs became dynamically unstable at some point of their evolution; systems that form USPs are more likely to become unstable due to their larger initial eccentricities, so dynamical instability may be an impediment to USP formation, although the effect is minor.

We evolve our systems for 10 Gyr. In some cases, the inner planet’s semi-major axis can shrink to a value less than R_\star ; when this occurs, we assume the planet is tidally disrupted and/or engulfed by the star, and we remove it from the system and halt the simulation.

We found that our initial population of planet systems indeed formed USPs during its evolution, with statistical properties similar to the observed population. The USP population show substantial statistical differences with the longer period planets. We summarize their main properties below.

- **Final period:** Our initial population of 3-planet systems is capable of producing USPs, with the final periods attained being as low as $P_1 \sim 5$ hrs. Most notably, we can reproduce both the sudden change in the slope of the period distribution at

$P_1 \sim 1$ day and the mild excess of planets around $P_1 \sim 1$ day in our simulations (see Fig. 4.12). This trend persists over a moderate range of planet masses m_1 , and inner planet tidal Q_1 , but depends sensitively on the initial planet eccentricities $e_{2,0}$, $e_{3,0}$ (both equal to \bar{e} ; see above) and the stellar tidal Q'_\star . Note that in our simulations, the final distribution for P_1 is not the same as the distribution for P (of all the planets), since in some cases P_2 can also be in the range $[1, 8]$ days, although this mixing does not affect our conclusions.

- **The value of Q'_\star :** The final period distribution of USPs has a strong dependence on the value of Q'_\star . We show a histogram of the initial and final periods for various choices of Q'_\star in Fig. 4.12. For systems with $Q'_\star = 10^6$, the period distribution of USPs is strongly carved by stellar tides over Gyr timescales, which results in fewer USP planets observed at smaller periods. On the other hand, systems with $Q'_\star = 10^8$ are not strongly affected by stellar tides, resulting in a much larger fraction of planets surviving at smaller periods. Our simulations suggest that for $\Delta t_{L,1} = 100$ s, a value of Q'_\star between 10^6 and 10^7 best matches the power-law period distribution of USPs given by Petigura et al. (2018) and Lee and Chiang (2017), and $Q'_\star \gtrsim 10^8$ is incompatible with observations in our scenario.
- **The value of Q_1 :** The final period distribution of USPs also depends moderately on the inner planet's tidal Q_1 (see Fig. 4.13). We find that as expected, a larger value of Q_1 leads to fewer USPs: systems with $Q_1 = 70$ and 7 feature 2 and 3.5 times more USPs respectively than systems with $Q_1 = 700$.
- **Inner planet mass:** Less massive inner planets are more likely to become USPs. Over our sample, the inner planet's mass is smaller for USPs, with $\langle m_1 \rangle = 1.25M_\oplus$ for USPs versus $1.5M_\oplus$ for the entire population (see Fig. 4.14). Systems with $0.5M_\oplus < m_1 < 0.75M_\oplus$ were 60% more likely to form USPs than systems with $1.75M_\oplus < m_1 < 2.25M_\oplus$. This is because USP formation is limited by the amount

of angular momentum deficit (section 4.3.2), and systems with less massive inner planets have an easier time reaching the required amount of AMD.

- **Outer planet masses:** Conversely, we find that USP production favors systems with more massive outer planets, although this is a weak effect. The average mass for the exterior planets across all samples is $11.5M_{\oplus}$, and $12.1M_{\oplus}$ for the subset that ended up producing USPs.
- **Initial eccentricities:** We find that USP generation is strongly dependent on the initial eccentricities, with the fraction of systems producing USPs roughly doubling for every 0.05 increase in \bar{e} : systems with $0.075 < \bar{e} < 0.125$ and $0.125 < \bar{e} < 0.175$ produce 1.7 and 3.8 times more USPs respectively than systems with $0.025 < \bar{e} < 0.075$. We show the dependence of the final period distribution for various initial eccentricities in Fig. 4.15.
- **Initial inner period cutoff P_{\min} :** Our results can be used to constrain the minimum period P_{\min} for the initial planet population. We show the dependence of the USP period distribution on P_{\min} in Fig. 4.16. The systems with $P_{\min} = 0.5$ day show little difference compared to those with $P_{\min} = 1$ day, because virtually all planets with initial $P_1 \leq 1$ day spiral into their host stars through a combination of planetary and stellar tidal dissipation. In other words, the low- e USP migration mechanism is not sensitive to planets with initial $P \lesssim 1$ day. On the other hand, the results of experiments with $P_{\min} = 2$ or 3 days show a substantial deviation from the $P_{\min} = 1$ day case, and disagrees with the observed period distribution. Thus, planets must be formed in the $1 < P < 3$ days range to reproduce the currently observed period distribution of USPs, although we cannot rule out the possibility of planets forming in-situ at $P_1 \lesssim 1$ day.
- **Mutual inclinations:** Observationally, USPs show substantially larger mutual inclinations with their closest neighbors compared with typical Kepler multis (Dai

et al., 2018). We find that our low- e formation mechanism for USPs naturally generates larger mutual inclinations between the inner planets. We show a histogram of the final RMS mutual inclinations between the inner planets $\theta_{12,f}$ after 10 Gyr of low- e migration in Fig. 4.17. The final value of $\theta_{12,f}$ for systems that produced USPs is $\langle \theta_{12,f}^2 \rangle^{1/2} \approx 18$ deg., which is more than double the value of $\langle \theta_{12,f}^2 \rangle^{1/2} \approx 8$ deg. for systems that did not end up producing USPs. A condition for the i -th planet to transit its host star is that the orbital plane be inclined relative to the line of sight by less than $\arcsin\left(\frac{R_i + R_\star}{a_i}\right)$. Using this criterion, we find that 17.5% of USPs had transiting companions, compared with 63.5% of inner planets with $P_1 > 1$ day. This result is consistent with empirical studies, which found USPs to have a transiting companion fraction of 4 - 12 %, compared to 43 – 59% for small planets with $1 \leq P \leq 3$ days (Weiss et al., 2018).

- **Inner Pair Period Ratio:** We find that systems which resulted in USPs have substantially larger period ratios P_2/P_1 : USP systems have a mean period ratio of $P_2/P_1 = 14$, whereas for non-USP systems the mean period ratio is only 3.5. Fig. 4.18 shows the PDF of the initial and final period ratios. We also find the period ratio P_2/P_1 increases as P_1 decreases: the mean period ratio is 4.0, 5.2 and 7.0 for $P_1 = 3, 2$ and 1 day respectively. This is consistent with the observation that USPs and their companions have period ratios ≥ 15 , while non-USPs have a broader period ratio range between $1.4 \lesssim P_2/P_1 \lesssim 5$ (Petrovich et al., 2018).

4.7 Discussion

We have studied the formation of USPs through low- e tidal dissipation driven by secular forcings from exterior (super-Earth/mini-Neptune) companions of proto-USPs. In this

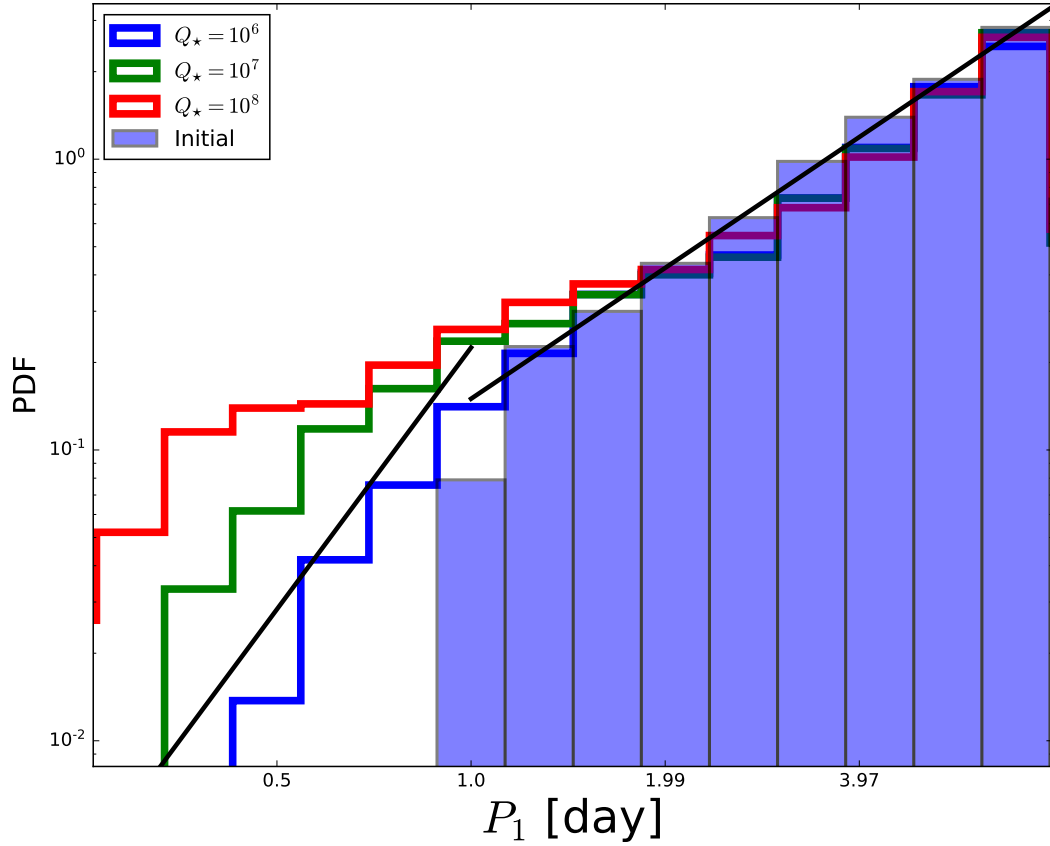


Figure 4.12: Histogram of the initial and final period of the inner-most planet P_1 for systems with inner planet tidal lag time $\Delta t_{L,1} = 100$ s. The blue bars shows the initial distribution of P_1 , while the blue, green and red lines show the final USP period distribution for values of $Q'_\star = 10^6$, 10^7 and 10^8 respectively. The two solid black lines are given by the power-law distribution $dN/d \log P_1 \propto P_1^\alpha$, where $\alpha = 3.0$ for $P_1 \leq 1$ day and $\alpha = 1.5$ for $1 < P_1 < 8$ days; we also adopt the discontinuous “bump” at $P_1 = 1$ day corresponding to an excess of 50% more planets just below $P = 1$ day as proposed by Lee & Chiang (2017). The normalization of the black lines is chosen so that the total probability density integrates to unity.

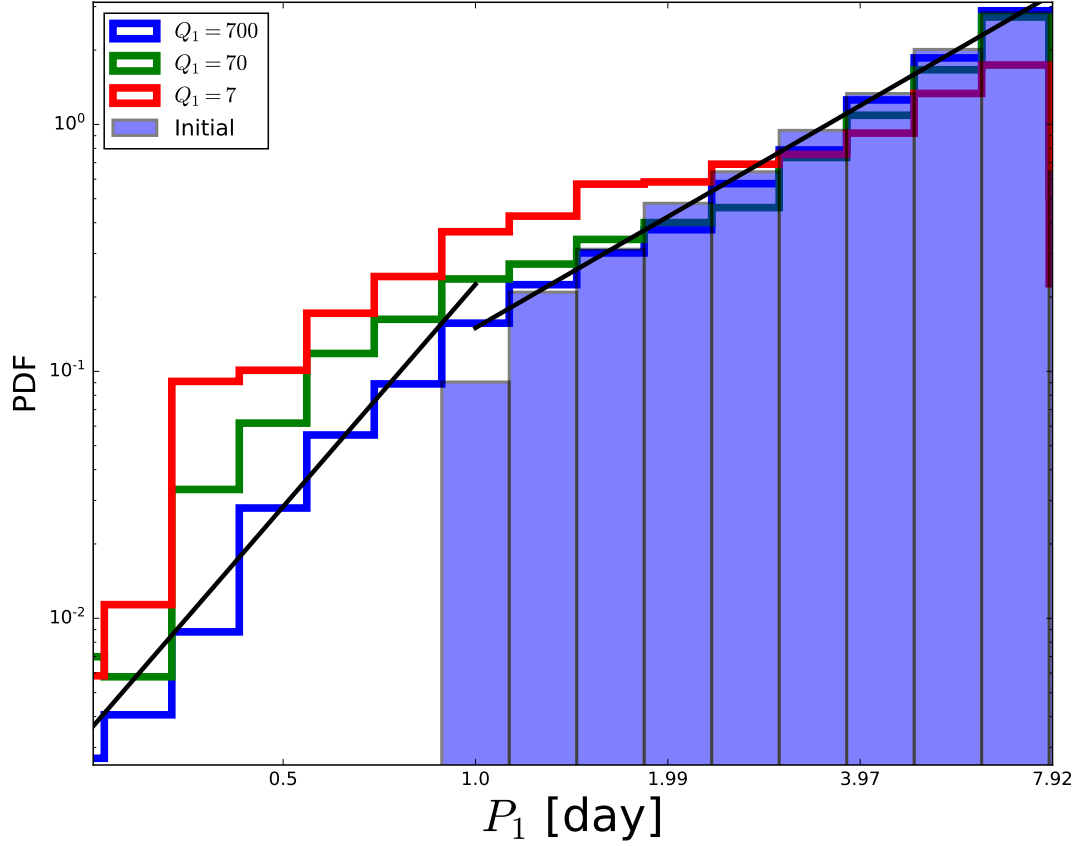


Figure 4.13: Same as Fig. 4.12 except that we fix the value of $Q'_\star = 10^7$ and instead vary $\Delta t_{L,1} = 10, 100, 1000$ s, corresponding to tidal $Q_1 = 700, 70$, and 7 (at $P_1 = 1$ day), for the blue, green and red lines respectively.

section we evaluate this proposed formation mechanism in light of the observations of USPs and their population statistics. We then discuss some specific USP sources, potential uncertainties and future extensions to this work.

4.7.1 Low- e USP migration and observations

As discussed in section 4.1, USPs have a number of distinct properties compared to the bulk of longer-period Super-Earth systems (see Winn et al., 2018). Our study shows that

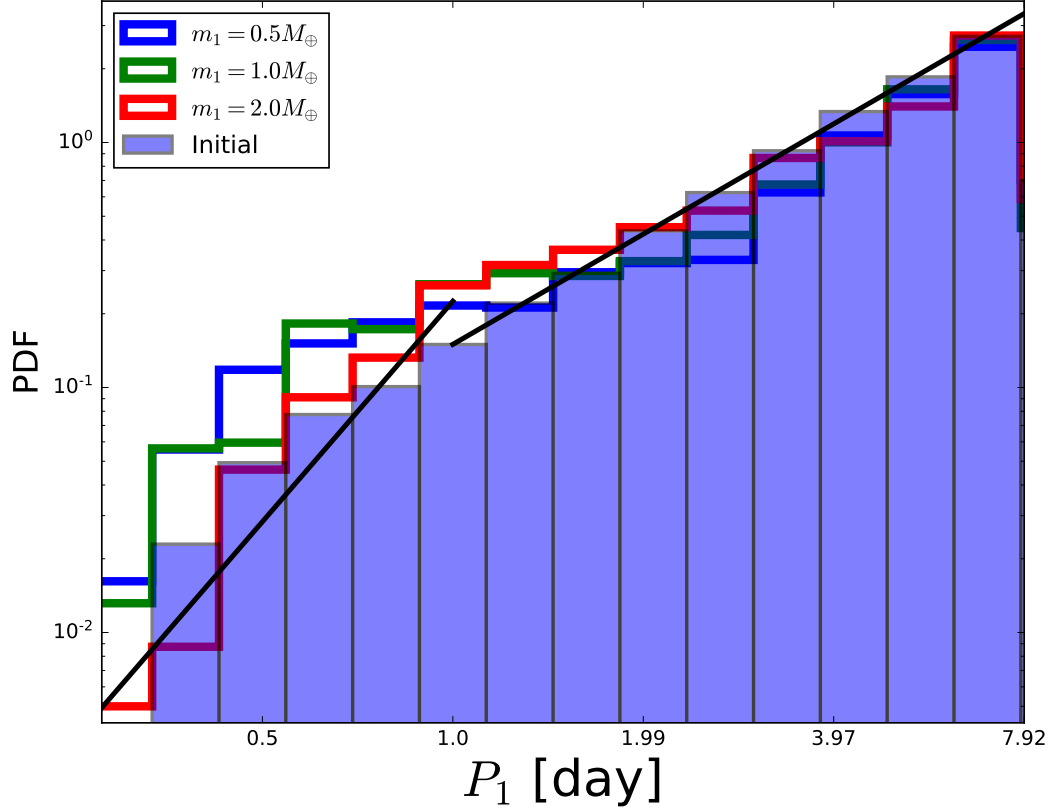


Figure 4.14: Same as Fig. 4.12 except that we fix the value of $Q'_\star = 10^7$, $\Delta t_{L,1} = 100$ s and instead vary $m_1 = 0.5 \pm 0.25$, 1.0 ± 0.25 and $2.0 \pm 0.25 M_\oplus$, for the blue, green and red lines respectively.

our low- e migration scenario produce USPs with the observed properties under a variety of initial conditions (see section 4.6). USPs are preferentially formed from smaller terrestrial planets with more eccentric external companions. A fiducial set of systems, with inner planet masses $M_\oplus < m_1 < 3M_\oplus$, exterior planet masses $3M_\oplus < m < 20M_\oplus$, inner planet $\Delta t_{L,1} = 10$ s (corresponding to $Q_1 = 700$ at $P_1 = 1$ day) and $Q'_\star = 10^7$ ended up producing a posterior USP period distribution that qualitatively matched the observed one, without any fine-tuning. Note that this combination of parameters is not the only one that can produce the observed P_1 distribution; there is a hyper-surface of possible initial system parameters that can fit the observations. For example, a set of systems with

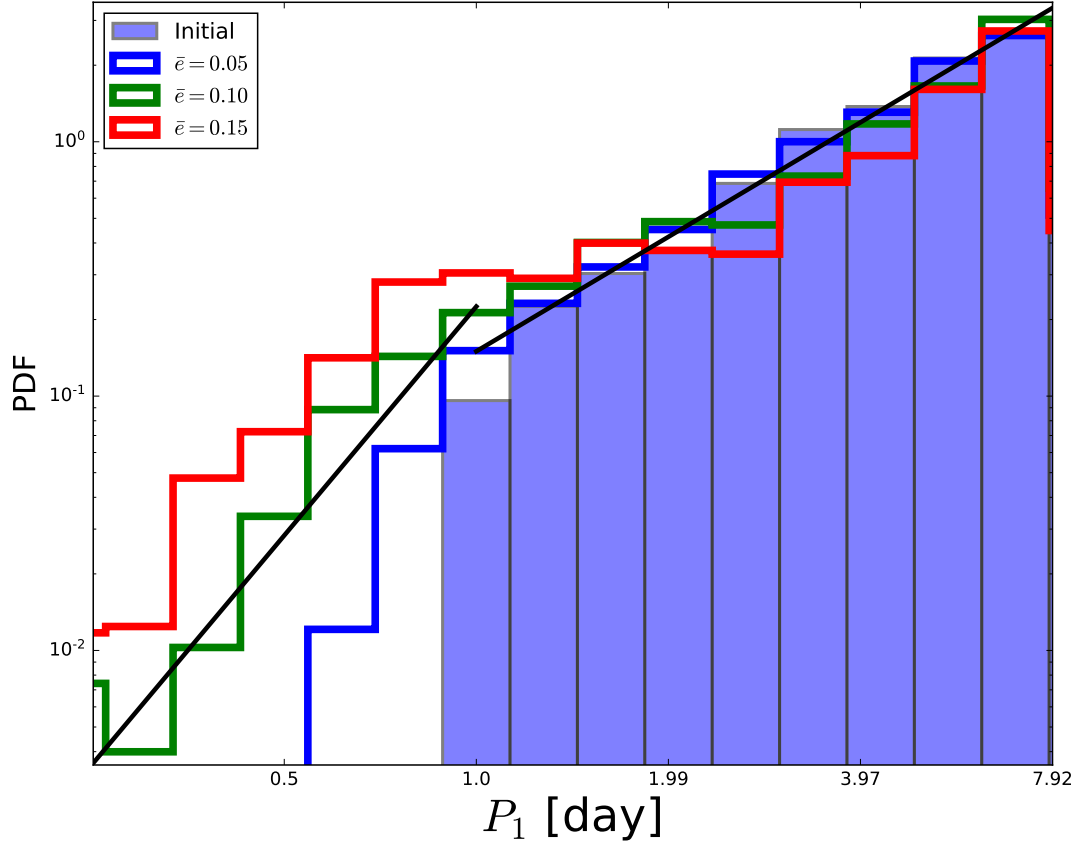


Figure 4.15: Same as Fig. 4.12 except that we fix the value of $Q'_\star = 10^7$, $\Delta t_{L,1} = 100$ s and instead vary the initial eccentricity $\bar{e} = 0.05 \pm 0.025$, 0.1 ± 0.025 , and 0.15 ± 0.025 for the blue, green and red lines respectively.

$Q'_\star = 3 \times 10^6$ and $\Delta t_{L,1} = 100$ s would fit the observations similarly well. Nevertheless, the fact that our set-up was able to reproduce observations without tuning of parameters, and that similar looking distributions can be obtained when varying the parameters Q_1 , Q'_\star , m_1 and \bar{e} (see Figs. 4.12 - 4.16) over factors of a few lends us confidence in the robustness of this mechanism.

Even more encouragingly, this formation mechanism naturally produces higher mutual inclinations between USPs and their closest companions, a trend which has been observed by empirical studies. Petrovich et al. (2018) found that a mutual inclination of

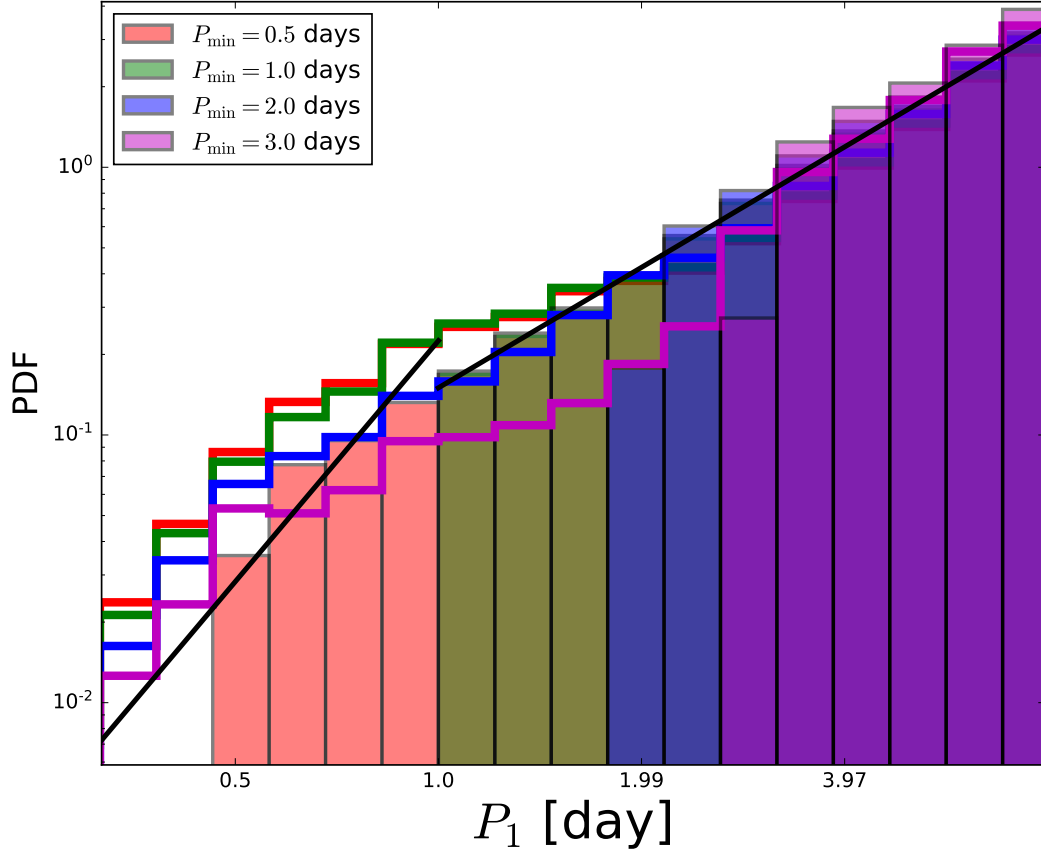


Figure 4.16: Same as Fig. 4.12 except that we fix the value of $Q'_\star = 10^7$, $\Delta t_{L,1} = 100$ s and instead vary $P_{\min} = 0.5, 1.0, 2.0$ and 3.0 days (the minimum period of the initial planet population), for the red, green, blue and magenta colors respectively. The solid bars show the initial period distribution for the four values of P_{\min} while the lines show the final distribution.

$\langle \theta_{12,f}^2 \rangle^{1/2} \gtrsim 20$ deg is needed to account for the observed dearth of transiting companions to USPs. In our population synthesis model, we found that systems that produced USPs featured a value of $\langle \theta_{12,f}^2 \rangle^{1/2} \approx 18$ deg, which more than doubles the amount for systems that did not end up with USPs and is comparable to the value required by empirical studies. USPs formed in our mechanism have a transiting companion fraction of 18% compared with 64% for planets with $1 \leq P_1 \leq 3$ days, close to empirical values of 4-12% and 43-59% respectively (Weiss et al., 2018). We also reproduce the observation

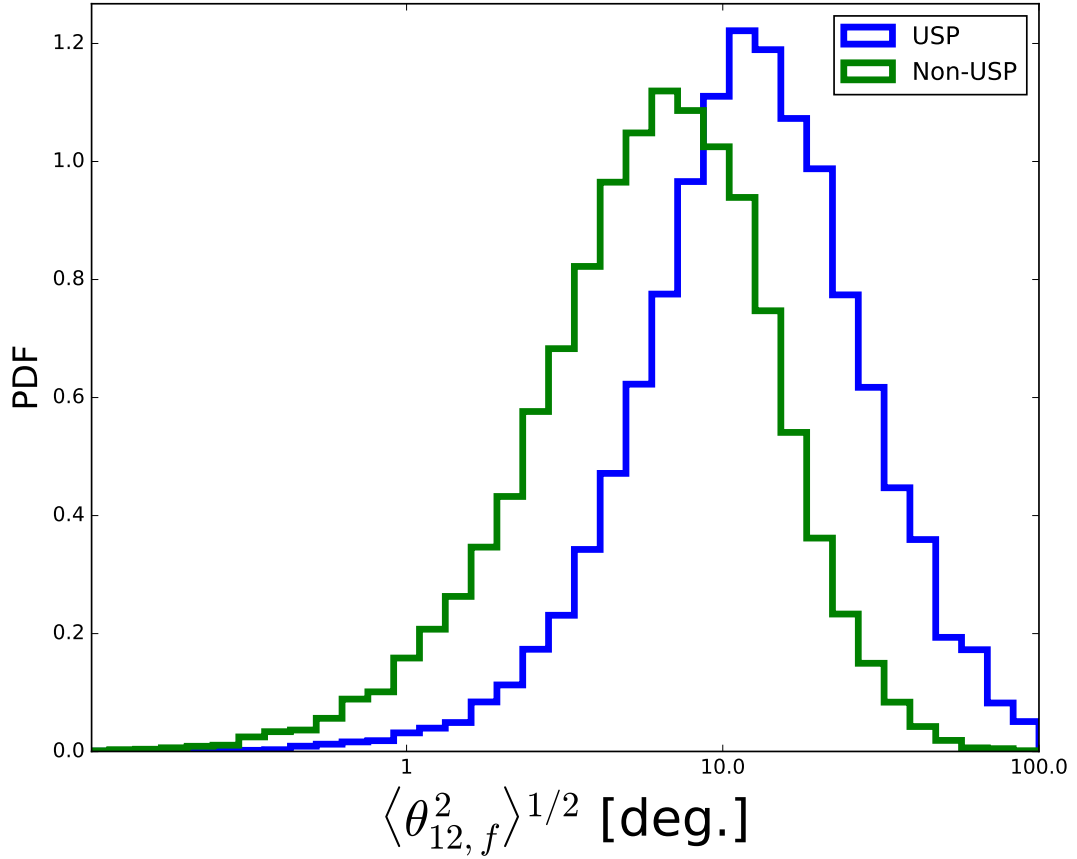


Figure 4.17: PDF of the final RMS mutual inclination between the two inner planets after 10 Gyrs of integrations for all systems in our population synthesis. The blue line shows the mutual inclination for planets that became USPs, while the green line is for non-USPs.

that the period ratio between USPs and its companions tends to be large ($P_2/P_1 \gtrsim 15$) and increases with decreasing P_1 (see also Steffen and Farr, 2013).

The feasibility of the low- e formation mechanism for USPs hinges mostly on the magnitude of the initial eccentricities of multi-planet systems: for systems with initial proto-USP periods between 1 - 3 days, our population model suggests that an initial eccentricity of $\bar{e} \gtrsim 0.1$ is required. In contrast, present-day Kepler multis have typical eccentricities of $\sigma_e = 0.05 - 0.08$, although with the caveat that the presently observed planet eccentricities may have suffered damping over Gyrs by tidal dissipation, and their

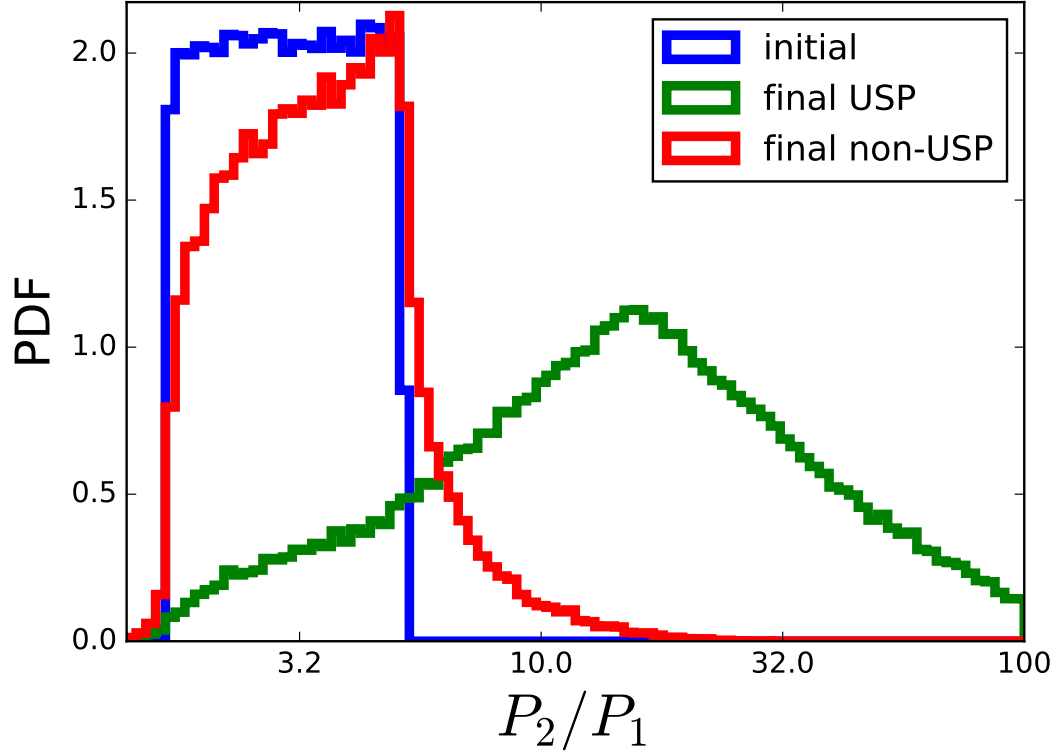


Figure 4.18: PDF of the final initial and final period ratio of the inner planets P_2/P_1 distribution for systems in our population synthesis. The blue curve is the initial period ratio, while the green and red curves are the final period ratios for systems that resulted in USPs and no USPs respectively.

initial values may be larger.

It is interesting to compare our mechanism with the secular chaos “high-eccentricity” mechanism proposed by Petrovich et al. (2018). These two mechanisms require different initial conditions and produce USPs with distinct final configurations. In the Petrovich et al. (2018) scenario, proto-USPs with $a_{1,0}$ between 0.05 - 0.1 au attain large eccentricities ($1 - e_1 \ll 1$) through to secular interactions with exterior planets; as the proto-USP pericenter reaches $\sim 2R_\odot$, the planet is tidally captured and eventually circularized, becoming an USP. In contrast, our low- e migration mechanism requires a proto-USP with

$a_{1,0}$ between 0.02 – 0.04 au, driven to mild eccentricities ($e_1 \sim 0.05 - 0.2$) through secular interactions with exterior planets, followed by tidal decay. USPs formed via secular chaos have a smaller ratio $a_{1,f}/a_{1,0}$, and therefore a larger amount of AMD is needed (see Eq. 4.48): one typically requires $N \geq 3$ exterior planets with $m_i \gtrsim 10M_\oplus$, $e_i \gtrsim 0.1$ and period ratios $P_{i+1}/P_i \gtrsim 3.0$, and planet companions with $a_2 \lesssim 0.2$ au are ruled out due to dynamical instability. In contrast, our low- e migration mechanism requires less AMD to succeed: $N \geq 2$ exterior planets with $m_i \gtrsim 3M_\oplus$ can satisfy the AMD constraint, and there is no need for large values of P_{i+1}/P_i . Observations (e.g. Steffen and Hwang, 2015) suggest that Kepler multis have typical period ratios $1.4 \leq P_{i+1}/P_i \leq 3.0$, and do not support the existence of large numbers of sparsely-spaced (i.e. $P_{i+1}/P_i \gtrsim 3.0$) multi-planet systems. In addition, while Petrovich et al. (2018) did not attempt to reproduce the final period distribution of USPs formed in their scenario, the low- e migration mechanism can robustly reproduce the observed period distribution over a range of initial parameters (see section 4.6).

Another difference between the high- e and low- e migration is the final distribution of the USP inclination (θ_1). For a system undergoing secular chaos, whenever e_1 grows to a very large value so too will the value of θ_1 due to the equipartition principle (e.g. Lithwick and Wu, 2014). In the absence of strong spin-orbit coupling, Petrovich et al. (2018) found that USPs can often reach very large values of inclination, with potentially a third of systems attaining $\theta_1 \geq 30$ deg. In contrast, the low- e migration scenario produces USPs with more mild inclinations ($\theta_1 \sim 18$ deg), although this value is still enhanced relative to non-USPs.

4.7.2 Specific sources

We comment below on the feasibility of USP low- e migration for two well-studied USP systems.

- **Kepler 10** (with $M_\star = 0.91M_\odot$, $R_\star = 1.065R_\odot$, Batalha et al., 2011b; Fressin et al., 2011) is a system with 2 transiting planets: Kepler-10b is an USP with $m_1 = 3.72M_\oplus$, $R_1 = 1.47R_\oplus$ and $a_1 = 0.0168$ au, while Kepler-10c is a sub-Neptune with $m_2 = 7.37M_\oplus$, $R_2 = 2.35R_\oplus$ and $a_2 = 0.24$ (Rajpaul et al., 2017). Kepler-10b has an inclination $\theta_{12} = 5.2$ deg relative to the orbital plane of Kepler-10c. TTV analysis suggests the existence of a third, non-transiting planet (Kepler-10d) with $a_3 = 0.366$ au and $m_3 = 7M_\oplus$ (Weiss et al., 2016). Petrovich et al. (2018) found that in order for Kepler-10b to migrate to its current orbit from $a_{1,0} = 0.1$ au through high- e migration, one requires three additional Neptune-mass planets with periods of about 122, 480 and 2100 days.

We found that low- e migration can naturally reproduce Kepler-10b’s current orbit, if one hypothesizes an additional fourth planet (Kepler-10e) located between Kepler-10b and Kepler-10c. For example, an initial configuration with $\Delta t_{L,1} = 100$ s, $a_{1,0} = 0.035$ au, $e_{2,0} = e_{3,0} = e_{4,0} = 0.2$, $m_4 = 7M_\oplus$ and $0.074 \leq a_{4,0} \leq 0.121$ au can reproduce the final orbit of Kepler-10b. This configuration makes Kepler-10b and Kepler-10e “tightly-coupled”, such that their orbits are aligned with each other and misaligned relative to Kepler-10c and Kepler-10d ($\theta_{42} \simeq \theta_{43} \sim 5$ deg). In this scenario, the fact that the hypothetical Kepler-10e would fail to transit is compatible with observations.

- **Kepler-290** (with $M_\star = 0.8M_\odot$, $R_\star = 0.7R_\odot$, Rowe et al., 2014) has a transiting USP accompanied by two outer planets. The USP (KOI 1360.03) with $R_1 = 0.97R_\oplus$ and $a_1 = 0.151$ was discovered by Sanchis-Ojeda et al. (2014) and not

formally vetted by *Kepler*; the outer planets have $a_2 = 0.11$ au, $a_3 = 0.205$ au, $R_2 = 2.7R_\oplus$ and $R_3 = 2.3R_\oplus$. Given the location and mass of the outer planets, this system can naturally produce USPs “out-of-the-box” through low- e migration: assuming masses $m_1 = M_\oplus$, $m_2 = 9M_\oplus$, $m_3 = 7M_\oplus$ and $\bar{e} = e_{2,0} = e_{3,0} = 0.2$, the final system can be reproduced as long as $a_{1,0} \lesssim 0.038$ au and $Q'_\star \lesssim 6 \times 10^6$. Decreasing the initial eccentricity to $\bar{e} = 0.15$ would instead require $a_{1,0} \lesssim 0.032$ au. The value of $a_{1,f}$ depends moderately on $a_{1,0}$ but is highly sensitive to \bar{e} and Q'_\star .

4.7.3 Are USPs photo-evaporated cores of mini-Neptunes?

The observed population of USPs have radii that are mostly within the range $1.0R_\oplus < R < 1.4R_\oplus$, and there is a dearth of planets with intermediate radius $2R_\oplus < R < 4R_\oplus$ with sub-day periods, despite such planets being ubiquitous amongst *Kepler*’s longer-period planet population. One common explanation for this observation is the scenario that USPs were initially mini-Neptunes that have had their envelopes stripped due to photo-evaporation (e.g. Winn et al., 2017). This picture may be incompatible with our model, and an alternative explanation might be preferred. Our results show that because low- e USP formation is generally AMD-limited (section 4.4.3), more massive planets are severely disfavored from becoming USPs. This would preclude higher-mass super-Earths or mini-Neptunes from becoming USPs. As a result, USP formation is limited to smaller mass planets ($m_1 \lesssim M_\oplus$), which would have a hard time maintaining their atmospheres against various escape mechanisms.

Another factor that can potentially explain the lack of larger-radius USPs is the dichotomy in tidal Q_1 between rocky planets and those with more extended gaseous

envelopes. Our results show a reduction in USP formation efficiency by a factor of ~ 2 , when Q_1 is increased by a factor of 10. In the Solar System, values of tidal Q_1 are in the range of 10 – 500 for terrestrial planets and satellites, but planets with substantial gaseous envelopes (such as Jupiter, Saturn, Uranus and Neptune) have values of Q_1 that are hundreds of times larger (Goldreich and Soter, 1966; Lainey, 2016). If this trend can be extrapolated to exoplanetary systems, then this dichotomy in tidal Q_1 between planets with and without gaseous envelopes can also explain the lack of USPs with $R_1 \gtrsim 2R_\oplus$.

4.7.4 Uncertainties and Future Work

In carrying out this work, we made several simplifications, which may cause additional uncertainties; we discuss them below.

- **Effects of Mean Motion Resonance:** One source of uncertainty is the role of mean-motion resonance (MMR) in modulating the secular interactions between planets. In our population synthesis model, we considered planet systems with semi-major axes ratios $1.41 \leq a_2/a_1 \leq 3$. In many cases, as the inner planet migrates in-wards the system may encounter MMRs (see also Hansen and Murray, 2015). A careful study of the effect of MMRs on the secular interactions of multi-planet systems is beyond the scope of this work. MMRs can excite the eccentricities of the planets, independent of secular interactions. One example is Kepler-80, a system containing an USP accompanied by 5 external planets. MacDonald et al. (2016) found that the outer 4 planets of Kepler-80 are interlocked in 4 sets of three-body mean-motion resonances, each with a libration of around a few degrees. The resulting librations may provide the entire system with an additional source of AMD that ameliorates the effect of tidal dissipation. Another possibility is that

MMRs can result in ‘resonant repulsion’, which would cause the semi-major axes of the two planets in resonance to suddenly diverge outside of the MMR (Batygin and Morbidelli, 2013; Lithwick and Wu, 2012). MMRs could bring about unexpected and interesting interactions in proto-USP systems and deserves to be the subject of further study.

- **Secular Chaos and Dynamical Instability:** In this work, we adopted a linear theory in the planet eccentricities and inclinations (by assuming $e_i, \theta_i \ll 1$). In this linear regime, the eccentricity and mutual inclination evolution of the planet orbits are decoupled. In reality, planet systems that produce USPs will often have inner planets with moderately large values of $e_1 \gtrsim 0.3$. Such values would make higher-order terms in e and θ important, and our linear theory would break down. A non-linear coupling between planet eccentricities and inclinations can bring about secular chaos (Lithwick and Wu, 2014), which can enhance the inner planet eccentricities even further as AMD diffuses throughout the system.

Another issue is that as planet eccentricities increase, their orbits may become dynamically unstable leading to orbit crossings. In our population study, we found that a small proportion ($\sim 17\%$, Sec. 4.6) of systems that became USPs may become dynamically unstable. For these inner systems, the dominant final outcome of dynamical instability is physical collision between the two unstable planets. Once two planet have crossing orbits, for large eccentricities and inclinations (i.e. $e_1, \theta_{12} \gg [(m_1 + m_2)/3M_\star]^{1/3}$) the timescale to the first physical collision is given by (e.g. Ida and Nakazawa, 1989):

$$T_{\text{coll}} \sim P_1 \left(\frac{R_1 + R_2}{a_1} \right)^{-2} = 700 \left(\frac{a_1}{0.03\text{au}} \right)^{7/2} \left(\frac{R_1 + R_2}{2R_\oplus} \right)^{-2} \text{ yr.} \quad (4.85)$$

Since the collisional timescale is much shorter than the eccentricity damping and orbital decay timescale, once two planets cross orbits, they will quickly undergo

a physical collision, which can potentially inhibit USP formation. The extent to which these dynamical instabilities occur requires investigations using numerical N-body simulations and is outside the scope of this work.

- **Effect of Additional Planets:** In this work we have limited our attention to USP formation in systems with 2 or 3 planets. What happens when additional planets are present? Our framework for 3-planet proto-USP systems can be easily generalized to systems with more than 3 planets. In general, the generation of USPs is constrained by the dual criteria that the system must have sufficient AMD (Eq. 4.46), and the forced eccentricity on the inner planet must be sufficiently large (Eq. 4.47). In section 4.4, we found that for planet systems with $\bar{e} \gtrsim 0.1$, the AMD criterion is usually more stringent. The presence of additional exterior planets only help to overcome this constraint and bolster the chances of USP generation, since having more outer planets will increase the total reservoir of AMD to maintain the tidal decay of the inner planet. Moreover, the presence of additional planets (and thereby eigenmodes) increases the likelihood of hitting one of eccentricity secular resonances that can speed up the tidal orbital decay timescale. As a result, we expect USP formation in systems with $N \geq 4$ planets to be similar to systems with $N = 3$ planets, albeit at an enhanced rate.

4.8 Summary and Conclusion

In this paper we have studied a “low-eccentricity” migration scenario for the formation of USPs. In this scenario, a low-mass ($m_1 \sim M_\oplus$) inner planet with initial period of a few days is accompanied by several external planets in configurations typical of Kepler multi-planetary systems; the companion planets excite and maintain the eccentricity of the innermost planet, which then experiences orbital decay due to tidal dissipation and

eventually becomes a USP. Tidal dissipation in the host star further enhances this orbital decay when the inner planet reaches a sufficiently small period. We find that this low- e mechanism naturally produce USPs from the large population of Kepler multis, and can explain most of the observed population properties of USPs. The key findings of this paper are:

- We study analytically the condition for orbital decay of the inner planet induced by secular forcing from the outer planetary companions for systems with $N = 2$ (section 4.3) or $N = 3$ (section 4.4) planets. USP formation is governed by two criteria (section 4.3.2): (i) the total system angular momentum deficit (AMD) must be sufficiently large, and (ii) the forced eccentricity on the inner planet must be sufficiently large so that decay occurs within the lifetime of the system. We find that it is difficult for 2-planet systems to simultaneously satisfy both criteria due to the suppression of forced eccentricity on the inner planet by short-range forces. On the other hand, 3-planet systems have a much easier time forming USPs (section 4.4), as the presence of the 3rd planet introduces secular resonances that can boost the inner planet eccentricity, in addition to enhancing the AMD reservoir.

- Although the basic equations (based on secular Laplace-Lagrange theory) for eccentricity excitation and orbital decay in multi-planet systems are standard, in practice they are computationally difficult to evolve for long periods of time due to the “stiffness” of the equations: whereas orbital decay occurs on Gyr timescales, secular interactions proceed on timescales as short as ~ 100 yr. To resolve this, we develop an approximate method based on the evolution of eigenmodes (section 4.2.1). We find that eigenmode crossing during orbital decay can lead to secular resonances, which can excite large eccentricities in the inner planet.

- We extend our analysis to the mutual inclination evolution in section 4.5. We

find that secular inclination resonances can also excite mutual inclinations between the innermost planet and its companions as it undergoes tidal decay. Moreover, the range of parameters for which the secular inclination resonance and secular eccentricity resonance occur usually coincides with one another, which results in large mutual inclinations being generated whenever a USP is formed.

- Using our approximate “eigenmode” method, we carry out a large population synthesis study to examine the statistical properties of USPs formed in the low- e migration scenario (section 4.6). We find that USPs can be robustly produced from typical Kepler multis under a range of initial conditions. This formation mechanism favors smaller inner planets, and requires the initial eccentricities of the companion planets to be $\bar{e} \gtrsim 0.1$. We find that the final USP period distribution depends on the values of planet tidal Q_1 and stellar tidal Q'_\star ; in particular, a configuration with proto-USP mass $M_\oplus < m_1 < 3M_\oplus$ and tidal lag time $\Delta t_{L,1} \sim 10 - 1000\text{s}$, outer planet masses $3M_\oplus < m_i < 20M_\oplus$ ($i \geq 2$) and $Q'_\star \sim 10^6 - 10^7$ produces USPs with a final period distribution that matches closely with the observed one.

- Confronting with observations, we find that our low- e migration mechanism can reproduce the empirical population properties of USPs. The final period distribution of USPs matches with the empirical distribution, and the radius distribution of USPs are biased towards small, Earth-like planets, in agreement with observations. Moreover, we find that in our low- e formation mechanism, systems with USPs have more than twice as large mutual inclinations between the innermost planets as do systems without USPs, in agreement with other empirical studies. Our mechanism also reproduces the empirical fraction of USPs with transiting companions, as well as the period ratio distribution of such USPs, without fine tuning of initial parameters.

Overall, we conclude that the low- e migration mechanism can more robustly produce

the observed USPs than some of the other proposed mechanism (see section 4.7). For some systems (e.g. Kepler-10), our scenario makes specific predictions for the existence of unseen planets which can be tested by future observations.

APPENDIX A

HYBRID SECULAR EQUATIONS

Our hybrid secular equations are based on the equations given by Liu et al. (2015) that govern the secular evolution of hierarchical triples (where the semi-major axes of the inner and outer binaries satisfy $a_{\text{in}} \ll a_{\text{out}}$) with arbitrary eccentricities and inclinations. These equations are expressed in terms of the dimensionless angular momentum vector and eccentricity vector,

$$\mathbf{j} = \sqrt{1 - e^2} \hat{\mathbf{n}}, \quad \mathbf{e} = e \hat{\mathbf{u}} \quad (\text{A.1})$$

(where $\hat{\mathbf{n}}$ and $\hat{\mathbf{u}}$ are unit vectors), and extend previous results (e.g. Milankovic, 1939; Tremaine et al., 2009) by expanding the interaction potential to the octupole order (see also Boué and Fabrycky, 2014a; Petrovich, 2015a). While the Liu et al. (2015) equations accurately capture the interaction between a planet in the inner system and the distant perturber, they are not valid for describing the interaction between the inner planets. We therefore modify these equations by replacing the quadrupole and octupole strengths with ones given by appropriate Laplace coefficients in the standard Laplace-Lagrange secular theory. Obviously, the Laplace-Lagrange theory is valid only for $e_j, \theta_j \ll 1$. But when the inner planets develop large eccentricities and/or mutual inclinations, dynamical instability is likely to set in.

In our hybrid equations, the rates of change of the dimensionless angular momentum vector \mathbf{j}_j and eccentricity vector \mathbf{e}_j of an inner planet j induced by an outer planet k

(including the perturber planet p) are given by:

$$\begin{aligned}
\left(\frac{d\mathbf{j}_j}{dt}\right)_k &= \frac{\omega_{jk}}{(1-e_k^2)^{3/2}} \left[(\mathbf{j}_j \cdot \hat{\mathbf{n}}_k) \mathbf{j}_j \times \hat{\mathbf{n}}_k - 5(\mathbf{e}_j \cdot \hat{\mathbf{n}}_k) \mathbf{e}_j \times \hat{\mathbf{n}}_k \right] \\
&\quad - \frac{5\nu_{jk}e_k}{4(1-e_k^2)^{5/2}} \left\{ \left[2[(\mathbf{e}_j \cdot \hat{\mathbf{u}}_k)(\mathbf{j}_j \cdot \hat{\mathbf{n}}_k) \right. \right. \\
&\quad \left. \left. + (\mathbf{e}_j \cdot \hat{\mathbf{n}}_k)(\mathbf{j}_j \cdot \hat{\mathbf{u}}_k) \right] \mathbf{j}_j + 2[(\mathbf{j}_j \cdot \hat{\mathbf{u}}_k)(\mathbf{j}_j \cdot \hat{\mathbf{n}}_k) \right. \\
&\quad \left. \left. - 7(\mathbf{e}_j \cdot \hat{\mathbf{u}}_k)(\mathbf{e}_j \cdot \hat{\mathbf{n}}_k) \right] \mathbf{e}_j \right] \times \hat{\mathbf{n}}_k \\
&\quad + \left[2(\mathbf{e}_j \cdot \hat{\mathbf{n}}_k)(\mathbf{j}_j \cdot \hat{\mathbf{n}}_k) \mathbf{j}_j + \left[\frac{8}{5}e_j^2 - \frac{1}{5} \right. \right. \\
&\quad \left. \left. - 7(\mathbf{e}_j \cdot \hat{\mathbf{n}}_k)^2 + (\mathbf{j}_j \cdot \hat{\mathbf{n}}_k)^2 \right] \mathbf{e}_j \right] \times \hat{\mathbf{u}}_k \Big\}, \tag{A.2}
\end{aligned}$$

$$\begin{aligned}
\left(\frac{d\mathbf{e}_j}{dt}\right)_k &= \frac{\omega_{jk}}{(1-e_k^2)^{3/2}} \left[(\mathbf{j}_j \cdot \hat{\mathbf{n}}_k) \mathbf{e}_j \times \hat{\mathbf{n}}_k + 2\mathbf{j}_j \times \mathbf{e}_j \right. \\
&\quad \left. - 5(\mathbf{e}_j \cdot \hat{\mathbf{n}}_k) \mathbf{j}_j \times \hat{\mathbf{n}}_k \right] \\
&\quad - \frac{5\nu_{jk}e_k}{4(1-e_k^2)^{5/2}} \left\{ \left[2(\mathbf{e}_j \cdot \hat{\mathbf{n}}_k)(\mathbf{j}_j \cdot \hat{\mathbf{n}}_k) \mathbf{e}_j \right. \right. \\
&\quad \left. \left. + \left[\frac{8}{5}e_j^2 - \frac{1}{5} - 7(\mathbf{e}_j \cdot \hat{\mathbf{n}}_k)^2 + (\mathbf{j}_j \cdot \hat{\mathbf{n}}_k)^2 \right] \mathbf{j}_j \right] \times \hat{\mathbf{u}}_k \right. \\
&\quad \left. + \left[2[(\mathbf{e}_j \cdot \hat{\mathbf{u}}_k)(\mathbf{j}_j \cdot \hat{\mathbf{n}}_k) + (\mathbf{e}_j \cdot \hat{\mathbf{n}}_k)(\mathbf{j}_j \cdot \hat{\mathbf{u}}_k) \right] \mathbf{e}_j \right. \right. \\
&\quad \left. \left. + 2[(\mathbf{j}_j \cdot \hat{\mathbf{n}}_k)(\mathbf{j}_j \cdot \hat{\mathbf{u}}_k) - 7(\mathbf{e}_j \cdot \hat{\mathbf{n}}_k)(\mathbf{e}_j \cdot \hat{\mathbf{u}}_k) \right] \mathbf{j}_j \right] \times \hat{\mathbf{n}}_k \\
&\quad \left. + \frac{16}{5}(\mathbf{e}_j \cdot \hat{\mathbf{u}}_k) \mathbf{j}_j \times \mathbf{e}_j \right\}. \tag{A.3}
\end{aligned}$$

Meanwhile, the outer planet k being influenced by the inner planet j is described by

the equations:

$$\begin{aligned}
\left(\frac{d\mathbf{j}_k}{dt}\right)_j &= \frac{\omega_{kj}}{(1-e_k^2)^{3/2}} \left[(\mathbf{j}_j \cdot \hat{\mathbf{n}}_k) \hat{\mathbf{n}}_k \times \mathbf{j}_j - 5(\mathbf{e}_j \cdot \hat{\mathbf{n}}_k) \hat{\mathbf{n}}_k \times \mathbf{e}_j \right] \\
&\quad - \frac{5\nu_{kj}e_k}{4(1-e_k^2)^{5/2}} \left\{ 2 \left[(\mathbf{e}_j \cdot \hat{\mathbf{n}}_k)(\mathbf{j}_j \cdot \hat{\mathbf{u}}_k) \hat{\mathbf{n}}_k \right. \right. \\
&\quad \left. \left. + (\mathbf{e}_j \cdot \hat{\mathbf{u}}_k)(\mathbf{j}_j \cdot \hat{\mathbf{n}}_k) \hat{\mathbf{n}}_k + (\mathbf{e}_j \cdot \hat{\mathbf{n}}_k)(\mathbf{j}_j \cdot \hat{\mathbf{n}}_k) \hat{\mathbf{u}}_k \right] \times \mathbf{j}_j \right. \\
&\quad \left. + \left[2(\mathbf{j}_j \cdot \hat{\mathbf{u}}_k)(\mathbf{j}_j \cdot \hat{\mathbf{n}}_k) \hat{\mathbf{n}}_k - 14(\mathbf{e}_j \cdot \hat{\mathbf{u}}_k)(\mathbf{e}_j \cdot \hat{\mathbf{n}}_k) \hat{\mathbf{n}}_k \right. \right. \\
&\quad \left. \left. + \left[\frac{8}{5}e_j^2 - \frac{1}{5} - 7(\mathbf{e}_j \cdot \hat{\mathbf{n}}_k)^2 + (\mathbf{j}_j \cdot \hat{\mathbf{n}}_k)^2 \right] \hat{\mathbf{u}}_k \right] \times \mathbf{e}_j \right\}, \tag{A.4}
\end{aligned}$$

$$\begin{aligned}
\left(\frac{d\mathbf{e}_k}{dt}\right)_j &= \frac{\omega_{kj}}{(1-e_k^2)^{3/2}} \left[(\mathbf{j}_j \cdot \hat{\mathbf{n}}_k) \mathbf{e}_k \times \mathbf{j}_j - 5(\mathbf{e}_j \cdot \hat{\mathbf{n}}_k) \mathbf{e}_k \times \mathbf{e}_j \right. \\
&\quad \left. - \left[\frac{1}{2} - 3e_1^2 + \frac{25}{2}(\mathbf{e}_j \cdot \hat{\mathbf{n}}_k)^2 - \frac{5}{2}(\mathbf{j}_j \cdot \hat{\mathbf{n}}_k)^2 \right] \hat{\mathbf{n}}_k \times \mathbf{e}_k \right] \\
&\quad - \frac{5\nu_{kj}e_k}{4(1-e_k^2)^{5/2}} \frac{e_2}{\sqrt{1-e_2^2}} \frac{L_1}{L_2} \left\{ 2 \left[(\mathbf{e}_j \cdot \hat{\mathbf{n}}_k)(\mathbf{j}_j \cdot \mathbf{e}_k) \hat{\mathbf{u}}_k \right. \right. \\
&\quad \left. \left. + (\mathbf{j}_j \cdot \hat{\mathbf{n}}_k)(\mathbf{e}_j \cdot \mathbf{e}_k) \hat{\mathbf{u}}_k + \frac{1-e_2^2}{e_2} (\mathbf{e}_j \cdot \hat{\mathbf{n}}_k)(\mathbf{j}_j \cdot \hat{\mathbf{n}}_k) \hat{\mathbf{n}}_k \right] \times \mathbf{j}_j \right. \\
&\quad \left. + \left[2(\mathbf{j}_j \cdot \mathbf{e}_k)(\mathbf{j}_j \cdot \hat{\mathbf{n}}_k) \hat{\mathbf{u}}_k - 14(\mathbf{e}_j \cdot \mathbf{e}_k)(\mathbf{e}_j \cdot \hat{\mathbf{n}}_k) \hat{\mathbf{u}}_k \right. \right. \\
&\quad \left. \left. + \frac{1-e_2^2}{e_2} \left[\frac{8}{5}e_1^2 - \frac{1}{5} - 7(\mathbf{e}_j \cdot \hat{\mathbf{n}}_k)^2 + (\mathbf{j}_j \cdot \hat{\mathbf{n}}_k)^2 \right] \hat{\mathbf{n}}_k \right] \times \mathbf{e}_j \right. \\
&\quad \left. - \left[2 \left(\frac{1}{5} - \frac{8}{5}e_1^2 \right) (\mathbf{e}_j \cdot \hat{\mathbf{u}}_k) \mathbf{e}_k \right. \right. \\
&\quad \left. \left. + 14(\mathbf{e}_j \cdot \hat{\mathbf{n}}_k)(\mathbf{j}_j \cdot \hat{\mathbf{u}}_k)(\mathbf{j}_j \cdot \hat{\mathbf{n}}_k) \mathbf{e}_k + 7(\mathbf{e}_j \cdot \hat{\mathbf{u}}_k) \left[\frac{8}{5}e_1^2 \right. \right. \right. \\
&\quad \left. \left. \left. - \frac{1}{5} - 7(\mathbf{e}_j \cdot \hat{\mathbf{n}}_k)^2 + (\mathbf{j}_j \cdot \hat{\mathbf{n}}_k)^2 \right] \mathbf{e}_k \right] \times \hat{\mathbf{n}}_k \right\}. \tag{A.5}
\end{aligned}$$

In the above equations, $L_j \simeq m_j \sqrt{GM_* a_j}$ is the angular momentum, and the quantities ω_{jk} and ν_{jk} are given by Eqs. (2.4) and (2.5) respectively.

For planet j , one would sum over the contributions from all other planets according

to the above formulae. Note that j, k includes the perturber p . The time evolution of the j -th planet is thus:

$$\frac{d\mathbf{j}_j}{dt} = \sum_{k \neq j} \left(\frac{d\mathbf{j}_j}{dt} \right)_k, \quad (\text{A.6})$$

$$\frac{d\mathbf{e}_j}{dt} = \sum_{k \neq j} \left(\frac{d\mathbf{e}_j}{dt} \right)_k. \quad (\text{A.7})$$

For $a_j \ll a_k$, we have

$$\omega_{jk} \simeq \frac{3Gm_j m_k a_j^2}{4a_k^3 L_j} \quad \text{and} \quad \nu_{jk} \simeq \frac{15Gm_j m_k a_j^3}{4a_k^4 L_j}, \quad (\text{A.8})$$

and equations (A.2)-(A.5) reduce to the equations (17)-(20) of (Liu et al., 2015). For $e_j, e_k \ll 1$ and $\hat{\mathbf{n}}_j \simeq \hat{\mathbf{n}}_k$ (i.e., the mutual inclination between planets is small), equations (A.2)-(A.5) reduce to the linearized Laplace-Lagrange equations given in Section 2.2.

APPENDIX B

PRESCRIPTION FOR ECCENTRICITY AND INCLINATION OF “N PLANETS + PERTURBER” SYSTEMS

We summarize the short sequence of calculations that should be applied to determine the predicted RMS eccentricities and mutual inclinations and its regime of validity for a “N planets + perturber” system with inner planets on initially circular and co-planar orbits based on our hybrid secular equations. The necessary parameters required are the planet semi-major axes a_j , masses m_j (with $j \in [1, 2, 3, \dots, N, p]$) and the perturber’s inclination and eccentricity θ_p and e_p .

1. First, calculate the “quadrupole” and “octupole” precession frequencies ω_{jk} and ν_{jk} for all possible pairs of planets (including perturber p) from Eqs. (2.4) - (2.5).
2. For the perturber p only, calculate the ‘adjusted’ precession frequencies $\tilde{\omega}_{jp}$ and $\tilde{\nu}_{jp}$ for each of the inner planets $j \in [1, 2, 3, \dots, N]$ (Eqs. 2.47 - 2.48). From here onwards, all calculations involving the quantities ω_{jk} and ν_{jk} should be replaced with the tilded versions $\tilde{\omega}_{jp}$ and $\tilde{\nu}_{jp}$.
3. Compute the coupling matrices **A** and **C** from Eqs. (2.62) and (2.71). Note that $\tilde{\omega}_{jp}$ and $\tilde{\nu}_{jp}$ should be used in place of ω_{jk} and ν_{jk} .
4. Evaluate the $N \times N$ matrix of eigenvectors **Y** and **V** for the matrices **A** and **C** respectively.
5. Write down the forcing vectors **B** and **D**, given by $B_j = \tilde{\nu}_{jp}$ and $D_j = \tilde{\omega}_{jp}$.
6. Using Eqs. (2.66) and (2.73), compute the coefficients b_n and c_n .
7. The RMS eccentricity of the j -th planet $\langle e_j^2 \rangle^{1/2}$ is given by Eq. (2.67), and the RMS eccentricity of the system σ_e is given by Eq. (2.59).

8. The RMS mutual inclination between the j -th and k -th planet $\langle \theta_{jk}^2 \rangle^{1/2}$ is given by Eq. (2.74), and the RMS mutual inclination of the system σ_θ is given by Eq. (2.75).
9. Check the planet pairs for mutual inclinations exceeding the Kozai critical angle: If any planet pairs have $(\theta_{jk})_{\max} \gtrsim 39^\circ$, they will undergo Lidov-Kozai-like oscillations and the hybrid secular equations break down, and one should resort to N-body integrations. The maximum mutual inclination is given approximately by $(\theta_{jk})_{\max} \simeq \sqrt{2} \langle \theta_{jk}^2 \rangle^{1/2}$.
10. Check the planet pairs for orbital crossings: If any planet pairs have $a_j[1 + (e_j)_{\max}] \geq a_{j+1}[1 - (e_{j+1})_{\max}]$, then their orbits cross and the hybrid secular equations break down; such systems are unstable and should be evaluated using N-body integrations. The maximum eccentricity is given approximately by $(e_j)_{\max} \simeq \sqrt{2} \langle e_j \rangle^{1/2}$.

APPENDIX C

CALCULATION OF MOMENTS OF \mathcal{E}_A

We demonstrate how to calculate the various moments of an inner planet subject to a stochastic secular forcing. For case 1, the unconstrained perturber, from Eq. (3.55) the mean of \mathcal{E}_a is given by

$$\begin{aligned}\langle \mathcal{E}_a \rangle &= \left\langle \int_0^{t_{\text{ej}}} e^{i\omega_{a1}(s-t_{\text{ej}})} i\nu_{a1} Z(s) ds \right\rangle \\ &= \int_0^{t_{\text{ej}}} e^{i\omega_{a1}(s-t_{\text{ej}})} i\nu_{a1} \langle Z(s) \rangle ds = 0.\end{aligned}\tag{C.1}$$

The variance of \mathcal{E}_a is

$$\begin{aligned}\langle |\mathcal{E}_a|^2 \rangle &= \left\langle \left| \int_0^{t_{\text{ej}}} e^{-i\omega_a(s-t_{\text{ej}})} i\nu_{a1} Z(s) ds \right|^2 \right\rangle \\ &= \nu_{a1}^2 \left\langle \left(\int_0^{t_{\text{ej}}} e^{ii\omega_{a1}(s-t_{\text{ej}})} Z(s) ds \right) \left(\int_0^{t_{\text{ej}}} e^{i\omega_{a1}(r-t_{\text{ej}})} Z^*(r) dr \right) \right\rangle \\ &= \nu_{a1}^2 \left(\int_0^{t_{\text{ej}}} \int_0^{t_{\text{ej}}} e^{i\omega_{a1}(r-s)} \langle Z(s) Z^*(r) \rangle ds dr \right) \\ &= 2\sigma_{\mathcal{E}1}^2 \nu_{a1}^2 \left(\int_0^{t_{\text{ej}}} \int_0^r e^{i\omega_a(r-s)} s ds dr + \int_0^{t_{\text{ej}}} \int_r^{t_{\text{ej}}} e^{i\omega_{a1}(r-s)} r ds dr \right) \\ &= 4 \left(\frac{\nu_{a1}}{\omega_a} \right)^2 \left[1 - \frac{\sin(\omega_a t_{\text{ej}})}{\omega_a t_{\text{ej}}} \right] \sigma_{\mathcal{E}1}^2 t_{\text{ej}}.\end{aligned}\tag{C.2}$$

Similarly the covariance between $\mathcal{E}_{a,\text{ej}}$ and its forced eccentricity is given by

$$\begin{aligned}\langle \text{Re}(\mathcal{E}_{a,\text{ej}} \mathcal{E}_{a,\text{forced}}^*) \rangle &= \left\langle \text{Re} \left(\int_0^{t_{\text{ej}}} -i\nu_{a1} e^{-i\omega_{a1}(s-t_{\text{ej}})} Z(s) \frac{\nu_{a1}}{\omega_{a1}} Z^*(s) ds \right) \right\rangle \\ &= \text{Im} \left(\int_0^{t_{\text{ej}}} \nu_{a1} e^{-i\omega_{a1}(s-t_{\text{ej}})} \frac{\nu_{a1}}{\omega_{a1}} \langle Z(s) Z^*(s) \rangle ds \right) \\ &= 2 \text{Im} \left(\int_0^{t_{\text{ej}}} \nu_{a1} e^{-i\omega_a(s-t_{\text{ej}})} \frac{\nu_{a1}}{\omega_{a1}} \sigma_{\mathcal{E}1}^2 s ds \right) \\ &= 2 \left(\frac{\nu_{a1}}{\omega_{a1}} \right)^2 \left[1 - \frac{\sin(\omega_{a1} t_{\text{ej}})}{\omega_{a1} t_{\text{ej}}} \right] \sigma_{\mathcal{E}1}^2 t_{\text{ej}}.\end{aligned}\tag{C.3}$$

The case of the constrained perturber (Brownian bridge) is analogous to the case for the unconstrained perturber, except with $Z(s) \rightarrow B(s)$. The expectations of $B(s)$ are given by Eqs. (3.60) - (3.62).

APPENDIX D

BRANCHING RATIO OF UNSTABLE SYSTEMS

D.1 Introduction

When two planets in a planet system are spaced too closely, their orbits will interact strongly and become unstable. Such instability inevitably results in the loss of one of the planets, through either planet-planet collisions, planet ejections, or inspiral into the host star. The question of which final fate is finally resulted in such unstable systems has observational relevance to astronomy, but remains poorly understood. In this work, I present a novel theoretical result for the final fate of such systems; this theoretical result is based on an intuitively simple model based on modelling the effect of close encounters between planets as Weiner processes in orbital energy.

The dynamical evolution of multi-planet systems is an old and well-studied problem in celestial mechanics. The premise of the problem is as follows. Imagine a central star with mass M_\star and radius R_\star , being orbited by N planets whose orbits are mutually unstable. Each planet has mass m_i , radius R_i , position vector \mathbf{r}_i and velocity vector \mathbf{v}_i ($i \in [1, 2, \dots, N]$). Often, the position-velocity vectors are converted into a coordinate system called ‘orbital elements’, with variables $(a, e, i, \Omega, \varpi, f)$, where a is the orbital semi-major axis, e is the eccentricity, i is the inclination, Ω is the longitude of the ascending node, ϖ is the longitude of pericenter, and f is the true anomaly. Gladman (1993) found that for the case when $N = 2$, the orbits of two planets are unstable and they will rapidly undergo close encounters if their semi-major axis difference is less than

$$a_2 - a_1 \leq 2\sqrt{3}r_H, \quad \text{where} \quad r_H \equiv \frac{a_1 + a_2}{2} \left(\frac{m_1 + m_2}{M_\star} \right)^{1/3} \quad (\text{D.1})$$

is the mutual Hill radius of the two planets. Once two planets reach the point of instability,

they will quickly undergo a series mutual close encounters at each orbital conjunction. The close encounters occur indefinitely until the removal of one of the planets, finally resulting in a one-planet system that is indefinitely stable. The final stable state is reached via. one of three scenarios: a planet is ejected from the system (2), the planets collide with one another (3), or a planet spirals into the host star (4). The criteria for each is given by

$$\mathbf{v}_i^2 \geq \sqrt{\frac{2GM_\star}{r_i}} \quad (\text{D.2})$$

for ejection of the i -th planet,

$$|\mathbf{r}_1 - \mathbf{r}_2| \leq R_1 + R_2 \quad (\text{D.3})$$

for physical collision between the planets, and

$$|\mathbf{r}_i| \leq R_\star + R_i \quad (\text{D.4})$$

for collision between the i -th planet and the host star.

When any of the above three criterion are met, one of the planets is removed from the system and the remaining system is stable for all time. Each final outcome leads to different observational consequences: If planet ejections are prevalent, then we would expect to see large populations of 'rogue' free-floating planets throughout the galaxy; if planet-planet collisions are important, then we may expect to see more planets with unusual densities; if planet inspirals into the stars are common, such planets can be tidally captured to form Hot Jupiters or ultra-short period planets. Our task at hand is to predict, given some initial parameters, which outcome is most likely to occur.

D.2 Theoretical Model

Here is a simple statistical model to classify the outcome of unstable planet systems. This model ignores the possibility of inspiral into the host star, and only considers the possibility of planet collisions and ejections. This is appropriate when planets scatter at $a \gtrsim 1$ AU distances, where the planets are sufficiently far from the host star that inspirals are exceedingly rare.

In the discussion below we consider the limiting case that $M_\star \gg m_1 \gg m_2$, this model will be fairly accurate as long as $m_1/m_2 \gtrsim 2$. When mass ratios are more comparable, our model will under-estimate collisions and over-estimate ejections.

Whether the scattering results in final ejection or collision is a competition between two timescales. The ejection occurs because at each planet-planet close encounter, the planets exchange a random amount of orbital energy. This exchange is equally likely to lead to energy gain or loss, as a result over long timescales the orbital energies of the two planets undergo a random-walk-like process. If one of the planets eventually drifts to a positive amount of orbital energy, it is ejected.

At the same time, if the planets are orbit crossing, there is a finite chance that their closest approach distance is less than the sum of their radii. If this occurs first before the ejection, the two planets undergo a merger instead.

The ejection is a long, gradual process requiring many steps to build up significant energy drift. As a result, the timescale to ejection has a long tail and very low likelihood at earlier times. On the other hand, the likelihood of a physical collision depends on the orbital eccentricities and inclinations, but is roughly constant (to order unity) at each close encounter; as a result, the distribution for the collision time is exponentially

distributed and biased towards earlier values.

D.2.1 Collisional Timescale

If one can somehow compare the typical timescales to ejection vs. collisions, then there is a simple criterion to see which occurs first. We now estimate first the collisional timescale. The collisional cross-section of planets 1 and 2 in the 3-D configuration is given by (Ida and Nakazawa, 1989; Higuchi et al., 2006)

$$\sigma_{12}^2 = \pi R_{12}^2 (1 + F_{12}), \quad (\text{D.5})$$

where $R_{12} = R_1 + R_2$ is the sum of planet radii, and $v_{12,\infty}$ is the relative velocity between planets 1 and 2 at infinity, and F_{12} is the gravitational focussing parameter. Note that F_{12} is also known as the Safronov number in some contexts. In the 2-body limit when the solar potential is negligible, we have

$$F_{12} \equiv 2 \left(\frac{v_{1,\text{esc}}}{v_{12,\infty}} \right)^2 = 2 \left(\frac{GM_1}{R_{12}v_{12,\infty}^2} \right). \quad (\text{D.6})$$

A caveat is that the above assumes that the mutual inclination $\theta_{12} \gg R_1/a_1$. If this is not satisfied, then we are instead in the planar limit and

$$\sigma_{12,2D} = 2R_{12} (1 + F_{12})^{1/2}. \quad (\text{D.7})$$

We will first begin by assuming that gravitational focussing is negligible. This is usually not the case for scattering between Cold Jupiters (gravitational focussing is typically important), but this simple case helps us understand the big picture without getting bogged down in some details. In the no-focussing regime, the collision probability can be approximated as

$$P_{co} = \frac{\sigma_{12}^2}{4\pi a_1^2} = \frac{1}{4} \left(\frac{R_{12}}{a_1} \right)^2. \quad (\text{D.8})$$

The mean collision timescale is $\bar{N}_{co} \sim 1/P_{co}$ which is

$$\bar{N}_{co} \sim 1.8 \times 10^7 \left(\frac{R_{12}}{R_J} \right)^{-2} \left(\frac{a_1}{\text{AU}} \right)^2. \quad (\text{D.9})$$

In this no-focussing limit the probability of collision per close encounter is constant. The distribution of the collision time is therefore an exponential distribution (since there is an equal chance of collision per unit time, the surviving fraction decays exponentially). This fact will be useful in calculating later the branching ratio.

D.2.2 Ejection Timescale

The orbital evolution of gravitationally scattering planets can be approximated as a series of close encounters, with each encounter resulting in a change of orbital energy, eccentricity and inclination with zero mean. The resulting time evolution is therefore consistent with a Brownian motion. Planet ejections occur when the random walk in energy has drifted to a positive value equal to the initial orbital energy. For planets with crossing orbits (e.g. Wiegert and Tremaine, 1999; Figueira et al., 2012), the mean energy drift per step of the lessor planet is of order

$$\langle \delta E_2^2 \rangle^{1/2} \sim c \left(\frac{GM_1 M_2}{a_1} \right), \quad (\text{D.10})$$

where c is a constant of order unity. In 3.2.3 we determined statistically that $c \sim 15$. The typical timescale to reach ejection (in terms of number of orbits) \bar{N}_{ej} is

$$\bar{N}_{ej} \sim \left(\frac{E_{2,0}}{\langle \delta E_2 \rangle} \right)^2. \quad (\text{D.11})$$

When the ejected planet is not a test particle but has some mass of its own, the ejection process becomes less efficient. Empirically, a good estimate for the ejection timescale is (see Sec. 3.2.3)

$$\bar{N}_{ej} \approx 3600 \left(\frac{M_1}{M_J} \right)^{-2} \left(1 + \frac{m_2}{m_1} \right)^4 \left(\frac{a_{1,0}}{a_{2,0}} \right)^{-2}. \quad (\text{D.12})$$

D.2.3 The Branching Ratio

Having estimated the two timescales now, we have a simple criterion for knowing whether we should expect collisions vs. ejections: If $\bar{N}_{ej} \gg \bar{N}_{co}$, then collisions should be most likely. Otherwise, ejections should occur. But what is the exact fraction of collisions to ejections?

Before proceeding, it is useful to define the dimensionless parameter λ :

$$\lambda \equiv \bar{N}_{co} / \bar{N}_{ej}. \quad (\text{D.13})$$

We have that

$$\lambda \sim 5000 F_{12}^{-1} \left(\frac{M_1}{M_J} \right)^2 \left(1 + \frac{m_2}{m_1} \right)^{-4} \left(\frac{a_{1,0}}{a_{2,0}} \right)^2 \left(\frac{R_{12}}{R_J} \right)^{-2} \left(\frac{a_1}{\text{AU}} \right)^2. \quad (\text{D.14})$$

If $\lambda \ll 1$, then collisions are most likely, while when $\lambda \gg 1$, ejections are most likely.

Now, we attack the branching ratio. First, we write down the conditional distribution of the actual ejection timescale N_{ej} and collision timescale N_{co} , conditioned on their mean value. These conditional PDFs are

$$f(N_{ej} | \bar{N}_{ej}) = \sqrt{\frac{\bar{N}_{ej}}{2\pi N_{ej}^3}} \exp(-\bar{N}_{ej}/2N_{ej}), \quad (\text{D.15})$$

$$f(N_{co} | \bar{N}_{co}) = \frac{1}{\bar{N}_{co}} \exp(N_{co}/\bar{N}_{co}). \quad (\text{D.16})$$

Given that the planet is either ejected or collided, that the probability that a planet is

ejected is equal to the probability that $N_{ej} < N_{co}$, and is therefore given by:

$$P(\text{ej}) = P(N_{ej} < N_{co}) = \int_0^\infty \int_0^{N_{co}} f(N_{ej}|\bar{N}_{ej})f(N_{co}|\bar{N}_{co}) dN_{ej} dN_{co} \quad (\text{D.17})$$

$$= e^{-\sqrt{2/\lambda}}. \quad (\text{D.18})$$

The branching ratio B is thus given by

$$B \equiv P(\text{ej})/P(\text{co}) = \frac{e^{-\sqrt{2/\lambda}}}{1 - e^{-\sqrt{2/\lambda}}}. \quad (\text{D.19})$$

The behavior of the branching ratio is as follows: When $\lambda \ll 1$, b is essentially zero, as it's the exponent of a large negative number. On the other hand, when $\lambda \gtrsim 1$, Taylor expansion gives

$$b \simeq \sqrt{\lambda/2} \sim 50F_{12}^{-1/2} \left(\frac{M_1}{M_J} \right) \left(1 + \frac{m_2}{m_1} \right)^{-2} \left(\frac{a_{1,0}}{a_{2,0}} \right) \left(\frac{R_{12}}{R_J} \right)^{-1} \left(\frac{a_1}{\text{AU}} \right). \quad (\text{D.20})$$

Now, let us consider the problem of two planets with $M_1 = 2M_J$, $M_2 = M_J$, $R_1 = R_2 = R_J$ and $k_0 = 2.5$. These parameters give $R_{12} = 2R_J$ and $b \sim 18F_{12}^{-1/2}\Theta$, where $\Theta \equiv (a_1/\text{AU})(R_{12}/R_J)^{-1}$. The observed branching ratio is $b \sim \Theta/4$ (Li et al., 2020). Thus, we see that for this particular configuration the gravitational focussing factor is nearly $F_{12} \sim 5000$. This is much larger than expected since at orbit crossing we only have $e_2 \sim 0.25$. However, note that the simulation used an initial mutual inclination of $\theta_{12,0} \sim \mathcal{U}[0, 2]$ degrees. This is much less than the Hill's inclination $\theta_{12,H} = 0.1 \simeq 6$ deg., and the system may be in the coplanar regime, which explains the very efficient merging.

D.3 Gravitational Focussing

We now discuss the effects of gravitational focussing. The nature of gravitational focussing depends on whether m_2 can be treated as test particle.

Hierarchical Mass Case

We assume $m_1 \gg m_2$. Much has already been written about this case, since it is relevant to planet formation and building of planet embryos. To first order the orbital properties of m_1 are constant, i.e. it stays in a circular orbit at its original semi-major axis. In the 2-body limit (i.e. neither planet perturbers the orbit of one another), the relative velocity at the point of orbit crossing is given by Bertotti et al. (2003)

$$v_{12,\infty}^2 = v_1^2 \left[3 - 2 \cos \theta_{12} \sqrt{(a_1/a_2)(1 - e_2^2)} - a_2/a_1 \right] \quad (\text{D.21})$$

where $v_{1,K}^2 = GM_\star/a_1$ is the Keplerian orbital velocity of planet 1. In the limit that $e_2, \theta_{12} \ll 1$ and $(a_2 - a_1) \ll a_1$, we have

$$v_{12,\infty}^2 \approx v_1^2(e_2^2 + \theta_{12}^2). \quad (\text{D.22})$$

Now, the above analysis all assumed the two-body limit where the solar potential plays no role. In reality, the solar potential is dominant until the the planets enter the hill sphere. This places a maximum limit on the effectiveness of gravitational focussing: at most, $F_{12} \lesssim R_H/R_{12}$. For scattering between two Jupiters the typical gravitational focussing parameters is well with-in this limit.

Thus the collision probability can be approximated as

$$P_{co} = \frac{\sigma_{12}^2}{4\pi a_1^2} = \frac{1}{4} \left(\frac{R_{12}}{a_1} \right)^2 \left[1 + 2 \left(\frac{M_1}{M_\star} \right) \left(\frac{a_1}{R_{12}} \right) \left(\frac{1}{e_2^2 + \theta_{12}^2} \right) \right]. \quad (\text{D.23})$$

Now, for a swarm of planetesimals around a single, more massive embryo, there is typically dynamical friction and dynamical equipartition, such that $e_2 \sim 2\theta_{12}$ (Lissauer, 1993). On the other hand, for the scattering between two giant planets, the mutual inclination θ_{12} is, to a large extent conserved and constant (due to the conservation of angular momentum around the z-axis), while the eccentricity grows over time in a random-walk-like fashion and can reach values between 0 and 1.

The largest collision probability occurs when e_2 is smallest. However, e_2 cannot be arbitrarily small because two circular orbits cannot have orbit crossings. Since we have assumed $m_1 \gg m_2$, the minimum eccentricity for orbit crossing is given by

$$e_{2,0} = (a_{\text{out}}/a_{\text{in}} - 1). \quad (\text{D.24})$$

If the two giant planets start out on circular orbits, then e_2 will increase from 0; the first time it reaches $e_2 \gtrsim e_{2,0}$ is the time of greatest collisional probability. If the collision does not occur at this point, then e_2 will increase further ($e_2^2 \propto N$ the number of pericenter passages of planet 2) and the collisional cross-section is decreased. This is why the collisional time-scale is skewed towards shorter values, and has a short tail that decays rapidly.

The extent to which the growth in e_2 over time is important depends on the planet masses. The typical eccentricity change per orbit is of order $\delta e_2 \sim M_1/M_\star$. If $(e_2^2 + \theta_{12}^2)/(e_2 \delta e_2) \gtrsim P_{co}$, then the per-orbit change in eccentricity is important. For typical Jupiter-mass planets $M_1 \sim 10^{-3}$, the rate of change of the eccentricity is pretty small, and we can assume that $P_{co} \simeq \text{const}$. We can then assume that, for purposes of the collisional timescale, $e_2 \sim e_{2,0}$ for all time. Now, in order for the two planets to be unstable, one requires $a_2 - a_1 \leq 2\sqrt{3}r_H$. If we define $k_0 \equiv (a_2 - a_1)/r_H$, then

$$e_{2,0} = k_0 \left(\frac{M_1}{3M_\star} \right)^{1/3} \approx 0.2 \left(\frac{k_0}{3} \right) \left(\frac{M_1}{M_J} \right)^{1/3} \left(\frac{M_\star}{M_\odot} \right)^{-1/3}. \quad (\text{D.25})$$

The mean collision timescale is $\bar{N}_{co} \sim 1/P_{co}$, which is (assuming that $e_2 \gtrsim \theta_{12}$)

$$\bar{N}_{co} \sim 1.8 \times 10^7 \left(\frac{R_{12}}{R_J} \right)^{-2} \left(\frac{a_1}{\text{AU}} \right)^2 [1 + F_{12}]^{-1}, \quad (\text{D.26})$$

and

$$F_{12} \simeq 100 \left(\frac{k_0}{3} \right)^{-2} \left(\frac{M_1}{M_J} \right)^{1/3} \left(\frac{M_\star}{M_\odot} \right)^{-1/3} \left(\frac{R_{12}}{R_J} \right)^{-1} \left(\frac{a_1}{\text{AU}} \right). \quad (\text{D.27})$$

The depending on whether gravitational focussing is important. When gravitational focussing is negligible, we have:

$$\bar{N}_{co} \sim 1.8 \times 10^7 \left(\frac{R_{12}}{R_J} \right)^{-2} \left(\frac{a_1}{\text{AU}} \right)^2. \quad (\text{D.28})$$

On the other hand, if gravitational focussing is dominant, then

$$\bar{N}_{co} \sim 1.8 \times 10^5 \left(\frac{R_{12}}{R_J} \right)^{-1} \left(\frac{a_1}{\text{AU}} \right)^1 \left(\frac{k_0}{3} \right)^2 \left(\frac{M_1}{M_J} \right)^{-1/3} \left(\frac{M_\star}{M_\odot} \right)^{1/3}. \quad (\text{D.29})$$

The criterion for gravitational focussing being dominant is when

$$\left(\frac{k_0}{3} \right)^{-2} \left(\frac{M_1}{M_J} \right)^{1/3} \left(\frac{M_\star}{M_\odot} \right)^{-1/3} \left(\frac{R_{12}}{R_J} \right)^{-1} \left(\frac{a_1}{\text{AU}} \right) \gtrsim 10^{-2}. \quad (\text{D.30})$$

For gas giants with $R_{12} \sim 2R_J$ and $M_1 \sim M_J$, gravitational focussing is always dominant. For systems of initially well-separated Super-Earths or Mini-Neptunes, gravitational focussing becomes important when $a_1 \gtrsim 0.2 \text{ AU}$.

Comparable Mass Case

When the masses are comparable it is much more difficult to estimate F_{12} from first principles. In general, F_{12} should be much smaller when masses are comparable, because the two planets spend a large amount of time at high eccentricities, and the relative velocities also tend to be larger. One would have to resort to N-body simulations to determine F_{12} empirically for this case.

D.4 Finite Integration Time-limit Effects

We see that in the limit when the ejection timescale is much larger than the collisional timescale, the probability of an ejection is much less than one; conversely, when the timescale for ejection is much shorter, the probability of ejections tends to unity.

In our previous analysis, we have assumed that an infinite amount of time could occur before either collision or ejection; in reality, any physical process or numerical simulation has a finite timescale, and observations are biased towards events that happen earlier. We can correct for this time truncation by applying Bayes theorem: Let the maximal time (in units of number of orbits) be $N = N_{max}$, then the probability that an ejection occurs before the maximal time has elapsed is given by

$$P(\text{ej}|N \leq N_{max}) = \frac{P(N \leq N_{max}|\text{ej})P(\text{ej})}{P(N \leq N_{max})}. \quad (\text{D.31})$$

Similarly, the conditional probability for collision is given by

$$P(\text{co}|N \leq N_{max}) = \frac{P(N \leq N_{max}|\text{co})P(\text{co})}{P(N \leq N_{max})}. \quad (\text{D.32})$$

Dividing the above two equations, we have that

$$\frac{P(\text{ej}|N \leq N_{max})}{P(\text{co}|N \leq N_{max})} = \frac{\text{Erfc}(\sqrt{\bar{N}_{ej}/2N_{max}})e^{-\sqrt{2/\lambda}}}{(1 - e^{-N_{max}/\bar{N}_{co}})(1 - e^{-\sqrt{2/\lambda}})}. \quad (\text{D.33})$$

Thus we see that the effect of truncating the integration at some finite stop limit serves to add a Bayesian prior factor to the indefinite-time limit. When $N_{max} \gg \max(\bar{N}_{ej}, \bar{N}_{co})$, the Bayesian prior factor approaches 1 and we recover our old limit. On the other hand, when $N_{max} \rightarrow 0$, we have $\text{Erfc}(x) \approx e^{-x^2} / \sqrt{\pi x^2}$ and therefore

$$\frac{P(\text{ej}|N \leq N_{max})}{P(\text{co}|N \leq N_{max})} \approx \sqrt{\frac{N_{max}}{2\bar{N}_{ej}}} \frac{\bar{N}_{co}}{N_{max}} \left(\frac{e^{-\sqrt{2/\lambda}}}{1 - e^{-\sqrt{2/\lambda}}} \right) e^{-\bar{N}_{ej}/2N_{max}}. \quad (\text{D.34})$$

BIBLIOGRAPHY

- Alexander, M. E. (1973). The Weak Friction Approximation and Tidal Evolution in Close Binary Systems. *ApSS*, 23:459–510.
- Anderson, K. R. and Lai, D. (2018). Teetering stars: resonant excitation of stellar obliquities by hot and warm Jupiters with external companions. *MNRAS*, 480:1402–1414.
- Anderson, K. R., Lai, D., and Pu, B. (2020). In situ scattering of warm jupiters and implications for dynamical histories. *Monthly Notices of the Royal Astronomical Society*, 491(1):1369–1383.
- Bakos, G. Á., Torres, G., Pál, A., Hartman, J., Kovács, G., Noyes, R. W., Latham, D. W., Sasselov, D. D., Sipőcz, B., Esquerdo, G. A., Fischer, D. A., Johnson, J. A., Marcy, G. W., Butler, R. P., Isaacson, H., Howard, A., Vogt, S., Kovács, G., Fernandez, J., Moór, A., Stefanik, R. P., Lázár, J., Papp, I., and Sári, P. (2010). HAT-P-11b: A Super-Neptune Planet Transiting a Bright K Star in the Kepler Field. *ApJ*, 710(2):1724–1745.
- Ballard, S. and Johnson, J. A. (2016). The Kepler Dichotomy among the M Dwarfs: Half of Systems Contain Five or More Coplanar Planets. *ApJ*, 816:66.
- Baranec, C., Ziegler, C., Law, N. M., Morton, T., Riddle, R., Atkinson, D., Schonhut, J., and Crepp, J. (2016). Robo-AO Kepler Planetary Candidate Survey. II. Adaptive Optics Imaging of 969 Kepler Exoplanet Candidate Host Stars. *AJ*, 152:18.
- Batalha, N. M., Borucki, W. J., Bryson, S. T., Buchhave, L. A., Caldwell, D. A., Christensen-Dalsgaard, J., Ciardi, D., Dunham, E. W., Fressin, F., Gautier, III, T. N., Gilliland, R. L., Haas, M. R., Howell, S. B., Jenkins, J. M., Kjeldsen, H., Koch, D. G., Latham, D. W., Lissauer, J. J., Marcy, G. W., Rowe, J. F., Sasselov, D. D., Seager, S., Steffen, J. H., Torres, G., Basri, G. S., Brown, T. M., Charbonneau, D., Christiansen, J., Clarke, B., Cochran, W. D., Dupree, A., Fabrycky, D. C., Fischer, D., Ford, E. B.,

- Fortney, J., Girouard, F. R., Holman, M. J., Johnson, J., Isaacson, H., Klaus, T. C., Machalek, P., Moorehead, A. V., Morehead, R. C., Ragozzine, D., Tenenbaum, P., Twicken, J., Quinn, S., VanCleve, J., Walkowicz, L. M., Welsh, W. F., Devore, E., and Gould, A. (2011a). Kepler's First Rocky Planet: Kepler-10b. *ApJ*, 729:27.
- Batalha, N. M., Borucki, W. J., Bryson, S. T., Buchhave, L. A., Caldwell, D. A., Christensen-Dalsgaard, J., Ciardi, D., Dunham, E. W., Fressin, F., Gautier, III, T. N., Gilliland, R. L., Haas, M. R., Howell, S. B., Jenkins, J. M., Kjeldsen, H., Koch, D. G., Latham, D. W., Lissauer, J. J., Marcy, G. W., Rowe, J. F., Sasselov, D. D., Seager, S., Steffen, J. H., Torres, G., Basri, G. S., Brown, T. M., Charbonneau, D., Christiansen, J., Clarke, B., Cochran, W. D., Dupree, A., Fabrycky, D. C., Fischer, D., Ford, E. B., Fortney, J., Girouard, F. R., Holman, M. J., Johnson, J., Isaacson, H., Klaus, T. C., Machalek, P., Moorehead, A. V., Morehead, R. C., Ragozzine, D., Tenenbaum, P., Twicken, J., Quinn, S., VanCleve, J., Walkowicz, L. M., Welsh, W. F., Devore, E., and Gould, A. (2011b). Kepler's First Rocky Planet: Kepler-10b. *ApJ*, 729:27.
- Batygin, K. and Laughlin, G. (2008). On the Dynamical Stability of the Solar System. *ApJ*, 683(2):1207–1216.
- Batygin, K., Laughlin, G., Meschiari, S., Rivera, E., Vogt, S., and Butler, P. (2009). A Quasi-stationary Solution to Gliese 436b's Eccentricity. *ApJ*, 699:23–30.
- Batygin, K. and Morbidelli, A. (2013). Dissipative Divergence of Resonant Orbits. *AJ*, 145:1.
- Becker, J. C. and Adams, F. C. (2017). Effects of unseen additional planetary perturbors on compact extrasolar planetary systems. *MNRAS*, 468:549–563.
- Bertotti, B., Farinella, P., and Vokrouhlick, D. (2003). *Physics of the Solar System*, 293.
- Borodin, A. and Salminen, P. (2002). *Handbook of Brownian Motion - Facts and Formulae*.

- Borucki, W. J., Koch, D. G., Basri, G., Batalha, N., Boss, A., Brown, T. M., Caldwell, D., Christensen-Dalsgaard, J., Cochran, W. D., DeVore, E., Dunham, E. W., Dupree, A. K., Gautier, Thomas N., I., Geary, J. C., Gilliland, R., Gould, A., Howell, S. B., Jenkins, J. M., Kjeldsen, H., Latham, D. W., Lissauer, J. J., Marcy, G. W., Monet, D. G., Sasselov, D., Tarter, J., Charbonneau, D., Doyle, L., Ford, E. B., Fortney, J., Holman, M. J., Seager, S., Steffen, J. H., Welsh, W. F., Allen, C., Bryson, S. T., Buchhave, L., Chandrasekaran, H., Christiansen, J. L., Ciardi, D., Clarke, B. D., Dotson, J. L., Endl, M., Fischer, D., Fressin, F., Haas, M., Horch, E., Howard, A., Isaacson, H., Kolodziejczak, J., Li, J., MacQueen, P., Meibom, S., Prsa, A., Quintana, E. V., Rowe, J., Sherry, W., Tenenbaum, P., Torres, G., Twicken, J. D., Van Cleve, J., Walkowicz, L., and Wu, H. (2011). Characteristics of Kepler Planetary Candidates Based on the First Data Set. *ApJ*, 728(2):117.
- Boué, G. and Fabrycky, D. C. (2014a). Compact Planetary Systems Perturbed by an Inclined Companion. I. Vectorial Representation of the Secular Model. *ApJ*, 789:110.
- Boué, G. and Fabrycky, D. C. (2014b). Compact Planetary Systems Perturbed by an Inclined Companion. II. Stellar Spin-Orbit Evolution. *ApJ*, 789:111.
- Brakensiek, J. and Ragozzine, D. (2016). Efficient Geometric Probabilities of Multi-Transiting Exoplanetary Systems from CORBITS. *ApJ*, 821:47.
- Brinch, C., Jørgensen, J. K., Hogerheijde, M. R., Nelson, R. P., and Gressel, O. (2016). Misaligned Disks in the Binary Protostar IRS 43. *ApJL*, 830:L16.
- Bryan, M. L., Knutson, H. A., Howard, A. W., Ngo, H., Batygin, K., Crepp, J. R., Fulton, B. J., Hinkley, S., Isaacson, H., Johnson, J. A., Marcy, G. W., and Wright, J. T. (2016). Statistics of Long Period Gas Giant Planets in Known Planetary Systems. *ApJ*, 821:89.
- Bryan, M. L., Knutson, H. A., Lee, E. J., Fulton, B. J., Batygin, K., Ngo, H., and Meshkat, T. (2019). An Excess of Jupiter Analogs in Super-Earth Systems. *AJ*, 157(2):52.

- Burke, C. J., Christiansen, J. L., Mullally, F., Seader, S., Huber, D., Rowe, J. F., Coughlin, J. L., Thompson, S. E., Catanzarite, J., Clarke, B. D., Morton, T. D., Caldwell, D. A., Bryson, S. T., Haas, M. R., Batalha, N. M., Jenkins, J. M., Tenenbaum, P., Twicken, J. D., Li, J., Quintana, E., Barclay, T., Henze, C. E., Borucki, W. J., Howell, S. B., and Still, M. (2015). Terrestrial Planet Occurrence Rates for the Kepler GK Dwarf Sample. *ApJ*, 809:8.
- Carrera, D., Davies, M. B., and Johansen, A. (2016). Survival of habitable planets in unstable planetary systems. *MNRAS*, 463:3226–3238.
- Chatterjee, S., Ford, E. B., Matsumura, S., and Rasio, F. A. (2008). Dynamical Outcomes of Planet-Planet Scattering. *ApJ*, 686:580–602.
- Chiang, E. and Laughlin, G. (2013). The minimum-mass extrasolar nebula: in situ formation of close-in super-Earths. *MNRAS*, 431:3444–3455.
- Cumming, A., Butler, R. P., Marcy, G. W., Vogt, S. S., Wright, J. T., and Fischer, D. A. (2008). The Keck Planet Search: Detectability and the Minimum Mass and Orbital Period Distribution of Extrasolar Planets. *PASP*, 120:531.
- Dai, F., Masuda, K., and Winn, J. N. (2018). Larger mutual inclinations for the shortest-period planets. *ArXiv e-prints*.
- Damasso, M., Sozzetti, A., Lovis, C., Barros, S. C. C., Sousa, S. G., Demangeon, O. D. S., Faria, J. P., Lillo-Box, J., Cristiani, S., Pepe, F., Rebolo, R., Santos, N. C., Osorio, M. R. Z., Hernández, J. I. G., Amate, M., Pasquini, L., Zerbi, F. M., Adibekyan, V., Abreu, M., Affolter, M., Alibert, Y., Aliverti, M., Allart, R., Prieto, C. A., Álvarez, D., Alves, D., Avila, G., Baldini, V., Bandy, T., Benz, W., Bianco, A., Borsa, F., Bossini, D., Bourrier, V., Bouchy, F., Broeg, C., Cabral, A., Calderone, G., Cirami, R., Coelho, J., Conconi, P., Coretti, I., Cumani, C., Cupani, G., D’Odorico, V., Deiries, S., Dekker, H., Delabre, B., Marcantonio, P. D., Dumusque, X., Ehrenreich, D., Figueira, P., Fragoso, A., Genolet, L., Genoni, M., Santos, R. G., Hughes, I., Iwert, O., Kerber, F.,

- Knudstrup, J., Landoni, M., Lavie, B., Lizon, J. L., Curto, G. L., Maire, C., Martins, C. J. . A. P., Mégevand, D., Mehner, A., Micela, G., Modigliani, A., Molaro, P., Monteiro, M. A., Monteiro, M. J. P. F. G., Moschetti, M., Mueller, E., Murphy, M. T., Nunes, N., Oggioni, L., Oliveira, A., Oshagh, M., Pallé, E., Pariani, G., Poretti, E., Rasilla, J. L., Rebordão, J., Redaelli, E. M., Riva, M., Tschudi, S. S., Santin, P., Santos, P., Ségransan, D., Schmidt, T. M., Segovia, A., Sosnowska, D., Spanò, P., Mascareño, A. S., Tabernero, H., Tenegi, F., Udry, S., and Zanutta, A. (2020). A precise architecture characterization of the *trappist-1* planetary system.
- Darwin, G. H. (1880). On the Secular Changes in the Elements of the Orbit of a Satellite Revolving about a Tidally Distorted Planet. *Philosophical Transactions of the Royal Society of London Series I*, 171:713–891.
- Dawson, R. I. and Fabrycky, D. C. (2010). Radial Velocity Planets De-aliased: A New, Short Period for Super-Earth 55 Cnc e. *ApJ*, 722:937–953.
- Dawson, R. I., Lee, E. J., and Chiang, E. (2016). Correlations between Compositions and Orbits Established by the Giant Impact Era of Planet Formation. *ApJ*, 822:54.
- Denham, P., Naoz, S., Hoang, B.-M., Stephan, A. P., and Farr, W. M. (2018). Hidden Planetary Friends: On the Stability Of 2-Planet Systems in the Presence of a Distant, Inclined Companion. *ArXiv e-prints*.
- Fabrycky, D. C., Lissauer, J. J., Ragozzine, D., Rowe, J. F., Steffen, J. H., Agol, E., Barclay, T., Batalha, N., Borucki, W., Ciardi, D. R., Ford, E. B., Gautier, T. N., Geary, J. C., Holman, M. J., Jenkins, J. M., Li, J., Morehead, R. C., Morris, R. L., Shporer, A., Smith, J. C., Still, M., and Van Cleve, J. (2014). Architecture of Kepler’s Multi-transiting Systems. II. New Investigations with Twice as Many Candidates. *ApJ*, 790:146.
- Fang, J. and Margot, J.-L. (2012). Architecture of Planetary Systems Based on Kepler Data: Number of Planets and Coplanarity. *ApJ*, 761:92.

- Fang, J. and Margot, J.-L. (2013). Are Planetary Systems Filled to Capacity? A Study Based on Kepler Results. *ApJ*, 767:115.
- Figueira, P., Marmier, M., Boué, G., Lovis, C., Santos, N. C., Montalto, M., Udry, S., Pepe, F., and Mayor, M. (2012). Comparing HARPS and Kepler surveys. The alignment of multiple-planet systems. *AAP*, 541:A139.
- Ford, E. B., Kozinsky, B., and Rasio, F. A. (2000). Secular Evolution of Hierarchical Triple Star Systems. *ApJ*, 535:385–401.
- Ford, E. B. and Rasio, F. A. (2008). Origins of Eccentric Extrasolar Planets: Testing the Planet-Planet Scattering Model. *ApJ*, 686:621–636.
- Fouchard, M., Rickman, H., Froeschlé, C., and Valsecchi, G. B. (2013). Planetary perturbations for Oort Cloud comets. I. Distributions and dynamics. *Icarus*, 222:20–31.
- Frelikh, R., Jang, H., Murray-Clay, R. A., and Petrovich, C. (2019). Signatures of a Planet-Planet Impacts Phase in Exoplanetary Systems Hosting Giant Planets. *ApJL*, 884(2):L47.
- Fressin, F., Torres, G., Désert, J.-M., Charbonneau, D., Batalha, N. M., Fortney, J. J., Rowe, J. F., Allen, C., Borucki, W. J., Brown, T. M., Bryson, S. T., Ciardi, D. R., Cochran, W. D., Deming, D., Dunham, E. W., Fabrycky, D. C., Gautier, III, T. N., Gilliland, R. L., Henze, C. E., Holman, M. J., Howell, S. B., Jenkins, J. M., Kinemuchi, K., Knutson, H., Koch, D. G., Latham, D. W., Lissauer, J. J., Marcy, G. W., Ragozzine, D., Sasselov, D. D., Still, M., Tenenbaum, P., and Uddin, K. (2011). Kepler-10 c: a 2.2 Earth Radius Transiting Planet in a Multiple System. *ApJS*, 197:5.
- Gladman, B. (1993). Dynamics of Systems of Two Close Planets. *Icarus*, 106(1):247–263.
- Goldreich, P. and Soter, S. (1966). Q in the Solar System. *Icarus*, 5:375–389.

- Gratia, P. and Fabrycky, D. (2017). Outer-planet scattering can gently tilt an inner planetary system. *MNRAS*, 464:1709–1717.
- Hadden, S. and Lithwick, Y. (2017). Kepler Planet Masses and Eccentricities from TTV Analysis. *AJ*, 154:5.
- Hansen, B. M. S. (2017). Perturbation of Compact Planetary Systems by Distant Giant Planets. *MNRAS*, 467:1531–1560.
- Hansen, B. M. S. and Murray, N. (2013). Testing in Situ Assembly with the Kepler Planet Candidate Sample. *ApJ*, 775:53.
- Hansen, B. M. S. and Murray, N. (2015). Secular effects of tidal damping in compact planetary systems. *MNRAS*, 448:1044–1059.
- Hansen, B. M. S. and Zink, J. (2015). On the potentially dramatic history of the super-Earth ρ 55 Cancri e. *MNRAS*, 450:4505–4520.
- Herman, M. K., Zhu, W., and Wu, Y. (2019). Revisiting the long-period transiting planets from kepler. *The Astronomical Journal*, 157(6):248.
- Higuchi, A., Kokubo, E., and Mukai, T. (2006). Scattering of planetesimals by a planet: Formation of comet cloud candidates. *The Astronomical Journal*, 131(2):1119–1129.
- Huang, C. X., Burt, J., Vanderburg, A., Günther, M. N., Shporer, A., Dittmann, J. A., Winn, J. N., Wittenmyer, R., Sha, L., Kane, S. R., and et al. (2018a). Tess discovery of a transiting super-earth in the pi mensae system. *The Astrophysical Journal*, 868(2):L39.
- Huang, C. X., Burt, J., Vanderburg, A., Günther, M. N., Shporer, A., Dittmann, J. A., Winn, J. N., Wittenmyer, R., Sha, L., Kane, S. R., Ricker, G. R., Vanderspek, R. K., Latham, D. W., Seager, S., Jenkins, J. M., Caldwell, D. A., Collins, K. A., Guerrero, N., Smith, J. C., Quinn, S. N., Udry, S., Pepe, F., Bouchy, F., Ségransan, D., Lovis, C., Ehrenreich, D., Marmier, M., Mayor, M., Wohler, B., Haworth, K., Morgan, E. H., Fausnaugh, M., Ciardi, D. R., Christiansen, J., Charbonneau, D., Dragomir,

- D., Deming, D., Glidden, A., Levine, A. M., McCullough, P. R., Yu, L., Narita, N., Nguyen, T., Morton, T., Pepper, J., Pál, A., Rodriguez, J. E., Stassun, K. G., Torres, G., Sozzetti, A., Doty, J. P., Christensen-Dalsgaard, J., Laughlin, G., Clampin, M., Bean, J. L., Buchhave, L. A., Bakos, G. Á., Sato, B., Ida, S., Kaltenegger, L., Palte, E., Sasselov, D., Butler, R. P., Lissauer, J., Ge, J., and Rinehart, S. A. (2018b). TESS discovery of a transiting super-earth in the pi mensae system. *The Astrophysical Journal*, 868(2):L39.
- Huang, C. X., Petrovich, C., and Deibert, E. (2017). Dynamically Hot Super-Earths from Outer Giant Planet Scattering. *AJ*, 153:210.
- Hut, P. (1981). Tidal evolution in close binary systems. *AAP*, 99:126–140.
- Ida, S. and Lin, D. N. C. (2004). Toward a Deterministic Model of Planetary Formation. II. The Formation and Retention of Gas Giant Planets around Stars with a Range of Metallicities. *ApJ*, 616:567–572.
- Ida, S., Lin, D. N. C., and Nagasawa, M. (2013). Toward a Deterministic Model of Planetary Formation. VII. Eccentricity Distribution of Gas Giants. *ApJ*, 775:42.
- Ida, S. and Nakazawa, K. (1989). Collisional probability of planetesimals revolving in the solar gravitational field. III. *AAP*, 224(1-2):303–315.
- Jensen, E. L. N. and Akeson, R. (2014). Misaligned protoplanetary disks in a young binary star system. *Nature*, 511:567–569.
- Johansen, A., Davies, M. B., Church, R. P., and Holmelin, V. (2012). Can Planetary Instability Explain the Kepler Dichotomy? *ApJ*, 758:39.
- Jontof-Hutter, D., Weaver, B. P., Ford, E. B., Lissauer, J. J., and Fabrycky, D. C. (2017). Outer Architecture of Kepler-11: Constraints from Coplanarity. *AJ*, 153:227.
- Jurić, M. and Tremaine, S. (2008). Dynamical Origin of Extrasolar Planet Eccentricity Distribution. *ApJ*, 686:603–620.

- Kokubo, E. and Ida, S. (2002). Formation of Protoplanet Systems and Diversity of Planetary Systems. *ApJ*, 581:666–680.
- Kozai, Y. (1962). Secular perturbations of asteroids with high inclination and eccentricity. *AJ*, 67:591.
- Kunovac Hodžić, V., Triaud, A. H. M. J., Cegla, H. M., Chaplin, W. J., and Davies, G. R. (2020). Orbital misalignment of the super-Earth π Men c with the spin of its star. *arXiv e-prints*, page arXiv:2007.11564.
- Lai, D., Anderson, K. R., and Pu, B. (2018). How do external companions affect spin-orbit misalignment of hot Jupiters? *MNRAS*, 475(4):5231–5236.
- Lai, D. and Pu, B. (2017). Hiding Planets behind a Big Friend: Mutual Inclinations of Multi-planet Systems with External Companions. *AJ*, 153:42.
- Laine, V. (2016). Quantification of tidal parameters from Solar System data. *Celestial Mechanics and Dynamical Astronomy*, 126:145–156.
- Laskar, J. and Boué, G. (2010). Explicit expansion of the three-body disturbing function for arbitrary eccentricities and inclinations. *AAP*, 522:A60.
- Laskar, J. and Gastineau, M. (2009). Existence of collisional trajectories of Mercury, Mars and Venus with the Earth. *Nature*, 459(7248):817–819.
- Lee, E. J. and Chiang, E. (2017). Magnetospheric Truncation, Tidal Inspiral, and the Creation of Short-period and Ultra-short-period Planets. *ApJ*, 842:40.
- Léger, A., Rouan, D., Schneider, J., Barge, P., Fridlund, M., Samuel, B., Ollivier, M., Guenther, E., Deleuil, M., Deeg, H. J., Auvergne, M., Alonso, R., Aigrain, S., Alapini, A., Almenara, J. M., Baglin, A., Barbieri, M., Bruntt, H., Bordé, P., Bouchy, F., Cabrera, J., Catala, C., Carone, L., Carpano, S., Csizmadia, S., Dvorak, R., Erikson, A., Ferraz-Mello, S., Foing, B., Fressin, F., Gandolfi, D., Gillon, M., Gondoin, P., Grasset, O., Guillot, T., Hatzes, A., Hébrard, G., Jorda, L., Lammer, H., Llebaria, A.,

- Loeillet, B., Mayor, M., Mazeh, T., Moutou, C., Pätzold, M., Pont, F., Queloz, D., Rauer, H., Renner, S., Samadi, R., Shporer, A., Sotin, C., Tingley, B., Wuchterl, G., Adda, M., Agogu, P., Appourchaux, T., Ballans, H., Baron, P., Beaufort, T., Bellenger, R., Berlin, R., Bernardi, P., Blouin, D., Baudin, F., Bodin, P., Boisdard, L., Boit, L., Bonneau, F., Borzeix, S., Briet, R., Buey, J.-T., Butler, B., Cailleau, D., Cautain, R., Chabaud, P.-Y., Chaintreuil, S., Chiavassa, F., Costes, V., Cuna Parrho, V., de Oliveira Fialho, F., Decaudin, M., Defise, J.-M., Djalal, S., Epstein, G., Exil, G.-E., Fauré, C., Fenouillet, T., Gaboriaud, A., Gallic, A., Gamet, P., Gavalda, P., Grolleau, E., Gruneisen, R., Gueguen, L., Guis, V., Guivarc'h, V., Guterman, P., Hallouard, D., Hasiba, J., Heuripeau, F., Huntzinger, G., Hustaix, H., Imad, C., Imbert, C., Johlander, B., Jouret, M., Journoud, P., Karioty, F., Kerjean, L., Lafaille, V., Lafond, L., Lam-Trong, T., Landiech, P., Lapeyrere, V., Larqué, T., Laudet, P., Lautier, N., Lecann, H., Lefevre, L., Leruyet, B., Levacher, P., Magnan, A., Mazy, E., Mertens, F., Mesnager, J.-M., Meunier, J.-C., Michel, J.-P., Monjoin, W., Naudet, D., Nguyen-Kim, K., Orcesi, J.-L., Ottacher, H., Perez, R., Peter, G., Plasson, P., Plessier, J.-Y., Pontet, B., Pradines, A., Quentin, C., Reynaud, J.-L., Rolland, G., Rollenhagen, F., Romagnan, R., Russ, N., Schmidt, R., Schwartz, N., Sebbag, I., Sedes, G., Smit, H., Steller, M. B., Sunter, W., Surace, C., Tello, M., Tiphène, D., Toulouse, P., Ulmer, B., Vandermarcq, O., Vergnault, E., Vuillemin, A., and Zanatta, P. (2009). Transiting exoplanets from the CoRoT space mission. VIII. CoRoT-7b: the first super-Earth with measured radius. *AAP*, 506:287–302.
- Li, J., Lai, D., Anderson, K. R., and Pu, B. (2020). Giant Planet Scatterings and Collisions: Hydrodynamics, Merger-Ejection Branching Ratio, and Properties of the Remnants. *arXiv e-prints*, page arXiv:2006.10067.
- Lidov, M. L. (1962). The evolution of orbits of artificial satellites of planets under the action of gravitational perturbations of external bodies. *Planetary Space Science*,

9:719–759.

Lin, D. N. C. and Ida, S. (1997). On the Origin of Massive Eccentric Planets. *ApJ*, 477:781–791.

Lissauer, J. J. (1993). Planet formation. *ARAA*, 31:129–174.

Lissauer, J. J., Ragozzine, D., Fabrycky, D. C., Steffen, J. H., Ford, E. B., Jenkins, J. M., Shporer, A., Holman, M. J., Rowe, J. F., Quintana, E. V., Batalha, N. M., Borucki, W. J., Bryson, S. T., Caldwell, D. A., Carter, J. A., Ciardi, D., Dunham, E. W., Fortney, J. J., Gautier, III, T. N., Howell, S. B., Koch, D. G., Latham, D. W., Marcy, G. W., Morehead, R. C., and Sasselov, D. (2011). Architecture and Dynamics of Kepler’s Candidate Multiple Transiting Planet Systems. *ApJS*, 197:8.

Lithwick, Y. and Wu, Y. (2012). Resonant Repulsion of Kepler Planet Pairs. *ApJL*, 756:L11.

Lithwick, Y. and Wu, Y. (2014). Secular chaos and its application to Mercury, hot Jupiters, and the organization of planetary systems. *Proceedings of the National Academy of Science*, 111:12610–12615.

Lithwick, Y., Xie, J., and Wu, Y. (2012). Extracting Planet Mass and Eccentricity from TTV Data. *ApJ*, 761:122.

Liu, B., Muñoz, D. J., and Lai, D. (2015). Suppression of extreme orbital evolution in triple systems with short-range forces. *MNRAS*, 447:747–764.

MacDonald, M. G., Ragozzine, D., Fabrycky, D. C., Ford, E. B., Holman, M. J., Isaacson, H. T., Lissauer, J. J., Lopez, E. D., Mazeh, T., Rogers, L., Rowe, J. F., Steffen, J. H., and Torres, G. (2016). A Dynamical Analysis of the Kepler-80 System of Five Transiting Planets. *AJ*, 152:105.

Mardling, R. A. (2007). Long-term tidal evolution of short-period planets with companions. *MNRAS*, 382:1768–1790.

- Mardling, R. A. (2010). The determination of planetary structure in tidally relaxed inclined systems. *MNRAS*, 407:1048–1069.
- Masuda, K., Winn, J. N., and Kawahara, H. (2020). Mutual Orbital Inclinations between Cold Jupiters and Inner Super-Earths. *AJ*, 159(2):38.
- Matsumura, S., Ida, S., and Nagasawa, M. (2013). Effects of Dynamical Evolution of Giant Planets on Survival of Terrestrial Planets. *ApJ*, 767:129.
- Milankovic, M. (1939). Über die verwendung vektorieller bahnelemente in der störungsrechnung. *Bull. Serb. Acad. Math. Nat. A*, 1:6.
- Mills, S. M., Howard, A. W., Weiss, L. M., Steffen, J. H., Isaacson, H., Fulton, B. J., Petigura, E. A., Kosiarek, M. R., Hirsch, L. A., and Boisvert, J. H. (2019). Long-period giant companions to three compact, multiplanet systems. *The Astronomical Journal*, 157(4):145.
- Moriarty, J. and Ballard, S. (2016). The Kepler Dichotomy in Planetary Disks: Linking Kepler Observables to Simulations of Late-stage Planet Formation. *ApJ*, 832(1):34.
- Morton, T. D., Bryson, S. T., Coughlin, J. L., Rowe, J. F., Ravichandran, G., Petigura, E. A., Haas, M. R., and Batalha, N. M. (2016). False Positive Probabilities for all Kepler Objects of Interest: 1284 Newly Validated Planets and 428 Likely False Positives. *ApJ*, 822:86.
- Mullally, F., Coughlin, J. L., Thompson, S. E., Rowe, J., Burke, C., Latham, D. W., Batalha, N. M., Bryson, S. T., Christiansen, J., Henze, C. E., Ofir, A., Quarles, B., Shporer, A., Van Eylen, V., Van Laerhoven, C., Shah, Y., Wolfgang, A., Chaplin, W. J., Xie, J.-W., Akeson, R., Argabright, V., Bachtell, E., Barclay, T., Borucki, W. J., Caldwell, D. A., Campbell, J. R., Catanzarite, J. H., Cochran, W. D., Duren, R. M., Fleming, S. W., Fraquelli, D., Girouard, F. R., Haas, M. R., Hełminiak, K. G., Howell, S. B., Huber, D., Larson, K., Gautier, III, T. N., Jenkins, J. M., Li, J., Lissauer, J. J.,

- McArthur, S., Miller, C., Morris, R. L., Patil-Sabale, A., Plavchan, P., Putnam, D., Quintana, E. V., Ramirez, S., Silva Aguirre, V., Seader, S., Smith, J. C., Steffen, J. H., Stewart, C., Stober, J., Still, M., Tenenbaum, P., Troeltzsch, J., Twicken, J. D., and Zamudio, K. A. (2015). Planetary Candidates Observed by Kepler. VI. Planet Sample from Q1–Q16 (47 Months). *ApJS*, 217:31.
- Murray, C. D. and Dermott, S. F. (1999). *Solar system dynamics*.
- Mushkin, J. and Katz, B. (2020). A Simple Random-Walk Model Explains the Disruption Process of Hierarchical, Eccentric 3-Body Systems. *arXiv e-prints*, page arXiv:2005.03669.
- Mustill, A. J., Davies, M. B., and Johansen, A. (2017a). The dynamical evolution of transiting planetary systems including a realistic collision prescription. *ArXiv e-prints*.
- Mustill, A. J., Davies, M. B., and Johansen, A. (2017b). The effects of external planets on inner systems: multiplicities, inclinations and pathways to eccentric warm Jupiters. *MNRAS*, 468:3000–3023.
- Nakazawa, K., Ida, S., and Nakagawa, Y. (1989). Collisional probability of planetesimals revolving in the solar gravitational field. II - The validity of the two-body approximation. *AAP*, 221(2):342–347.
- Newton, I. (1999). *The Principia: mathematical principles of natural philosophy*. Univ of California Press.
- Ogilvie, G. I. (2014). Tidal Dissipation in Stars and Giant Planets. *ARAA*, 52:171–210.
- Owen, J. E. and Wu, Y. (2013). Kepler Planets: A Tale of Evaporation. *ApJ*, 775:105.
- Penev, K., Bouma, L. G., Winn, J. N., and Hartman, J. D. (2018). Empirical Tidal Dissipation in Exoplanet Hosts From Tidal Spin-up. *AJ*, 155:165.

- Petigura, E. A., Marcy, G. W., Winn, J. N., Weiss, L. M., Fulton, B. J., Howard, A. W., Sinukoff, E., Isaacson, H., Morton, T. D., and Johnson, J. A. (2018). The California-Kepler Survey. IV. Metal-rich Stars Host a Greater Diversity of Planets. *AJ*, 155:89.
- Petrovich, C. (2015a). Steady-state Planet Migration by the Kozai-Lidov Mechanism in Stellar Binaries. *ApJ*, 799:27.
- Petrovich, C. (2015b). The Stability and Fates of Hierarchical Two-planet Systems. *ApJ*, 808:120.
- Petrovich, C., Deibert, E., and Wu, Y. (2018). Ultra-short-period planets from secular chaos. *ArXiv e-prints*.
- Petrovich, C., Tremaine, S., and Rafikov, R. (2014). Scattering Outcomes of Close-in Planets: Constraints on Planet Migration. *ApJ*, 786:101.
- Pu, B. and Lai, D. (2018). Eccentricities and Inclinations of Multi-Planet Systems with External Perturbers. *MNRAS*.
- Pu, B. and Lai, D. (2019). Low-eccentricity migration of ultra-short-period planets in multiplanet systems. *MNRAS*, 488(3):3568–3587.
- Pu, B. and Wu, Y. (2015). Spacing of Kepler Planets: Sculpting by Dynamical Instability. *ApJ*, 807:44.
- Rajpaul, V., Buchhave, L. A., and Aigrain, S. (2017). Pinning down the mass of Kepler-10c: the importance of sampling and model comparison. *MNRAS*, 471:L125–L130.
- Rasio, F. A. and Ford, E. B. (1996). Dynamical instabilities and the formation of extrasolar planetary systems. *Science*, 274(5289):954–956.
- Read, M. J., Wyatt, M. C., and Triaud, A. H. M. J. (2017). Transit probabilities in secularly evolving planetary systems. *MNRAS*, 469:171–192.
- Rein, H. and Liu, S.-F. (2012a). REBOUND: an open-source multi-purpose N-body code for collisional dynamics. *AAP*, 537:A128.

- Rein, H. and Liu, S.-F. (2012b). REBOUND: an open-source multi-purpose N-body code for collisional dynamics. *AAP*, 537:A128.
- Rein, H. and Spiegel, D. S. (2015). IAS15: a fast, adaptive, high-order integrator for gravitational dynamics, accurate to machine precision over a billion orbits. *MNRAS*, 446:1424–1437.
- Rein, H. and Tamayo, D. (2015). WHFAST: a fast and unbiased implementation of a symplectic Wisdom-Holman integrator for long-term gravitational simulations. *MNRAS*, 452:376–388.
- Rosa, R. J. D., Dawson, R., and Nielsen, E. L. (2020). A significant mutual inclination between the planets within the mensae system.
- Rowe, J. F., Bryson, S. T., Marcy, G. W., Lissauer, J. J., Jontof-Hutter, D., Mullally, F., Gilliland, R. L., Issacson, H., Ford, E., Howell, S. B., Borucki, W. J., Haas, M., Huber, D., Steffen, J. H., Thompson, S. E., Quintana, E., Barclay, T., Still, M., Fortney, J., Gautier, T. N., I., Hunter, R., Caldwell, D. A., Ciardi, D. R., Devore, E., Cochran, W., Jenkins, J., Agol, E., Carter, J. A., and Geary, J. (2014). Validation of Kepler’s Multiple Planet Candidates. III. Light Curve Analysis and Announcement of Hundreds of New Multi-planet Systems. *ApJ*, 784:45.
- Sanchis-Ojeda, R., Rappaport, S., Winn, J. N., Kotson, M. C., Levine, A., and El Mellah, I. (2014). A Study of the Shortest-period Planets Found with Kepler. *ApJ*, 787:47.
- Sanchis-Ojeda, R., Rappaport, S., Winn, J. N., Levine, A., Kotson, M. C., Latham, D. W., and Buchhave, L. A. (2013). Transits and Occultations of an Earth-sized Planet in an 8.5 hr Orbit. *ApJ*, 774:54.
- Schlaufman, K. C., Lin, D. N. C., and Ida, S. (2010). A Population of Very Hot Super-Earths in Multiple-planet Systems Should be Uncovered by Kepler. *ApJL*, 724:L53–L58.

- Schmitt, J. R., Wang, J., Fischer, D. A., Jek, K. J., Moriarty, J. C., Boyajian, T. S., Schwamb, M. E., Lintott, C., Lynn, S., Smith, A. M., Parrish, M., Schawinski, K., Simpson, R., LaCourse, D., Omohundro, M. R., Winarski, T., Goodman, S. J., Jebson, T., Schwengeler, H. M., Paterson, D. A., Sejkpa, J., Terentev, I., Jacobs, T., Alsaadi, N., Bailey, R. C., Ginman, T., Granado, P., Vonstad Guttormsen, K., Mallia, F., Papillon, A. L., Rossi, F., and Socolovsky, M. (2014). Planet Hunters. VI. An Independent Characterization of KOI-351 and Several Long Period Planet Candidates from the Kepler Archival Data. *AJ*, 148:28.
- Skumanich, A. (1972). Time Scales for CA II Emission Decay, Rotational Braking, and Lithium Depletion. *ApJ*, 171:565.
- Smith, A. W. and Lissauer, J. J. (2009). Orbital stability of systems of closely-spaced planets. *Icarus*, 201:381–394.
- Steffen, J. H. and Farr, W. M. (2013). A Lack of Short-period Multiplanet Systems with Close-proximity Pairs and the Curious Case of Kepler-42. *ApJ*, 774(1):L12.
- Steffen, J. H. and Hwang, J. A. (2015). The period ratio distribution of Kepler’s candidate multiplanet systems. *MNRAS*, 448:1956–1972.
- Stone, N. C. and Leigh, N. W. (2019). A statistical solution to the chaotic, non-hierarchical three-body problem. *Nature*, 576(7787):406–410.
- Sussman, G. J. and Wisdom, J. (1988). Numerical evidence that the motion of pluto is chaotic. *Science*, 241(4864):433–437.
- Swift, J. J., Johnson, J. A., Morton, T. D., Crepp, J. R., Montet, B. T., Fabrycky, D. C., and Muirhead, P. S. (2013). Characterizing the Cool KOIs. IV. Kepler-32 as a Prototype for the Formation of Compact Planetary Systems throughout the Galaxy. *ApJ*, 764:105.

- Terquem, C. (2014). On the formation of the Kepler-10 planetary system. *MNRAS*, 444:1738–1746.
- Touma, J. R. and Sridhar, S. (2015). The disruption of multiplanet systems through resonance with a binary orbit. *Nature*, 524:439–441.
- Tremaine, S. and Dong, S. (2012). The Statistics of Multi-planet Systems. *AJ*, 143:94.
- Tremaine, S., Touma, J., and Namouni, F. (2009). Satellite Dynamics on the Laplace Surface. *AJ*, 137:3706–3717.
- Uehara, S., Kawahara, H., Masuda, K., Yamada, S., and Aizawa, M. (2016). Transiting Planet Candidates Beyond the Snow Line Detected by Visual Inspection of 7557 Kepler Objects of Interest. *ApJ*, 822:2.
- Valencia, D., Ikoma, M., Guillot, T., and Nettelmann, N. (2010). Composition and fate of short-period super-Earths. The case of CoRoT-7b. *AAP*, 516:A20.
- Van Eylen, V. and Albrecht, S. (2015). Eccentricity from Transit Photometry: Small Planets in Kepler Multi-planet Systems Have Low Eccentricities. *ApJ*, 808:126.
- Van Eylen, V., Albrecht, S., Huang, X., MacDonald, M. G., Dawson, R. I., Cai, M. X., Foreman-Mackey, D., Lundkvist, M. S., Silva Aguirre, V., Snellen, I., and Winn, J. N. (2019). The Orbital Eccentricity of Small Planet Systems. *AJ*, 157(2):61.
- Vick, M. and Lai, D. (2018). Dynamical tides in highly eccentric binaries: chaos, dissipation, and quasi-steady state. *MNRAS*, 476(1):482–495.
- Volk, K. and Gladman, B. (2015). Consolidating and Crushing Exoplanets: Did It Happen Here? *ApJL*, 806:L26.
- Wang, J., Fischer, D. A., Xie, J.-W., and Ciardi, D. R. (2015). Influence of Stellar Multiplicity on Planet Formation. IV. Adaptive Optics Imaging of Kepler Stars with Multiple Transiting Planet Candidates. *ApJ*, 813:130.

- Weidenschilling, S. J. and Marzari, F. (1996). Gravitational scattering as a possible origin for giant planets at small stellar distances. *Nature*, 384:619–621.
- Weiss, L. M., Fabrycky, D. C., Agol, E., Mills, S. M., Howard, A. W., Isaacson, H., Petigura, E. A., Fulton, B., Hirsch, L., and Sinukoff, E. (2020). The discovery of the long-period, eccentric planet kepler-88 d and system characterization with radial velocities and photodynamical analysis. *The Astronomical Journal*, 159(5):242.
- Weiss, L. M., Isaacson, H. T., Marcy, G. W., Howard, A. W., Petigura, E. A., Fulton, B. J., Winn, J. N., Hirsch, L., Sinukoff, E., Rowe, J. F., and California Kepler Survey, T. (2018). The California-Kepler Survey. VI. Kepler Multis and Singles Have Similar Planet and Stellar Properties Indicating a Common Origin. *AJ*, 156(6):254.
- Weiss, L. M., Rogers, L. A., Isaacson, H. T., Agol, E., Marcy, G. W., Rowe, J. F., Kipping, D., Fulton, B. J., Lissauer, J. J., Howard, A. W., and Fabrycky, D. (2016). Revised Masses and Densities of the Planets around Kepler-10. *ApJ*, 819:83.
- Wiegert, P. and Tremaine, S. (1999). The Evolution of Long-Period Comets. *Icarus*, 137:84–121.
- Winn, J. N., Sanchis-Ojeda, R., and Rappaport, S. (2018). Kepler-78 and the Ultra-Short-Period Planets. *ArXiv e-prints*.
- Winn, J. N., Sanchis-Ojeda, R., Rogers, L., Petigura, E. A., Howard, A. W., Isaacson, H., Marcy, G. W., Schlafman, K. C., Cargile, P., and Hebb, L. (2017). Absence of a Metallicity Effect for Ultra-short-period Planets. *AJ*, 154:60.
- Wittenmyer, R. A., Butler, R. P., Tinney, C. G., Horner, J., Carter, B. D., Wright, D. J., Jones, H. R. A., Bailey, J., and O’Toole, S. J. (2016). The Anglo-Australian Planet Search XXIV: The Frequency of Jupiter Analogs. *ApJ*, 819:28.
- Wright, J. T., Marcy, G. W., Howard, A. W., Johnson, J. A., Morton, T. D., and Fischer,

- D. A. (2012). The Frequency of Hot Jupiters Orbiting nearby Solar-type Stars. *ApJ*, 753:160.
- Wright, J. T., Upadhyay, S., Marcy, G. W., Fischer, D. A., Ford, E. B., and Johnson, J. A. (2009). Ten New and Updated Multiplanet Systems and a Survey of Exoplanetary Systems. *ApJ*, 693(2):1084–1099.
- Wu, Y. and Goldreich, P. (2002). Tidal Evolution of the Planetary System around HD 83443. *ApJ*, 564:1024–1027.
- Xie, J.-W., Dong, S., Zhu, Z., Huber, D., Zheng, Z., De Cat, P., Fu, J., Liu, H.-G., Luo, A., Wu, Y., Zhang, H., Zhang, H., Zhou, J.-L., Cao, Z., Hou, Y., Wang, Y., and Zhang, Y. (2016). Exoplanet orbital eccentricities derived from LAMOST-Kepler analysis. *Proceedings of the National Academy of Science*, 113:11431–11435.
- Xu, W. and Lai, D. (2016). Disruption of planetary orbits through evection resonance with an external companion: circumbinary planets and multiplanet systems. *MNRAS*, 459:2925–2939.
- Xuan, J. W. and Wyatt, M. C. (2020). Evidence for a high mutual inclination between the cold jupiter and transiting super earth orbiting men. *Monthly Notices of the Royal Astronomical Society*.
- Yee, S. W., Petigura, E. A., Fulton, B. J., Knutson, H. A., Batygin, K., Bakos, G. Á., Hartman, J. D., Hirsch, L. A., Howard, A. W., Isaacson, H., Kosiarek, M. R., Sinukoff, E., and Weiss, L. M. (2018). HAT-P-11: Discovery of a Second Planet and a Clue to Understanding Exoplanet Obliquities. *AJ*, 155(6):255.
- Zeng, L., Sasselov, D. D., and Jacobsen, S. B. (2016). Mass-Radius Relation for Rocky Planets Based on PREM. *ApJ*, 819:127.
- Zhu, W., Petrovich, C., Wu, Y., Dong, S., and Xie, J. (2018). About 30% of Sun-like

Stars Have Kepler-like Planetary Systems: A Study of their Intrinsic Architecture.

ArXiv e-prints.

Zhu, W. and Wu, Y. (2018). The Super Earth-Cold Jupiter Relations. *ArXiv e-prints.*